UNIVERSIDAD COMPLUTENSE DE MADRID

FACULTAD DE CIENCIAS QUÍMICAS

TESIS DOCTORAL

Bases moleculares de la interacción esticolisina-membrana sobre la estructura del poro y los efectos de los lípidos

Molecular basis of the sticholysin-membrane interaction on the structure of the pore and the effects of lipids

MEMORIA PARA OPTAR AL GRADO DE DOCTOR

PRESENTADA POR

Juan Palacios Ortega

DIRECTORES

Álvaro Martínez del Pozo
Johan Peter Slotte

UNIVERSIDAD COMPLUTENSE DE MADRID
FACULTAD DE CIENCIAS QUÍMICAS

TESIS DOCTORAL

Bases Moleculares de la Interacción Esticolisina-Membrana Sobre la Estructura del Poro y los Efectos de los Lípidos

Molecular Basis of the Sticholysin-Membrane Interaction On the Structure of the Pore and the Effects of Lipids

MEMORIA PARA OPTAR AL GRADO DE DOCTOR

PRESENTADA POR

Juan Palacios Ortega

DIRECTORES

Dr. Álvaro Martínez del Pozo
Dr. Johan Peter Slotte

2021

MOLECULAR BASIS OF THE STICHOLYSIN-MEMBRANE INTERACTION

On the Structure of the Pore and the Effects of Lipids

Juan Palacios Ortega

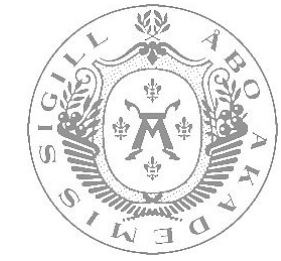

Åbo Akademi University

UNIVERSIDAD COMPLUTENSE MADRID

Biochemistry, Faculty of Science and Engineering
Åbo Akademi University
Turku, Finland

Bioquímica y Biología Molecular, Facultad de Ciencias Químicas
Universidad Complutense de Madrid
Madrid, España

2021

Supervised by:

Professor J. Peter Slotte
Biochemistry, Faculty of Science and Engineering
Åbo Akademi University
Turku, Finland

Professor Álvaro Martínez-del-Pozo
Department of Biochemistry and Molecular Biology, Faculty of Chemistry
Complutense University of Madrid
Madrid, Spain

Reviewed by:

Docent Katariina Öörni
Biochemistry
Wihuri Research Institute and University of Helsinki
Helsinki, Finland

Professor Alicia Alonso Izquierdo
Dept. of Biochemistry and Molecular Biology, Faculty of Science and Technology
University of the Basque Country
Leioa, Spain

Opponent:

Professor Ilpo Tapio Vattulainen
Department of Physics
University of Helsinki
Helsinki, Finland

Cover: Artistic all-atom representation of the process of pore formation of fluorescently labeled sticholysins. Table of contents from paper IV. Copyright (2021) American Chemical Society.

ISBN XXX-XXX-XX-XXXX-X (print)
ISBN XXX-XXX-XX-XXXX-X (pdf)
Painosalama Oy – Turku, Finland 2021

To everyone that
got me here

Table of Contents

LIST OF ORIGINAL PUBLICATIONS

The thesis is based on the original publications listed below. These are referred to by the indicated Roman numerals throughout the thesis.

I. Palacios-Ortega, J., García-Linares, S., Rivera-de-Torre, E., Gavilanes, J. G., Martínez-del-Pozo, Á., & Slotte, J. P. (2017). **Differential Effect of Bilayer Thickness on Sticholysin Activity**. *Langmuir*, 33(41), 11018-11027.

II. Palacios-Ortega, J., García-Linares, S., Rivera-de-Torre, E., Gavilanes, J. G., Martínez-del-Pozo, Á., & Slotte, J. P. (2019). **Sticholysin, Sphingomyelin, and Cholesterol: A Closer Look at a Tripartite Interaction**. *Biophysical Journal*, 116(12), 2253-2265.

III. Palacios-Ortega, J., Rivera-de-Torre, E., Gavilanes, J. G., Martínez-del-Pozo, Á., & Slotte, J. P. (2020). **Evaluation of Different Approaches Used to Study Membrane Permeabilization by Actinoporins on Model Lipid vesicles**. *Biochimica et Biophysica Acta (BBA)-Biomembranes*, 1862(9), 183311.

IV. Palacios-Ortega, J., García-Linares, S., Rivera-de-Torre, E., Gavilanes, J. G., Martínez-del-Pozo, Á., & Slotte, J. P. (2021**). Oligomerization of Sticholysins from Förster Resonance Energy Transfer**. *Biochemistry*, 60(4), 314-323. (The author is the corresponding author of this publication.)

Publications II and III were selected by the Spanish Society of Biochemistry and Molecular Biology (SEBBM) to feature in the section *Article of the Month* of the Society's webpage in August 2019 and August 2020, respectively.

CONTRIBUTIONS OF THE AUTHOR

I. The author designed the experiments together with supervisors. The author performed the anisotropy, SPR, ITC and calcein release experiments. The author analyzed the results and conceived the model presented in the paper. Professor Slotte synthesized 14:0-SM. The author contributed to the manuscript writing together with Professor Slotte and Professor Martínez-del-Pozo, with help from the other authors.

II. The author designed the calcein release experiments together with supervisors and Sara García-Linares. Professor Slotte devised the pyrene excimer-monomer experiments. The author came up with the SLPC-CTL experiment and optimized it with help from Professor Slotte. The author developed the FRET experiments together with both supervisors. Sara García-Linares performed and analyzed the calcein release experiments. The author performed all remaining experiments, calculations, and analyses. The author contributed to the manuscript writing together with Professor Slotte and Professor Martínez-del-Pozo, with aid from the other authors.

III. The author designed the experiments together with supervisors. The author suggested the use of R6G and Tb^{3+}. The author and Esperanza Rivera-de-Torre suggested and designed the H^{+}-fluorescein experiment. Professor Martínez-del-Pozo proposed the test of the dithionite-induced quenching of NBD-PE assay. The author and Esperanza Rivera-de-Torre performed the probe release experiments. The author performed the dithionite experiments. The author contributed to the manuscript writing together with Professor Slotte and Professor Martínez-del-Pozo, with help from the other authors.

IV. The author designed the experiments. The author designed, produced, purified, and labeled the sticholysin mutants. The author preformed the experiments and analyzed the results. The author developed the model used to evaluate stoichiometry from FRET. The author wrote the manuscript with contributions from Professor Slotte and Professor Martínez-del-Pozo, with help from the other authors.

ADDITIONAL PUBLICATIONS NOT INCLUDED IN THE THESIS MANUSCRIPT

García-Linares, S., Palacios-Ortega, J., Yasuda, T., Åstrand, M., Gavilanes, J. G., Martínez-del-Pozo, Á., & Slotte, J. P. (2016). **Toxin-induced Pore Formation Is Hindered by Intermolecular Hydrogen Bonding in Sphingomyelin Bilayers.** *Biochimica et Biophysica Acta (BBA)-Biomembranes,* 1858(6), 1189-1195.

Palacios-Ortega, J., García-Linares, S., Åstrand, M., Al Sazzad, M. A., Gavilanes, J. G., Martínez-del-Pozo, Á., & Slotte, J. P. (2016). **Regulation of Sticholysin II-induced Pore Formation by Lipid Bilayer Composition, Phase State, and Interfacial Properties**. *Langmuir*, 32(14), 3476-3484.

Rivera-de-Torre, E., Palacios-Ortega, J., García-Linares, S., Gavilanes, J. G., & Martínez-del-Pozo, Á. (2017). **One Single Salt Bridge Explains the Different Cytolytic Activities Shown by Actinoporins Sticholysin I and II from the Venom of *Stichodactyla helianthus***. *Archives of Biochemistry and Biophysics*, 636, 79-89.

García-Linares, S., Rivera-de-Torre, E., Palacios-Ortega, J., Gavilanes, J. G., & Martínez-del-Pozo, Á. (2017). **The Metamorphic Transformation of a Water-soluble Monomeric Protein into an Oligomeric Transmembrane Pore**. *Advances in Biomembranes and Lipid Self-Assembly* (Vol. 26, pp. 51-97). Academic Press.

García-Ortega, L. Palacios-Ortega, J., & Martínez-del-Pozo, Á. (2017). **Fungal Ribotoxins**. *eLS*, 1 9.

Al Sazzad, M. A., Möuts, A., Palacios-Ortega, J., Lin, K-. L., Nyholm, T. K. M., & Slotte, J. P. (2019). **Natural Ceramides and Lysophospholipids Cosegregate in Fluid Phosphatidylcholine Bilayers**. *Biophysical Journal*, 116(6), 1105-1114.

Rivera-de-Torre, E., Palacios-Ortega, J., Gavilanes, J. G., Martínez-del-Pozo, Á., & García-Linares, S. (2019). **Pore-Forming Proteins from Cnidarians and Arachnids as Potential Biotechnological Tools**. *Toxins*, 11(6), 370.

Rivera-de-Torre, E., Palacios-Ortega, J., Garb, J. E., Slotte, J. P., Gavilanes, J. G., & Martínez-del-Pozo, Á. (2020). **Structural and Functional Characterization of Sticholysin III: A Newly Discovered Actinoporin within the Venom of the Sea Anemone *Stichodactyla helianthus***. *Archives of Biochemistry and Biophysics*, 108435.

Rivera-de-Torre, E., Palacios-Ortega, J., Slotte, J. P. Gavilanes, J. G., Martínez-del-Pozo, Á., & García-Linares, S. (2020). **Functional and Structural Variations among Sticholysins, Pore-forming Proteins from the Sea Anemone *Stichodactyla helianthus*.** *International Journal of Molecular Sciences*, 21(23), 8915.

Palacios-Ortega, J., Rivera-de-Torre, E., Gavilanes, J. G., Slotte, J. P., Martínez-del-Pozo, Á., & García-Linares, S. (2021) **Biophysical Approaches to Study Actinoporin-lipid Interactions.** *Methods in Enzymology*, *649*, 307-339.

ACKNOWLEDGEMENTS

This work was performed at the Laboratory of Lipid and Membrane Biochemistry at the Faculty of Science and Engineering of Åbo Akademi University, Turku, and at the Laboratory of Protein Structure and Function, at the Faculty of Chemistry of Complutense University of Madrid, from 2017 to 2020.

I would like to thank my supervisors, Professor *J. Peter Slotte* and Professor *Álvaro Martínez del Pozo*, for giving me the chance to work in their respective research groups, first as an undergrad, then as a master's, and, finally, as a PhD student, and for their guidance and help while I worked on the research presented here. I would also like to thank them for their help when travelling back and forth between Finland and Spain.

I would also like to thank Professor *Mark S. Johnson* for agreeing to be my official supervisor once Professor *Slotte* retired from office. I also wish to thank Professor *José G. Gavilanes*, who has always been a source of wisdom and counsel.

Next, I would like to thank *Esperanza Rivera de Torre* and *Sara García Linares* for initially taking me on as their apprentice and instructing me on how to work in a laboratory. I would also like to thank them for their collaboration in all the projects we have shared over the years, and for helping me whenever I needed them.

I would also like to thank all present and past members of both research groups—especially *Thomas Nyholm, Oskar Engberg, Kai-Lan Lin, Anna Moüts, Henrik Nurmi, Victor Hautala,* and *Max Lönnfors* from the Finnish laboratory. From the Spanish side, *Moisés Maestro López*, *Rodrigo Lázaro Gorines, Javier Narbona Corral*, *Diego Heras Márquez*, and everyone from the L1, our neighbor laboratory.

My most especial thanks to *Sara Hernández Pérez*, for sharing this adventure in the cold lands of Finland with me, and for always being there for me.

Finally, I would like to express my deepest gratitude to my family, specially to my parents *Francisco Javier Palacios Muñoz* and *Concepción Ortega Pérez*, my sister *María Palacios Ortega*, my grandparents, and the rest of my family. With their care, their wisdom, and the value they have always place on knowledge, culture, and hard work, they made me the person I am today.

I am grateful for the financial support provided by Åbo Akademi University and the National Doctoral Program of Informational and Structural Biology (ISB). This work was supported by grants from the Sigrid Juselius Foundation, the Magnus Ehrnrooth foundation, and the Jane and Aatos Erkko foundation.

Juan Palacios Ortega
May 2021

ABBREVIATIONS

14:0-SM	*N*-myristoyl-D-*erythro*-sphingosylphosphorylcholine
7-SLPC	1-palmitoyl-2-(7-doxyl)-stearoyl-*sn*-glycero-3-phosphocholine
BLAST	Basic local alignment search tool
$C_{12}E_8$	Octaethylene glycol monododecyl ether
Cer	Ceramide
CHAPS	3-[(3-cholamidopropyl)-dimethylammonio]-1-propanesulfonate
Chol	Cholesterol
CTL	Cholestatrienol
di-14:1-PC	1,2-dimirystoleoyl-*sn*-glycero-3-phosphocholine
di-16:1-PC	1,2-dipalmitoleoyl-*sn*-glycero-3-phosphocholine
di-18:1-PC	1,2-dioleoyl-*sn*-glycero-3-phosphocholine, also DOPC
di-20:1-PC	1,2-dieicosenoyl-*sn*-glycero-3-phosphocholine
di-22:1-PC	1,2-dierucoyl-*sn*-glycero-3-phosphocholine
DOPC	1,2-dioleoyl-*sn*-glycero-3-phosphocholine, also di-18:1-PC
DPH	1,6-diphenyl-1,3.5-hexatriene
E/M	Excimer/monomer
eSM	Egg sphingomyelin
FraC	Fragaceatoxin C
FRET	Förster resonance energy transfer
ITC	Isothermal titration calorimetry
L/P	Lipid / protein
L_d	Liquid-disordered phase
L_o	Liquid-ordered phase
LUV	Large unilamellar vesicle
M_w	Molecular weight
NBD	*N*-(7-Nitrobenz-2-Oxa-1,3-Diazol-4-yl)
OCer	*N*-oleoyl-D-*erythro*-sphingosine
PC	Phosphatidylcholine
PFTs	Pore-forming toxins
p*I*	Isoelectric point
PL	Phospholipid
PnSL	Phosphonosphingolipids
POC	Phosphocholine
POPC	1-palmitoyl-2-oleoyl-*sn*-glycero-3-phosphocholine
PSM	*N*-palmitoyl-D-*erythro*-sphingosylphosphorylcholine
Pyr-SM	*N*-C10-pyrene-D-*erythro*-sphingosylphosphorylcholine

R_0	Förster distance
SEM	Standard error of the mean
SM	Sphingomyelin
S_o	Solid-ordered or gel phase
StnI	Sticholysin I
StnII	Sticholysin II
TCDB	Transporter classification database
tPa	*trans*-Parinaric acid
tPa-SM	*trans*-Parinaroyl- D-*erythro*-sphingosylphosphorylcholine
WT	Wild type

ABSTRACT

The usefulness of toxicity across the tree of life is far beyond doubt. Most, if not all, organisms produce compounds that can be used for attack and/or defense against external entities. Some of the most specialized of these compounds are toxic proteins, among which pore-forming toxins (PFTs) particularly excel. PFTs are present in all kingdoms of life. Given the wide variety of PFTs, one can expect a multitude of different specificities and mechanisms of action, of which we will certainly take advantage at some point. For that, a thorough characterization of PFTs and their functionality is necessary. In this thesis, we have taken further the characterization of sticholysins, small PFTs produced by the sea anemone *Stichodactyla helianthus*.

In paper I, the influence of bilayer thickness on the pore forming activity of sticholysins has been studied. Model lipid bilayers made mainly of a phosphatidylcholine (PC), with two monounsaturated acyl chains that determined membrane thickness, were used. Myristoyl-sphingomyelin (14:0-SM) was included to ensure membrane recognition by sticholysins. The effect of cholesterol (Chol) was also evaluated. The preferred thickness for sticholysins was that of di-18:1-PC membranes. This seems to be a result of evolutionary pressure since it agrees with the most common acyl chains found in analyzed fish.

In paper II, different fluorescent derivatized lipids, Sticholysin II (StnII) tryptophan mutants, and oleoyl-ceramide (OCer) were used to delve into the relationship between StnII and Chol and sphingomyelin (SM). We found that Chol favored SM recognition by StnII while, concomitantly, StnII rearranged the membrane, extracting Chol from the SM-rich domains. In fact, Chol was preferentially distributed near StnII.

In paper III, we evaluated the mechanism of the release of aqueous contents from vesicles. Several different probes were employed. We found that the StnII pore is too small for calcein to leak through. We propose that molecules of comparable size to calcein are released through the membrane perturbations produced by StnII during pore formation. The final pore would only let through very small molecules, such as dithionite.

In paper IV, a single-cysteine mutant of StnI was used to study oligomerization directly in unrestrained environments, such as that of model membranes. The results are consistent with previous structures obtained for other actinoporins. Furthermore, we have observed that the stoichiometry of the complex was maintained when StnII was included in the complex. The results in solution also support the previously observed ability of StnII to promote StnI binding to membranes.

SAMMANDRAG

Nyttan av toxicitet hos olika organismer är långt bortom tvivel. De flesta, om inte alla, organismer producerar föreningar som kan användas för attack och/eller försvar mot externa hot. Några av de mest specialiserade av dessa föreningar är toxiska proteiner, bland vilka por-bildande toxiner (eng., *pore-forming toxins*, PFT) är särskilt utmärkande. PFT finns i alla livets riken. Med tanke på det stora utbudet av PFT kan man förvänta sig en mängd olika specificiteter och verkningsmekanismer, som vi kan komma att dra nytta i olika tillämpningar. Därför är en grundlig karakterisering av PFT-peptider och deras funktionalitet nödvändig. I denna avhandling har vi undersökt och karakteriser olika stickolysiner, vilka är små PFT-peptider producerade av havsanemonen *Stichodactyla helianthus*.

I arbete I har påverkan av membraners dubbelskiktstjocklek på den porbildande aktiviteten hos stikolysiner studerats. Modellmembraner tillverkade huvudsakligen av en fosfatidylkolin (PC), med två enkelomättade acylkedjor. Genom att variera acylkedjans längd kunde de bildade bilagrens tjocklek påverkas. Myristoyl-sfingomyelin (14:0-SM) inkluderades för att säkerställa membranigenkänning hos stickolysinerna. Effekten av kolesterol (eng., cholesterol, Chol) utvärderades också eftersom det också påverkar bilagertjockleken. Den mest optimala membrantjockleken för stickolysiner var den tillverkad av di-18: 1-PC. Detta verkar vara ett resultat av evolutionärt tryck eftersom det överensstämmer med de vanligaste acylkedjorna som finns i membraner hos tex fisk.

I arbete II användes olika fluorescerande lipider, tryptofanmutanter av sticholysin II (StnII) och oleoyl-ceramid (OCer) för att studera samverkan mellan StnII och membrane innehållande Chol och sfingomyelin (SM). Vi fann att Chol gynnade SM-igenkänning av StnII medan StnII samtidigt ordnade upp membranet och drog ut Chol från de SM-rika domänerna. I själva verket distribuerades Chol företrädesvis nära StnII.

I arbete III utvärderade vi mekanismen för frisättning av vattenlösliga småmolekylära föreningar från membranvesikler. Flera olika sonder användes vid studierna. Vi fann att StnII-poren är för liten för att kalcein skall läcka igenom. Eftersom kalcein ändå frigörs från vesikler när de exponeras för stickolysiner, antar vi att andra orsaker än porer förorsakar ökad membranpermeabilitet i närvaro av stickolysiner. Den slutliga poren kan bara släppa igenom mycket små molekyler, såsom ditionit.

I arbete IV användes en cysteinmutant av StnI för att studera oligomerisering direkt i lösning eller i bilagermembraner. Resultaten som erhölls överensstämmer med tidigare visade strukturer för andra aktinoporiner. Vidare har vi observerat att

porkomplexets stökiometri bibehölls när StnII inkluderades med StnI i komplexet. Resultaten med Stn i lösning stöder den tidigare observerade förmågan hos StnII att främja Stnl-bindning till membran.

RESUMEN

La toxicidad es indudablemente útil para los seres vivos. La mayoría, si no todos los organismos, producen compuestos para usarlos contra otros seres vivos, ya sea con fines de defensa o de ataque. Algunos de los más especializados de estos compuestos son las proteínas tóxicas, entre las que destacan las toxinas formadoras de poros (ing., *pore-forming toxins*, PFT). Estas proteínas pueden encontrarse en todos los reinos de la vida. Dada su amplia diversidad, puede esperarse que tengan una gran variedad de especificidades y mecanismos de acción. Una caracterización detallada de las PFT y su funcionalidad es un requisito fundamental para, en un futuro, poder beneficiarse de la acción de estas toxinas. Por ello, en esta tesis se ha profundizado en el comportamiento de las esticolisinas, pequeñas PFT producidas por la anémona del mar Caribe *Stichodactyla helianthus*.

En el artículo I, se estudió la influencia del grosor de membrana en la actividad de formación de poros de las esticolisinas. Para ello, se utilizaron bicapas lipídicas hechas principalmente de fosfatidilcolina (PC) con cadenas de acilo monoinsaturadas, cuya longitud determinaba el grosor de la membrana. La miristoil-esfingomielina (14:0-SM) fue incluida para asegurar la unión a la membrana de las esticolisinas. Se evaluó también el efecto del colesterol (ing., *cholesterol*, Chol). El grosor preferido resultó ser el de las membranas que incluían di-18:1-PC. Esta preferencia parece ser resultado de la presión evolutiva, ya que coincide con la longitud de las cadenas de acilo más comunes en los peces analizados.

En el artículo II, se profundizó en la relación entre la esticolisina II (StnII), el Chol y la esfingomielina (SM). Para ello, se utilizaron diferentes lípidos fluorescentes, mutantes de triptófano de la esticolisina II (StnII) y oleoil-ceramida (OCer). Los resultados obtenidos sugieren que el Chol favorece el reconocimiento de la SM por parte de StnII mientras que, simultáneamente, StnII remodela la membrana, extrayendo el Chol de los dominios ricos en SM. De hecho, una vez alcanzado el equilibrio, el Chol resulta estar distribuido preferentemente cerca de StnII.

En el artículo III, se evaluó el mecanismo de liberación de contenidos acuosos de vesículas modelo, empleando diferentes sondas fluorescentes. De acuerdo con las observaciones, el poro de StnII es demasiado pequeño para que la calceína pueda pasar a través de él. Se propone, por tanto, que la liberación de moléculas de tamaño comparable al de la calceína se produce a través de perturbaciones en la membrana inducidas por StnII durante la formación del poro. El poro final sólo dejaría pasar moléculas de menor tamaño, como puede ser la molécula de ditionito.

En el artículo IV, se utilizó un mutante puntual de cisteína de StnI para estudiar la oligomerización de las esticolisinas directamente en un ambiente sin restricciones, como es el de la superficie de las membranas modelo. Los resultados obtenidos son coherentes con las estructuras anteriores obtenidas para otras actinoporinas. Además, hemos observado que la estequiometria del complejo se mantiene cuando al mezclar ambas esticolisinas. Los resultados obtenidos en ausencia de membranas refuerzan las observaciones previas que sugerían que StnII es capaz de facilitar la actividad de StnI, presumiblemente porque estaría favoreciendo su unión a la membrana.

1. INTRODUCTION

Toxicity, though not always obvious, is widespread in life. All kind of organisms, from bacteria to mammals, produce toxic compounds. The nature and targets of these compounds, however, can be extremely varied. Toxins can be as simple as small molecules or as intricate as a large protein complex. Their targets can be structures inside of cells, such as ribosomes, or on their outside, such as membrane receptors. There is, however, one structure that particularly stands out as a target for toxins, which is the cellular membrane, and particularly the lipid bilayer. The structure of the bilayer is very similar in all living beings. The plasma membrane is of capital importance to all cells, providing the barrier between the self and the non-self, while fulfilling many other functions. In eukaryotes, membranes additionally provide compartmentalization, helping optimize cellular processes [1]. Most cells have lipid membranes that are completely exposed to the outside world.

For these reasons, membranes can be considered as excellent toxin targets due to their availability and vital importance. They are targeted various toxins, many of which are pore-forming toxins (PFTs) [2-5]. PFTs are usually produced by bacteria, but many other organisms produce them as well. In many animals, PFTs are a constituent of the immune system [6-9]. In many other organisms, they are a fundamental component of their venoms. Such is the case with many sea anemones, in whose venom actinoporins play a major role [10].

Actinoporins are small, basic proteins [11-13]. They specifically bind to their target membranes by recognition of sphingomyelin (SM), often considered to be the actinoporin receptor [14-16]. However, other physicochemical features of the membrane can greatly influence actinoporin functionality [16-25]. The presence and effect of cholesterol (Chol) in the membrane is possibly the most remarkable of these [15, 19, 22, 23, 25-28]. The pores made by these toxins, which are cation-selective, are formed once the oligomers are bound to the membrane [17]. The oligomerization steps, however, as well as the stoichiometry of the pore complex, remain to be solved in full detail.

Various actinoporins, from many different sea anemones, have been found and described so far. Nevertheless, the soluble structure of only four of them, sticholysin I (StnI) and II (StnII), equinatoxin II (EqtII), and fragaceatoxin C (FraC), has been resolved in atomic detail [29-35]. StnI and StnII are both produced by the same sea anemone, *Stichodactyla helianthus*, and despite years of research, many details regarding their behavior and mechanism of action still remain unknown. Some of those questions, such as the effect of membrane thickness and the details of Chol's

effect on actinoporin activity, the probe selectivity of the pores, and the stoichiometry adopted by these proteins in unrestrained environments, have been tackled here. Using a variety of biophysical techniques, new information is brought to light regarding these issues. The results obtained have contribute to a better understanding of the behavior of these metamorphic proteins.

2. REVIEW OF THE LITERATURE

2.1. Early reports on *Stichodactyla helianthus'* toxins and other actinoporins

Sea anemones have been known to be toxic since ancient times. One only needs to touch these animals to feel the effect of their venom. However, it was not until after the coming of the molecular sciences that the attention of a part of the scientific community was drawn to venomous animals in order to systematically find within them compounds and substances that might have potential therapeutic uses. This attention first focused on coelenterates in the 1960s and early 1970s [36-38]. The purification of toxins from the sea anemone, then known as *Stoichactis helianthus*, was first reported in Canada in 1974 by J. P. Devlin who had obtained the anemones from Barbados [39]. The toxin was not shown to be purified to homogeneity. However, the obtained cocktail displayed strong hemolytic activity.

As early the following year, in 1975, Bernheimer and co-workers at New York University (New York, NY) reported the specific binding of that toxin to SM [40]. In their paper, the researchers also presented the first estimates of the molecular weight (M_w), amino acid composition, and p*I* of the toxin. Not only that but they also pointed out the resemblance of the purified toxin with "*the nematocysts toxin of the sea anemone* Actinia equina" [40], which would be referred to as equinatoxin. Follow-up studies were published by the same group, focusing mainly on the SM-specificity displayed by the toxin, and its potential interaction with the choline moiety of SM [41, 42]. One paper presented the earliest report of toxin-induced release of aqueous contents by a *S. helianthus* toxin, performed using ^{14}C-labeled glucose [41]. In another paper, a toxin-ferritin conjugate was used to highlight the toxin specificity for sphingomyelin by taking electron micrographs of liposomes with and without SM. The researchers observed that liposomes were only labeled if SM was present. However, the authors apparently missed what was their most remarkable result: the first micrographs of the pore structures. These can be clearly appreciated in Figure 8A of the paper, shown here in Figure 1 [42].

Figure 1. *Electron micrograph of* S. helianthus *toxin's membrane-bound structures, now known to be pores, as shown by Linder* et al.*, 1977 [42]. Reproduced under Elsevier's license number 4961291129782.*

After that, in 1979, a double paper was published by D. W. Michaels and colleagues from the Johns Hopkins University in Baltimore, MD, still using Devlin's extract and/or the New York purified version [43, 44]. These papers were the first to report that the formation of transmembrane channels was responsible for increased membrane permeability. Furthermore, the cation-selectivity of these pores was then first demonstrated. Channel conductance was further explored by Varanda and Finkelstein at the Albert Einstein College of Medicine in New York [17]. They showed that the channels were selective to univalent cations in a pH-dependent manner, which was indicative of negatively charged residues at the pore lumen. Poor selectivity to Ca^{2+} was observed, being accounted for by Ca^{2+} binding to negatively charged sidechains and blocking the pore lumen.

In 1982, Blumenthal and Kem, at the University of Florida, were the first to sequence the toxin, termed by them "Cytolysin III," with no mention of the previous I and II [45, 46]. They also made the first prediction of its secondary structure elements. From their analysis, now we can see that, even with some flaws (essentially, residues 30 to 52 are missing), they sequenced StnII. It was not until 1988 that Kem and Dunn reported the discovery of four "sequence variants" of the *S. helianthus* toxin, still referring to them as Cytolysins [47]. Cytolysin III, being hemolytically strongest, was chosen to be further characterized in subsequent studies [48, 49]. At the same time, other smaller peptide components, which turned out to be neurotoxins, were being found in the venom of *S. helianthus* [50]. After this, however, no more studies would be published on this subject by groups based in the United States. Nevertheless, in the late 1980s, the first immunotoxins based on these proteins would be reported from a group in Cuba [51, 52]. This country would be the origin of the second wave of studies of *S. helianthus* toxins.

Meanwhile, equinatoxin, from *A. equina*, was being characterized in Europe. It had been first purified and characterized, as the *Stoichactis* toxin, in 1974, by the group of Ferlan and Lebez in Ljubljana, Slovenia [53-55]. The first partial sequence of equinatoxin was reported nine years later, in 1983 [56]. By that time, equinatoxin had been described as hemolytic and assayed *in vivo* [54, 57-59], and three different equinatoxin isoforms would be identified shortly after [60]. In fact, equinatoxins would be subject to much more scrutiny over the following 10 years [61-67], when it was reported that EqtII also formed cation-selective channels, modifying the Ca^{2+} fluxes in the affected cells and, most importantly, that its N-terminal sequence would fold as an amphipathic α-helix, which was in turn responsible for membrane penetration. EqtII would then be the first actinoporin to be cloned, sequenced at the DNA level, and produced in a heterologous system in 1996 [68].

It was in 1994 when the term *sticholysin* first appeared in the literature in a report from the group of Lanio and Pazos at the University of Havana, in La Habana, Cuba [69]. In that report, the full amino acid sequence of a sticholysin (in fact, StnII) was first reported complete and compared to those of the former Cytolysin III and EqtII. Shortly after, StnI and StnII were given the names they still have today [70, 71]. The group from La Habana would then continue characterizing these proteins, both on their own and in collaboration with Spanish and Italian groups [18, 72], forming the seed from which this thesis, many years later, would come to be.

The major findings of the subsequent studies in the field, by the aforementioned groups and some other researchers, shall be the focus of the subsequent sections. Before moving on, it should be mentioned that the first reports on FraC, now one of the four best characterized actinoporins, did not appear until 2009 [33, 73]. Finally, we should also acknowledge the great number of studies regarding toxins (both actinoporins and other) from many other sea anemones, such as *Anemonia sulcata*, *Heteractis magnifica*, *Heteractis crispa*, and *Actinia tenebrosa*, to name a few, that were published during the years reviewed in this section [74-84].

2.2. Classification and general characteristics of sticholysins

Sticholysins belong to the actinoporin family. They are small, cysteinless proteins with basic p*I* [11-13, 85]. They form cation-selective pores of 1–2 nm in diameter on their targeted cells, provoking cell death by means of osmotic shock [17, 18, 66, 72, 86]. These proteins are said to be hemolytic since they have the ability to disrupt erythrocytes, which is the basis of a widely used activity assay [60, 65, 84]. The classification, origin, and structural and functional features of these proteins are detailed in the following sections.

2.2.1. Channels, pore-forming toxins, and the actinoporin family

The Transporter Classification Database (TCDB) has organized all membrane transport proteins according to their class, subclass (which usually refers to the energy source of the transporter), family, and subfamily. PFTs are classified as channels, under the code 1.C and, in this classification, comprise 128 different families. Actinoporins, which in the TCDB are referred to as "the Pore-forming Equinatoxin Family," are classified in a single subfamily under the code 1.C.38.1 [87].

The classic way of classifying PFTs, however, ranks actinoporins as one of the three major families of α-PFTs [3]. The basis of this classification, unlike that of the TCDB, lies on the secondary structure lining the walls of the pores of the corresponding PFT

[4, 5, 88-93]. Actinoporins, as colicins and cytolysin A-related toxins, form a pore whose walls are lined with α-helices. The remaining PFTs, which comprise the families of bacterial haemolysins, cholesterol-dependent cytolysins, and aerolysins, are β-PFTs, based on their pore walls being lined by β-strands [3]. In spite of sharing a category, each of the families displays its own fold and pore formation mechanism. Membrane specificities can differ within the families, with the receptors being as varied as specific sugar moieties, lipids, such as Chol or SM, and specific proteins of the target organism, which can be the case of some pathogen-produced toxins.

2.2.2. Actinoporins in sea anemones and other organisms

Actinoporins, among which sticholysins are found, are cytolysins produced by sea anemones. These proteins are the main component of their venom, used for hunting purposes. Yet since they can be found not only in the venom but also in the coelomic fluid and the surroundings of these animals as well, they are also considered to play a role in the defense of these organisms [11, 94]. The reason for the existence of several actinoporin isoforms within a single species of sea anemones is not known, although it has been proposed that it could, among other things, broaden the range of targets [95, 96].

At least 20 different species of sea anemones have been observed to produce actinoporins though not all actinoporins have been sequenced [11, 13, 73, 97]. In spite of having multiple actinoporin sequences encoded in their genome, most sea anemones generally produce only a small number of these toxins in detectable quantities [10, 11, 13, 96, 98, 99]. If a basic local alignment (with the basic local alignment search tool, BLAST) is performed on UniProtKB [100] using the sequence of StnII as the query, 31 of the obtained results (as of November 2020) are proteins produced by species in the Cnidaria phylum, of which 24 come from the Actinaria order (sea anemones), and 8 from the Scleractinia order (stony corals). All sequenced and characterized actinoporins display high sequence identity (57–90%, Figure 2). If a sequence alignment is performed with the 20 sequences that have been reviewed in UniProtKB, the analysis shows that 55 residues are conserved in all of them, 36 have "strongly similar properties," and 19 show weakly similar properties, according to the scoring they obtain in the Gonnet PAM 250 matrix. There are still five positions more that are conserved in at least 18 of the sequences, adding up to 115 out of the 175 residues that make StnII (~66%).

It is interesting to note that, among all the reviewed sequences that showed up on the BLAST, there was a protein, bryoporin, from *Physcomitrella patens* (a moss), which shows some of the conserved motifs that are considered to be landmarks in the

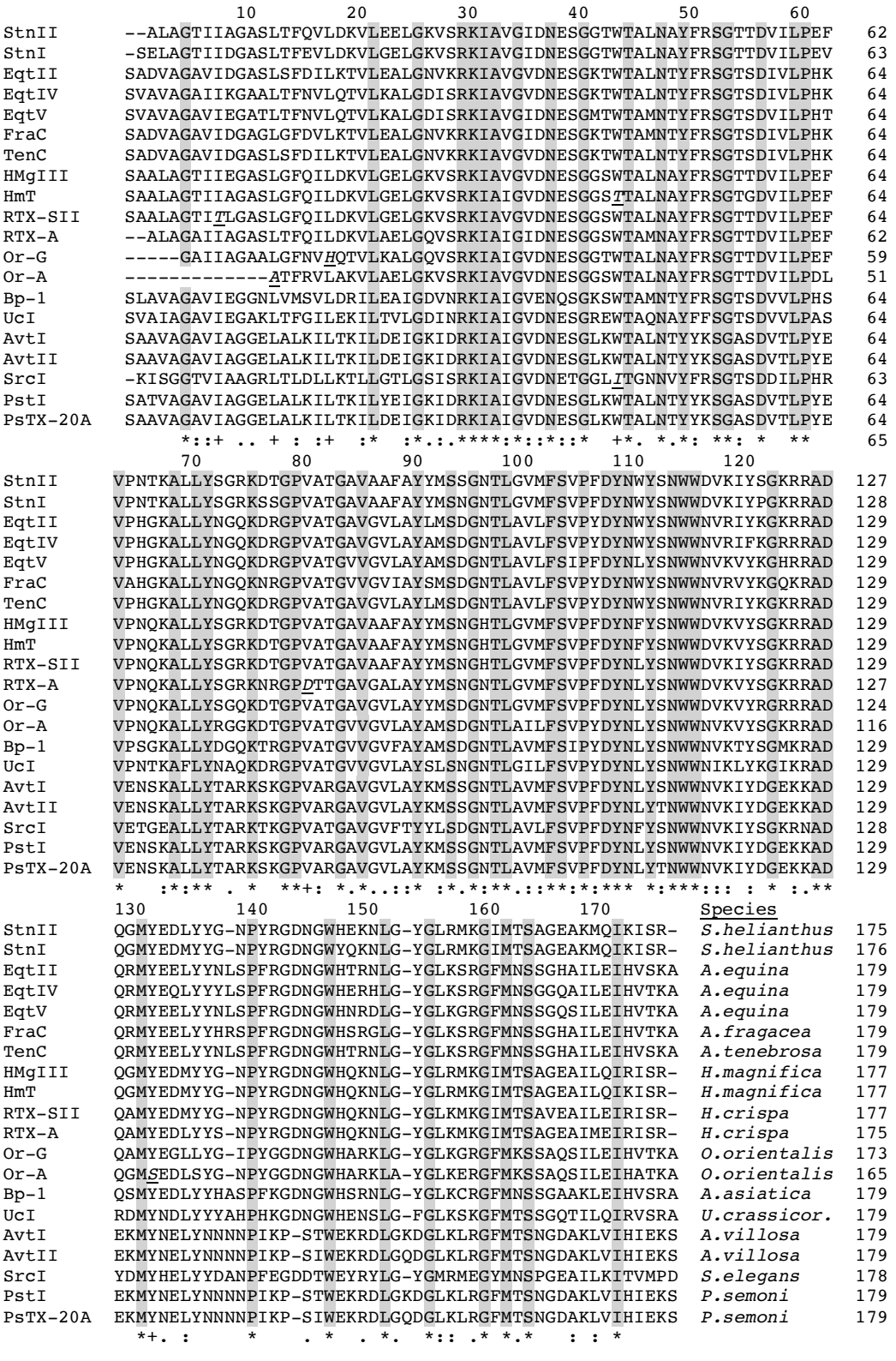

Figure 2. *Sequence alignment of known actinoporin sequences made with ClustalΩ. Consensus, calculated by ClustalΩ using the Gonnet PAM-250 matrix, is indicated in the last line: asterisk (*) indicates total conservation, colon (:), strong conservation of similar properties, and period (.) conservation of weakly similar properties. A plus (+), added afterward, outside of the analysis, indicates that the residue is conserved in all but one or two of the aligned sequences. The numbering is that of StnII.* P. semoni*, which produces the last two proteins, is a stony coral.*

actinoporin fold. The presence of such a protein in a moss appears to have been a result of convergent evolution or horizontal gene transfer [101].

From the sequences, it can be readily observed that actinoporins are cysteinless (all but one in the alignment), with lengths ranging between 165 and 179 residues, with most being closer to the latter number (Figure 2). This is one of the features presented by most of them, along with, in most cases, a basic p*I* [11-13, 85]. The alignment also reveals some sequence motifs. Indicated according to StnII numbering, the most important ones are at positions 29 to 40, at 67 to 71, and the region between residues 92 and 127, in which the P[F/I]DYN[W/L/F]Y[S/T]NWW part (residues 105 to 115) is an essential component of the actinoporin aromatic cluster and is used to identify new possible actinoporins [10, 101]. The high degree of conservation of these residues is indicative of their importance in the folding and function of these proteins, as is pointed out below.

2.3. The structure of sticholysins and the actinoporin fold

The most remarkable ability of these proteins, which is also the basis for their function, is that they are capable of adopting two different folds. One is water-soluble, whereas the other is adopted upon an encounter with a membrane with suitable properties. Most of the three-dimensional structure of actinoporins remains the same in both folds [31, 35]. Nevertheless, nearly 20% of the residues significantly change their relative position upon this structural metamorphosis. Furthermore, a concomitant oligomerization process is started. This is a clear confirmation that the three-dimensional structure adopted by a protein is not only dependent in its sequence, but as well as on the environment that it is exposed to.

To date, the water-soluble structures of StnI, StnII, EqtII, and FraC have been resolved in atomic detail, either by X-ray crystallography or by nuclear magnetic resonance [29-35]. In all cases, this fold consists of a β-sandwich flanked by two α-helices (Figure 3). The α-helices rest on the exterior surface of each of the two β-sheets. The first β-sheet is made up of five to six antiparallel β-strands. The first of those β-strands is just four residues long and a part of the segment of the protein that is eventually responsible of membrane penetration. Likewise, the other β-sheet is also made up of antiparallel β-strands.

From a structural and functional point of view, these proteins have the following four significant regions/features: the N-terminal α-helix, the exposed cluster of aromatic residues, the phosphocholine (POC) binding site, and an array of basic amino acids.

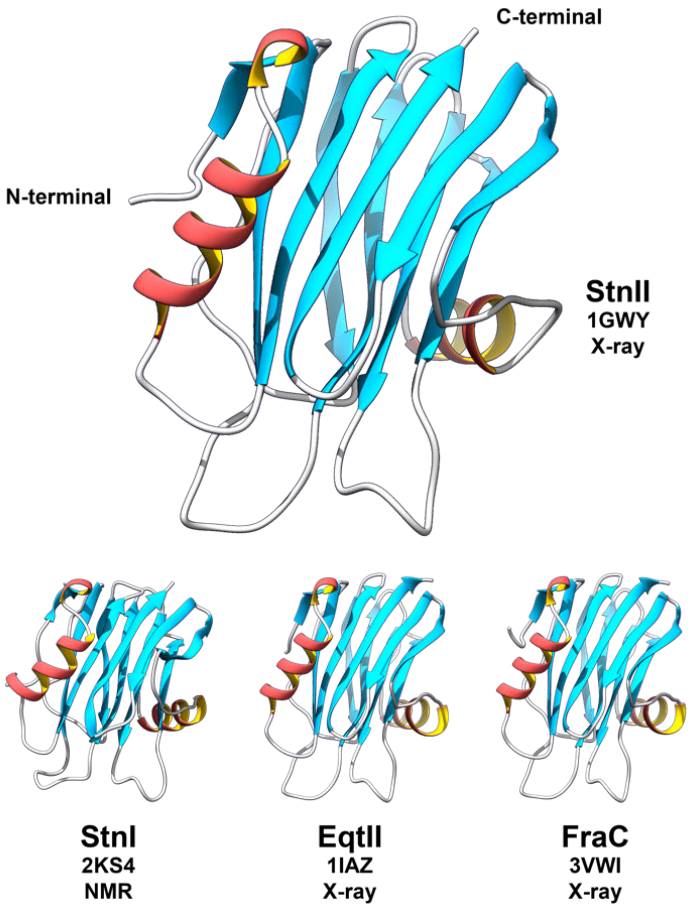

Figure 3. *The three-dimensional structures of actinoporins resolved to date. The name of each protein, along with its PDB accession code and method used to obtain the structure is indicated. The α and 3_{10} helices are depicted in red and yellow. β-strands are in light blue. Regions with non-periodic secondary structures are in light gray. The PDB structure of StnII is used in subsequent figures, unless otherwise indicated. All figures are made with UCSF Chimera, unless otherwise indicated [108].*

2.3.1. The N-terminal α-helix and the β-strands holding it

The first 30 residues of the protein are folded into a short β-strand, followed by a 3_{10} helix and a 10-residue-long α-helix [29, 31, 32, 34, 35, 102, 103]. This stretch has the highest conformational freedom of these proteins. It detaches from the β-sandwich and can fold into an amphipathic α-helix. While the first 30 residues focus most of the variability in these proteins, the β-sheet on which the helix lies in the soluble fold has two of the most conserved sequences: the 29-RKIA[I/V]G[V/I][D/E]N[E/Q][S/T]G-40 and the 67-KA[L/F]LY-71 stretches (Figure 4a). The N-terminal α-helix, by changing its extension and relative orientation to the rest of the protein, is responsible for membrane penetration and lining the pore lumen [102, 104-107].

All actinoporins have polar residues among their first 30 residue stretch. They are sorted so that they face the pore lumen. Their identity, however, is quite varied. In the

first half of this stretch, some present only uncharged polar amino acids, such as Thr and Ser. This is the case with StnII. In turn, StnI, has three acidic residues in addition to the polar amino acids. Thus, its helix has a much more marked negative character [109-111] (Figure 4b). At positions 18 and 19, all actinoporins have polar, complementary residues, most often charged. The sequence in StnI and StnII is Asp-Lys, while in EqtII and FraC it is Lys-Thr. The sidechains of those residues might establish interactions among different subunits to stabilize the final oligomer. Another pair of acid-basic residues appears at positions 22/23 and 26. There is no evidence that these residues interact between them in any of the folds. Nevertheless, it is interesting to note that some actinoporins have a Glu-Lys pair, while others have a Lys-Asp pair, positioned the other way around. In all actinoporins, those two residues have a different charge. These residues might interact with the head groups of lipids in the fenestrations observed in the available pore structures [35].

The hydrophobic residues that form the apolar part of the helix, on the contrary, are, in general, much more conserved, with Leu12 and Phe14 particularly standing out. In fact, they appear to play a double role: they are the part of the helix that stays in contact with the lipids when the helix penetrates the membrane, but they are also responsible, for the most part, for keeping the helix attached to the β-sandwich when the protein is in its soluble form. Phe14 has also been said to be relevant in oligomerization in membranes with tightly packed lipids, such as those with a high Chol content [112].

Residues Arg29 and Lys30 are conserved among all actinoporins as well. In the soluble form of these proteins, Arg29 is likely involved in a cation-π interaction with Phe106 (Tyr in some actinoporins) (Figure 4c) [113]. It is possible that, upon membrane binding, the loop at which Phe106 is located is displaced, releasing the sidechain of Arg29, triggering the deployment of the N-terminal α-helix. Lys30 appears to also play a role in this process. In all resolved structures except that of StnI, Lys30 forms a hydrogen bond with the carbonyl oxygens of Leu21 and Gly25, a residue that is also always conserved (Figure 4c). This hydrogen bond might be affected by Arg29 as part of the mechanisms triggering N-terminal helix deployment.

These last two residues are part of the first significantly conserved segment of the sequence, which expands from positions 29 to 40. Most of this and the following conserved segment (positions 67 to 71) are the part of the β-sandwich responsible for keeping the N-terminal helix attached to the main body of the protein. Ala32 fills a small gap between residues in the helix, and Gly34, in turn, leaves space for the sidechains of Leu12 and Leu17 (Figure 4d). These two Leu residues are also conserved in all but one (different one each) of the proteins shown in the alignment (Figure 2).

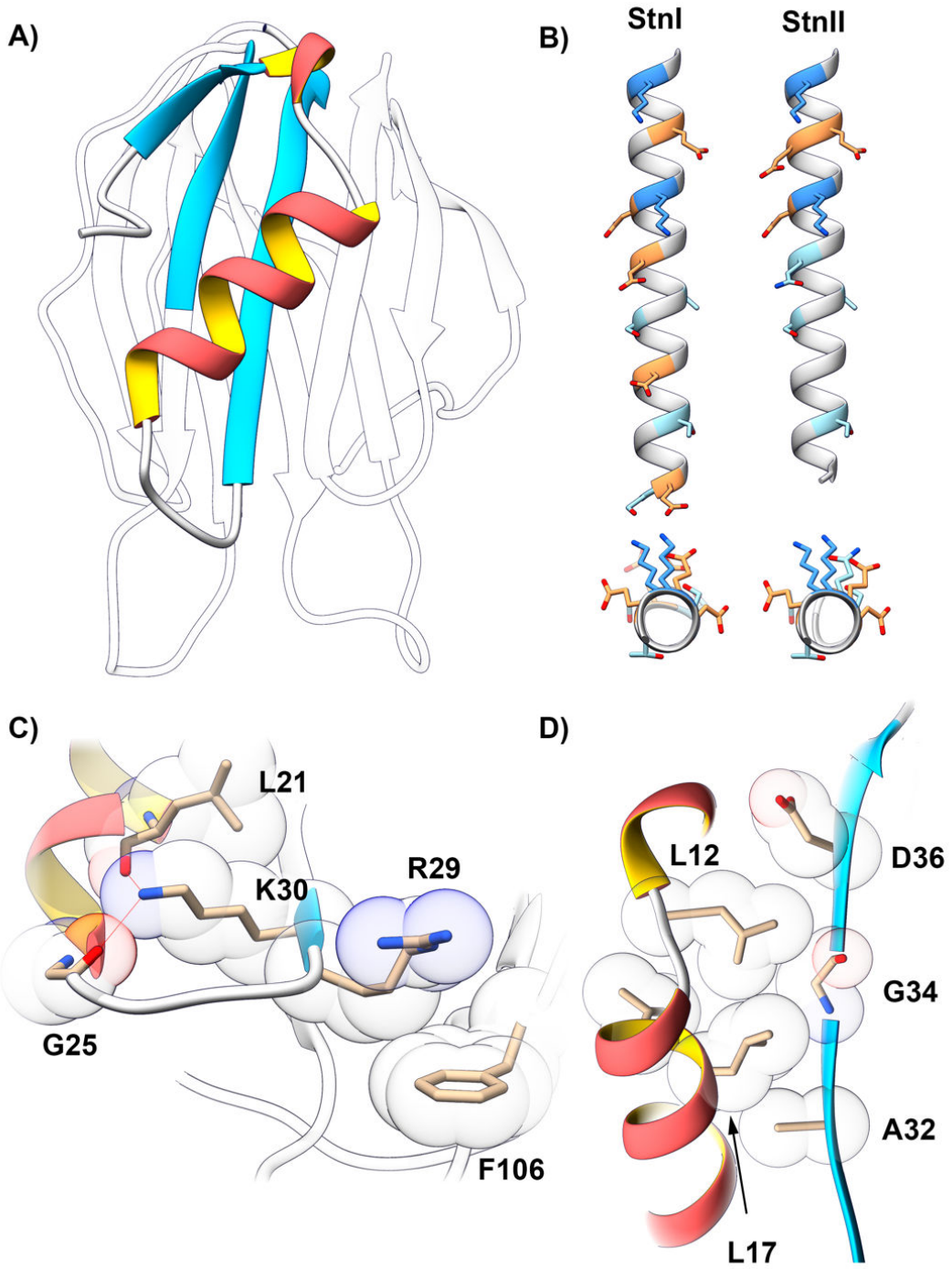

Figure 4. **A)** *N-terminal α-helix and the β-strands that keep it attached to the rest of the protein. Color code as in Fig.3.* **B)** *Top: Stretched helices (C-terminal up) of StnI and StnII, from the N-terminal to V27, made* in silico *with UCSF Chimera using the Richardson rotamer library for the amino acid sidechains. Negatively charged residues in orange, positively charged in blue. Other polar residues, in light blue. Hydrophobics are hidden for clarity. Bottom: C-terminal view of the helices. Note that all polar residues face the same side of the helix.* **C)** *Close up on the structure of StnII. On the right, hydrogen bonds between the carbonyl oxygens of G25 and L21 and the ε-amino group of K30. On the left, R29 is in close range of F106, involved in a cation-π interaction.* **D)** *Close up on StnII showing hydrophobic contacts between the N-terminal α-helix and the first β-strand of the actinoporin fold (see main text for details).*

The residues in between the ones mentioned, whose hydrophobic character and overall volume is conserved, are facing the inside of the β-sandwich and are thus essential for the overall folding of the protein. The remaining residues, from 35 to 40, are also highly conserved, but their roles are more difficult to decipher.

Lys67 has been shown to be related to the hemolytic activity of actinoporins. It can establish a salt bridge with the residue in position 8, as long as it is of acidic nature, as in StnI, but not in StnII. This way, the energy required to release the N-terminal helix is increased by the contribution of this salt bridge. In fact, the StnII mutant A8D, which can form the salt bridge, had its hemolytic activity reduced to that of StnI. Meanwhile, the reverse StnI mutant, D9A, which can no longer form that bond, presented increased hemolytic activity, almost that of StnII [114]. The same effect was observed regarding calcein release [114]. This effect could also explain the differences in hemolytic activity between StnII and FraC and EqtII which, like StnI, have an acidic residue at that position [26]. As in the previous highly conserved section, the next four residues also fulfill folding duties. Ala68 is required to be small and hydrophobic to allow the helix to be properly folded on the surface of the β-sheet. Leu 70 plays an important role in holding the helix folded by filling the void among Leu2, Ile7, Leu12, Val16, and Leu17, giving them a hydrophobic surface to interact with, reducing the likelihood of helix deployment by means of the hydrophobic effect.

It should be noted that the small β-strand at the beginning of the sequence also plays a role in holding the helix folded onto the β-sandwich, by means of being part of that same β-sheet that the helix lies on.

Finally, the first 30-residue stretch of sticholysins has been produced and assayed independently of the whole protein (Figure 4b). The results show that those peptides alone are still able to induce hemolysis [109, 115, 116].

2.3.2. The exposed aromatic cluster

Most of the exposed aromatic cluster is part of the highly conserved sequence between positions 92 and 127, which also contains residues that are included in the other functional regions of these proteins. Briefly, it can be mentioned that most residues in this sequence are conserved, with the remaining being conservatively substituted. This stretch makes up two of the β-strands that constitute the β-sandwich, one of the most exposed and flexible loops in the actinoporin structure, and two other connecting loops. In fact, residues 97 to 104 make the β-strand that is complementary to the aforementioned conserved strand made by the residues 30 to 38 (Figure 5, arrow).

The complete list of residues in the aromatic cluster is: Phe106, Trp110, Trp111, Trp114, Tyr131, Tyr135, and Tyr136 (Figure 5). Amino acids with aromatic

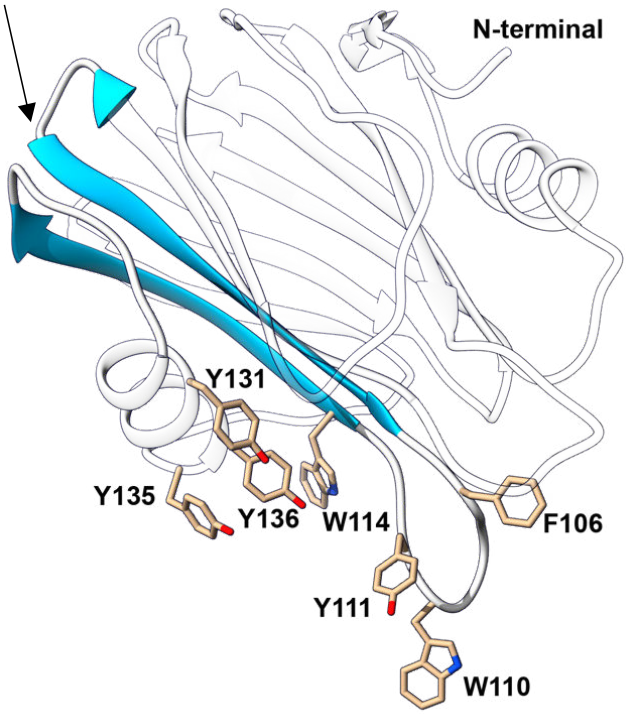

Figure 5. *The exposed aromatic cluster of actinoporins and the conserved sequence between residues 92 and 127. The sidechains of the amino acids that make up the aromatic cluster are shown. Ribbon is shown in color for positions between 92 (arrowhead in blue at the top) and 127 (loop connecting with the second α-helix of the structure). The black arrow is pointing at a β-strand whose role is discussed in the text.*

sidechains in many proteins have been previously shown to be distributed preferentially at the water-membrane interface [117]. The study of several mutants evidenced that the residues in this aromatic cluster were implied in membrane recognition [107, 118].

In EqtII, Trp112, equivalent to Trp110 of StnII, was demonstrated to be key for SM-recognition [119, 120]. However, the residue in this position is only Trp in six of the 20 sequences aligned in Figure 2. In fact, the residue that appears most often in that position is Leu. Nevertheless, the EqtII W112L mutant still retained the specificity for SM [120]. This indicates that that amino acid is only required to have a hydrophobic and large sidechain. The interactions in which it is involved, thus, are presumably not specific.

Phe106, in turn, is much more conserved. The residue in this position is Phe in 13 of the aligned sequences, and Tyr in the remaining ones, denoting that what is important here is the presence of a phenyl-ring. Thus, what seems to be essential is its capability to establish cation-π interactions, such as indicated before with Arg29 (Figure 4d).

In the resolved structures of actinoporins, Tyr111 is always very exposed, not interacting with any other residue in the protein. However, this amino acid is

conserved in all actinoporin sequences. In contrast with most of the residues reviewed this far, Tyr111 does not seem to play a role in protein folding. Instead, it is most likely essential for protein functionality. In fact, when StnII is co-crystallized with POC, Tyr111 is observed to interact with that moiety [29]. Its importance is further highlighted if it is mutated. The mutant Y111N of StnII is essentially incapable of membrane binding [107, 118, 121, 122].

The remaining residues of the exposed aromatic cluster, Trp114, Tyr131, Tyr135, and Tyr136, are conserved in most of the aligned sequences (Trp114 is always conserved). As with Tyr111, it appears that these amino acids are more related to protein functionality than to folding. In fact, all the aforementioned Tyr residues, including Tyr111, play an essential part as constituents of the POC-binding site.

2.3.3. The phosphocholine-binding site

The POC-binding site plays a fundamental role in actinoporin functionality. It is responsible for the direct interaction with the head group of SM [29]. The amino acids that form the site are Arg51, Ser52, Val85, Ser103, Pro105, Tyr111, Tyr131, Tyr135, and Tyr136. Of these, the Tyr residues are also part of the exposed cluster of aromatic residues, and their importance in membrane folding has been discussed above. The remaining amino acids of the POC-binding site, except for Arg51, are conserved in all sequences (Figure 2). Arg51 is preserved in most sequences or conservatively substituted by a Lys residue.

StnII has been co-crystallized with POC (the headgroup of SM), revealing the POC-binding site [29]. Careful inspection of that structure reveals that Tyr111 is involved in a cation-π interaction with the trimethylamine moiety of the POC molecule. Computer simulations have predicted that Tyr111 also interacts with the phosphate moiety of SM via its phenolic hydroxyl group [123]. This residue has been proven to be fundamental for SM recognition regardless of the presence of Chol in the membrane [113].

Similarly, Tyr136 is both predicted and shown to form a hydrogen bond with that same phosphate group [29, 123]. Tyr135 is predicted to interact with the 2NH and 3OH groups of SM, but in the crystal, which does not contain those groups, it helps maintain a network of solvating waters around the POC alongside Arg51, Ser52, Ser103, and Tyr131 [29]. The mutation of Tyr135 showed that this residue is also essential for membrane recognition in the absence of Chol. However, the presence of this sterol seems to compensate for this substitution, both in terms of activity and membrane binding [113]. According to the simulations, the ∂-guanidinium group of Arg51 is predicted to interact with the phosphate moiety as well [123]. This residue

was shown to be, like Tyr111, fundamental for the activity of these proteins [113]. However, it is still capable of binding Chol-containing membranes [113].

The sidechain of Val85 is hydrophobic, whereas that of Pro105 can be considered to be essentially hydrophobic. Both of these residues appear to be in close proximity with the methyl groups of the trimethylamine moiety of POC. In the three-dimensional structure of the StnII-POC complex, there is no major displacement of the sidechains of these amino acids when compared to the orientation they present in the POC-free StnII structure. Nevertheless, it is possible that the interaction with SM does cause a change in the conformation of these residues. This is especially relevant for Pro105 since it is adjacent to Phe106, which was previously mentioned to be involved in a cation-π interaction with Arg29. It is possible that Pro105 acts as the trigger for the deployment of the N-terminal α-helix.

POC binding has been shown to be essential for membrane recognition and binding when facing Chol-lacking bilayers. The presence of Chol compensates for the single substitutions of one of these amino acids. However, even though membrane binding still takes place, Arg29 (which is not part of this site) and Tyr135, and especially Arg51 and Tyr111, are essential for membrane permeabilization [113, 121].

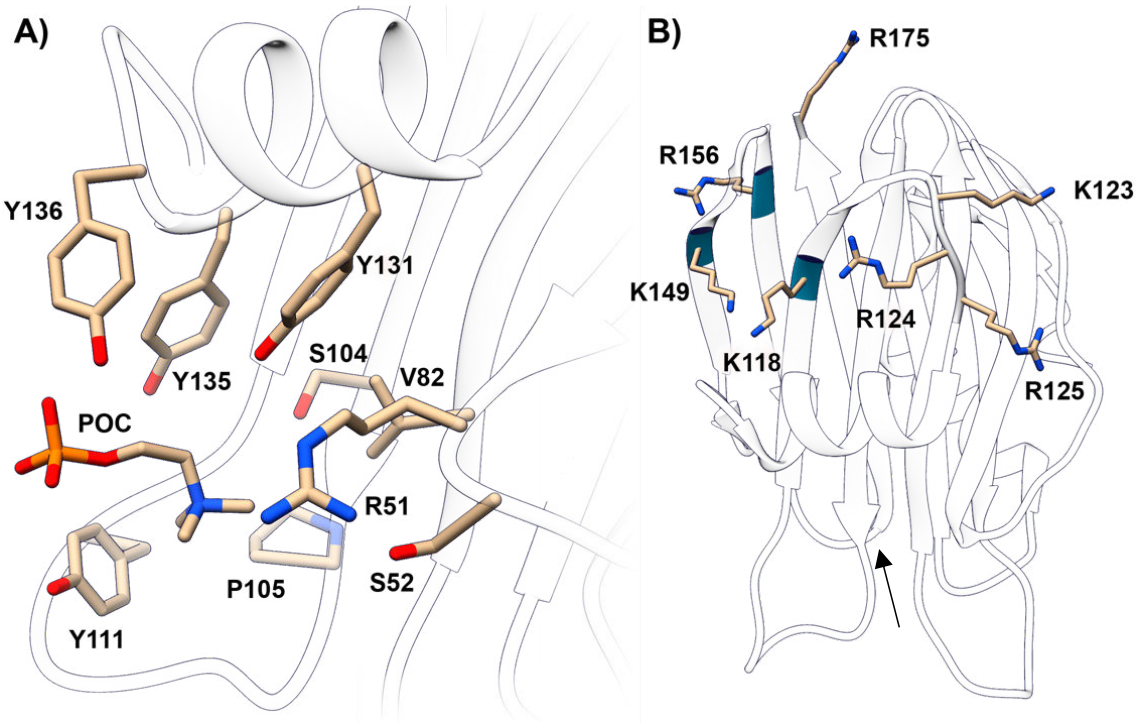

Figure 6. A) *Residues that conform the POC-binding site. Close-up at the structure of StnII complexed with POC (PDB accession code 1O72). All identified hydrogen bonds and solvating waters are omitted for clarity.* **B)** *Positioning of the residues that make up the array of basic amino acids within the complete structure of StnII. The arrow indicates the location of the POC-binding site, shown in* A.

Finally, Arg29, which has already been mentioned to be important for the activity of these proteins (see section 2.3.1), has also been observed to play a role in terms of electrostatic surface potential [122]. The potential of the StnII mutant R29Q is in fact much less positive than that calculated for the wild type (WT) variant of the protein, most likely unpairing the interaction with the phosphate moieties of the lipid in the membrane [122].

2.3.4. The array of basic amino acids

All characterized actinoporins display an array of basic amino acids. These are Lys118, Lys123, Arg124, Arg125, Lys149, Arg156 and Arg175. This array has been shown to be involved in the early steps of membrane recognition in EqtII [32]. In the aligned sequences shown in Figure 2, these residues are conserved or conservatively substituted in most cases. In EqtII, for example, and compared to sticholysins, most of these amino acids are reversed, substituting Lys by Arg and vice versa. It has been hypothesized that this difference could be responsible for the different lipid selectivity displayed by StnII and EqtII [99, 106, 107, 120, 124]. However, it is not clear what the role of these residues is at the detailed molecular level since, though helpful, negatively charged lipids in the membrane are not a strict requirement for actinoporin activity.

2.3.5. Structural differences between StnI and StnII

StnI and StnII are the main actinoporins produced by *S. helianthus* [10]. StnII is made by 175 amino acids, while StnI has an extra residue at the N-terminal. Only 12 amino acids, plus the extra residue at the N-terminal, differ between these two proteins (Figure 7). Of those differences, five are located at the N-terminal α-helix in the part that is exposed in the soluble fold. Two are found in one of the exposed loops that penetrate the membrane upon membrane interaction, and two more are at one side of the structure, which might be involved in monomer-monomer interactions.

In spite of sharing 93.7% sequence identity, the comparative hemolytic activity of these proteins is substantially different [26]. In fact, their membrane binding, as measured by isothermal titration calorimetry (ITC), and their induced calcein release are also unequal and dependent on the membrane composition [26]. Nevertheless, it has been shown that the difference between StnI and StnII at position 8, as mentioned in the section regarding the N-terminal stretch, is responsible, to a very large degree, for the behavior differences between StnI and StnII [114]. The role of the remaining differences is not clear and, so far, it has not been studied systematically. However, it is likely that these residues are responsible for the observed synergy that these two proteins display when assayed together [95].

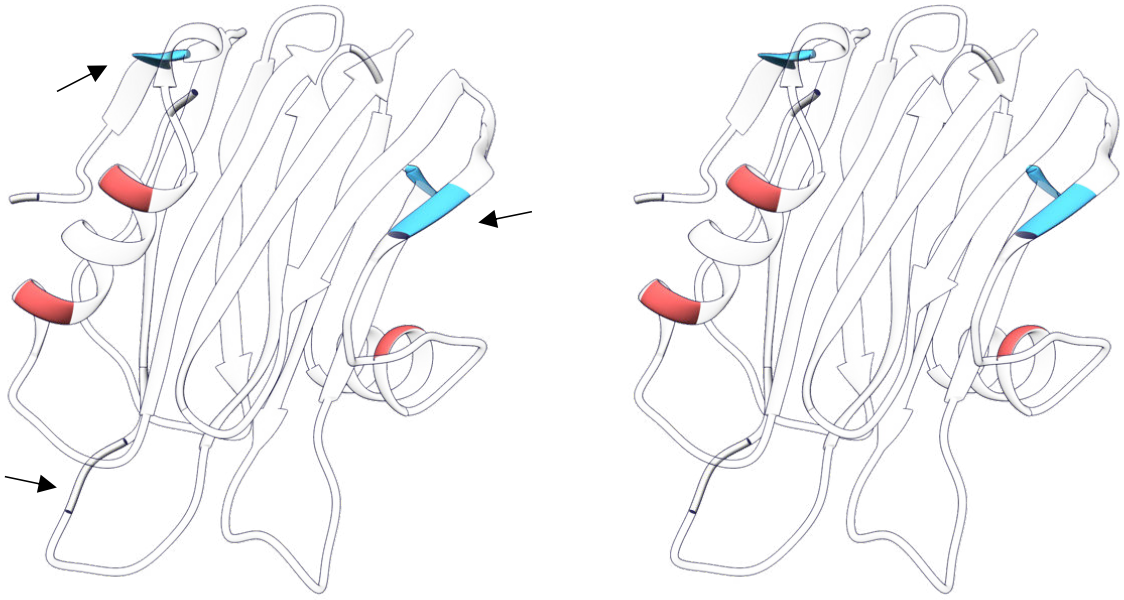

Figure 7. *Cross-eye stereo projection showing the positions differing between StnI and StnII. Arrows point at the residues whose importance is highlighted in the main text, namely position 8 (top left), which is Ala in StnII and Asp in StnI; positions 76 and 77 (lower left), which are Ser-Ser in StnII and Asp-Thr in StnI; and positions 147 and 148 (right), which are His-Glu in StnII and Tyr-Gln in StnI.*

2.4. The target: Lipid bilayers

2.4.1. Biological membranes summarized

Biological membranes are the natural target of actinoporins. They conform the basic compartmentalization structure of all living beings. They determine the extension of the cells, providing the frontier between the self and the non-self, while also supporting all the elements required to maintain the communication and material exchange with the outside world [125]. The fundamental component of biological membranes are lipids. Proteins, fulfilling most of the biological functions, and oligosaccharides, attached to lipid-head groups or to proteins, are also essential from a biological point of view [126]. All lipid bilayers are held together by the hydrophobic effect, which maximizes the entropy of the surrounding water molecules [127, 128]. Nonetheless, the building blocks of membranes are highly varied structurally [128]. These differences cause the membranes to be found in different phase states, which depend on the relative concentration of each of the molecules and on the environment surrounding them [129-135].

The lipids that make up most animal membranes are glycerophospholipids, sphingolipids, and Chol (Figure 8)[136, 137]. Very often the term phospholipid (PL) is used. It refers to phosphate-containing glycerophospholipids and sphingolipids,

such as PC or SM [137]. The structure of PLs and no-PL sphingolipids can be simplified in two parts, the hydrophobic hydrocarbon chains and the hydrophilic head group. [1] The length and degree of unsaturation of the acyl chains is responsible, to a great degree, for the phase behavior of PLs. Briefly, the longer and the more saturated the acyl chains, the more ordered is the phase of a given PL [125]. The head group is exposed to the aqueous phase and has a variety of net charges and sizes [125]. The head group in glycerophospholipids is attached to a glycerol moiety, and to the long sphingoid base in sphingolipids [125]. Although the effect of the head group is more complex than that of the acyl chains [138, 139], the relation between the cross-sectional area of the head group and the hydrophobic moiety can be used to predict which lipid aggregate a lipid will assemble into [140, 141].

The structure and membrane effects of Chol are unlike those of any other lipid (Figure 8) [142]. The hydrophobic part of Chol consists of a sterane moiety with a double bond at position 5 and an isooctyl chain at position 17 [143]. The hydrophilic part is just its 3β-hydroxyl group [143]. Chol has a condensing effect on co-lipids, reducing the average cross-sectional area of their acyl chains by increasing the number of *trans* conformational isomers [144]. Thus, Chol can have a larger number of van der Waals contacts with saturated PLs, interacting preferentially with them [142]. Chol also interacts preferentially with SMs over PCs even if the acyl chains are

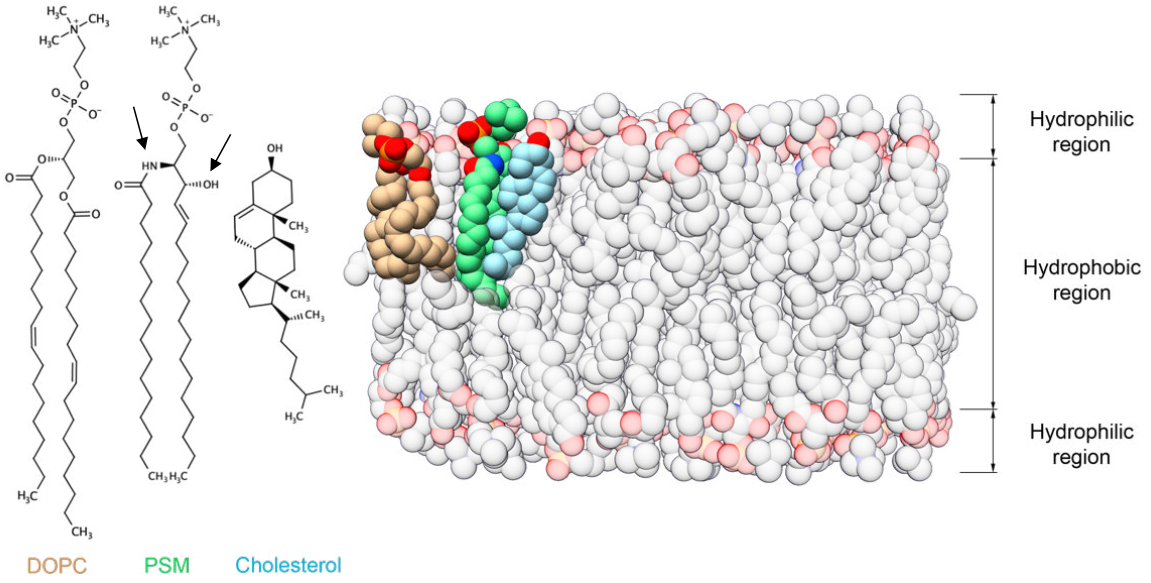

Figure 8. *Left: Schematic representation of the structures of DOPC, PSM and Chol. Arrows point at the 2NH and 3OH groups of PSM, referred in the main text. Schemes made with Marvin Sketch 19.23 (ChemAxon, 2019). Right: space-filling depiction of a lipid bilayer. A molecule of each DOPC, PSM, and Chol is highlighted in the color indicated on the left. Notice Chol's location beneath the head group of PSM.*

[1] Most often, the term *head group* refers to the moiety attached to the phosphate group. Here, *head group* refers to that moiety *plus* the phosphate group.

matched and their order is the same [145]. The presence of hydrogen bond donors and acceptors in the SM structure, namely the 2NH and the 3OH groups, which can form a hydrogen bond network in which Chol can be included, might explain this preference [146, 147]. In contrast, PCs only present donors [147].

Combinations between these molecules can give rise to the most common lipid lamellar phases: solid-ordered phase, commonly called gel phase (S_o), the crystalline phase (L_c), and the liquid crystalline phase ($L_{\alpha'}$), the latter of which is also called the liquid-disordered phase (L_d) [125, 148]. In certain lipid mixtures, and depending on the temperature, these phases can co-exist in a single bilayer, giving rise to lateral segregation [131, 149].

2.4.2. Influence of membrane composition on actinoporin activity

Lipids, and particularly SM, are the only membrane elements that actinoporins require to interact with a membrane. This is clearly shown by their interaction with model membranes that lack non-lipid components and the fact that incubation with SM, or the removal of SM from erythrocytes with sphingomyelinase, inhibits their action [18, 40, 42, 44, 65, 72, 150]. The presence of Chol, membrane phase coexistence, the fluidity and compactness of the bilayer, and the interfacial hydrogen bonding network of SM also affect the activity that actinoporins display when encountering a given membrane [16-19, 21-25, 151, 152]. Since actinoporins present an array of basic amino acids (see section 2.3.4), a preference toward anionic PLs could be expected. However, net charge of the membrane has not been observed to play a significant role in the interaction [102, 120]. In fact, charged residues are essentially absent from the binding site of these toxins, which is mostly unaffected by the overall charge distribution on the protein [120, 153].

The presence of SM in the membrane, however, does not guarantee actinoporin binding to the bilayer, which is largely influenced by the aforementioned phase state of the membrane [18, 24, 25, 44, 65, 72, 150, 153, 154]. If ceramide (Cer) and SM, both fully saturated, are used together, the membrane will contain a highly ordered phase [155-157]. SM and Cer will then partition together, rendering SM out of the actinoporins' reach [23]. Thus, it can be said that the requirement for membrane binding is not just SM presence in the membrane but SM availability.

The SM selectivity displayed by actinoporins happens despite of PC and SM sharing the same head group moiety, POC. Therefore, the capability of discriminating between them must be based on the parts of the molecules that differ between them under the head group [120]. The 2NH and 3OH groups of SM, which constitute the main structural difference between SM and PC, should thus take part in the

interaction with the toxin. Using the analogs of SM that were methylated in either of the groups, it was shown that replacing palmitoyl-SM (PSM) with either of its modified analogs impaired sticholysin activity, as reported by calcein release assays, and membrane binding, as measured by ITC and surface plasmon resonance (SPR), just as if the membrane were made of pure POPC [123]. The residues that take part in this interaction, which have been pointed out previously (see section 2.3.3), also interact with the phosphate moiety of the POC. Just as the 2NH and the 3OH of SM are essential for the interaction, so is the phosphate group, and to a similar level of detail. In fact, it has been shown that the basis for avoiding self-toxicity lies precisely at the head group of SM [158]. This was done studying the activity displayed by the cytolysin of the sea anemone *Phymactis clematis*, which also belongs to the actinoporin family, when it faces *P. clematis* lipids or other exogenous lipids [158-160]. The membrane composition of the sea anemone *P. clematis* does not include SM. Instead, it presents phosphonosphingolipids (PnSL), which are structural analogs of SM. In these molecules, the oxygen atom between the choline moiety and the phosphorus atom is missing, resulting in a direct bond between the phosphorus and the corresponding carbon atom of the choline [158]. Moreover, the degree of methylation of the nitrogen group of the ethanolamine moiety is also different, being mostly unsubstituted or monomethylated, though it can also be found trimethylated [158, 161, 162]. Based on later research, it appears that, while the trimethylation of the nitrogen of choline is likely important in terms of occupancy, the missing oxygen, which never appears in PnSL, is the basis of the selectivity. In fact, the sidechain of Arg51 in StnII is predicted to interact, precisely, with this oxygen [123]. Going back to section 2.3.3, the mutation of Arg51 resulted in a mutant unable to induce calcein release in all instances and in membrane binding in the absence of Chol [113]. The cause would most likely be that the interaction with that oxygen can no longer take place. PnSL have also been observed in other sea anemones, including *S. helianthus*, and, in general, in the Cnidaria phylum [163-166]. This reinforces the hypothesis that these lipids are responsible for the actinoporins' ineffectiveness on the membranes of sea anemones, which can contain 20 mol% of PnSL [166].

Still, some exceptions to the need for SM availability have been observed. In such cases, the vesicles employed were made of PC with significant amounts of Chol, which can induce phase separation [14, 15, 18]. It has also been observed that SM is not enough to ensure pore formation on giant unilamellar vesicles (GUVs), requiring the coexistence of the L_o and L_d phases, with pores being formed at the interface [15]. Nevertheless, it should be pointed out that that last report was made using EqtII mutants labeled with a large, highly hydrophilic fluorophore placed at positions in the N-terminal α-helix that correspond to hydrophobic residues in the WT protein. Back

to phase separation, it has been shown that StnII forms pores on COS-7 cells precisely at the regions of the membrane that are enriched in SM and Chol [151]. Although much more complex than model membranes with L_d and L_o phases, these parts of the cell membrane are also considered to be laterally segregated.

The role played by Chol in the actinoporin-membrane interaction is unclear. For example, pore formation by StnI and StnII is enhanced by the presence of different sterols, regardless of their domain-formation capability [22, 25]. In fact, it was shown that the hydrogen-bond acceptor capability of the sterol 3β-OH and an increase in membrane fluidity were responsible for enhancing the sticholysin-induced release of contents from LUVs, without a concomitant ordering of the SM phase [22, 24, 25]. In a way, this is consistent with the observations that actinoporins preferentially bind at the domain boundaries. These regions and fluid, more disordered membranes are richer in imperfections than the homogeneous, ordered phases. Thus, domain boundaries could facilitate membrane penetration, both increasing the local concentration of toxin and by reducing the energy barrier of the penetration step itself [16]. SM head groups at domain boundaries would be further exposed to the solvent as a consequence of the membrane's imperfections, easing the recognition process. Chol would be responsible for promoting phase separation. Incidentally, Chol is also able to modify the orientation and dynamics of the SM head group, according to the "umbrella hypothesis" (Figure 8) [167, 168]. This can be helpful for actinoporins when it comes to SM recognition [16]. Using an SM analog derivatized with *trans*-parinaric acid (tPa) as its acyl chain (tPa-SM), it was shown that, while including 10 mol% of Chol significantly increased StnII-induced calcein release, the acyl chain order of SM only increased modestly, as shown by the fluorescence anisotropy of tPa, indicating that something else was affected in SM [23].

Chol increasing lipid packing is a consequence of its interaction with the acyl chains of co-lipids, consequently affecting membrane fluidity [169, 170]. Due to Chol's preference for SM, it will mostly affect the acyl chain order of SM when included in a model membrane made of PC-SM as well as the SM hydrogen-bonding network and, overall, the properties of the SM-rich phase [171-173]. The N-terminal α-helix residue Phe16 of FraC (equivalent to Phe14 in StnII) has been proven essential when facing tightly packed membranes, with its substitution resulting in mutants whose ability to induce calcein release is nearly abolished [112].

One of the hypotheses regarding the final configuration of the pore consists of actinoporins bending the membrane so that a toroidal pore is created. The pore walls would then be lined by both the toxins and the polar head groups of lipids [174]. The presence of lipids that induce non-lamellar phases could increase the efficiency of pore

formation. However, no substantial difference was observed when StnII was assayed against model membranes made of SM:Chol:glycerophospholipid in a 50:35:15 ratio, where the glycerophospholipid was PC or phosphatidylethanolamine (PE) [175, 176]. PE induces an inverted hexagonal phase (H_{II}), which is characterized by having a curvature opposite to the one needed [140]. Nevertheless, phosphatidic acid (PA), which also induces the H_{II} phase, has been observed to increase the initial rate of calcein release [140, 150]; perhaps the negative charge of this lipid also played a role in this observation. EqtII has been shown to induce non-lamellar phases which are consistent with toroidal pores [177]. The formation of toroidal pores is also consistent with the observed increased rate of flip-flop induced by sticholysins [150].

Finally, some other potential acceptors for actinoporins have been proposed on the grounds that erythrocytes can be lysed at a comparatively smaller concentrations than those required to induce leakage on model vesicles [11, 65]. Most actinoporins (11 out of the 20 aligned in Figure 2) present an RGD-motif at position 141, which is located at one of the protein sides and, supposedly, close to the membrane in the pore structure. The RGD-motif is involved in the integrins' recognition of fibronectin [178]. It was proposed that this motif could be used by actinoporins to recognize integrins at the cellular surface [97]. However, the mutation of the Gly residue to Ala resulted in mutants whose oligomerization capability was severely restricted [179]. Moreover, it has been proposed that glycolipids could also facilitate actinoporin membrane binding based on the fact that these toxins are eluted later than expected when put through a chromatography on a polysaccharide-based support using a buffer with low ionic strength. Nevertheless, this does not seem to be a specific interaction. Instead, it is probably a consequence of the negative charges displayed by the glycans and the positive charge of the protein [180].

2.5. Pore formation

As PFTs, the ultimate function of actinoporins is to form pores. To do so, actinoporins are required to bind the target membrane and oligomerize. The roles played by different parts of these proteins in the process are understood to quite a high level of detail. Nevertheless, the sequence of events leading to pore formation is still unclear, being a source of controversy in the field.

2.5.1. Membrane binding

In the absence of membranes, actinoporins remain water-soluble. They retain their usual fold, consisting of a β-sandwich flanked by two α-helices. However, when they encounter a membrane with suitable characteristics, they attach themselves to it [181].

The process of membrane binding involves all protein regions mentioned previously (sections 2.3.1 through 2.3.4) [181, 182]. Kinetic measurements made with SPR using EqtII indicate that pore formation is a two-step process [102, 120]. The first step would be membrane binding itself, with the second step comprising oligomerization and actual pore formation (Figure 9).

Membrane binding would be driven mainly by the exposed cluster of aromatic residues, the array of basic amino acids, and the POC-binding site [13, 181, 182]. These elements would provide the required affinity for membrane binding and recognition. The array of basic amino acids and the aromatic cluster would likely be responsible for favoring protein partition to the membrane surface [183]. However, this should not be a strong effect since no binding is observed when vesicles of pure PC are used [120, 123]. The POC-binding site would then provide a firm attachment by recognition of and binding to SM. At this stage, the toxins are unlikely to have undergone significant structural changes other than at the sidechain level.

2.5.2. Oligomerization and membrane penetration

The oligomerization state is at this point of the process not clear nor is whether several degrees of oligomerization are possible at this advanced stage of the mechanism. Though essentially monomeric in solution, there are reports showing that a part of the total population of StnII in solution consists of dimers, trimers, and tetramers, without the need for membrane binding [184]. Thus, it is possible that the oligomerization process starts before encountering a bilayer. Nevertheless, this has not been observed in other actinoporins. As to EqtII, for example, it has been proposed that this difference might lie in the different surface charge distribution of these two proteins [120].

Actinoporins undergo a significant structural change to transition from soluble, monomeric structures to oligomeric, transmembrane ensembles [13, 35, 106, 181, 182]. The biggest alteration of the soluble fold consists in the detachment of the N-terminal α-helix form the β-sandwich. The detachment of the N-terminal α-helix is associated with a conformational change in this segment so that approximately all first 30 residues of the structure adopt an α-helical structure. How these events happen and how membrane penetration occurs is unclear.

Studies on FraC suggest that monomers would serve as the membrane-binding unit, increasing the local concentration of toxin at the water-membrane interface (Figure 9). After that, dimerization would occur (Figure 9B) [35]. The sidechain of Phe16 of FraC (Phe14 in StnII; highly conserved among actinoporins) would be displaced by the sidechain of Val60 (Val62 of StnII; conserved in all sequences in

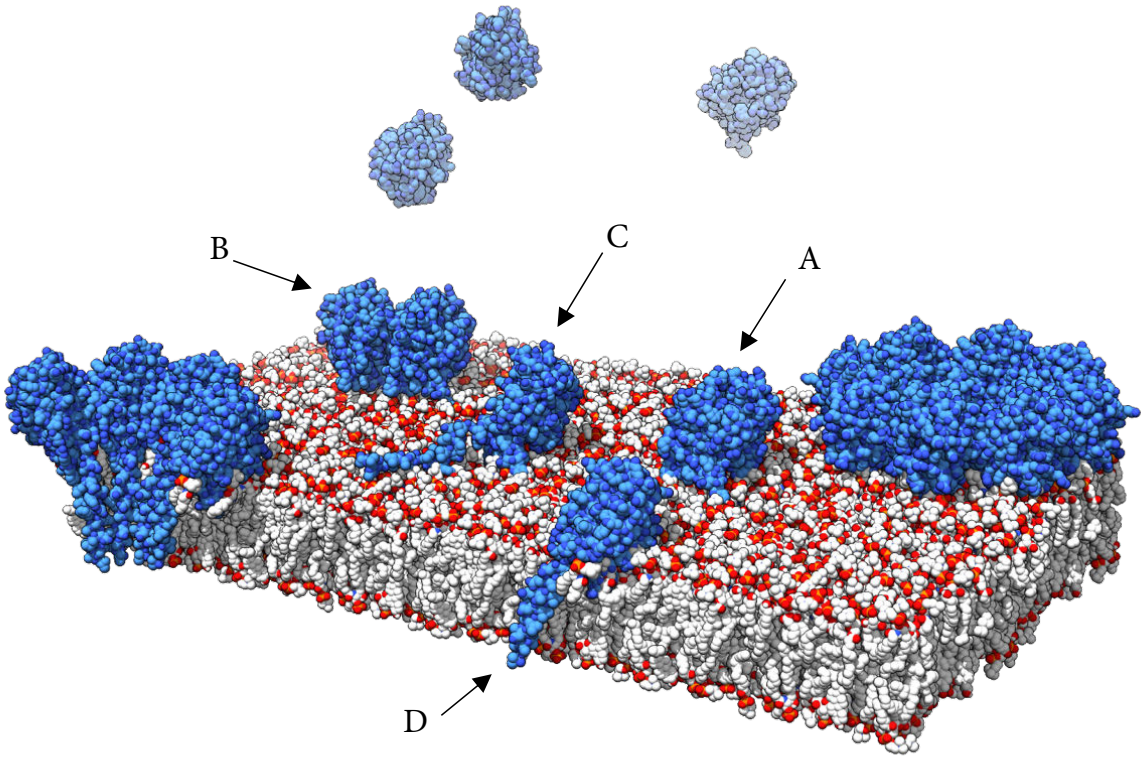

Figure 9. *Artistic all-atom representation of the process of pore formation by actinoporins, including some hypothetical intermediates. Lipids in white (carbon atoms), red (oxygen atoms), and orange (phosphorus atoms). Actinoporins in light blue (carbon atoms) and, for simplicity, dark blue (heteroatoms). Soluble monomers (top) would bind the membrane as monomers (A) or higher-order oligomers (dimers in B). Then the helix would be deployed, lying on the surface of the membrane (C). Eventually, the helix would penetrate the bilayer (D) causing a perturbation on membrane continuity (not shown). Finally, the monomers would assemble into the final pores (left, showing the transitable channel, and right).*

Figure 2) of the other subunit of the dimer, causing a partial unfolding of the N-terminal α-helix. In this case, it is proposed that further oligomerization would lead to the formation of a pre-pore ensemble, which would transition directly into the final pore [35, 185]. According to this model, helix-detachment would be mediated and induced by oligomerization. The existence of a pre-pore is highly controversial since some claim that it might not be large enough to allow the extension of the helices and their subsequent insertion in the bilayer.

However, it is also possible that helix-deployment occurs before, being triggered, as presented in sections 2.3.1 and 2.3.3, by SM binding. SM binding would be the only requirement in that scenario. After being released from the β-sandwich, the N-terminal α-helix would lie on the surface of the membrane, due to its amphipathic character (Figure 9C) [13]. Then, at some point, it would break the energy barrier and penetrate the bilayer (Figure 9D). Some results indicate that the membrane insertion of the helix takes place just after membrane binding [186]. Since no other monomers would be required to detach the helix, it is possible that oligomerization takes place

before helix detachment, while the helix lies on the membrane surface, once it has penetrated the membrane, or under any of the listed circumstances (Figure 9B). Helix insertion prior to oligomerization implies that the pre-pore state would not be required [186]. EqtII single-molecule live-imaging and subsequent analysis indicated that, as proposed for FraC, the pores would be formed by the condensation of dimeric intermediates [187]. This is also supported by the observation that preassembled StnI dimers cross-linked by disulfide bridges at the N-terminal end appear to improve pore formation [188].

2.5.3. The pore

The final structure and stoichiometry of the pore, as with the oligomerization process, remains unclear. Over the years, several different views and models of the structure have been obtained, with different degrees of acceptance in the scientific community.

The first direct observations of actinoporin pores, as mentioned in section 2.1 (see Figure 1), were electron micrographs of ferritin-labeled sticholysin, obtained in 1977 [42]. Much later, StnII was crystallized on egg-PC and DOPC monolayers [29, 189]. The volumes obtained could be used to fit the previously obtained soluble structures, including some modifications. The result was a tetrameric ensemble in which the contacts between the monomers would be minor, between the N-terminal α-helix and the C-termini of the neighboring monomer. The monomers would induce the formation of toroidal pores. The height of the complex was 43 Å, with its outer diameter being 110 Å and the inner diameter being 50 Å. These dimensions could be considered surprising since functional assays performed previously indicated that the hydrodynamic diameter of the sticholysins pore ranged between 6 and 12 Å [18, 86].

Years later, a crystal structure of FraC complexed with detergents was obtained [34]. This structure was that of a potential pre-pore ensemble, in which the sidechains of the aromatic residues are in contact with the molecules of detergent. Whether the pre-pore complex was or was not induced by the methodology can be considered controversial. In addition, some low-resolution volumes of FraC pores on LUVs were obtained. These two results were combined to obtain a structure of the pore consisting of nine subunits. In this structure, the N-terminal α-helices line the wall of the pore all by themselves. This time, the narrower constriction of the pore, at the tip of the α-helices, had a diameter of 15 Å, much closer to the aforementioned functionally predicted values for sticholysin. The outer vestibule of the complex was 50 Å wide, with the outer diameter of the whole structure being 130 Å.

In 2015, a new FraC complex was obtained [35]. This time, the structure, of 3.2 Å resolution, was composed of eight subunits, with the lumen of the pore being lined by

both the N-terminal α-helices and lipids. The α-helices of the different subunits are in contact with those of the adjacent monomer, helping stabilize the structure. They are also in contact with the corresponding intercalated lipid. There are three lipid molecules per toxin monomer. One is bound at the POC-binding site though with its head group adopting the inverse orientation to that of the POC shown in Figure 6a. Another one is sitting on top of Trp112 (Trp110 in StnII), surrounding it with its acyl chains, while its head group is engaged in a cation-π interaction with Trp116 (Trp114 in StnII) in what could be a non-canonical binding site for SM. The last lipid is the one that is exposed to the lumen of the pore. Strikingly, the parts of the lipid that are exposed to the lumen of the pore, and consequently to the solvent, are acyl chains. In this case, the head group is sitting between two toxin subunits involved in a cation-π interaction with Tyr110 (Tyr108 of StnII) of one subunit and the phosphate moiety being stabilized by Arg79 (which in StnII is T77) of the other. In spite of being an octameric structure instead of nonameric, the diameters are very similar. The narrowest pass in the lumen is 16 Å, while the distance between the highest points in the structure (using the theoretical position of the membrane as reference) is 60 Å. The total width and height of the structure are 110 and 70 Å respectively, with the part of the β-sandwich core being approximately 45 Å.

At this point, it is noticeable that the stoichiometry of the actinoporin pore is not clear. However, it is worth mentioning that all complexes have very similar dimensions. In fact, if the low-resolution volume used to fit sticholysin into a tetramer complex is inspected carefully, ignoring its four larger bumps, eight smaller, symmetrically-disposed bumps can be observed (see Figure 5b of ref. [29]). It could be said that the FraC octamer fits in that volume except for the N-terminal α-helices. Regardless of the stoichiometry, the retention of the β-sandwich fold and the extension of the N-terminal α-helix are common features of all the models. These features are supported by the characterization of a wide variety of mutants. For example, using EqtII, it was shown that the N-terminal region was required to be flexible while the β-sandwich could not be substantially perturbed if activity was to be maintained [105]. Similarly, covalently attaching the N-terminal region to the protein core or introducing a Pro residue in what would become the transmembrane α-helical segment significantly reduced the hemolytic activity of EqtII and StnII respectively [102, 107].

A widely accepted model in the field is that of a toroidal pore in which the lumen is lined by both the proteins and the head groups of PLs, with the pores having a small range of stoichiometries [186, 187, 190-192]. Besides a hydrodynamic size of ~10 Å, functional experiments have also shown that, at least for EqtII and sticholysins, the

pores are cation-selective [17, 18, 65, 66, 72]. This would be controlled by the character of the residues facing the lumen [65, 72, 104, 193]. It has also been observed that the presence of anionic lipids such as PA enhances the selectivity for cations, supporting the exposure of the lipid head groups to the pore lumen [177]. There are many observations showing that the conductance of the pores varies over time, which is indicative of the small size and dynamic nature of the pores [17, 193]. In spite of this, the average aperture of the pores appears to be concentration-independent [86]. In fact, experimental results indicate that a small number of monomers is enough to achieve the formation of functional pores [72, 190].

3. AIMS OF THE PRESENT STUDIES

The general aim of these studies was to better understand the functionality of sticholysins. With that purpose, several aspects of the interaction between actinoporins and suitable model lipid bilayers were examined. A wide variety of methods, such as fluorescence spectroscopy, isothermal titration calorimetry, and SPR, were used. When required, sticholysins mutants were designed and produced as well.

In **paper I**, the aim was to study the influence of bilayer thickness in the activity of sticholysins. Different functional assays were used to compare the behavior of sticholysins when facing model membranes of different thicknesses. Chol was included to examine its effect on each of the situations.

In **paper II**, the aim was to delve into the effect that StnII, SM, and Chol have on each other when they interact. Several Trp mutants of StnII were used in combination with two fluorescent derivates of Chol and SM, cholestatrienol (CTL) and pyrene-SM (pyr-SM). Fluorescence quenching and FRET involving CTL as well as excimer formation by pyrene were used to clarify their interactions.

In **paper III**, the aim was to better understand sticholysin-induced permeability. Probes with different structural and electrostatic features were selected to evaluate their release from model lipid vesicles as induced by sticholysin. NDB-labeled lipids were used to study the steady-state permeability of StnII pores in combination with dithionite.

In **paper IV**, the aim was to test the stoichiometry of sticholysin pores directly on model membranes, using as few perturbations as possible. With this purpose, single cysteine mutants of sticholysin were produced and labeled with ATTO-probes. Resonance energy transfer was used to evaluate the oligomerization of sticholysins in solution and the stoichiometry of the pores of StnI and StnI with StnII on membranes containing and lacking cholesterol.

4. MATERIALS AND METHODS

4.1. Materials

Lipids, lipid-precursors, and NBD-labeled POPE were purchased from Avanti Polar Lipids (Alabaster, AL, USA) or Sigma-Aldrich (St. Louis, MO, USA). Calcein, Rhodamine 6G, terbium chloride, dextran-labeled fluorescein, Triton X-100, octaethylene glycol monododecyl ether ($C_{12}E_8$), and bovine serum albumin were obtained from Sigma-Aldrich. 14:0-SM, pyr-SM, OCer, and CTL were synthesized and purified in house according to published procedures [194, 195]. PSM was purified from egg-SM using preparative high-performance liquid chromatography, as described in [196]. ATTO-labels were from ATTO-Tec GmbH (Siegen, Germany).

Mutant and WT variants of StnI and StnII were produced in *Escherichia coli*, strand RB791, and purified to homogeneity as previously described [197, 198].

4.2. Methods

Table 1. *Analytical methods used in the publications.*

	Publication			
Technique	I	II	III	IV
Steady state fluorescence anisotropy	X			X
Release of aqueous contents from LUVs	X	X	X	
Excimer/monomer (E/M) ratio of pyr-SM		X		
CTL emission in presence of quencher		X		
Intrinsic steady state fluorescence of proteins		X		
Förster Resonance Energy Transfer (FRET)		X		X
Quenching of NBD-labeled lipids			X	
Time-resolved anisotropy				X
Surface Plasmon Resonance (SPR)	X			
Isothermal Titration Calorimetry (ITC)	X			

4.2.1. Mutant production and protein purification

Mutants were produced using site-directed mutagenesis by overlap extension using polymerase chain reaction (PCR) [199]. Cell transformation, using competent *E. coli* cells (strand RB791), was performed with a procedure of thermal shock at 37 °C for 4 minutes. Transformed cells were selected with ampicillin at 10 mg/mL in a lysogeny

broth (LB) medium at 37 °C. Cells were grown, first in plaque and then in a liquid medium. Protein production was induced with 1 mM isopropyl β-D-1-thiogalactopyranoside when the culture reached an optical density of 1.0 at 600 nm. Production lasted 4 hours. Then, it was stopped by centrifugation at 6000 g for 30 minutes at room temperature. The pellet was frozen at -80 °C until the procedure could be continued.

The cell pellet was then resuspended in 50 mM TRIS containing 1% (v/v) Tween 20 and lysed by staff sonication. Soluble fraction was recovered by centrifugation at 40000 g for 30 minutes at 4 °C. The next step of protein purification was ion-exchange chromatography (carboxymethyl cellulose), eluted using a linear gradient of NaCl. Starting from 0 M NaCl, the upper limit of the gradient was 0.3 M NaCl for StnI and 0.5 M NaCl for StnII. The gradient for mutant purification was selected based on the similarity of their p*I* to that of StnI and StnII. Since sticholysins display no enzymatic activity, fractions were selected according to absorbance at 280 nm. Selected fractions were then applied to a size exclusion chromatography column (Biogel P-2). In the column, the buffer was changed to 50 mM NH_4HCO_3, pH 7.0. The selected fractions were lyophilized for long-term storage at -20 °C.

The amino acid composition of the purified proteins was analyzed for all purified protein batches. The analysis was performed on a Biochrom 20 automated analyzer (Pharmacia). The results allowed the calculation of the molar extinction coefficient of the proteins. The proper folding of resuspended proteins was ascertained using absorbance spectra, fluorescence emission, far- and near-UV circular dichroism, and thermostability analysis, performed by monitoring circular dichroism at 215 nm.

4.2.2. Vesicle preparation

Lipid vesicles were prepared by mixing organic solutions of the desired lipids to the desired final lipid molar ratio, followed by evaporation of the solvent at 40 °C under nitrogen flow and then by 1–2 hours in vacuum to ensure total elimination of the organic solvent. The dried lipid films were then hydrated 30–60 minutes in a water bath at a temperature higher than the melting temperature of the lipid mixture. The buffer used for hydration was 10 mM TRIS, 140 mM NaCl, pH 7.4. The buffer was argon-purged if required by the subsequent measurements. The prepared vesicles were then extruded, passing them at least 14 times through polycarbonate filters at the same temperature as that of hydration, to obtain LUV populations of the desired average vesicle diameter. In cases where steady-state fluorescence anisotropy measurements were aimed to measure membrane order, extrusion was substituted by water-bath sonication for 10 minutes at hydration temperature. In cases where

experiments on the release of aqueous contents were to be performed, the vesicles were freeze-thawed 10 times prior to extrusion using liquid nitrogen. Then, the vesicles were separated from the non-encapsulated dye by centrifugation-assisted filtration on Sephacryl-S200HR. Dye-loaded vesicles were used for permeabilization studies within the day.

4.2.3. Fluorescence spectroscopy

Two spectrofluorimeter models were used to measure steady-state fluorescence—SLM Aminco 8000 spectrofluorimeter (Aminco International, Inc., Rochester, NY, USA), and PTI Quanta-Master spectrofluorimeter (Photon Technology International, Lawrenceville, NJ, USA)—both operating in L- or T-format, depending on the experimental requirements. A FluoTime100 spectrofluorimeter, equipped with a PicoHarp300E time-correlated single photon-counting module (PicoQuant GmbH, Berlin, Germany) was used to perform time-resolved lifetime measurements. All fluorescence experiments were performed under constant stirring, with the temperature controlled by a Peltier element. To avoid inner filter effects, the optical density (OD) at the excitation wavelength was always such that $OD_{l/2} < 0.05$.

4.2.3.1. Steady-state fluorescence anisotropy

The steady-state anisotropy of fluorescence was measured and calculated according to Lakowicz [200]. The probe in the lipid samples contained diphenylhexatriene (DPH) in 1 mol%. The temperature was controlled by a Peltier element, with a probe submerged in a reference cell. When required, the temperature was increased at a rate of 1 °C /min.

The anisotropy of proteins in solution was also measured to see whether it was affected by the degree of labeling of the protein, as could be expected for an oligomerizing protein, according to [201, 202]. In such case, the label was ATTO-488. The excitation anisotropy spectrum of ATTO-488 was also recorded to measure the fundamental anisotropy of the probe at each wavelength (see appendix Figure A1). For this, maleimide-modified ATTO-488 was diluted at 250 nM in an 87% (v/v) glycerol solution to minimize molecular motions. With the spectra, the results from the steady-state and time-resolved experiments could be compared properly, since different wavelengths had to be used due to laser availability and signal sensitivity. The probe was excited at its maximum absorption in the steady-state experiments, at 500 ± 2 nm. In all, polarizers were used as needed.

4.2.3.2. Release of aqueous contents from LUVs

These experiments were carried out in the steady-state spectrofluorimeters using dye-loaded LUVs. Excitation and emission wavelengths were selected according to the spectral properties of the dye in use. The sample was measured prior to toxin addition to ensure a steady signal level. The release curve was followed until a steady plateau was reached or for a maximum of 13 minutes. Then, Triton X-100, or $C_{12}E_8$ if Triton X-100 had been observed to quench the dye in use, was added to obtain the fluorescence intensity corresponding to the maximum release. In publications I and II, only calcein was employed. In publication III, rhodamine 6G (R6G), Tb^{3+}, and H^+ were also used as probes. The use of these different probes required changes from the standard calcein protocol. For further details on the calcein method, see papers I and II. Please refer to paper III for details on the methods using other probes. The Tb^{3+} release assay is described in ref. [203], and was used with only minor modifications regarding lipid concentrations. Lipid concentration in sample was determined *a posteriori* using Rouser's method of phosphorous determination [204]. The quantitation of the lipid in the samples was done in this manner for all methods.

4.2.3.3. Time-dependent modeling of dye release

In paper III, a model that accounts for dye release upon membrane-perturbation was fitted to the kinetic data. The model is

$$\frac{F_{obs}(t)}{F_{max}} = 1 - \exp\left(J_2\left(e^{-\nu_{relax}t} - 1\right)\right), \qquad \textit{Eq. 1}$$

as defined by Andersson *et al.* [205]. It describes the fluorescent trace recorded for the membrane perturbation-induced release of fluorescent dyes. Once equilibrium is reached, perturbations cease, and leakage stops.

The model has two parameters, J_2 and ν_{relax}. J_2 is proportional to the intensity of the perturbations and, if a good fit is obtained, it can be obtained from $J_2 = -\ln|1-L_{max}|$, where L_{max} is the value of the final maximum release. The parameter ν_{relax} is related to the lifetime of the perturbations. The derivation of Eq. 1 with respect to t can be used to show that the product $J_2 \cdot \nu_{relax}$ is equal to the slope of the release curve at $t = 0$.

4.2.3.4. Measurement of the E/M ratio of pyrene-labelled SM

E/M ratio measurements were performed using LUVs with a composition consisting of POPC:PSM:pyr-SM:X, in a molar ratio of 5:3:2:1, in which X could be Chol, OCer, or nothing. Pyrene was excited using 345 nm. The E/M ratio was calculated from the steady-state fluorescence intensities corresponding to pyrene-monomer at 392 nm and pyrene-excimer emission at 480 nm. When the effect of sticholysin was analyzed,

the E/M ratio continuously followed, and the final value was determined 10 minutes after protein addition to ensure the system had reached equilibrium.

4.2.3.5. CTL emission in the presence of a phase-selective quencher

CTL emission was monitored on LUVs containing 7-SLPC, which has a doxyl-group in the *sn*-2 acyl chain. This group acts as a collisional quencher of CTL while also precluding 7-SLPC from the ordered domains due to its bulkiness. The membrane compositions used were POPC:7-SLPC:PSM:CTL in molar ratios of 50:30:20:5 and 30:20:50:5. These constituted the F samples. Emission in the absence of a quencher, that is, F_0 samples, was measured replacing 7-SLPC with POPC. CTL content was kept below 5 mol% to avoid self-quenching [206]. The sample was excited at 310 nm to avoid significant contribution of Trp emission from StnII. Still, Trp contribution was subtracted from the final signal. Emission was collected at 400 nm. Different toxin amounts, duplicated for the F and F_0 samples, were added after 100 seconds of steady levels of the CTL signal were recorded. Toxin contributions, though small, were quantified and subtracted from the raw fluorescence signal. Toxin effect on CTL emission was quantified as $\Delta(F/F_0)$, that is, the actinoporin-induced increment of CTL quantum yield when comparing samples with and without the quencher.

4.2.3.6. Intrinsic steady-state fluorescence of proteins

The emission spectra of the intrinsic fluorescence of StnII and StnII mutants were recorded between 280 and 500 nm using 260 nm for excitation. Wavelengths were selected so that CTL contribution, which was present in subsequent experiments, was minimized. Protein concentration was 200 nM. In cases where lipid vesicles were present, emission spectra were recorded once the system had reached equilibrium. Lipid titration of the proteins was performed by the addition of 1.3 μM increments of lipid to a final lipid concentration of 18.5 μM, that is, a 92.6 L/P molar ratio, to ensure that all proteins were bound to the bilayer. Toxin-free samples with the same lipid amount were used to correct for light scattering contributions. The lipid composition was DOPC:eSM:Chol, in a 1:1:1 molar ratio (eSM being egg-SM). Relative quantum yields were calculated using the numerically integrated areas of the emission spectra.

4.2.3.7. Förster Resonance Energy Transfer (FRET) measurements

FRET efficiencies were calculated fitting the donor spectra in the absence of the acceptor to that recorded in the presence of the acceptor, using nonlinear least-squares in the spectral region free of contributions other than that of the donor. The spectra were always corrected for dilution effects and scattering and non-sensitized acceptor contributions. When of interest, the acceptor-sensitized emission was obtained by the subtraction of the fitted donor-alone spectra from those in the presence of the

acceptor. Experimental FRET efficiency data were later used in combination with theoretical models to draw further conclusions.

In all cases where FRET was used, the Förster distance (R_0) of the employed donor-acceptor pair was calculated directly in Å as

$$R_0 = 0.2108\sqrt[6]{\kappa^2 n^{-4} Q_D J(\lambda)}, \qquad \textit{Eq. 2}$$

where κ^2 is the orientation factor, usually set to 2/3, representing the dynamic isotropic limit; n is the refractive index of the medium, set to 1.33 for water and 1.39, the average between n_{water} and n_{membrane}, when energy transfer occurred between fluorophores in different phases; Q_D is the quantum yield of the donor; and $J(\lambda)$ is the overlap integral between the emission spectra of the donor and the absorption spectra of the acceptor. This is calculated as

$$J(\lambda) = \int_0^\infty F_D(\lambda)\varepsilon_A(\lambda)\lambda^4 \, d\lambda \,, \qquad \textit{Eq. 3}$$

where $F_D(\lambda)$ is the emission spectra of the donor with its area normalized to 1, and $\varepsilon_A(\lambda)$ is the acceptor spectra in M^{-1} cm^{-1} units.

FRET from Trp in StnII to CTL (R_0 = 22.9 Å) was used in paper II to determine which Trp residues in StnII are located closer to sterols in the membrane and to discover whether sterols are preferentially distributed near StnII when the toxin is bound to the bilayer. FRET efficiencies were calculated at high L/P molar ratios to ensure that all proteins were bound to the bilayer in order to avoid contributions from toxin subunits in an acceptor-free environment.

The distribution was estimated with the aid of a model that calculates the theoretical FRET efficiency that is to be expected for an unlinked donor-acceptor pair in which each class of molecules diffuses randomly in a separate plane. The basis of the model was derived by Davenport *et al.* [207]. Specifically, the model calculates the time-dependent probability of the donor decay of remaining unquenched as a function of the spectral properties of both fluorophores and the range of available distances, expressed as

$$\rho_{cis'}(t) = \exp\left(-2\pi h^2 m \int_0^\omega \left\{1 - \exp\left[-\left(\frac{R_0}{R_e}\right)^6 \times \left(\frac{t}{\langle\tau\rangle}\right)\alpha^6\right]\right\}\alpha^{-3} d\alpha\right), \qquad \textit{Eq. 4}$$

where h is the distance between the diffusion planes, m is the surface density of the acceptor, R_e is the exclusion radius between the donor and the projection of the

acceptor in the donor diffusion plane, and $\langle\tau\rangle$ is the average lifetime of the donor. The parameter α is defined as $\alpha = h/\sqrt{h^2 + r^2}$, where r is the distance between the donor and the projection of the acceptor in the donor's diffusion plane. The parameter ω represents the maximum value of α, achieved at the particular case at which $r = R_e$. The expected fluorescent decay of the donor in the presence of randomly distributed acceptors is then obtained as $I_{DA}(t) = I_D(t)\rho_{cis'}(t)$. The theoretical FRET efficiency is calculated as

$$E = 1 - \frac{\int_0^\infty I_D(t)\rho_{cis'}(t)\,dt}{\int_0^\infty I_D(t)\,dt}, \qquad \textit{Eq. 5}$$

where $I_D(t)$ is the decay of the donor in the absence of the acceptor. From the results, it can be concluded that the acceptor is preferentially, randomly distributed near the acceptor or excluded from its vicinity as the experimental efficiency values are higher, equal, or smaller than those predicted, respectively.

In paper IV, FRET between labels attached at a specific position in the structure of sticholysins was used to delve into the process of oligomerization. The mutant used was StnIT43C. Its design takes advantage of the lack of Cys residues of actinoporins, which enables labeling them specifically at a convenient position, safe from the point of view of functionality. The labels used were ATTO-488 and ATTO-542. The R_0 for the self-transfer of ATTO-488 was calculated to be 49.3 Å, whereas the R_0 for the ATTO-488/ATTO-542 FRET pair was 63.8 Å.

The mutant StnI-T43C was characterized structurally and functionally using circular dichroism, intrinsic fluorescence emission, and hemolytic assays, as previously described [113, 114] (Figure A2). Its hemolytic activity was the same as that of StnI-WT, indicating the unaffected functionality of the protein. Labeling was performed using maleimide-modified ATTO probes (5-8 molar excess) O/N after a previous two-day incubation with TCEP (50:1 molar excess) in a phosphate buffer (140 mM NaCl, 10 mM phosphate), pH 7.4. The excess of label was removed using Pierce™ dye removal columns (ThermoFisher), following manufacturer specifications. The degree of labeling varied between 17 and 25%. This was calculated using the absorption spectra of each sample, using extinction coefficients of ε = 49450 M^{-1} cm^{-1} for the mutant StnI-T43C at 280 nm, ε = 9.0 x 10^4 M^{-1} cm^{-1} at 500 nm for ATTO-488, and ε = 1.2 x 10^5 M^{-1} cm^{-1} at 542 nm for ATTO-542. Corrections for label contributions at 280 nm were made using the corresponding correction factors provided by the manufacturer, which are 0.09 and 0.08 for ATTO-488 and ATTO-542, respectively. These factors represent the fraction of the absorbance of the label at 280 nm relative to their absorbance at the maximum. Protein mixtures assayed were

made by a combination of aliquots of WT (StnI and StnII, as indicated) and labeled StnI-T43C (with donor or acceptor) stocks. Fractional amounts were calculated according to the corresponding fractional labeling and concentration of the stocks. StnI-WT was added last, if needed, to adjust the overall fraction of labeling of the final mixtures. StnI-WT and StnI-T43C have been considered to be equal in terms of activity and structure, as evidenced by their structural and functional characterization by circular dichroism and hemolysis rates, respectively (Figure A2).

A model was constructed to calculate the FRET efficiencies for each possible stoichiometry in a way that was dependent on the fraction of acceptor-labelled toxin in the sample, keeping the fraction of donor constant. Using single-point mutants allowed the assumption that the fluorophores were distributed as the vertices of regular polygons. Distance from the center of each protein to the center of the polygon is

$$r_c = \frac{r_{mm}}{2\sin\left(\frac{\pi}{N}\right)}, \qquad \textit{Eq. 6}$$

where r_c is the radius of the polygon, r_{mm} is the distance between fluorophores on adjacent subunits, and N is the number of subunits per pore. The value used for r_{mm} was 29.0 Å since that was the measured diameter of a sticholysin subunit (see below, section 4.2.3.9). However, r_c cannot be used directly. Instead, the offset of the fluorophore relative to the center of the protein has to be taken into account. The distance to the center of the polygon to the fluorophore is then

$$r_{cf} = \sqrt{\left(r_c + r_f\cos(\omega)\right)^2 + \left(r_f\sin(\omega)\right)^2}, \qquad \textit{Eq. 7}$$

where r_f is the distance from the mass center of the protein to the labelled position as observed from a top view (distance in the z axis is ignored), and ω is the angle between the line that joints them and the prolongation of the line that unites the center of the monomer and the center of the oligomer. r_f and ω were 10 Å and 66 °, respectively, based on the position of the residue Thr43 on the available structure of StnI (PDB ID: 2KS4).

Once r_{cf} is known, the distance between any two subunits can be calculated using the following equation:

$$r_{ij} = 2r_{cf}\sin\left(\frac{\pi(i-j)}{N}\right), \qquad \textit{Eq. 8}$$

where i and j are the indices of the subunits of interest. Usually, it is easiest to assume $j = 1$, as will be done onwards (subscript j is thus omitted), so that Eq. 8 yields the distance between the selected (number 1) and the i^{th} subunit. The obtained values for the distances were then used to calculate the corresponding rates of energy transfer according to

$$k_T(r_i) = \frac{1}{\tau_D}\left(\frac{R_0}{r_i}\right)^6, \qquad \textit{Eq. 9}$$

where τ_D is the lifetime of the donor. In our case, ATTO-488 acted as donor. Its fluorescence lifetime was measured to be 4.09 ± 0.05 ns, in good agreement with the value provided by the manufacturer (4.1 ns).

Next, to have the highest precision, all possible arrangements of all possible combinations of unlabeled and donor- and acceptor-labeled subunits were calculated for each of the stoichiometries considered, assuming that monomer associations were random and unbiased by the labeling, using a Python program made by the author (attached as Appendix 4 to this thesis; the program also performs all other calculations indicated here except for the calculation of the RMSD of the experimental values when compared to the predictions). The arrangements of the subunits were made so that possible redundancies due to rotational symmetry were avoided. In all cases, it must be maintained that $N_D+N_A+N_U = N$, that is, the sum of unlabeled (N_U) and donor- (N_D) and acceptor-labeled (N_A) subunits must equal the total number of subunits.

The expected FRET efficiency was then calculated for each of the possible arrangements, using the additive property of rates [200], as

$$E_{Nqv} = \frac{\sum_{i=2}^{N} k_T(r_i)}{\frac{1}{\tau_D} + \sum_{i=2}^{N} k_T(r_i)}, \qquad \textit{Eq. 10}$$

where E_{Nqv} denotes that that is the FRET efficiency for a stoichiometry of N subunits (for example, $N = 8$), a combination q of unlabeled and donor- and acceptor-labeled subunits (for example, $N_D = 1$, $N_A = 3$, and $N_U = 4$), in a particular arrangement v. For each arrangement, E will depend on the order of the subunits. However, since we assumed that monomer associations were random and unaffected by the labeling, the observed FRET efficiency for each combination q will be the average of the E values for all the possible arrangements since it is assumed that they are all equally likely within each combination.

The final FRET efficiency to be observed would then depend on the fraction of toxins labeled with acceptor or donor in the sample (f_A and f_D, respectively). These

fractions determine which combinations are more likely to happen. In this case, the respective fractions of the labeled and unlabeled subunits must sum to one, that is, $f_A+f_D+f_U = 1$. The probability of each combination, including all its possible arrangements, is then calculated as

$$P(N_D, N_A, N_U, f_D, f_A, f_U) = \frac{(N-1)!}{(N_D-1)!\,N_A!\,N_U!} f_D^{N_D-1} f_A^{N_A} f_U^{N_U}, \qquad Eq.\ 11$$

which is a version of the trinomial distribution adapted to rule out redundancies due to rotational symmetries. The sum of all probabilities calculated in this manner must sum to one. This probability is used to weight the energy transfer efficiencies of each combination so that the final result yields the expected FRET efficiency for a given stoichiometry and fraction of labeling.

A comparison of the experimental data with the model using root minimum squared deviations (RMSD) allowed the estimation of the stoichiometry of the pores of actinoporins. The errors on the measurements were used to weight the importance of each experimental value so that those with the smallest error were more significant to the final RMSD value. FRET efficiencies were measured in a large L/P molar ratio to avoid energy transfer between different pore complexes. The estimation of the right L/P ratio was done as $r_{av} = \sqrt{1/\sigma}/2$, where r_{av} is the average distance between oligomers, and σ is the surface density of the complexes [202]. Lipid contributions were measured separately and subtracted to avoid scattering contributions to the final fluorescence signal. Accordingly, assuming that the stoichiometry was eight, the average separation between complexes would be ~$3R_0$. Even if the stoichiometry was equal to four, the average separation would be ~$2R_0$, at which E is < 2%. Ideal L/P molar ratios, which would be even larger, could not be used due to experimental limitations, namely, light scattering by LUVs, lack of availability of materials, and instrumental sensitivity.

4.2.3.8. Quenching of NBD-labeled lipids

The quenching of NBD-labeled lipids assay is also termed the equilibrium pore assay. LUVs containing 1 mol% of NBD-POPE were employed. A freshly prepared solution of 0.6 M sodium dithionite in 1.0 M sodium phosphate buffer, at pH 10, was used to quench NBD emission. The excitation wavelength was 470 nm. Fluorescence emission was recorded at 520 nm. Dithionite was added to a final concentration of 55 mM. LUVs were disintegrated using Triton X-100. For further details, please see paper III and ref. [203].

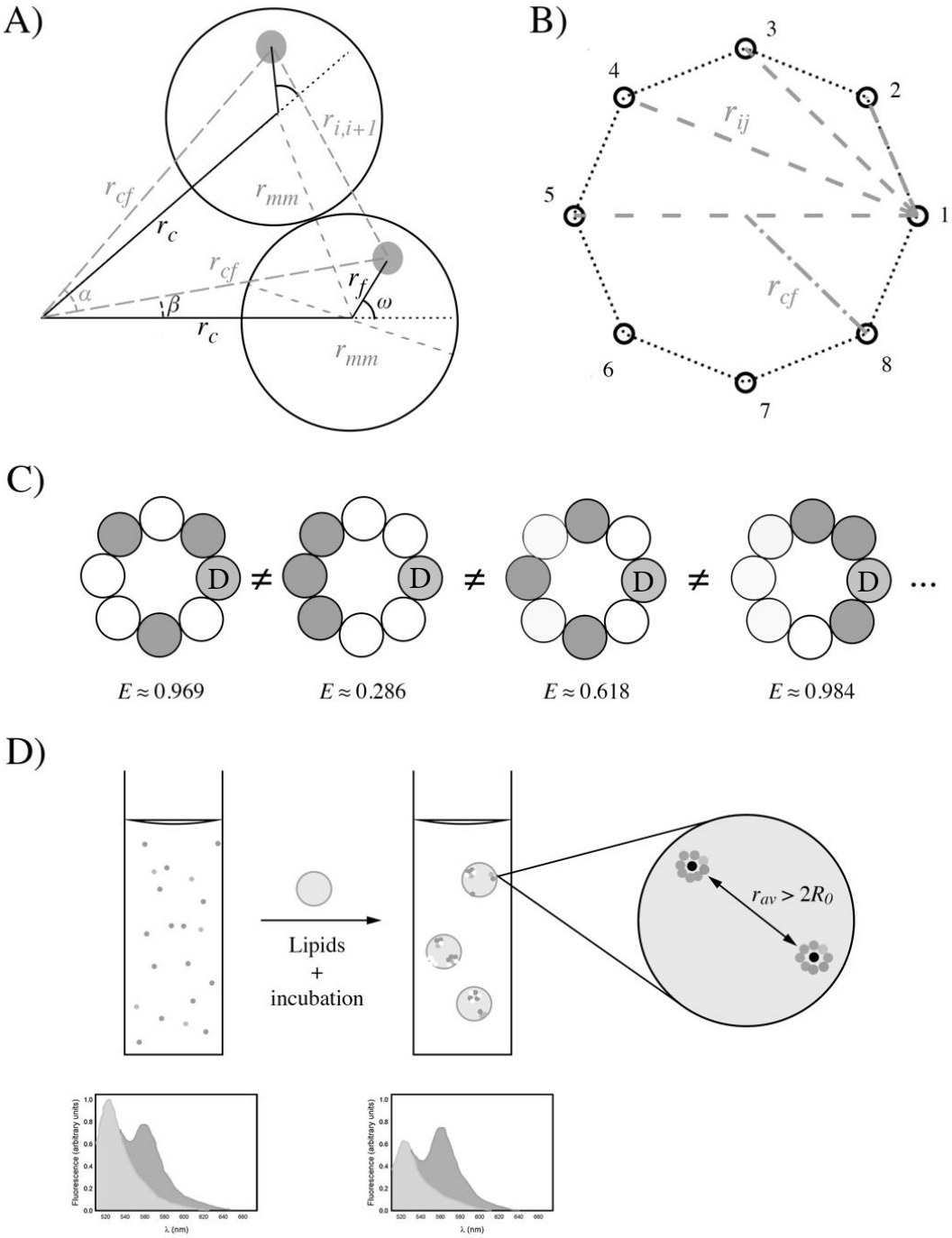

Figure 10. A) *Representation of the geometrical arrangement of two adjacent labeled proteins in a given* n*-mer (only two subunits are shown). Fluorophores are depicted as solid gray circles. Parameters shown are those in Eqs. 6 to 8. The value of* r_{mm}*, the distance between the centers of two adjacent subunits, is the same as the diameter of one subunit. This rule cannot be applied to the position of the fluorophores since they are not at the center of the protein (given a top-down projection). Their offset,* r_j*, by an angle* ω*, has to be taken into account. Consequently,* $r_{mm} \neq r_{i,i+1}$*. This is solved by using Eq. 7, which enables the calculation of* r_{cf}*, and with that* $r_{i,j}$*. Angle* α *has a value of* $2\pi/N$ *radians,* N *being the number of subunits in the oligomer. Angle* β *represents the offset of* r_{cf} *relative to* r_c*, and is a function of* r_c*,* r_f*, and* ω*. It is a consequence of this that* r_{mm} *and* $r_{i,i+1}$ *are not parallel to one another. This scheme is valid for any* n*-mer.* **B)** *Representation of an exemplary oligomer, an octamer. Circles represent the fluorophores in oligomerizing proteins (omitted)(cont.)*

4.2.3.9. Time-resolved measurements

Lifetime decays of fluorescence were recorded using suitable excitation LED-lasers (Pico-Quant, Berlin, Germany) and cut-off and bandpass filters, according to the photophysical characteristics of the fluorophores used. If lifetime decays were to be studied directly, these were recorded in the absence of polarizers until the channel with the maximum counts reached 10000 counts. If anisotropy decays were to be obtained, the corresponding lifetime decays were recorded for 200 seconds using polarizers. If needed, neutral density filters were used to attenuate the excitation intensity, to avoid artificial shortening of the lifetime due to artifacts caused by excessive input signal. The instrument response function (IRF) was recorded in the absence of colored filters using buffer up to 10,000 counts. For measurements with ATTO-488, a 457 ± 15 nm pulsed diode laser was used for excitation. Emission was collected though a long-pass filter (> 480 nm). If Trp fluorescent decays were recorded, a 297 ± 10 nm pulsed diode laser was used. Emission was collected with a long-pass filter (> 350 nm).

The decays were analyzed using the FluoFit Pro software from PicoQuant. In the case of lifetime decays, the multiple exponential model was used for fitting. Fluorescence anisotropy decays were fitted using a sum of discrete exponential terms. In both cases, the number of exponential components used was the smallest required to obtain a satisfactory fit as judged from the fitting parameters, the trace of residuals, and the autocorrelation plot. Errors in the values of the obtained parameters were obtained performing bootstrap analysis. To simplify, if the upper and lower error values obtained were approximately symmetrical relative to the value of the parameter, they were averaged so that the final value could be indicated as value ± average of errors.

(cont.) The parameter $r_{i,j}$ *is presented as dashed lines, some of which are omitted for clarity.* **C)** *Following the example in B) of eight subunits, we can assume* $N_D = 1$ *(light grey, with a "D"),* $N_A = 3$ *(dark gray), and* $N_U = 4$ *(white), we have that those can assemble into 35 possible arrangements (discarding those that differ only by circular symmetries). Four of those possible arrangements are shown in the figure. In the model, the assumption is made that the probability of those subunits (*$N_D = 1$*,* $N_A = 3$*, and* $N_U = 4$*) assembling into any of the 35 possible arrangements is the same. The FRET that a donor experiences from being at each arrangement, however, is different (see figure), hence the need to average them. Then, those averages need to be weighted since the probability of an assembly as those considered (regardless of the arrangement) is different from that of those with a different composition (say,* $N_D = 1$*,* $N_A = 1$*, and* $N_U = 6$*). These probabilities depend on the fractional population of donor- and acceptor-labeled proteins in the sample.* **D)** *Scheme of the experimental design. Non-labeled toxins, together with donor- and acceptor-labeled toxins, are placed in a cuvette, and the emission is registered (light gray for donor, darker gray for acceptors). After that, lipids are added. The sample is left for a few minutes to ensure that binding is complete. After that, emission is registered again, revealing the FRET from a diminished donor emission. The L/P ratio is such that the average distance,* r_{av}*, between oligomers is, at least, larger than* $2R_0$*.*

Molecular diameters were calculated from the correlation times obtained from the time-resolved anisotropy decays using the following equation:

$$\emptyset(\text{Å}) = 20\sqrt[3]{\frac{\theta RT}{\eta N_A}10^{27}\frac{3}{4\pi}}, \qquad \textit{Eq. 12}$$

which derives from the Perrin equation [200], and then was modified to yield the molecular diameter directly in Å. In the equation, θ is the correlation time of the rotating unit in s; R is the ideal gas constant, with a value of 8.314 m^3 Pa mol^{-1} K^{-1}; T is the temperature in K; η is the viscosity of the solvent, used as 0.94 x 10^{-3} Pa s; and N_A is Avogadro's constant. The numeric constants that appear in the equation transform the values from m to nm and then to Å and from radius to diameter. The cubic root and the 3/(4π) factor transform the volume of the molecule into its radius, assuming its overall shape is that of a sphere, as expected for molecules that display a single correlation time.

4.2.4. Molecular Adsorption from Surface Plasmon Resonance (SPR)

SPR experiments were conducted on a BioNavis SPR Navi 200 instrument (BioNavis Ltd. Tampere, Finland). Gold chips were activated with *N*-hydroxysuccinimide and *N*-ethyl-*N*'-(dimethylaminopropyl)-carbodiimide and then coated with a layer of carboxymethylated dextran, competent for capturing LUVs of the appropriate composition. All solutions applied to the instrument were previously filtered through 0.2 μM membrane filters and degassed using bath sonication. Protein solutions, which cannot be sonicated, were degassed by centrifugation. The flow rate of the buffer was 5 μL/min. The chip surface was first washed with two injections of 10 mM 3-[(3-cholamidopropyl)-dimethylammonio]-1-propanesulfonate (CHAPS). LUVs were then applied to the surface at 0.5 mM lipid concentration with a 10-minute injection. The excess was removed by a 50 mM NaOH injection (2 min). A 2-minute injection of bovine serum albumin at 0.1 mg/mL was used to confirm total chip coverage with LUVs. The selected toxin was then applied at 4.0 μM for 10 minutes. The buffer was then applied to induce protein dissociation for 2 minutes. The chip was regenerated with CHAPS. The assay was performed at 25 °C.

Association and dissociation constants could not be calculated since sticholysins could not be substantially removed from the LUVs. Instead, the L/P molar ratio of the chip-bound LUV-protein complexes could be calculated based on the ng/cm^2 values of the sensograms once they reached a steady signal, given that the M_w of the proteins and the average values of the lipid mixtures are known.

4.2.5. Isothermal Titration Calorimetry (ITC)

The interaction of the toxins with LUVs was studied by ITC using a VP-ITC calorimeter (Malvern MicroCal, Worcestershire, U.K.). Briefly, 1.4 mL protein solutions, at concentrations between 0.7 and 4.0 μM, were titrated with 20 μL injections of lipid suspensions at concentrations ranging between 0.5 and 2.0 mM. The temperature was kept constant at 25 °C. The buffer employed consisted of 10 mM TRIS, 100 mM NaCl, and 1 mM EDTA at pH 7.4. The thermodynamic parameters of the interaction were obtained from data analysis in Origin using the "one set of identical sites" model, which is applicable to situations such as the one at hand, in which a protein binds the membrane. The situation is considered to be a protein binding a "binding-site" at the membrane, each of these consisting of n lipids [107, 208-210]. In all cases, the parameter c, which is defined as $K_b[P]_{cell}$, had values between 1 and 1,000, a range permitting the correct calculation of the value of K_b [107, 210].

5. RESULTS

5.1. Effect of membrane thickness on sticholysin activity

Results from publication I

The activity of sticholysins, and actinoporins in general, has been characterized by a wide variety of membranes with varying compositions and physicochemical properties [18, 21-25, 40, 42, 44, 72, 102, 120, 123, 150, 153]. However, the effect of membrane thickness on the activity of these toxins had not previously been studied with any actinoporin.

For this first study, a series of PC species was used. Each PC had acyl chains with different lengths, from 14 to 22 carbon atoms per chain, in intervals of two. In all cases, both acyl chains were equal and presented a double bond to *a priori* ensure that all membranes used were fluid at the experimental temperature of 25 °C. The position of the double bond was Δ^9, except for di-20:1-PC and di-22:1-PC, in which it was Δ^{11} and Δ^{13}, respectively. 14:0-SM was used instead of PSM, eSM, or brain-SM, as it has a shorter acyl chain than other SMs, displaying a smaller tendency to form ordered domains at the selected experimental temperature. Finally, Chol was included to study its influence in the systems. The lipid mixtures that StnI and StnII were assayed against were made of di-X:1-PC:14:0-SM:Chol in a molar ratio of 4:1:0 (no Chol) or 4:1:0.5.

5.1.1. Bilayer characterization

To rule out the presence of gel phases in any of the lipid mixtures, temperature-dependent DPH anisotropy measurements were performed. The plot of anisotropy as a function of temperature showed a smooth curvature in all cases, indicating that no phase transition occurred in the assayed temperature interval (Figure 11). A plot of the anisotropy values at 25 °C as a function of acyl chain showed that, in the absence of Chol, the membrane order varied linearly (inset in Figure 11). Chol slightly increased anisotropy values in all membrane systems. The increment was larger in the bilayers in which the PC had shorter acyl chains (insets in Figure 11).

5.1.2. Sticholysin-induced calcein release

Sticholysin-induced calcein release was measured for both StnI and StnII on all membrane systems. The initial rate of calcein release, that is, the slope of the release curves, was used as more representative parameter than the final release since the final release did not show any clear trend when plotted as a function of bilayer thickness.

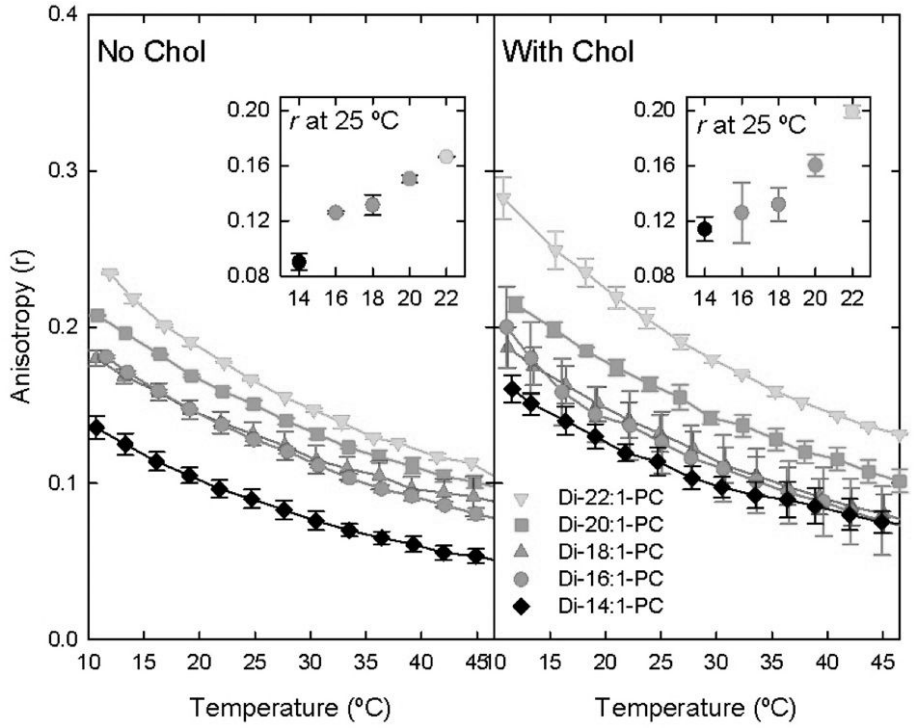

Figure 11. *Temperature-dependent DPH anisotropy measurements of membranes with compositions of di-X:1-PC:14:0-SM:Chol in molar ratios of 4:1:0 (left panel) and 4:1:0.5 (right panel). Each value is average ± standard error of the mean (SEM) of n = 2.* Insets*: DPH anisotropy values measured at 25 °C plotted as a function of the number of carbons in the acyl chains of the PC species present in each bilayer. Modified from publication I.*

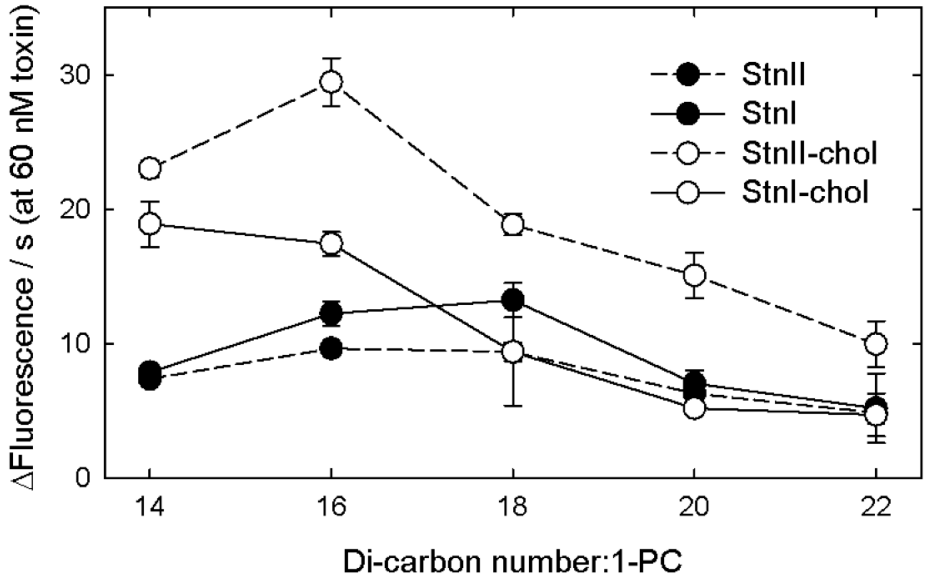

Figure 12. *Initial rates of calcein release measured for an L/P molar ratio of 42:1, i.e., 60 nM toxin. Lipid concentrations were 2.5 μM in all experiments. Composition of LUVs was di-X:1-PC:14:0-SM:Chol at molar ratios of 4:1:0 or 4:1:0.5. Values were calculated as normalized fluorescence units per second. Values are average ± SEM of n = 2. Modified from publication I.*

At an L/P molar ratio of 42/1, the results showed that, in the absence of Chol, both sticholysins were most active versus bilayers whose main component was di-16:1-PC or di-18:1-PC, with StnI being somewhat faster than StnII (Figure 12). A similar trend, with faster values, was observed in the presence of Chol. The trend was shifted toward bilayers with shorter acyl chains (Figure 12). In this case, and as previously observed [26], StnII was proven faster than StnI but, overall, induced calcein release was faster for both proteins as compared to the no-Chol situation.

5.1.3. Sticholysin association to LUVs as measured by SPR

Equal coverage of the chip by all membrane systems was ascertained comparing the theoretical mass ratio of the sticholysin-free vesicles with the ratio of the masses measured on the chip for the sticholysin-free LUVs, possible thanks to the SPR signal being in ng/cm^2 (see Table S1 of paper I). The results agreed with the expected values, confirming that all situations were comparable.

LUV-coated gold chips were then exposed to either sticholysin. The signal was registered as a function of time and the acyl chain length of the PC species and reached saturation after 100 to 200 seconds after toxin injection except for StnI and the bilayers containing di-14:1-PC, which were slightly delayed. The signal of the sensograms, given that the M_w of the proteins and the lipid mixtures were known, could be used to calculate the L/P molar ratios of the LUV-protein complexes at saturation. These data indicate that maximum binding was achieved to LUVs with the shortest acyl chain lipids (Figure 13). Binding was then reduced (higher L/P ratio) as the acyl chain increased. The behavior observed for both StnI and StnII was very similar. In either

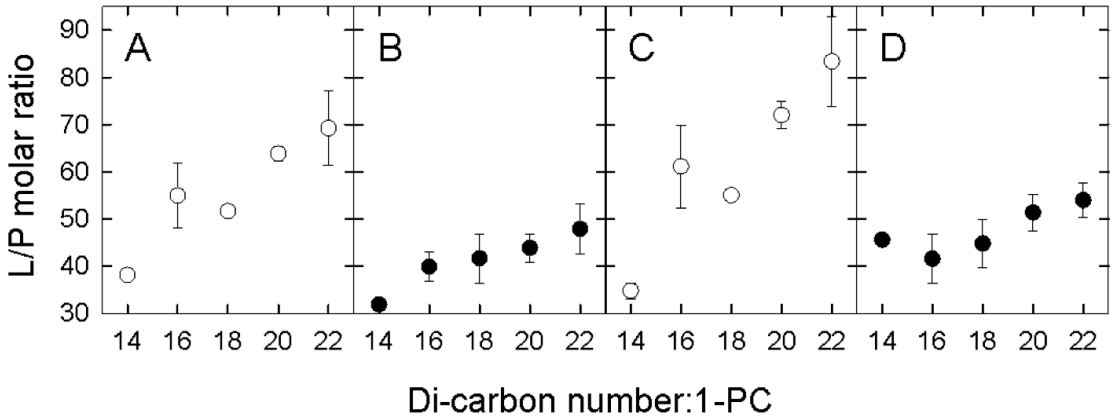

Figure 13. *SPR data for sticholysin binding to supported LUVs. The calculated L/P ratios are plotted as a function of the acyl chain length of the PC species making up each membrane. Values were calculated once SPR signal reached steady levels (500 s and 580 s after LUVs and toxin application). Panels* **A** *and* **B** *show StnI data. Panels* **C** *and* **D** *show StnII data. Filled symbols indicate lipid mixtures that include Chol. Since lipid concentration is constant, lower L/P ratio indicates higher binding. Modified from publication I.*

case Chol increased membrane binding (lower L/P ratio) and reduced the differences between all membranes, while maintaining the overall trend.

5.1.4. The interaction measured by ITC

The interaction of sticholysins with LUVs of varying bilayer thicknesses was also analyzed by means of ITC. Solutions of either sticholysin were titrated with a suspension of LUVs with selected composition until saturation was reached. The analysis of the thermograms allowed the determination of the values of the association constant (K_a), and the entropy (ΔS) and enthalpy (ΔH) of the interaction.

A plot of K_a values as a function of acyl chain length revealed that, in the absence of Chol, StnI presented a higher affinity toward membranes with di-14:1-PC, which was higher than for membranes with longer acyl chains (Figure 14). In fact, the heat change induced by the interaction of StnI with membranes composed of di-22:1-PC was beyond the detection limit of the instrument. StnII, however, presents higher affinity for membranes with intermediate thicknesses, between di-16:1-PC and di-22:1-PC, and similar to that of StnI in the same cases. The values of ΔH essentially followed the same trend as K_a. This was also true for ΔS except reversed, being less favorable when ΔH and K_a were more favorable.

The inclusion of Chol in the membranes drastically increased the affinity of the proteins toward the vesicles, especially in the case of StnI. The presence of Chol highlights the preference of both toxins for membranes with relative intermediate thicknesses, namely, those including di-18:1-PC and di-16:1-PC.

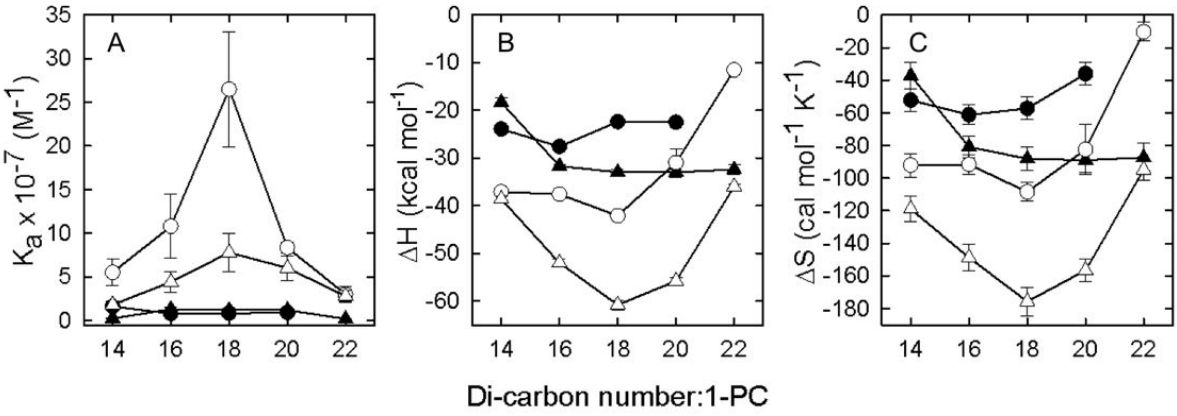

Figure 14. **Panel A**: *K_a values obtained from the ITC measurements.* **Panel B**: *enthalpy of the interaction between sticholysins and LUVs of varying bilayer thickness.* **Panel C**: *entropy of the same interactions. Open symbols depict experiments in absence of Chol. Circles and triangles are for StnI and StnII, respectively. Values are average ± SEM of n = 3. Modified from publication I.*

5.2. The tripartite interaction of sticholysins, SM, and Chol

Results from publication II

The results of the previous study brought up some standing questions of the field. One such question was what the effect of Chol's presence in the membrane was on the activity of sticholysins.

A fluorescently labeled SM analog, pyr-SM, and a fluorescent analog of Chol, CTL, were used to address this issue. OCer, a ceramide species that is unable to induce gel phase due to its oleoyl acyl chain, was used to compare its effect to that of Chol, with which it shares both the tendency to interact with SM and a hydroxyl moiety for a head group. The inability of OCer to induce gel phase formation was essential since the gel phase is known to hinder sticholysin activity [23]. CTL was used in combination with 7-SLPC, a phase-selective quencher, to better appreciate the effect of StnII on the membrane distribution of sterols. Finally, a series of StnII Trp-to-Phe mutants, available from a previous study [198], allowed detailed Trp-CTL FRET studies, to investigate the distribution of CTL near membrane-bound StnII.

5.2.1. SM-SM acyl chain contacts in the presence of OCer, Chol, and StnII

Pyrene molecules can form excited-state dimers (abbreviated excimers) if two of them are properly oriented and within close range of each other during the lifetime of their excited state. Pyrene emission, which regularly displays three peaks, becomes unstructured and red-shifted when excimers are formed [200]. Thus, the labeling of lipid acyl chains with pyrene can be used to detect lipid clustering by measuring the relative emission of the monomer and excimer species of pyrene, that is, the E/M ratio [211-213].

SM is known to cluster in membranes in which POPC is present in equimolar amounts [214]. Consistent with that, the highest E/M ratio observed (3.45 ± 0.09) was in membranes composed of POPC:PSM:pyr-SM in a 5:3:2 molar ratio (Figure 15, open circles at P/L ratio = 0). The inclusion of OCer or Chol (final composition POPC:PSM:pyr-SM:X, 5:3:2:1 molar ratio, where X is OCer or Chol) resulted, in both cases, in a reduction of the E/M ratio to 2.78 ± 0.03 and 2.38 ± 0.12, respectively (Figure 15, solid triangles and circles at P/L ratio = 0). The reported reduction of the acyl chain contacts of SM is a clear indication that OCer, and Chol, are interspersed between SM molecules. For this reason, these two lipids will be referred to, hereafter, as *intercalators*.

The E/M ratio was monitored after the addition of different StnII amounts to each of the membrane systems. The final values, determined at equilibrium, showed that

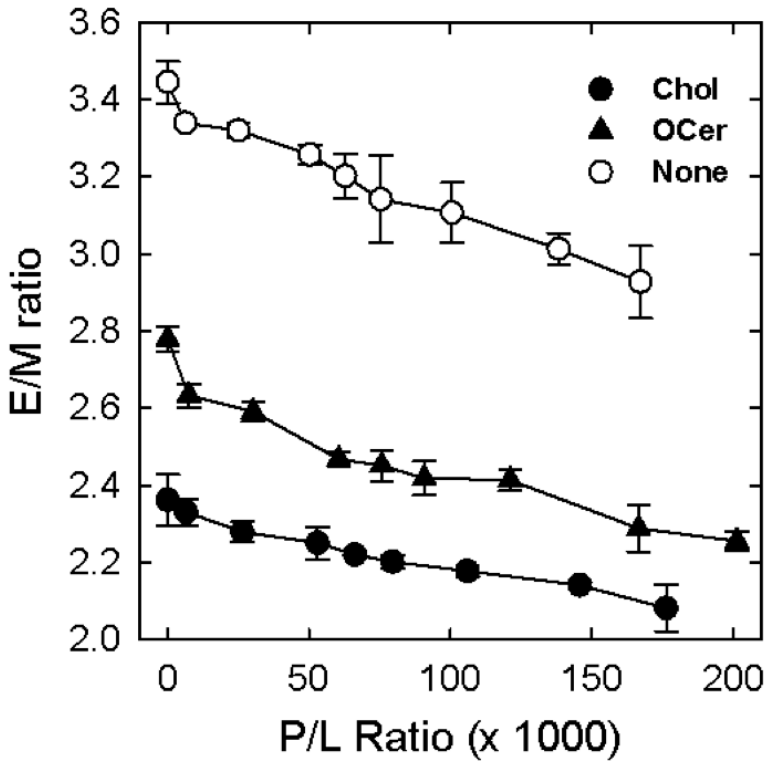

Figure 15. *Measured values of the E/M ratio of pyr-SM as a function of StnII concentration in bilayers composed of POPC:PSM:pyr-SM (5:3:2) (open circles), POPC:PSM:pyr-SM:Chol (5:3:2:1) (solid circles), or POPC:PSM:pyrSM:OCer (5:3:2:1) (solid triangles). Lipid concentration was ~1 μM (measured afterward). Stable E/M ratio values were determined 10 min following toxin addition. Each value is average ± SEM of n = 2-3. Adapted from publication II.*

StnII further reduced the acyl chain contacts between SM molecules. The slope was essentially independent of the presence or absence of OCer and Chol (Figure 15).

5.2.2. Dependence of StnII activity on Chol and OCer presence

Then, the effect of Chol and OCer on the activity of StnII was evaluated. For this, calcein release experiments were used. The assays were performed with DOPC:SM:Y (80:20:X molar ratio) LUVs, in which Y is OCer or Chol, and X ranged from 0 up to 30. The P/L molar ratio (equal to 0.09) was kept constant in all release experiments.

The results showed that Chol greatly increased the calcein release rates even when present in very low amounts (Figure 16). The effect was noticeable even at molar fractions of Chol below the limit required for the formation of Chol-induced domains [129]. Regarding OCer, inclusion was observed to enhance the activity of StnII. However, its effect was much less pronounced than that of Chol. In both cases, the effect of the intercalator lipid was stabilized at ~7 mol%. It is interesting to note that Chol presence at amounts over 20 mol%, at which L_d/S_o phase separation is induced by Chol itself, did not promote StnII activity any further.

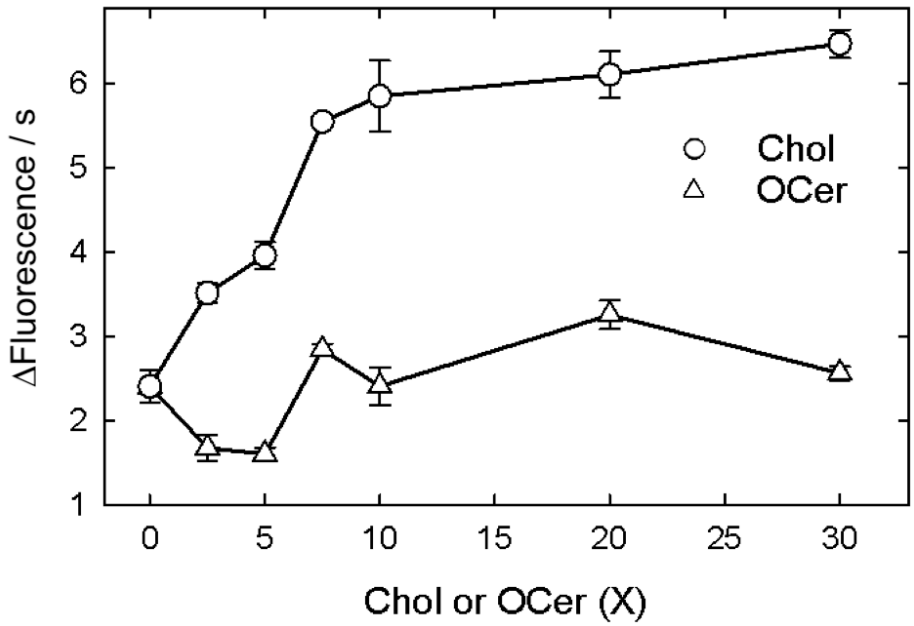

Figure 16. *Initial rates of StnII-induced calcein release from LUVs composed of DOPC:SM:Y, where Y is Chol or OCer, in a molar ratio of 80:20:X, plotted as a function of intercalator content (X). Values were normalized according to fluorescence corresponding to complete dye release, achieved by addition of Triton X-100. Values are average ± SEM (n = 3). Modified from publication II.*

5.2.3. Effect of StnII on the microenvironment of CTL

To study the effect of StnII on the microenvironment of Chol, CTL, a fluorescent analog of Chol, was used as a probe [130, 195, 206]. The relative location of the probe within the membrane could be estimated by means of a quencher, 7-SLPC, which is known to partition selectively in the L_d phase [215, 216]. Thus, the variation on the fluorescence signal of CTL allowed ascertaining whether StnII changed the distribution of CTL between the fluid, PC-rich regions of the membrane and the more ordered, SM-rich domains.

The signal was first compared between membranes that contained the quencher (F samples) and those in which it was replaced by POPC (F_0 samples). The F/F_0 value for the membranes with ~20 mol% PSM was 0.27, indicating a large exposure of CTL to the quencher. In the membranes with nearly 50 mol% PSM, the F/F_0 value was 0.78, consistent with a reduced exposure of CTL to the quencher. Since sterols are known to associate with SM [145], this effect could be expected upon the increment of PSM content in the bilayer. The addition of different amounts of StnII resulted in an increase in the F/F_0 value in a dose-dependent manner. The magnitude of the increments is shown in Figure 17. Though qualitatively the same, StnII-induced protection of CTL from the quencher was larger in membranes with lower SM mol%. This could be explained by CTL being already shielded from the quencher, in the PSM-rich phase, in the membranes with higher PSM content.

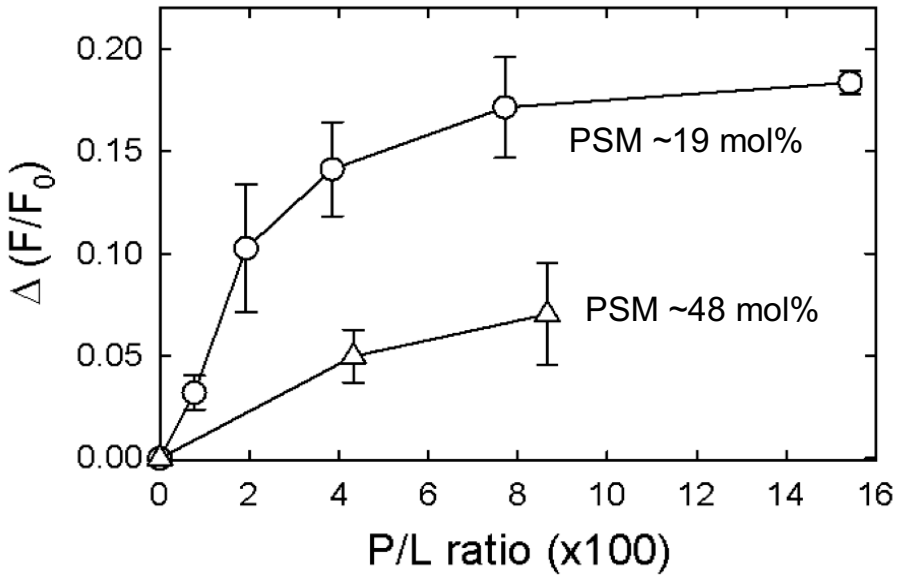

Figure 17. *Dose-dependent effect of StnII on the 7-SLPC-quenched quantum yield of CTL embedded in membranes composed of POPC:7-SLPC:PSM:CTL (50:30:20:5) (open circles) or POPC:7-SLPC:PSM:CTL (30:20:50:5) (open triangles). Bilayers in which 7-SLPC was replaced by POPC were used as reference (F_0 sample) in order to rule out direct effect of StnII. Each value is average ± SEM (n = 2). Modified from publication III.*

5.2.4. Membrane interaction of the Trp residues of StnII

To delve into a potential closeness of Chol and StnII, a FRET approach was chosen. This was possible thanks to the respective photophysical characteristics of CTL and Trp. Prior to the FRET assays, however, the effect of membrane binding on Trp emission from StnII was studied using the five Trp-to-Phe mutants available. Besides the WT protein, the proteins included the single mutant W43F, double mutants W43/110F and W43/114F, and triple and quadruple mutants W43/110/114F and W43/110/114/115F (Figure 18). The last mutant was particularly interesting because only a single Trp residue was left in its structure, W146.

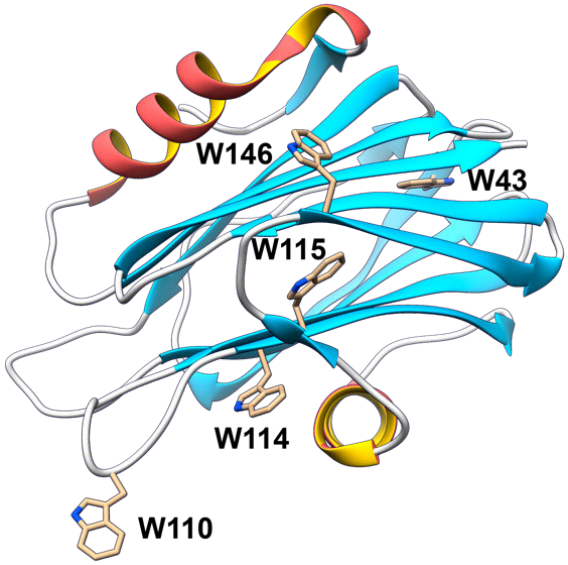

Figure 18. *The Trp residues on the structure of StnII. In the mutants available, all these residues, except for Trp146, have been replaced by Phe.*

All listed proteins were titrated with DOPC:eSM:Chol (1:1:1 molar ratio) LUVs. This composition was required to ensure membrane binding by some of the mutants [198]. In all cases, an increase in the quantum yield of Trp was observed (Figure 19).

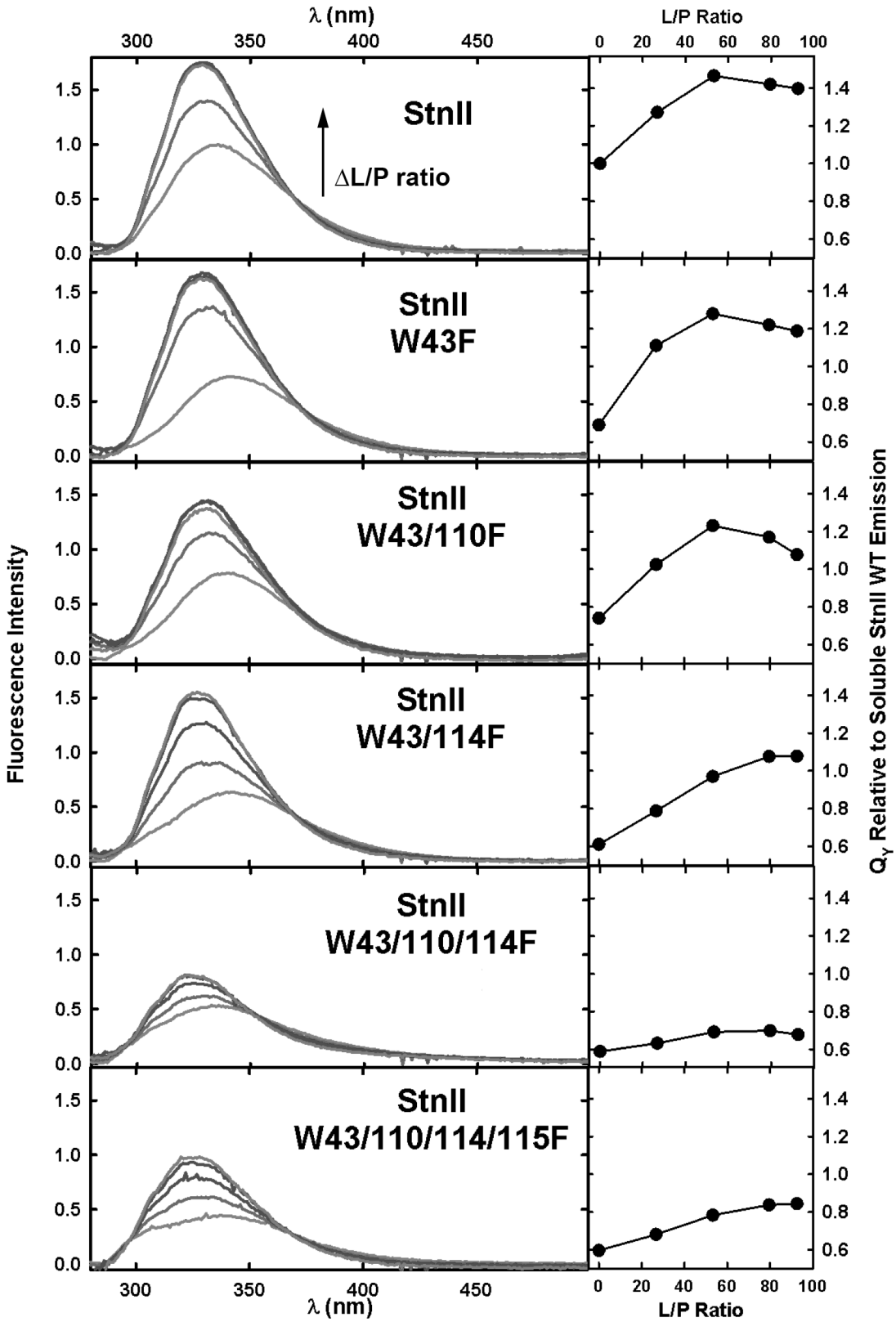

Figure 19. *Fluorescence spectra of StnII WT and its different Trp mutants as recorded while titrating with DOPC:eSM:Chol (1:1:1) LUVs. Arrow on top left panel indicates progression of the spectra as L/P ratio was increased. Panels on the right represent the change in the relative quantum yield of each protein as a function of the L/P ratio. Emission of soluble StnII WT as reference. Protein concentration was 200 nM. Adapted from publication II.*

Concomitant with the increase in quantum yield, spectral narrowing and blue-shifting were also observed. These effects are expected for Trp residues transitioning to an environment that is more hydrophobic. The results pointed W110 and W114 as the two residues whose environment is affected the most by membrane binding.

5.2.5. Location of CTL relative to Trp residues of StnII

A new titration was performed using StnII and the Trp-to-Phe mutants. This time, the vesicles were made of DOPC:eSM:sterol in a 1:1:1 molar ratio. Sterol content included CTL to a final amount of 5 mol%, with Chol being the remainder. To properly measure transfer efficiency, FRET should be quantified using quenched donor emission. However, these toxins all have several Trp residues, complicating the analysis. Hence, sensitized CTL emission was used instead since no further calculations were to be made using these data. This methodology provided a straightforward way of visualizing and comparing the contributions of each Trp residue to the total FRET observed for each toxin variant.

The results showed that the energy transfer from the Trp residues to CTL was taking place (Figure 20). As could be expected from the results above, the removal of

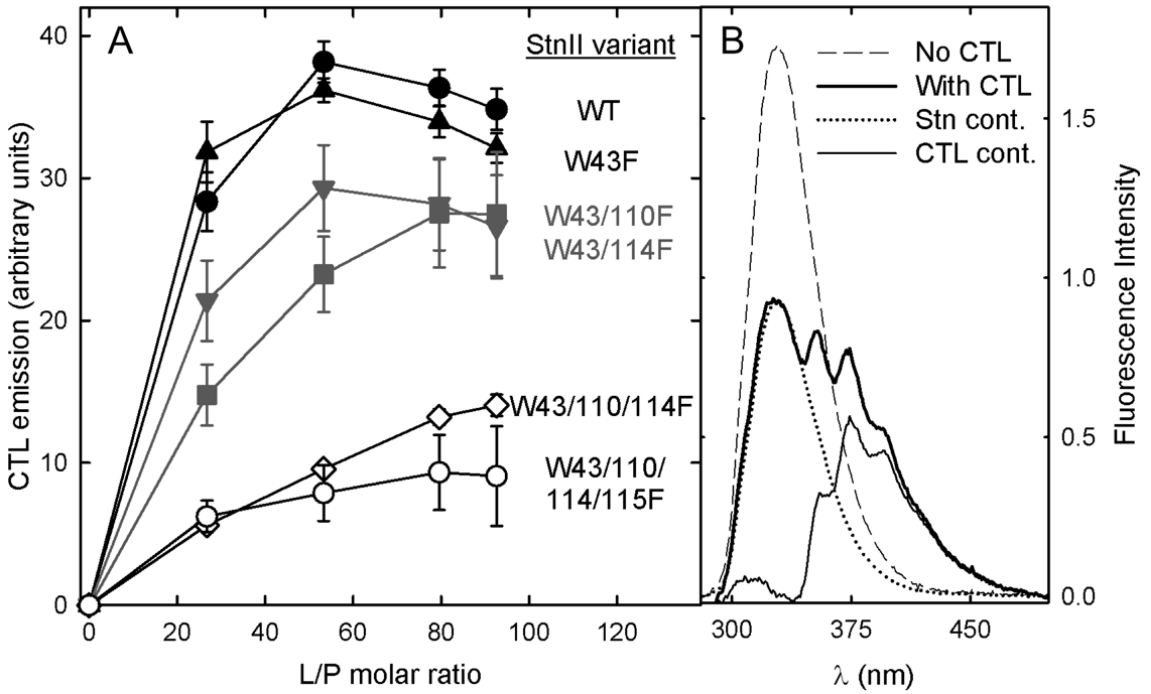

Figure 20. A: *Sensitized emission of CTL as measured when the indicated StnII variant was titrated using DOPC:eSM:Chol:CTL (33:33:28:5) LUVs. Each value is average ± SEM (n = 3).* **B**: *Example (at 93 L/P molar ratio) showing how CTL emission was quantified. Protein emission in presence of CTL-lacking LUVs (dashed line) was fitted (dotted line) to total emission (thick solid line) using the range between 325 and 340 nm (only Trp emission). CTL emission (thin solid line) was obtained by subtraction of the corresponding spectra. CTL emission was quantified by numerical integration from 340 nm. The small bump centered at 320 nm corresponds to unquenched Tyr emission. Modified from publication II.*

W110 and W114 greatly diminished the observed transfer efficiency and, hence, sensitized CTL emission. This effect is not observed when other Trp residues are replaced by Phe. Therefore, CTL can be said to be closest to Trp residues 110 and 114 (Figure 18).

5.2.6. Chol distribution around StnII

Previous results indicated that CTL was in close proximity to W110 and W114. However, given that StnII and CTL were both in the membrane, it was possible that the observed proximity happened by chance thanks to both the orientation of StnII relative to the membrane and CTL being at high enough local concentrations.

To resolve whether CTL was randomly distributed around StnII, the FRET efficiency from Trp to CTL was measured using the single Trp mutant of StnII. This mutant, which has only W146, was titrated with vesicles with increasing amounts of acceptor (CTL) in the membrane. Then, the experimental FRET efficiencies, calculated using quench donor emission, were compared to those expected for a pair of fluorophores randomly distributed in two parallel diffusion planes, namely, the *cis* leaflet of the membrane, and the plane at which W146 is located (Figure 21). The expected values were calculated using a modified version of a previous approach [207, 217]. Experimental results were always above the calculated values for random distributions even with different limiting parameters (Figure 21), indicating that CTL is preferentially distributed near StnII when this protein is bound to the membrane.

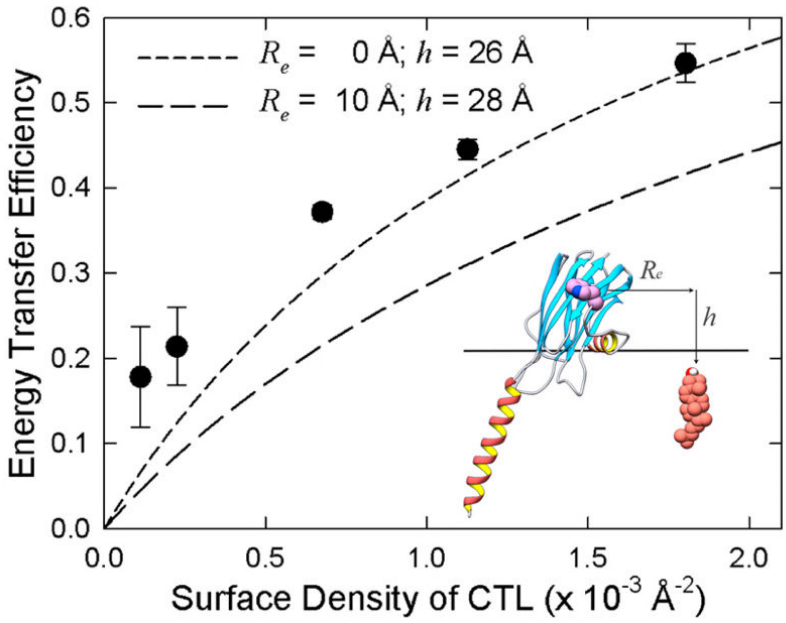

Figure 21. *Experimental Trp-to-CTL FRET efficiencies of the single Trp mutant of StnII (circles) as a function of CTL surface density, compared to the theoretically expected values for the indicated values of the parameters* R_e *and* h. *The scheme on the lower right of the figure depicts StnII, CTL and the model parameters* R_e *and* h. *Modified form publication II.*

5.3. Details of sticholysin-induced membrane permeability

Results from publication III

In the previous studies, the activity of sticholysins was evaluated based on their ability to induce the release of aqueous contents from vesicles of varied composition. In all cases, calcein was used as the probe. Always, the leakage trace reached a plateau before the complete release of the probe was reached, as shown by the maximum induced by Triton X-100. This brought up the following question: if actinoporins make holes in membranes, how was it possible that calcein stopped flowing to the outside of the vesicles?

To clarify this issue, a series of different assays were performed. These consisted in variations on the experiment of the release of aqueous contents. Some of the variations came from the literature, and some were developed in house. In the assays, a variety of probes were used. The probes were selected according to their charge and size in order to see how these two parameters affected sticholysin-induced permeability.

5.3.1. Calcein release

First, calcein release experiments were performed using StnII and vesicles composed of DOPC:eSM:Chol in a 1:1:1 molar ratio. These assays were used as the reference to which all later release experiments were compared. The addition of StnII to the LUVs of the aforementioned composition (2.5 μM) in a series of different P/L molar ratios yielded the results shown in Figure 22. In all cases, calcein release stabilized once it reached ~60% of the final possible release (Figure 22a), measured by applying Triton X-100. The LC_{50} value, calculated as the protein concentration required to induce 50% of the maximum possible protein-induced release, was 52 pM (Table 2).

The final release values can be reached relatively easy with a small concentration of protein, concealing otherwise differences that could otherwise be significant at those concentrations [26]. Thus, the initial rate of release, quantified as the slope of the leakage trace just after toxin addition to the cuvette was also measured (Figure 22b). The values obtained at 20 nM toxin, corresponding to a L/P molar ratio of 125 (a saturating concentration) were selected as representative from all experiments. In this case, a value of 0.061 ΔF units/s was obtained (Table 2).

5.3.2. Release of rhodamine 6G

Next, the release assay was performed by replacing calcein with R6G, while maintaining the lipid composition of the vesicles. The final release values plateaued at ~60%, as with calcein (Figure 22a). However, the LC_{50} was approximately six-fold

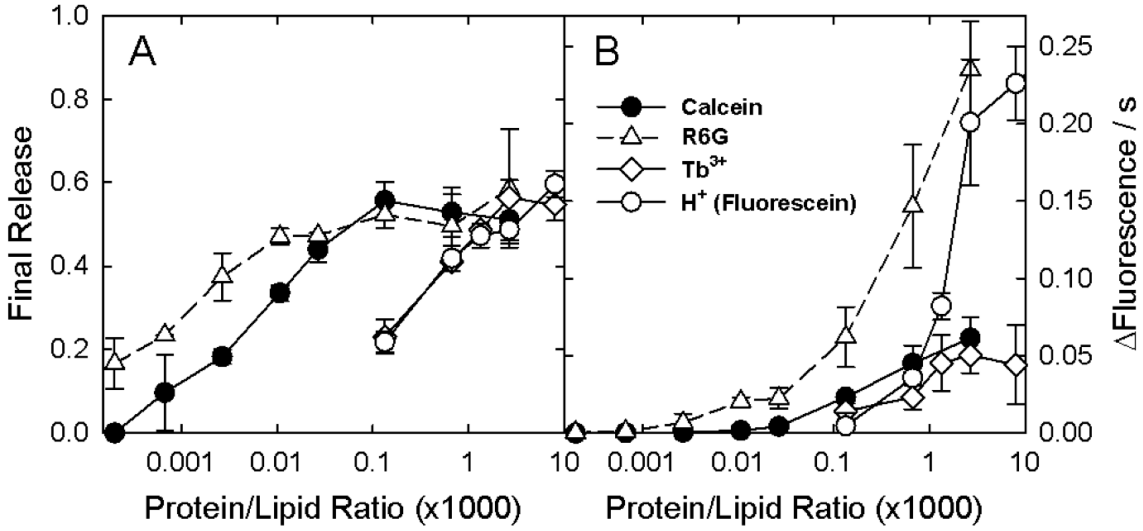

Figure 22. A: *Fraction of final release 5 min after toxin addition to dye-loaded LUVs composed of DOPC:SM/Chol (1:1:1) at different P/L molar ratios. Suitable detergents were added the samples to induce total release of the dye in order to register maximal fluorescence used to normalize each of the traces.* **B**: *Initial rates of dye release for the experiments in* A. *Ions used were calcein (solid circles), R6G (open triangles), Tb^{3+} (open diamonds), and H^+ (fluorescein (open circles). Values are average ± SEM of n = 2-3. Modified from publication III.*

Table 2. *Parameters obtained from each of the leakage assays.*

Assay	LC_{50} (nM)	Release rate at 20 nM (ΔF/s)	Saturation (% of release)
Calcein	0.052	0.061	53.2
R6G	0.009	0.235	53.5
Tb^{3+}	1.990	0.051	55.1
H^+ (fluorescein)	2.880	0.201	62.5

lower than when calcein was used (Table 2). Likewise, the rate at 125 L/P molar ratio was 0.235 ΔF units/s, faster than that observed when using calcein (Figure 22b and Table 2).

5.3.3. Release of cations (Tb^{3+} and H^+)

The permeability of StnII pores to small cations was evaluated using Tb^{3+} and H^+. In either case, and as in previous assays, the release never exceeded ~60% (Figure 22a). The measured LC_{50} values were 1.99 and 2.88 nM respectively (Table 2). The initial rate of release differed significantly between both approaches. For Tb^{3+}, the rate at 125 L/P molar ratio was slower than that observed for calcein (Table 2 and Figure 22). The leakage of H^+ was shown to be faster but only at high protein concentrations (Table 2 and Figure 22).

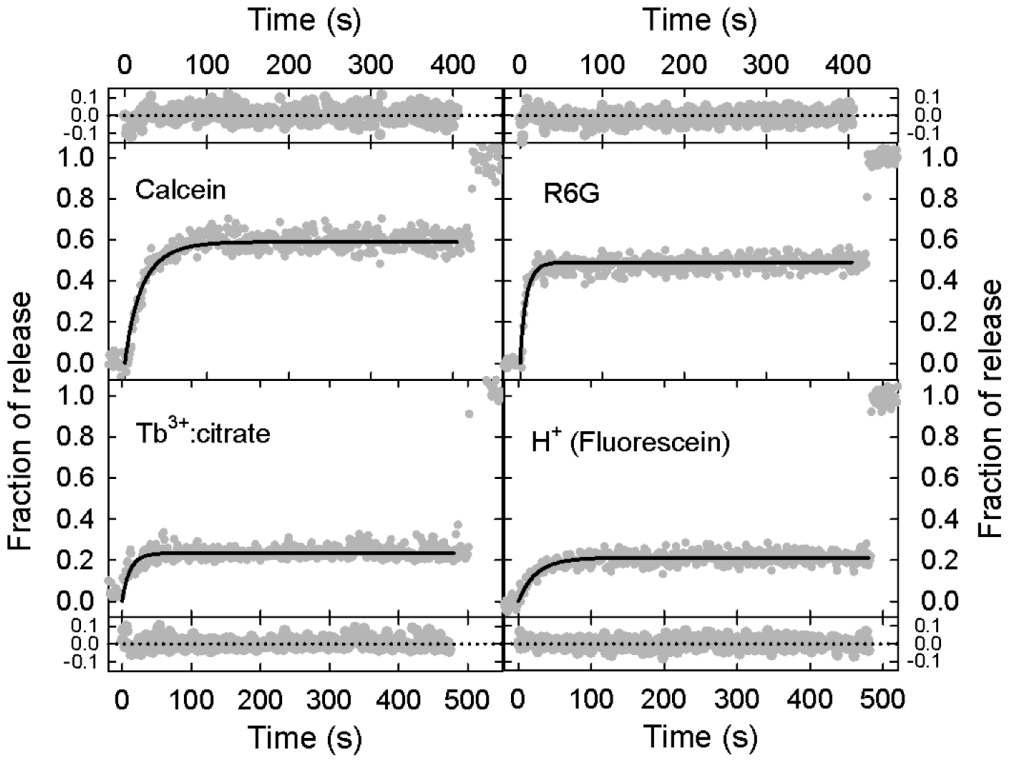

Figure 23. *Representative data from release experiments using calcein, R6G, Tb^{3+}, and H^+ (fluorescein), acquired using 1 nM StnII in all shown cases. Solid lines are fits of the perturbation model. Small panels show the residuals of each fit. Adapted from publication III.*

5.3.4. Agreement with kinetic models

The release traces form the above experiments were used to fit the perturbation model (see section 4.2.3.3) [205]. In all cases, the model provided very good fits (Figure 23), indicating agreement of the experimental results with the model's theoretical basis.

5.3.5. Equilibrium pore assay

In all previous assays, the probe was encapsulated in the LUVs and then freed by the action of StnII. Those experiments cannot differentiate between leakage induced by membrane perturbation and leakage through the stable pore lumen.

To reveal whether sticholysin pores were permeable once stabilized, LUVs made of DOPC:eSM:Chol (1:1:1 molar ratio) were prepared, including 1 mol% of POPE-NBD. NBD emission was quenched using sodium dithionite. The advantage of this assay is that dithionite can be applied to the sample *before* or *after* pore formation by StnII, that is, exposure of the LUVs to the toxin. Therefore, it allows the evaluation of dithionite's ability to pass through already-established pores.

The incubation of intact LUVs with dithionite resulted in a ~40% decrease in the observed NBD emission (Figure 24a), indicating that the employed vesicles were

impermeable to dithionite, at least at the time scale of these experiments. Triton X-100 was used to obtain the emission of fully exposed NBD, which should then be quenched completely, inducing a decrease in the fluorescence of the remaining 60%.

Once the LUVs were proven impermeable, dithionite was applied to LUVs that had been previously incubated at various StnII concentrations. This time, NBD's emission underwent a much more significant decrease (Figure 24b). The magnitude of the decrease was dependent of the concentration of toxin to which the LUVs had been exposed. The addition of Triton X-100 caused a modest reduction in NBD emission.

Finally, different amounts of StnII were added to the LUVs that had been exposed to dithionite (Figure 24c). NBD emission, which was already reduced by 40%, was further diminished by StnII addition in a dose-dependent manner.

Altogether, these results indicate that the stable pores of StnII are indeed open, and permeable, at least to dithionite. We observed that Triton X-100 distorted NBD emission. Although we were not able to correct the signal for that effect, we believe that the effect of Triton X-100 accounts for the deviation from the 50% quenching that should be observed due to the first dithionite addition. Nevertheless, this is not relevant to the conclusion obtained from these experiments since the larger decrease observed due to preincubation with StnII is sufficient to conclude that dithionite can pass through thermodynamically stable StnII pores.

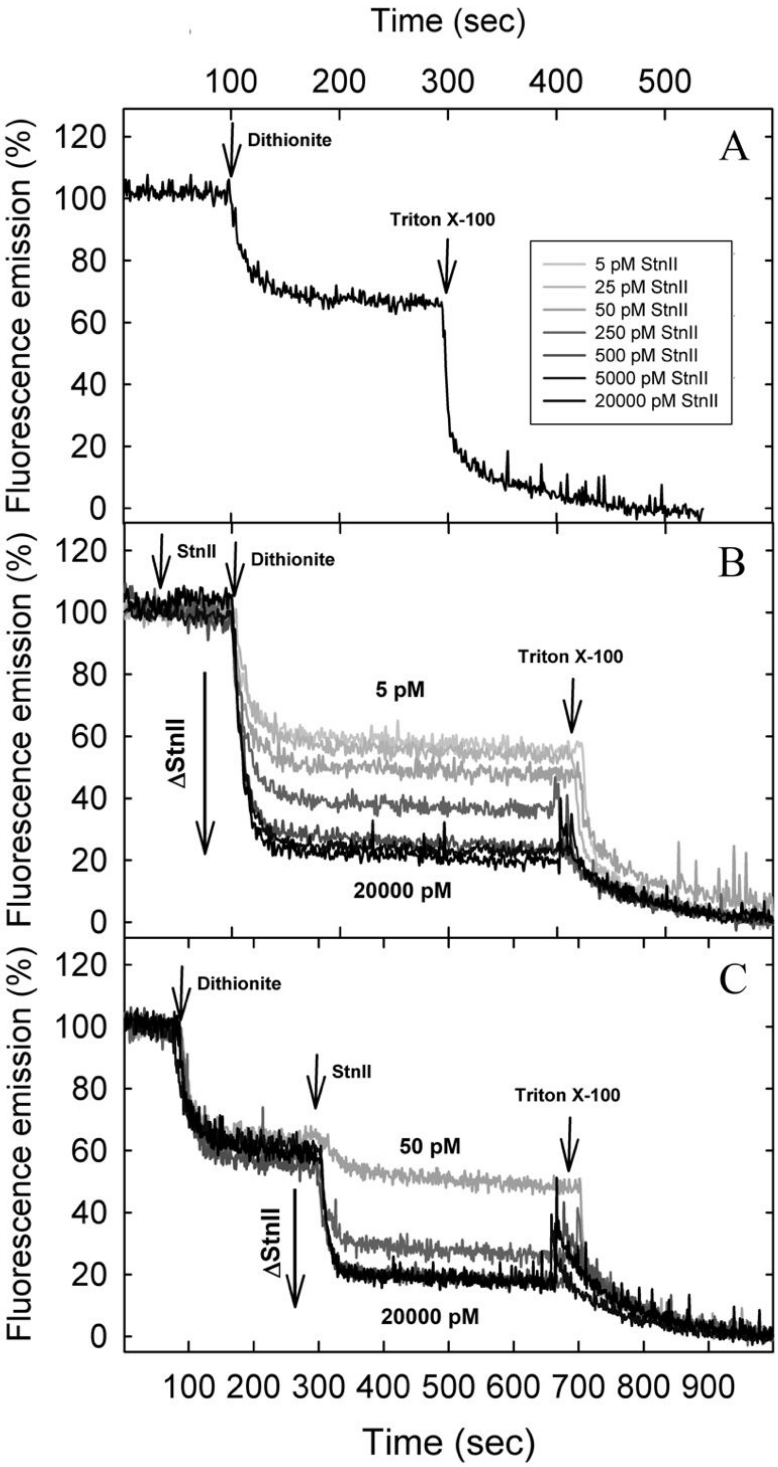

Figure 24. *Equilibrium pore assays. Sodium dithionite (final conc. 55 mM) was added to LUVs of DOPC:eSM:Chol (1:1:1) with 1 mol% POPE-NBD.* **A***: LUVs were first exposed to dithionite, then to Triton X-100 (final conc. 0.045% v/v) was applied to achieve complete vesicle disruption.* **B***: the procedure in* A *was repeated with LUVs that were preincubated with different amounts of StnII, which greatly increased LUVs permeability to dithionite.* **C***: StnII was added after dithionite addition to the sample. As in the previous experiments, LUVs were disintegrated with Triton X-100. Adapted from publication III.*

5.4. Oligomerization of sticholysins from Förster resonance energy transfer

Results from publication IV

The stoichiometry of the actinoporin pores has been long debated in the field. Several different structures of the final pore have been published so far [29, 34, 35, 189]. However, due to the difficulty of isolating the pore structure in a way that was suitable for analysis, such as X-ray crystallography or nuclear magnetic resonance, different methods, which involved non-native conditions, had to be used.

Our goal was to develop an approach that enabled us to determine the stoichiometry of these pores directly on model membranes with the least perturbation possible of the system. For this, a single Cys-mutant of StnI was produced. This mutant, which was essentially identical to StnI-WT from a structural and functional point of view (Figure A2), could be labeled at a specific position that was not expected to interfere either with protein-protein interactions or with membrane recognition and binding (Figure A3). This approach allowed the estimation of the stoichiometry of the complexes, while permitting us to delve into other details on the behavior of these toxins, such as the association in solution and the cooperativity of StnI with StnII.

5.4.1. Motions of sticholysins in solution and on membranes

StnI-T43C was first labeled with ATTO-488. The time-resolved anisotropy decays of the toxin as well as of the free label were recorded using solutions in which only 2% of the total sticholysin was labeled (Figure 25). For the free label, whose anisotropy rapidly decayed to zero, only a single, very short correlation time (0.2 ns) could be resolved. The toxin displayed two correlation times. The fast one was ~0.3 ns, very close to that of the free label, accounting for the segmental motions of the probe itself. The slower one was ~2.95 ns and corresponded to the rotational motions of the proteins within the solvent (Table 3). This correlation time could be used, with Eq. 12, to estimate the molecular diameter of sticholysins. The value obtained, 29.0 ± 1.3 Å, agreed with the molecular structures available, as evidenced when placing a sphere of that size at the mass center of those structures (not shown). The time-dependent anisotropy did not decay to zero, displaying a limiting anisotropy value of ~0.014.

Next, the same anisotropy decays were recorded in the presence of LUVs, composed of DOPC:eSM:Chol (1:1:1 molar ratio) and, separately, POPC:PSM (4:1 molar ratio). Energy transfer is a phenomenon that is known to reduce anisotropy [200, 202]. Hence, the fractional labeling of sticholysins was kept low, at 2% in

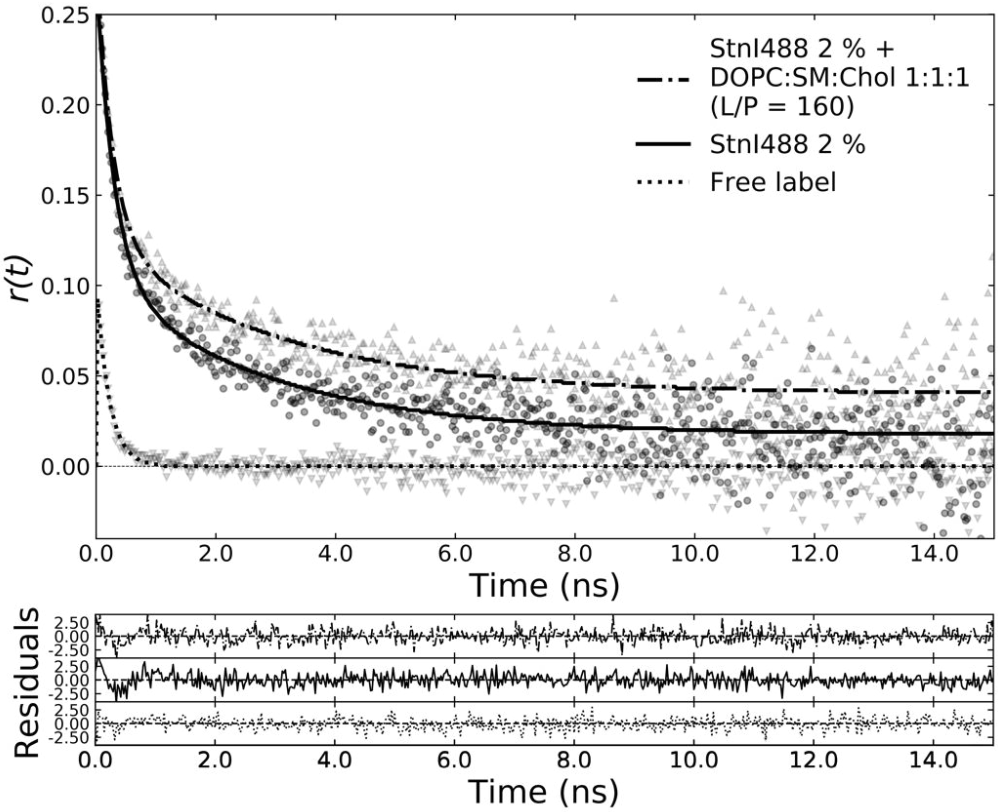

Figure 25. *Time-dependent anisotropy decays of StnI labeled with ATTO-488 free in solution (degree of labeling = 2%; solid line) or in presence of DOPC:eSM:Chol (1:1:1) membranes (L/P molar ratio = 160; dash-dot line). The decay of the free ATTO-488 label was also recorded (dotted line). Traces of residuals for each of the fits are shown below. The order of the graphs of the residuals is the same as that of the legend. Modified from publication IV.*

presence of Chol and 5% when it was absent, to minimize potential energy transfer between neighboring subunits in the pores. Not only that but the L/P molar ratio was also high, beyond saturation, so that energy transfer between the subunits of different pores was unlikely while also achieving maximum possible binding of the available toxin. The observed fast correlation time did not vary from the previously measured one, whereas the slow correlation time was slightly increased for StnI and reduced by ~0.6 ns for StnII. The limiting anisotropy was larger in both cases, with values of ~0.04, indicating a restricted mobility of the membrane-bound proteins (Table 3). This time, the correlation times could not be used to calculate molecular sizes due to the complex environment surrounding the toxins, and the unevenly restricted mobility of the complexes due to their very structure and the restrictions imposed by the membrane.

5.4.2. Oligomerization in solution

It has been shown that StnII is able to oligomerize in solution [184]. Hence, energy transfer could be expected to occur even in solution, at least to some extent, without the need for pore formation on membranes. As a first approach, steady-state

Table 3. *Parameters of the anisotropy decays of ATTO-488, StnI (degree of labeling = 2%) in absence and presence of lipids (DOPC:eSM:Chol 1:1:1 in L/P molar ratio = 160; POPC:PSM 4:1 in L/P molar ratio = 160). Indicated are the initial anisotropies (r_i) and correlation times (θ_i) of each component and the limiting anisotropy (r_∞). Values were obtained from fitting, errors from bootstrap analysis.*

	r_1	θ_1 (ns)	r_2	θ_2 (ns)	r_∞
ATTO-488	0.125 ± 0.005	0.228 ± 0.012	-	-	0.000 ± 0.0004
ATTO-488 + DOPC:eSM:Chol	0.135 ± 0.006	0.232 ± 0.012	-	-	0.001 ± 0.0004
StnI	0.200 ± 0.008	0.299 ± 0.030	0.089 ± 0.006	2.851 ± 0.530	0.014 ± 0.002
StnI + DOPC:eSM:Chol	0.195 ± 0.009	0.267 ± 0.034	0.088 ± 0.004	2.979 ± 0.587	0.040 ± 0.003
StnI + POPC:PSM	0.157 ± 0.007	0.224 ± 0.020	0.103 ± 0.005	2.273 ± 0.170	0.031 ± 0.002

anisotropy, which is affected by energy transfer, was measured. Anisotropy is expected to diminish as a consequence of energy transfer [202, 218]. Hence, the steady-state anisotropy of ATTO-488-labeled StnI in solution was measured at increasing degrees of labeling (DoL). The anisotropy appeared to decrease only slightly, not significantly, at high DoL values.

Thus, to increase the resolution, a sample of ATTO-488-labelled StnI-T43C (hereafter StnI-488 or donor) was titrated with ATTO-542-labelled StnI-T43C (hereafter StnI-542 or acceptor). The R_0 of this FRET pair is significantly larger than the distance over which the previous approach is effective (only at $r < 0.8R_0$ [218]). The titration was performed in the presence of WT StnI to properly control the relative amounts of donor and acceptor in the sample. The fraction of both the donor and the acceptor in the sample varied as a consequence of the titration process. The measured FRET efficiencies were plotted as a function of the acceptor fraction, which was deemed more representative (solid line in Figure 27). A small increase in the values of E was observed, indicating the presence of StnI oligomers in solution.

Incidentally, it has been shown that a minimal amount of StnII, just 1%, is able to significantly enhance the hemolytic activity of StnI, presumably by facilitating the membrane-binding step of the process of pore formation [95]. In such case, StnII could foreseeably oligomerize with StnI in solution. This could be revealed with the present FRET approach. The titration of StnI-488 with StnI-542 in the presence of WT StnII showed an increased FRET efficiency compared to the previous experiments in which WT StnI was used (dashed line in Figure 27).

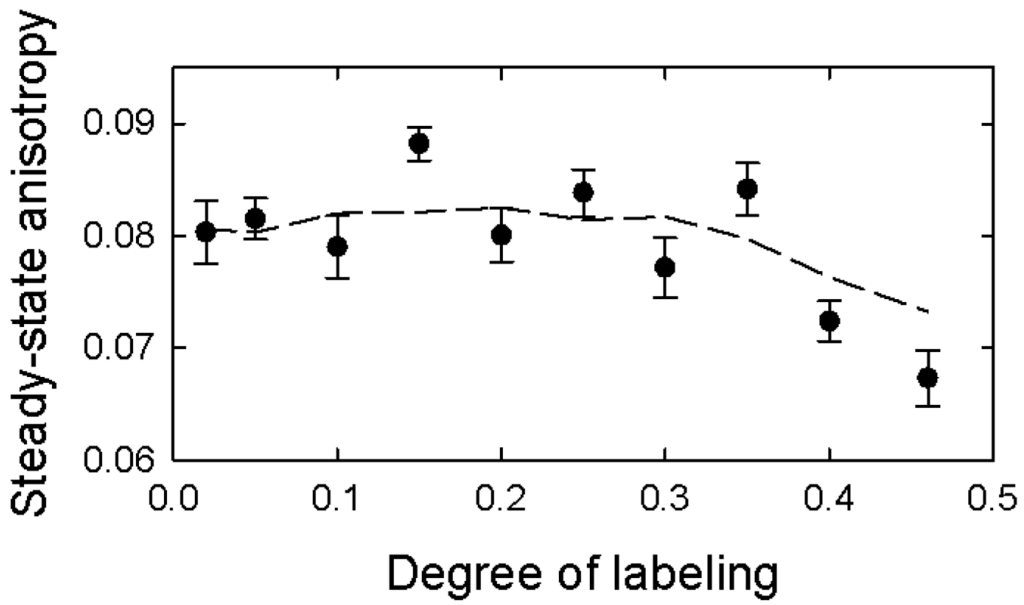

Figure 26. *Steady-state anisotropy dependence on the degree of labeling of StnI in solution. The dashed line is only a guide to the eye. Modified from publication IV.*

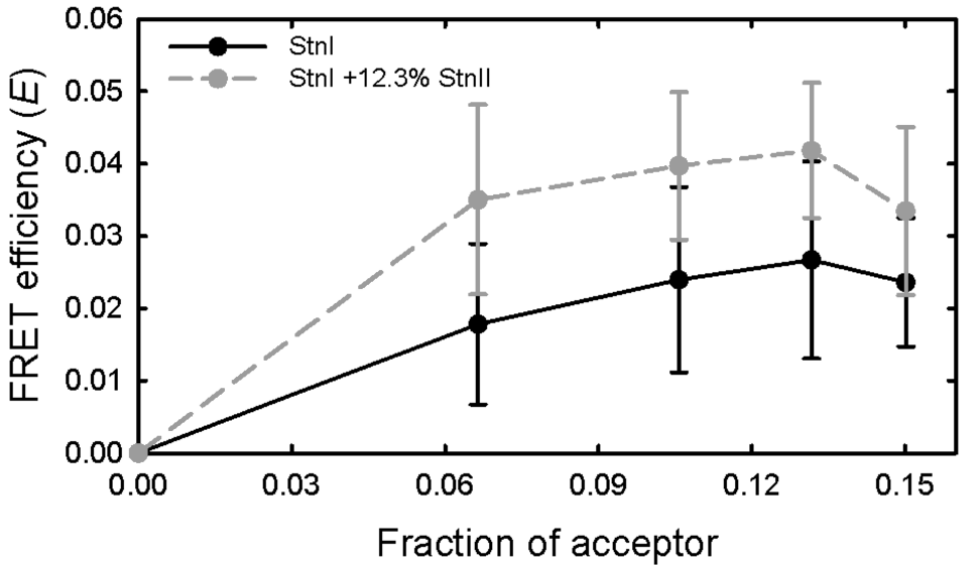

Figure 27. *FRET efficiencies observed for donor-labeled StnI with WT StnI (solid black trace) or with WT StnII (dashed gray trace) titrated with acceptor-labeled StnI to a final composition of 5% donor, 15% acceptor, and 12.3% of the corresponding WT sticholysin variant. Modified from publication IV.*

5.4.3. Stoichiometry of StnI on DOPC:eSM:Chol membranes

Energy transfer efficiency values were obtained from steady-state data using quenched donor emission from the deconvoluted sample emission.[2] Lipids were directly added to a 100 nM solution of StnI, with a fraction of 0.05 donor and the selected fraction of acceptor (up to 0.15), to a final L/P molar ratio of 160. The obtained *E* values were plotted as a function of the acceptor fraction in the sample and compared to the theoretical predictions (Figure 28, left panel). RMSD calculations showed that an octameric ensemble would be in best agreement with the observed signal obtained in the presence of DOPC:eSM:Chol (1:1:1 molar ratio) membranes (Figure 28, right panel). Nevertheless, this result should be taken cautiously due to the limited resolution of the model for large complexes. Based solely on this, it can be concluded that sticholysin pores are heptamers or larger structures.

5.4.4. Is the stoichiometry of StnI pores different in POPC:PSM 4:1?

The procedure in the previous section was repeated for StnI in combination with POPC:PSM (4:1 molar ratio) vesicles. The L/P molar ratio was increased to 320 this time, in spite of increased lipid-induced light-scattering, to ensure complete binding. This was necessary due to the smaller affinity of StnI for Chol-lacking membranes. Unexpectedly, the signal from StnI did not follow the trend expected from any of the theoretical predictions (Figure 29).

5.4.5. Inclusion of StnII does not affect stoichiometry

Once more, the procedure was repeated but this time including 12.3% of WT StnII in all samples to evaluate the effect the inclusion of StnII had on the stoichiometry of StnI pores. This was the result in both cases, when Chol and Chol-lacking membranes were used. The distribution of the RMSD values in the experiment including Chol closely resembles that observed for StnI alone (Figure 30). In the absence of Chol, the experimental FRET efficiency values also present the same trend as in the absence of StnII, again not following the predictions (Figure 31).

[2] This same procedure was also used in paper II. For more details, see Figure 20b and papers II and IV.

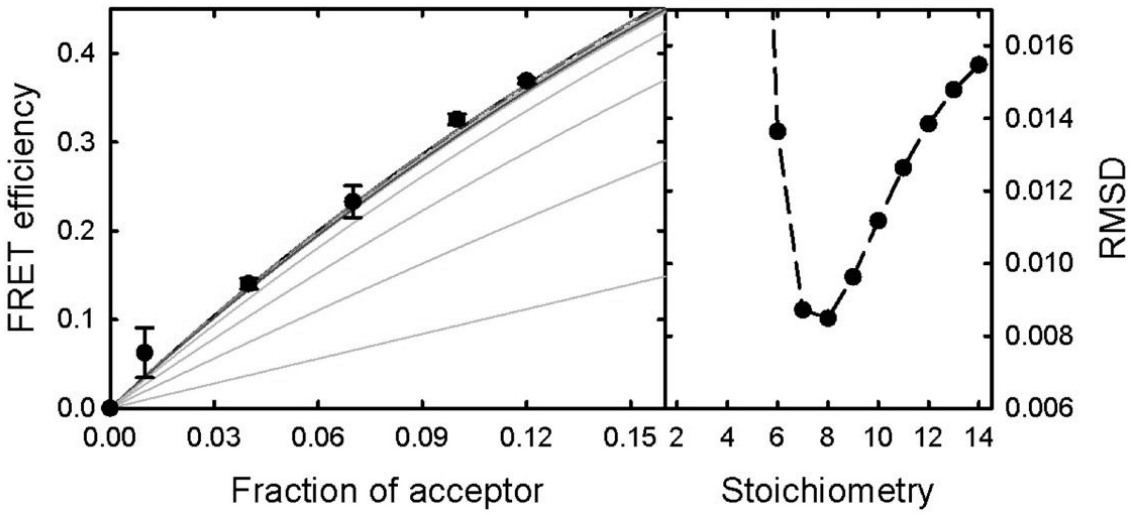

Figure 28. Left: *experimental FRET efficiency values (solid dots) using labeled StnI in combination with DOPC:eSM:Chol 1:1:1 molar ratio membranes plotted with the theoretical predictions made for stoichiometries from 2 to 10 (11 to 14 were removed for clarity). From bottom to top, predictions for 2, 3, 4, 5, and so on. Predictions from 6 on are hardly distinguishable at this scale. With the conditions considered, maximum FRET efficiency is reached for heptamers, being slowly reduced for higher values (see supplementary figure 2).* **Right**: *root mean squared distances (RMSD) obtained for the experimental values on the left compared relative to each of the predictions. Adapted from publication IV.*

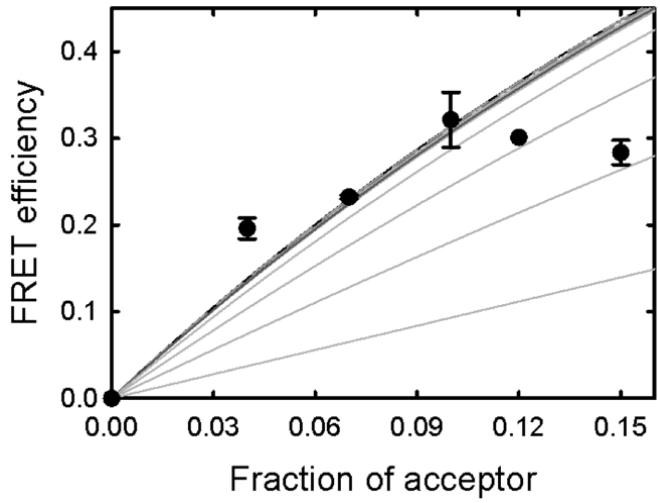

Figure 29. *FRET efficiency values observed for labeled StnI in combination with LUVs composed of POPC:PSM 4:1 molar ratio. Notice that experimental results do not agree with predictions as in the previous case. Adapted from publication IV.*

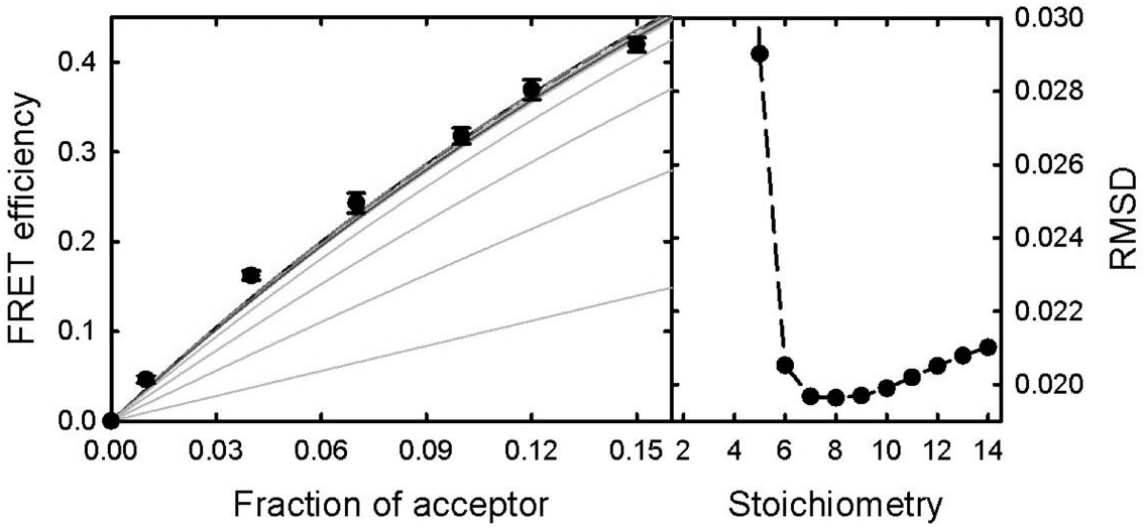

Figure 30. Left: *experimental FRET efficiency values (solid dots) obtained using labeled StnI with 12.3% StnII in combination with DOPC:eSM:Chol 1:1:1 molar ratio membranes plotted with the theoretical predictions as in Figure 28.* **Right**: *RMSD values for each of the predictions. In this case, the difference observed between the stoichiometries is reduced compared to the previous result in absence of StnII. Adapted from publication IV.*

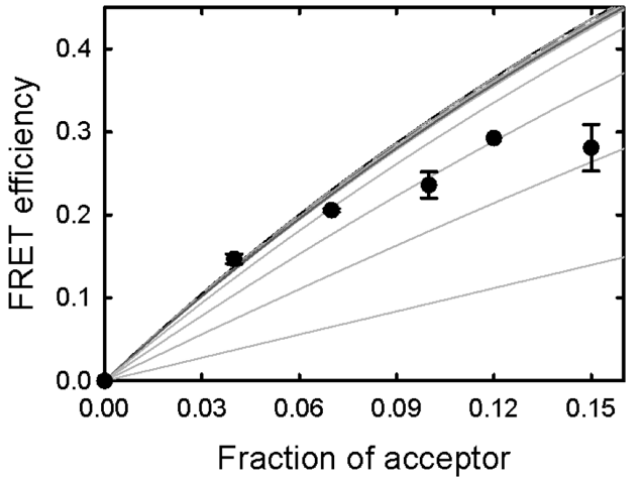

Figure 31. *FRET efficiency values observed for labeled StnI in presence of 12.3% StnII in combination with POPC:PSM 4:1 molar ratio LUVs. Again, the experimental values do not follow the expected trends. Adapted from publication IV.*

5.4.6. Pores of sticholysins are not remodeled once formed

Electrophysiological measurements have suggested that sticholysins pores might be unstable given the level of conductance noise they yield compared to those observed for β-pore-forming toxins [219]. This noisiness could be just a consequence of the thermal oscillations of the system given the characteristics of these pores, whose lumen would be lined by both the N-terminal α-helices of sticholysins and lipids. However, it has also been proposed that, once formed, the pores would be under continuous remodeling, with monomers transiting from one complex to another.

To test this idea, StnI or StnII, to a final increment of 57 nM, was added to 100 nM StnI already including 5% donor and 15% acceptor preincubated with lipids. The initial L/P molar ration was 240. This way, the final L/P molar ratio was 160, comparable to the results of the aforementioned assays. In both cases, the observed FRET efficiency was maintained after the addition of the extra amount of protein, regardless of it being StnI or StnII (Figure 32). These results indicate that already-formed pores could not be affected by the toxin supplied afterward.

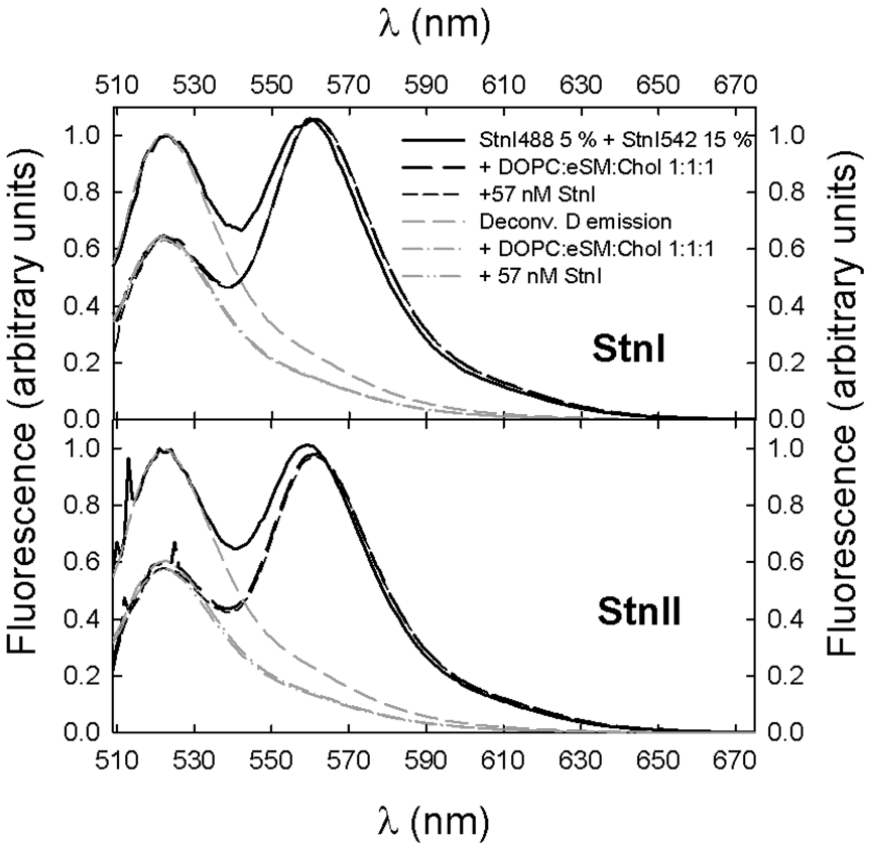

Figure 32. Top panel: *Emission spectra of StnI with 5% donor labeling and 15% acceptor labeling in solution (solid black line), with DOPC:eSM:Chol 1:1:1 (long dashed black line) and after addition of extra 57 nM unlabeled StnI (short dashed black line). Deconvoluted donor emission is also shown in gray. The later addition of StnI did not affect FRET efficiency, indicating that pores are not remodeled.* **Bottom panel:** *same as top, but the addition of WT StnI was replaced by WT StnII. Modified from publication IV.*

6. DISCUSSION

6.1. Sticholysins prefer bilayers of intermediate thicknesses

6.1.1. Properties of membranes differing in thickness

To understand the interaction between sticholysins and membranes of different thicknesses, it is essential to understand which membrane properties vary as acyl chain length is increased. Bilayer thickness has been shown to depend linearly on acyl chain length [220]. As membrane thickness is increased, so does acyl chain order (see Figure 11), thanks to the increased possibility of van der Waals interactions. In our membrane systems, the position of the unsaturations in the acyl chains (see section 5.1) might also play a role since the double bond distance from the water-membrane interface is known to result in higher order in the part of the acyl chains closer to the lipid head group [221, 222]. Taking all into account, we can say that the membrane surface is quite similar for all bilayers, which only differ in membrane thickness and essentially vary in packing, as shown from anisotropy measurements (Figure 11).

In general, the inclusion of Chol also increases acyl chain order [223]. This is a consequence of Chol's nearly perfectly planar phenanthrene surface, which forces a *trans*-gauche configuration on the single bonds of the neighboring lipids. For the same reason, Chol is also responsible for increasing bilayer thickness [224]. Generally, Chol is preferentially associated with SM molecules [145]. Thus, in our system, Chol is likely distributed with 14:0-SM, though some would remain with the PC molecules, increasing membrane thickness and, as observed for most cases (see Figure 11), acyl chain order.

6.1.2. Dependence of sticholysin activity on bilayer thickness

Sticholysin-induced calcein release experiments were used to test the activity of StnI and StnII when facing membranes with different bilayer thicknesses. In all cases, a final total release between 60 and 80% was reached in 15-minute experiments though saturation was reached in a much shorter time. In the absence of Chol, the fastest calcein release was observed for membranes with average thickness, in which the main component was di-16:1-PC or di-18:1-PC (Figure 12). When Chol was included, calcein release became faster for both toxins, with the maximum shifted towards bilayers whose main components were di-14:1-PC and di-16:1-PC (Figure 12).

Since the trend observed for calcein release in each case does not correlate with the observed acyl chain order, it can be assumed that bilayer thickness, rather than acyl

chain order, is a more important parameter from the point of view of the insertion of the N-terminal α-helix of sticholysins. The effect of the inclusion of Chol, in terms of increased release rates, is likely related to the observation in EqtII that Chol is required for complete helix insertion in the membrane [27]. The observed shift is probably related to the predicted Chol-induced increase of bilayer thickness.

6.1.3. SPR binding data

When sticholysin-to-LUV binding was measured using SPR, a linear dependence of bilayer thickness was observed. The trend showed that higher acyl chain order and thickness hindered membrane binding (Figure 13).

This is not consistent with the results from the calcein release assays. However, calcein is a functional assay, whereas SPR is not. Due to the conditions used in the SPR assay, these experiments report maximal protein association to LUVs. In fact, since LUVs are immobilized on the chip surface, they might behave differently from freely diffusing LUVs as LUVs are in the rest of the experiments, possibly explaining the different acyl chain-dependence levels observed in this assay.

6.1.4. Thermodynamic parameters of the interaction

In all cases, the interaction between the toxins and the membrane was enthalpy-driven. The entropy of the interaction was non-favorable but always compensated by enthalpy. Though this might seem surprising for an interaction that is essentially hydrophobic, this has been observed for many proteins that penetrate membranes, including actinoporins [107, 225]. The explanation assigns the favorable ΔH to the van der Waals energy of the interaction between the hydrophobic moieties, with contributions of protein-protein interactions. The non-favorable ΔS would then be a consequence of the ordering of water solvating the newly exposed surfaces.

It is noticeable that ITC results present a very similar trend to that of calcein release assays. Probably, as mentioned in the previous section, the difference from SPR results is due to LUVs being freely diffusing. In the absence and presence of Chol, sticholysins presented the highest values of K_a for vesicles with intermediate bilayer thickness (Figure 14a). The values were much higher when Chol was included, especially for membranes with di-16:1-PC and di-18:1-PC. Nevertheless, the trend remained unchanged. The effect of Chol, which does not seem to be related to membrane thickness or acyl chain order, might instead be related to specific effects that Chol might have on the membrane or on the recognition of SM by sticholysins [22, 25, 26].

6.1.5. A simple model to explain the thickness-dependence of sticholysins' activity

Calcein release was observed for all combinations of membrane systems and toxins. Release was membrane thickness-dependent, indicating that either oligomerization, final pore structure, or membrane penetration was affected by bilayer thickness.

To explain the observed membrane thickness effect, a very simple model was constructed (Figure 33). Using the membrane thickness values previously reported for bilayers composed of pure di-X:1-PC [220], the angle θ formed by the N-terminal α-helix with respect to the bilayer normal was estimated. For this, we considered that the first 30 residue stretch of the N-terminal formed into a 45 Å-long (1.5 Å/residue x 30 residues) α-helix. This parameter (length of the helix) will be referred to as *l*. Thus, the value of θ can be calculated as $\theta = \arccos(h/l)$, where *h* is the bilayer thickness. Once known, the angle was used to calculate the expected inner radius of the pore, *r'*, in each of the membranes as $r' = \sin(\theta) \times (l + l')$, where $l + l'$ is the distance from the N-terminal to half the height of the β-barrel. This was 57.8 Å, as measured on the FraC pore crystal structure (PDB code 4STY) using UCSF Chimera [108]. Monomer width, *w*, was measured to be 25.8 Å at that position. The value of *r'* was used to calculate the circumference along which the monomers would be located. Then, the number of monomers per pore was calculated dividing the calculated circumference over *w*.

The results of the model predict that, for membranes composed of di-18:1-PC, the angle θ would be 32.4º, and the pores would consist of 7.5 monomers each. These two values are consistent with previous reports. The angle of the N-terminal helix of StnII was measured previously to be ~31º on DOPC:SM:Chol 1:1:1 membranes using infrared spectroscopy [106], while the most accepted stoichiometry is eight monomers per pore, as shown in the FraC structure obtained through crystallization [35]. In membranes of different thicknesses, it is possible for the pore's structure to be slightly different in terms of the angle of the α-helix, stoichiometry, or overall pore conformation. This could result in less favorable and effective assemblies, as suggested by our results.

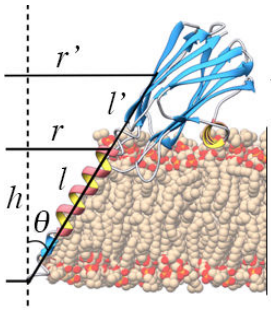

Pure lipid	Experimental *h* (Å)	Theoretical θ	Estimated *r'* (Å)	Estimated nº of monomers/pore
Di-14:1-PC	31.00	46.46	41.9	10.2
Di-16:1-PC	34.50	39.94	37.1	9.0
Di-18:1-PC	38.00	32.39	30.9	7.5
Di-20:1-PC	41.50	22.75	22.3	5.4
Di-22:1-PC	45.00	0.00	0.0	0.0

Figure 33. *Theoretical estimation of potentially bilayer thickness-dependent pore parameters. Parameters in the scheme and values in the table are explained in the main text. Adapted from publication I.*

6.2. Chol is preferentially distributed near StnII

6.2.1. StnII induces declustering of pyr-SM regardless of OCer or Chol presence

Sterols, regardless of the details of their structure, have been observed to enhance sticholysin activity [25]. We wondered if the interfacial hydroxyl group, shared by all of the assayed sterols, could be enough to explain their effect. Hence, OCer, which also presents an interfacial hydroxyl group, was selected. OCer was particularly convenient because, like Chol, it tends to associate with SM [156, 226, 227], but it does not induce gel phase formation, which hinders sticholysin activity [23].

First, the effect of OCer and Chol on SM was evaluated. As expected, if OCer and Chol partition preferentially in the SM-rich phase, the inclusion of either of them in the membranes used resulted in a significant reduction of acyl chain contacts between SM molecules, as reported by the E/M ratio of pyrene (Figure 15). The effect of Chol was larger than that of OCer, proving it a better intercalator.

However, the observed dose-dependent effect of StnII was nearly the same in all situations (Figure 15). The toxin also reduced SM-SM acyl chain contacts but independently of the presence of lipids that prefer the SM-rich phase. The effect of StnII could have two different, non-mutually excluding explanations. On one hand, the protein itself could be able to stand between the acyl chains of SM, reducing their contacts. On the other hand, it could promote a different lipid distribution in the membrane, somehow diluting SM molecules, either by driving them into the SM-poor domain or taking other lipids into the SM-rich phase.

6.2.2. Chol is a better enhancer of the activity of StnII than OCer

Since no significant difference had been observed in terms of StnII effect on SM contacts, we proceeded to compare the effect that the presence of OCer or Chol in the membrane had on the activity of StnII. For this, calcein release assays were chosen. While Chol has been long known to be a great enhancer of actinoporin activity [15, 19, 21-23, 25-28, 113], OCer had not been used in combination with StnII.

Chol proved itself a much better promotor of StnII activity when compared to OCer (Figure 16), revealing that having an interfacial hydroxyl group is not enough to enhance the activity of StnII. The effect of Chol was significantly larger than that of OCer even at Chol concentrations that do not promote phase separation [129]. Therefore, the improvement induced by Chol could not be solely attributed to its hydroxyl group. Instead, its overall structure, and the way it interacts with SM, which was shown to be different than that of OCer, could explain Chol's enhancing effect.

6.2.3. CTL microenvironment changes upon StnII binding

Using CTL in combination with a phase-selective quencher revealed that StnII binding to the membrane significantly altered the microenvironment surrounding CTL. CTL emission in the F_0 samples (no quencher) was already enhanced upon sticholysin addition (not shown), indicating that, at least, the toxin was able to improve CTL shielding from the water. However, the increase in the quantum yield of CTL compared to the situation of toxin absence, was much larger in the F samples. This difference was highlighted by the F/F_0 ratio. If water shielding was the only effect exerted by sticholysin, the F/F_0 ratio would have been constant and toxin-independent. Instead, a significant increase, quantified as $\Delta F/F_0$, was observed (Figure 17). This increment revealed that StnII not only shielded CTL from water, but it also protected it from 7-SLPC, that is, it changed the neighboring lipids of CTL. This was further clarified thanks to the samples in which the SM mol% was larger. In these, the effect of StnII was qualitatively equal but of much smaller amplitude. This was likely a consequence of most CTL being already protected from the quencher by preferentially partitioning in the SM-rich domains. Taken together, it could be said that StnII favored SM-Chol interactions since it appeared to drive CTL from SM-poor regions to SM-rich domains.

6.2.4. The fluorescent emission of the Trp residues of StnII

The intrinsic fluorescence emission of StnII-WT and Trp-to-Phe mutants (Figure 19) was recorded while titrating with LUVs using 260 nm excitation.[3] Fluorescence emission spectra showed that W110 and W114 were the two Trp residues whose environment was modified the most upon toxin binding to the membrane. These two residues appear to be highly similar in terms of solvent exposure and membrane penetration. This is consistent with their exposure in the soluble fold of the protein (Figure 18) and crucial role in membrane binding (see section 2.3.2), which implies the insertion of both in the hydrophobic region of the membrane.

Though not relevant regarding a potential interaction with Chol, an inspection of the emission spectra revealed some other details regarding Trp emission. First, W43 is the Trp residue with the highest quantum yield in the WT StnII. This could be expected from its location in the three-dimensional structure of StnII, buried and

[3] Tyr contributions could have been avoided by using 295 nm excitation instead of 260 nm. Regardless, they were very small in most cases (see main text). Excitation at 260 nm was used because it provided the highest Trp excitation while keeping direct CTL excitation at a minimum. It was selected so that the results were comparable with later experiments that included CTL as a FRET acceptor.

protected within the β-sandwich. For the triple and quadruple mutants, Tyr contribution is higher due to the absence of Trp residues that quench Tyr emission acting as acceptors (see refs. [198, 200] for further details). The emission of the triple and quadruple mutants in solution is, in spite of their one Trp difference, nearly the same. This can be clarified by their respective fluorescence spectrum in the presence of vesicles. The Trp emission of the quadruple mutant is increased more than that of the triple mutant (Figure 19). Apparently, when present, W115 acts as very low quantum yield acceptor for W146. This—which might seem surprising at first given that W146 is relatively exposed to the solvent, while W115 is completely buried inside the β-barrel—is explained by the presence of three Met sidechains in close contact with W115. The sidechain of Met is known to be an efficient Trp quencher [200, 228]. Finally, the increased quantum yield of W146, which is not expected to go into the membrane, is consistent with it playing an important role in oligomerization. Instead, it would be shielded from the solvent by the neighboring pore subunit, as reported previously for FraC [35, 229].

6.2.5. CTL is located close to the Trp residues 110 and 114 of StnII

FRET from the Trp residues to CTL was measured for StnII WT and the Trp mutants. The quantification of the sensitized emission of CTL was consistent with the results of the previous section. The substitution of W110 or W114, and especially both of them, resulted in a significant decrease in sensitized CTL emission (Figure 20a), indicating that W110 and W114 are the two residues closest to CTL in the membrane. Though W110 and W114 are the two Trp residues that are closest to CTL, the remaining Trp residues were close enough to CTL such that energy transfer occurred (Figure 20a).

6.2.6. Sterols are preferentially distributed close to StnII

In spite of StnII driving Chol and SM together, the observed toxin closeness to CTL could be a consequence of random motions in the membrane. To ascertain whether this was the case, the quadruple mutant, StnII W43/110/114/115F, was used. This protein has only W146, which was highly useful to avoid complications in subsequent calculations.

To predict the energy transfer efficiency between randomly distributed StnII and CTL, two situations were considered. In the less favorable one, the distance between the diffusion planes was considered to be 28 Å (based on the octameric crystal structure of FraC [35]), with CTL being unable to go closer than 10 Å to the projection of W146 in the membrane. In this case, CTL was considered to be excluded from that

area by the protein itself or other protein-bound lipids. In the other situation, the diffusion planes would be separated by 26 Å, and CTL would be able to go right beneath W146. In neither case the calculation took into account that membrane-bound sticholysins are forming pores. This is relevant because the predictions assume that all the area beneath the protein, and its surroundings, is available for acceptor diffusion. In this case, there is a large part of that area that is excluded for CTL since it is the lumen of the pore (Figure 34). Thus, in all considered situations, the predicted values were overestimations.

Even though the predictions overestimated the expected FRET efficiency, the experimental results were always higher than the predicted values (Figure 21). This shows that CTL is preferentially distributed close to StnII in membranes. In fact, given that previous studies revealed no difference between the enhancing capabilities of sterols on sticholysin activity [25], we can conclude that Chol is also preferentially distributed close to StnII.

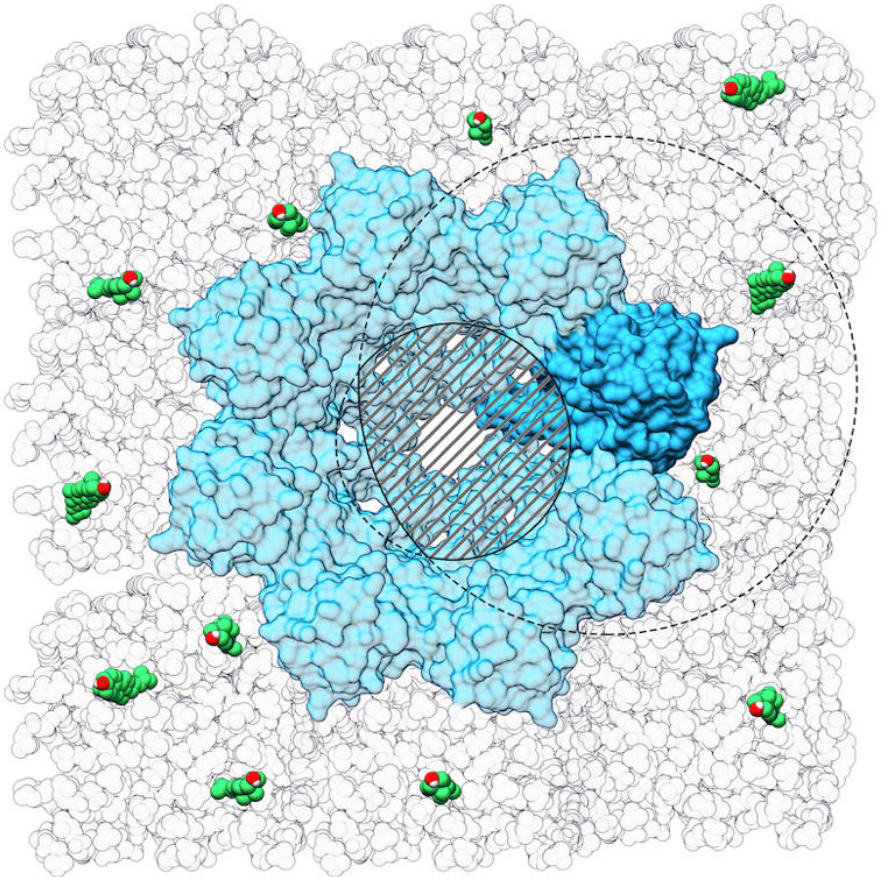

Figure 34. *Schematic illustration showing the expected situation of sticholysins in the membrane. A given monomer (darker one in the pore structure) can transfer energy to CTL molecules (highlighted lipids) within the larger dashed circle (not to scale). The model used assumed that the whole circle was accessible for CTL. However, since these proteins form pores, the lumen (smaller circle) is not accessible. Hence, the model overestimated the expected FRET for a random distribution by a factor that would be proportional to the overlapping area (striped area in the figure).*

6.3. Actinoporin pores are still open even if release traces show plateaus

Traditionally, two assays have been used to evaluate the activity of actinoporins: hemolysis and release of aqueous contents [18, 24-26, 60, 65, 84, 114, 123]. Hemolysis can be used, for example, to compare actinoporin mutants between them, since bilayer composition is equal in all cases [113, 114]. The experiment of release of aqueous contents, which can also be used to the same end, is especially useful when it comes to evaluating the effect of membrane composition on actinoporin activity since it is performed using model bilayers [23, 25, 123].

In the hemolysis experiments, the light scattering due to erythrocytes, and particularly the decrease due to the actinoporin-induced disruption of these cells, is the measured parameter. When using model vesicles, however, actinoporins do not induce vesicle breakage. In the experiments of release of aqueous contents, the measured parameter is the increase in fluorescence due to the dequenching caused by actinoporin-induced dye dilution (when released from the vesicles). This assay has been performed, traditionally, using calcein [18, 24-26, 60, 65, 84, 114, 123] or carboxyfluorescein [230-234]. However, the release traces always plateaued before reaching 100% release. This was surprising considering that, if actinoporin pores were permeable, the dye should keep leaking out of the vesicles until an equilibrium between the inside and outside concentrations of dye was reached. To delve into this issue, a series of probes was selected (Figure 35), first according to their charge and later to their size (Table 4).

6.3.1. The importance of charge

Actinoporin pores had been shown to be cation-selective using electrophysiological measurements [11, 17, 43, 64]. However, calcein and carboxyfluorescein, the probes used most often, are both negatively charged at the pH used in the experiments, as is the lumen of the pore. Based on this, the following working hypothesis was proposed: negatively charged probes would not be able to pass through the pore due to electric repulsion once the pore structure is stabilized. Instead, leakage would occur though membrane imperfections caused by the process of pore formation.

To test this hypothesis, R6G was used. R6G is a high quantum yield fluorescent probe that is positively charged at the pH used in these experiments. Due to its charge,

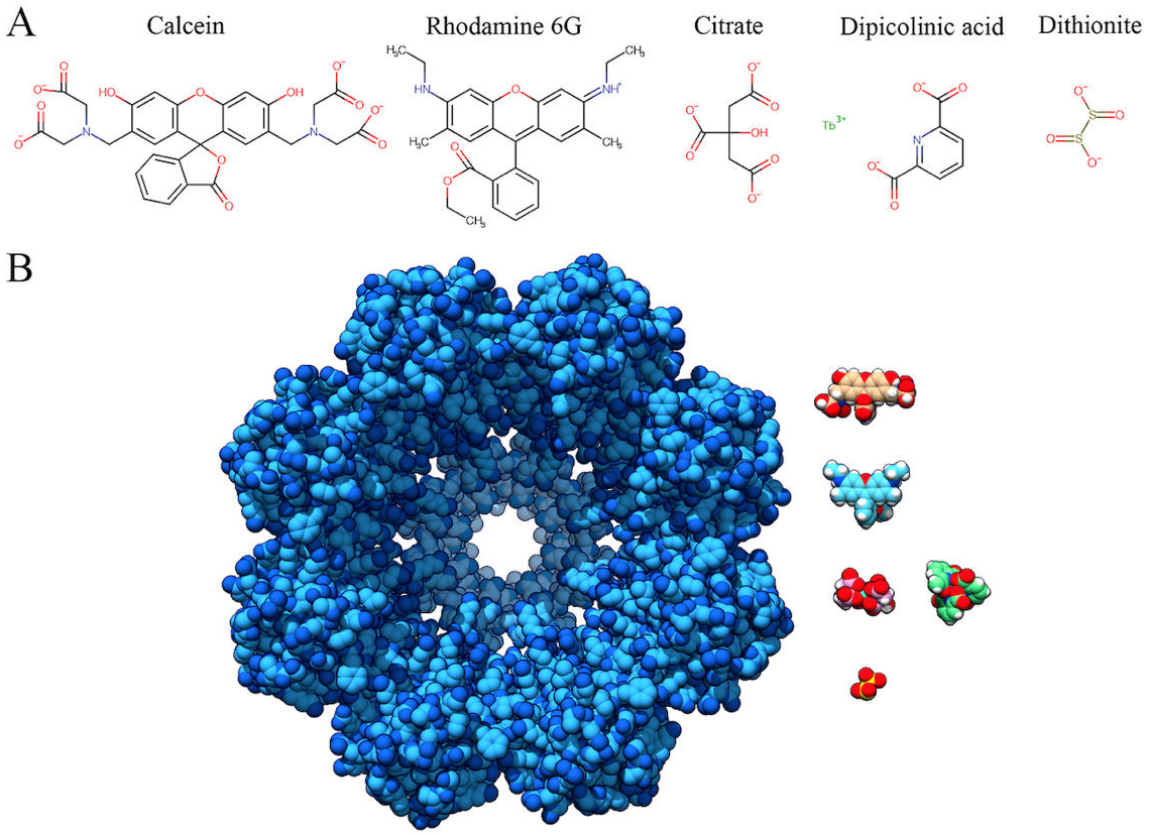

Figure 35. A: *Chemical structures of the probes used in this work to measure the rates and extent of release induced by actinoporins' pores. Citrate and DPA are shown because they are the chelating agents that keep* Tb^{3+} *in solution. Formulas were made using the Marvin 19.22 (2019) software by ChemAxon.* **B**: *Illustration showing the relative sizes of the complexes formed by the structures above, as compared to the StnII pore, based on that of FraC [35], using CPK representations.* Tb^{3+} *is depicted in a 1:2 complex with citrate (pink) and in a 1:3 complex with DPA (green). Adapted from publication III.*

Table 4. *Estimated radii of the probes used in this study.*

Probe	Calcein	R6G	Tb^{3+}	H^+	Dithionite
Estimated radius (nm)	0.74	0.59	0.12	0.10[a]	0.20[b]

[a] *[235]*

[b] *Estimated for dithionite. For comparison, the ionic radius of sulfate is 0.26 nm.*

it should be able to transit through the stable pores, being selectively allowed to pass. Hence, complete release was expected. The experiments showed that the rate of release was much faster than that measured for calcein (Figure 22b), indicating that probe charge is in fact relevant for actinoporin-induced membrane permeability. However, a plateau was still observed when using R6G (Figure 22a). Thus, as for calcein, StnII failed to induce complete release of R6G.

6.3.2. First attempts to show the relevance of size

In light of the results obtained with R6G, the working hypothesis was updated. Although charge had been shown to be important for the rate of release, it was possible that the probes employed were too large for actinoporin pores. In fact, the radius of these pores has been estimated to range between 1–2 nm [18, 29, 34, 35, 104, 236]. The hydrodynamic radii of calcein, carboxyfluorescein, and R6G is 0.74, 0.50, and 0.59 nm, respectively [237-239]. Hence, the probe diameters are very close to the estimated width of the pore's lumen, and that is without taking into account the potential size effect of the hydration layer surrounding both the probe and the pore walls. Thus, it appears that size, rather than charge, is what ultimately prevents complete leakage from taking place. In fact, the radii of Ca^{2+} and K^{+}, the two cations that are supposed to transit through the pores in natural circumstances [17, 43, 240], are about 0.10 and 0.14 nm, respectively—much smaller than those of the probes employed so far. Nevertheless, it should be pointed out that charge does help, as observed for R6G. We can speculate that this is due to R6G having a little longer time to transit through membrane imperfections since it would not be repelled by the StnII α-helices delimiting the zones of transient membrane disruption.

To test the influence of size, Tb^{3+} was the first probe selected. This fluorescent lanthanide, which is positively charged and has a diameter of ~0.12 nm, seemed like the perfect candidate. The results obtained, though valid, were poor in terms of rate and final release (Figure 22). The explanation may lie in the fact that Tb^{3+} is, by itself, insoluble. In order to remain in solution, it needs to be chelated (Figure 35b). When encapsulated, each Tb^{3+} atom was chelated with two citrate molecules. A citrate molecule displays three negatively charged groups at the experimental pH, thus rendering complexes that had a net charge of -3. Therefore, the situation would be essentially that of calcein since the complex would be larger than Tb^{3+} on its own, and negatively charged, both of which hinder the transit of the complex through the pore. Moreover, Ni^{2+} has been observed to inhibit EqtII action [66, 236]. This might have also played a role in the slow release observed for Tb^{3+}.

Given that Tb^{3+} did not result as expected, an experiment was designed in order to track proton release, the smallest possible cation. For this, fluorescein, a probe that displays a pH-dependent absorption maximum, was encapsulated at pH 4.2 coupled with 3,000 Da dextran. Dextran of that size is not released from LUVs upon sticholysin activity [18]. Thus, coupling of fluorescein with dextran prevented it from leaking out. This was essential in order to measure proton efflux to the outside of the vesicles, where the pH was kept at 7.2. Unfortunately, the fluorescent traces indicated that proton release was also slow and only noticeable at high protein concentrations within

the range used (Figure 22). This could be caused by StnII being less selective to cations at the pH found inside the vesicles [17], to which it would be suddenly exposed once it interacts with the membrane. In fact, the pK_a of the titratable groups was ~5.0 [17]. Hence, this assay would reflect pH influence on pore selectivity rather than proton permeability. It should be mentioned that cation flux through actinoporin pores has been shown to be favored asymmetrically [11] and that experiments using model vesicles such as those described so far would measure passage in the less favorable direction.

6.3.3. Results indicate release by transient membrane perturbations

Given the observed results, all assays so far could be said to be measuring leakage induced through transient membrane perturbation. The time-dependent traces of all experiments were used to fit the membrane perturbation model by Andersson *et al.* [205] (see section 4.2.3.3). In all cases, the model succeeded in describing the data (Figure 23), supporting that, in fact, the probe release observed in these assays occurs due to StnII-induced membrane perturbations, as hypothesized. Many proteins and peptides have been observed to use this mechanism to induce cell damage [241, 242]. It can be speculated that membrane perturbation during membrane penetration can also be useful for actinoporins.

6.3.4. StnII pores can be impermeable to calcein and still be open

Tb^{3+} and proton assays did not result as expected. As with calcein and R6G, the release traces reached plateaus, indicating that complete release was not possible with those probes. Thus, a new procedure was set up to clarify whether StnII-induced leakage was solely caused by transient permeation, or whether it could also occur through thermodynamically stable, open pores. This new approach consisted of measuring quenching of membrane-bound POPE-NBD using sodium dithionite, as described by Wimley [203].

LUVs were made including 1 mol% POPE-NBD, randomly distributed between both leaflets. The addition of dithionite to the vesicles resulted in the quenching of ~40% of the available NBD (Figure 24a). However, when the vesicles were preincubated with StnII, the addition of NBD resulted in a much larger decrease in NBD's emission (Figure 24b), indicating that the NBD on both leaflets was available for dithionite. The reverse experiment, in which StnII was added after dithionite had quenched all NBD available in the outer leaflet, was used as a control and showed that dithionite was still able to go into the LUVs, quenching the remaining NBD emission.

Therefore, these results allow the conclusion that StnII pores and, presumably, those formed by any actinoporin are indeed open after they stabilize. These proteins have been shown to also be able to induce membrane permeability during their process of pore formation. In fact, it was this effect, rather than pore-induced conductivity, that had been observed by calcein release assays. The calcein release results from papers I and II, which have been interpreted in terms of sticholysin activity, are actually consistent with this conclusion. According to this interpretation, calcein release is proportional to the number of pore formation events, and, undoubtedly, the toxin would be more active on those membranes upon which it is more prone to form pores.

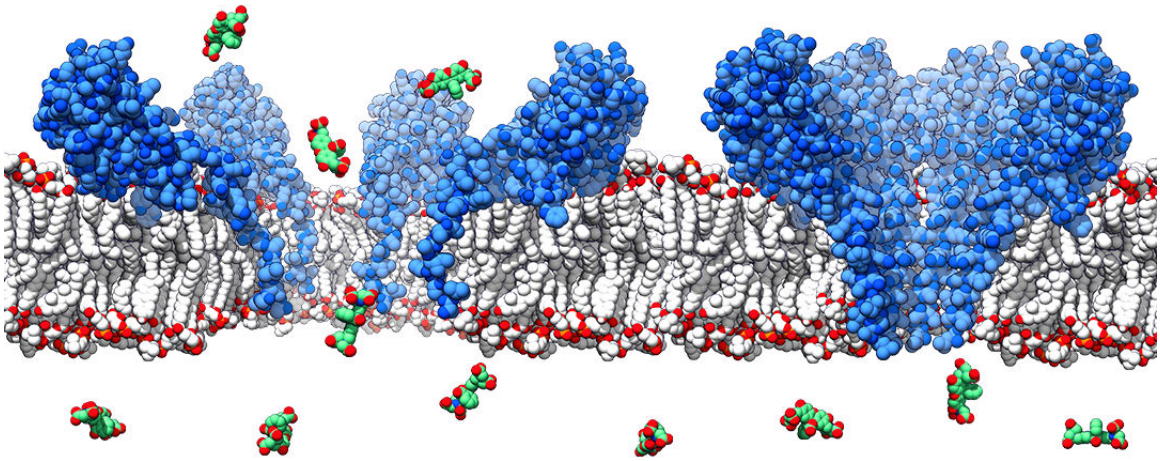

Figure 36. *Cartoon illustrating the conclusion regarding the calcein release assay. While a pore acquires its final conformation (right), membrane disruption would be large enough to allow calcein molecules to pass through. However, once the structure stabilizes (left), it would not permit passage anymore. Adapted from publication III.*

6.4. Oligomerization and stoichiometry of sticholysins

Many aspects of the behavior of actinoporins, such as SM-selectivity, the role of Trp residues, Chol's enhancing effect on the activity, and the importance of the N-terminal segment of these toxins during the process of pore formation have been resolved [18, 23, 44, 65, 72, 102, 104-107, 150, 198]. However, the oligomerization process and the final stoichiometry of the pores, two of the most relevant aspects of the behavior of any pore-forming toxin, have remained elusive for years. Important advances have been made using other actinoporins, such as FraC, which revealed that dimerization might be a step required for membrane binding while also showing that FraC forms octameric pores [35]. However, in order to do so, detergents had to be used to isolate and purify the mentioned intermediates. In our case, using a FRET-based approach,

we have shed some light onto the problem with a system that causes the least perturbation possible on the proteins.

6.4.1. Sticholysin size and mobility

The labelling of the single Cys-mutant with ATTO-488 allowed measurement of the anisotropy decay of StnI in both the presence and absence of membranes. In all cases, the decays could be fitted using just two components, accounting for the segmental motions of the label and the overall rotational motions of the protein itself (Table 3). The anisotropy did not decay to zero in either case, only when the decay of the probe free in solution was measured (Figure 25 and Table 3).

The slow correlation time enabled us to calculate the molecular diameter of these proteins. The result, 29.0 ± 1.2 Å, agrees with the molecular structures obtained using X-ray diffraction and nuclear magnetic resonance [29, 30]. Based on this alone, it could be said that the monomer is the fundamental organization unit for sticholysins when in solution. However, the fact that the limiting anisotropy did not decay completely even when the correlation time was shorter than the lifetime of the excited state of the probe (4.1 ns) could indicate the presence of yet slower correlation times, not resolvable, which would account for higher-order oligomers in solution. The existence of such complexes, which, apparently, would not be very abundant, is consistent with previous reports indicating that sticholysins can oligomerize in solution [184].

The addition of LUVs to these solutions resulted in a significant increase in the slow correlation time and the limiting anisotropy for StnI (Table 3), revealing the reduced mobility of the proteins as a consequence of membrane binding and oligomerization. The segmental motions of the label, whose situation had not changed significantly, remain the same (Table 3).

6.4.2. StnI oligomerizes in solution alone and with StnII

Time-resolved anisotropy results suggested that oligomers were present when StnI was in solution in the absence of membranes. This behavior had been described before for StnII using analytical ultracentrifugation [184]. To delve into this, StnI T43C was also labeled with ATTO-542, which would act as an acceptor of ATTO-488 (donor). The titration of donor-labeled StnI with the acceptor-labeled toxin revealed that energy transfer was taking place (Figure 27), indicating the presence of StnI oligomers in solution, as had been observed for StnII.

StnII has been observed to increase the activity of StnI, presumably by promoting the binding step of the pore-formation process [95]. Consequently, it could be

expected that StnII oligomerized with StnI while in solution. Indeed, the increase in the FRET signal when the previous experiment was repeated in the presence of StnII confirmed that not only the number, but also the size of the oligomers were increased (Figure 27). This conclusion can be achieved simply due to the increased signal and because, given that StnII was not labeled, it had to couple labeled StnI subunits in order to promote energy transfer, thus inducing the formation of, at least, trimeric ensembles.

6.4.3. Stoichiometry of sticholysin pores in DOPC:eSM:Chol membranes

The FRET approach was taken one step further in order to resolve the stoichiometry of StnI pores directly on model membranes. Again, the same StnI mutant, T43C, was used with the same labels previously specified, acting as FRET donor and acceptor.

The experimental values of energy transfer efficiency obtained using StnI with its labeled mutant were compared to those predicted taking into account the size of the proteins, the position of the label within the structure of the proteins, and the photophysical properties of the probes. The RMSD values exclude stoichiometries of five or fewer subunits (Figure 28). In fact, the results agree best with the signal expected for an octameric ensemble. However, the resolution of the predictions (Figure 37) does not allow for ruling out stoichiometries consisting of seven or more

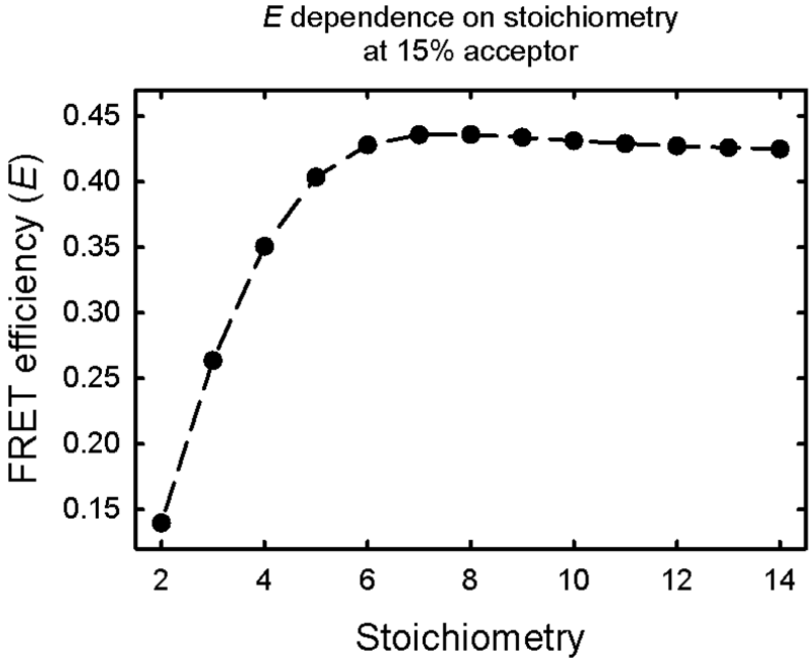

Figure 37. *Theoretical variation of the FRET efficiency at a fixed acceptor content in the sample o 15% as a function of the stoichiometry of the complexes, according to the physical restrictions imposed by the size of sticholysins, the position of the label in their structure, and the photophysical characteristics of the labels used. The differences in the predictions are further reduced as the acceptor content in the sample is increased. Modified from publication IV.*

subunits. It must be mentioned that the results are also compatible with the presence of several different stoichiometries simultaneously, which would yield the same final signal as if they were all octamers.

When the experiment was repeated in the presence of StnII (12.3%), the results were essentially the same. In fact, the distribution of the RMSD values was also maintained albeit with the differences between heptamers and higher-order oligomers somewhat reduced (Figure 30). It could be argued that the same stoichiometry is observed because StnI and StnII do not form heteropores. However, despite present (Figure 30) and previous evidence indicating otherwise [95], if this were the case, the observed signal should be higher than observed, since, in practice, the degree of the labeling of the StnI pores would be higher than assumed if StnII was collaborating in the formation of heteropores.

It is interesting to remember that oligomerization was observed to be promoted by the presence of StnII. Two of the 12 residues that differ between StnI and StnII are precisely located at the presumed protein-protein interfaces or very close to them. These two residues are Tyr148 and Gln149 in StnI and His147 and Glu148 in StnII. The properties of the residue are overall conserved: a hydrogen-bonding-capable aromatic residue (Tyr/His) followed by another relatively long-chained amino acid that is also capable of hydrogen bonding (Gln/Glu). Based on these properties, we can predict the properties of the complementary residues as being also capable of hydrogen-bonding, one of them probably cationic, in order to establish a potential cation-π interaction with the aromatic rings of Tyr/His. An inspection of the three-dimensional structures of StnI and StnII reveals that there are, in fact, two residues appropriately placed and oriented in both their structures. These are Arg126 and Lys124 in StnI and Arg125 and Lys123 in StnII (Figure 38). The difference in activity between StnI and StnII has been attributed, mostly, to the different attachment strength of the N-terminal α-helix to the β-sandwich [114]. Nevertheless, this does not rule out the possible contributions that could come from stronger monomer-monomer interactions mediated by the aforementioned residues. It is possible that a salt-bridge is established between the Glu148 of StnII and the corresponding Lys residue of StnI or StnII (Lys123/124, respectively). This comparatively stronger interaction could shift the equilibrium toward the multimeric ensembles, which could in turn facilitate membrane binding and later oligomerization.

It is also worth noting that these results are all compatible with the pore structure obtained for FraC using X-ray. Altogether, these observations support that the stoichiometry of the pores of actinoporins is always the same regardless of the specific proteins that form the pores, indicating that it would mainly depend on protein shape.

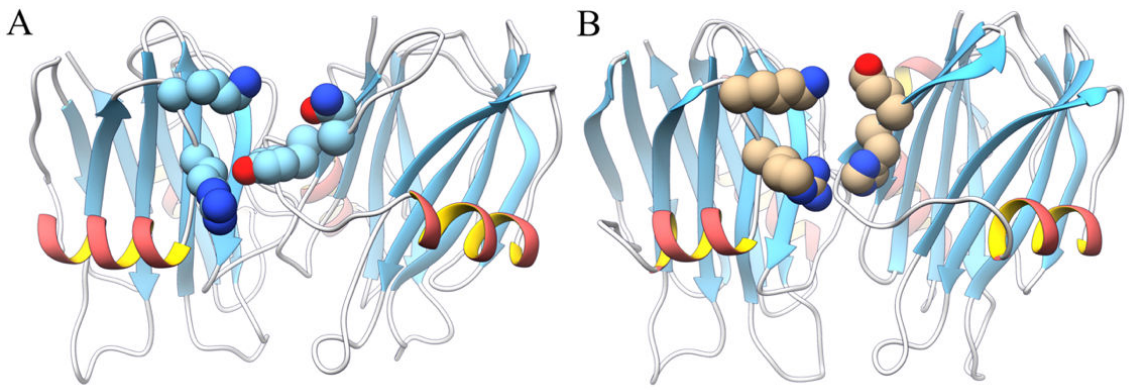

Figure 38. *Homodimers of StnI (***A***) and StnII (***B***). Side chains shown are those of the same amino acids in both cases for the monomer on the left, Lys124 and Arg126 of StnI (Lys123 and Arg125 of StnII). For the monomer on the right, the amino acids differ. For StnI, they are Tyr148 and Gln149, whereas for StnII, they are His147 and Glu148. The orientation of the residues is not necessarily that found upon oligomerization since the structures used to create the illustration were obtained in solution (A) and by crystallization (B). The Arg could interact with either of the aromatic residues either by hydrogen bonding or by a cation-π interaction. The latter kind of interaction can, in fact, be observed in the dimer structure published for FraC (PDB ID: 4TSL [35]) between its equivalent amino acids. Lys residues probably form a hydrogen bond with Gln149 and a salt bridge with Glu148. Adapted from publication IV.*

6.4.4. Results in the absence of Chol suggest binding by oligomers

The results yielded by the experiments using membranes that lack Chol can seem surprising at first. The predictions are not followed in any case (Figure 29 andFigure **31**). Furthermore, a feasible possibility—that the pores clustered on the membrane—is also discarded since the *E* values observed are not higher than the predictions, as could be expected if clustering had occurred. However, the fact that the first few points are closer to the theory and then stop rising accordingly can suggest that the binding unit for membranes with no Chol would be sticholysin dimers. At low acceptor content in the sample, the expected *E* would be less dependent on acceptors at the *i* + 1 subunit (from a donor placed at *i*). However, as the acceptor fraction grows, the relevance of the probability of finding acceptors increases simultaneously, at positions *i* + 1 and *i* - 1. Since, for these experiments, donor- and acceptor-labeled proteins are mixed right before the measurements are performed, and in the total final volume, a complete shuffling of the variants in the oligomers might not occur quickly enough. Thus, the oligomers in the sample would rarely have donor-acceptor pairs, yielding the observed effect. This observation is compatible with previous reports pointing to dimers being required for membrane binding in membranes with no Chol [35, 187]. It is possible that Chol's effect on SM's head group [168] orientation aids in SM recognition, allowing the dominant form in solution, monomers, to directly bind those membranes, which would in turn enable a proper shuffling of the subunits, according to the model used.

6.4.5. Further evidence for stable pores

Previously, we have presented evidence showing that sticholysins pores remain open once they are formed (see sections corresponding to paper III). However, these experiments were performed on vesicles with large pore populations. Because of this, these results did not rule out the "remodeling hypothesis" proposed for the noisiness of the electrophysiology measurements, in which the opening of individual pores can be observed [43, 219].

Our present FRET results discard the possibility that the aforementioned noisiness is a consequence of pore remodeling. The timescale of those events was of mere seconds, whereas ours was of the order of two to five minutes—enough, in principle, for the system to reach a new equilibrium, incorporating subunits added later to the sample. In such conditions, no FRET was observed after the addition of acceptor-labelled toxins to previously formed donor-containing complexes (Figure 32), supporting the idea that the pores are not remodeled and that, consequently, they maintain the same subunits once they stabilize.

In light of these results, the comparatively higher noisiness of the actinoporin pores relative to those formed by β-pore forming toxins can be attributed to the thermal-induced motions of the elements of the complex, which would be more significant in these pores due to the looser attachment of the trans-membrane segments, which are, for that reason, more susceptible to nearby lipid motions.

7. OPEN QUESTIONS, PERSPECTIVES, AND OTHER THOUGHTS

The results presented in this thesis provide answers to many questions in the research field. However, at the same time, these same results also show some details and nuances that allow for further discussion and, in the future, could be the starting points of new studies.

7.1.1. Anisotropy change with increasing bilayer thickness

It has been shown that in membranes composed of a single PC species, the thickness of the bilayer varies linearly with acyl chain length for both di-unsaturated and di-monosaturated lipids [220]. Similarly, one could expect a concomitant increase in the hydrophobic contacts between the acyl chains, increasing the overall acyl chain order. The results presented in paper I, using di-monounsaturated PC species, always in presence of 14:0-SM, show precisely that both in the absence and presence of Chol, membrane order is increased with acyl chain length, at least according to the steady-state anisotropy of DPH (Figure 11). However, it is interesting to observe that, at a temperature of 25 °C (Figure 39), when Chol is absent, anisotropy increases almost perfectly linearly with acyl chain length, with only one value falling outside the trend. That value corresponds to the bilayer composed of di-16:1-PC:14:0-SM (4:1 molar ratio). If all systems vary in the same manner relative to one another with just this exception, then this system could be expected to present a unique feature, causing the observed difference.

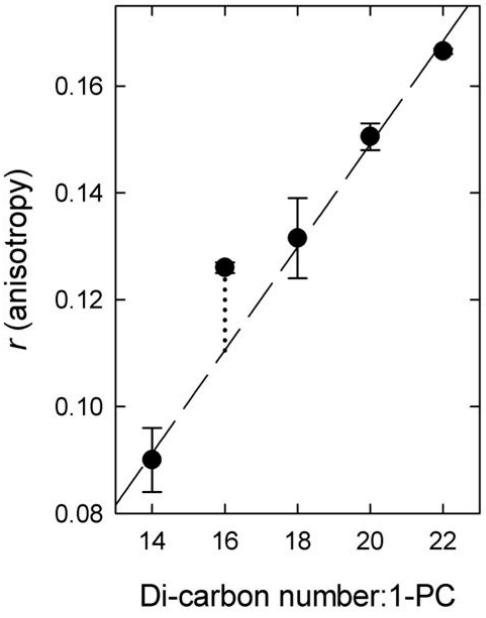

Figure 39. *Steady-state DPH anisotropy in di-X:1-PC:MSM (4:1 molar ratio) bilayers measured at 25 °C. The dashed line is obtained by linear regression ignoring the data from di-16:1-PC membranes (R^2 = 0.997). The dotted line highlights the deviation of the value mentioned in the main text.*

There are two components in all these systems if Chol-containing compositions are left aside (in these, Chol plays a major role and complicates this analysis). On one hand, 14:0-SM has a 14:0 acyl chain. On the other, all di-monounsaturated PCs used have one double bond in both of their acyl chains. The presence of this double bond makes the effective length of those acyl chains (assuming

an all *trans-gauche* isomerization) to be closer to that of an equivalent saturated chain with two fewer carbon atoms. The membranes composed of di-16:1-PC:14:0-SM are the only systems assayed in those experiments in which the hydrophobic mismatch between the PC species and 14:0-SM can be considered, at least theoretically, to be nearly inexistent. It is precisely this composition that displays a higher-than-expected anisotropy. In all the others, either the PC is shorter (di-14:1-PC) or it is larger (acyl chains of 18 to 22 carbons) than the acyl chain of the 14:0-SM, but the mixture always results in systems with a hydrophobic mismatch. The mismatch also varies between systems, but the different degree of mismatch (except when it appears to be zero) does not seem to have any significant effect on the anisotropy displayed by DPH when embedded in these lipid systems. Since DPH anisotropy reports lipid mobility at the membrane core, it is reasonable to think that it can move more freely in those systems that are more poorly packed (i.e., more prone to leave voids) than in similar systems with no or just smaller hydrophobic mismatches.

7.1.2. Does acyl chain order affect membrane binding?

It has been shown that the phase state of the membrane is an essential feature of the membrane if one is to predict binding and pore formation by actinoporins [18, 24, 25, 44, 65, 72, 150, 153, 154]. However, this section is referred to the possibility of smaller differences originating from differences in the acyl chain order of the lipid species of those membranes, assuming that they are all in the same phase state and are suitable targets for actinoporins and, particularly, sticholysins. To that end, the results from SPR measurements will be further discussed.

From a certain point of view, SPR-based methods that measure molecular adsorption (referred to in this work simply as SPR) could be said to work as extremely sensitive balances. In most cases, the k_{on} and k_{off} constants of the interaction of interest can be determined from the signal change over time. These values can then be used to calculate the K_a of the interaction. Moreover, the signal, which corresponds to the changes in the refractive index of the surface of the chip as a consequence of the binding of molecules, can also be readily converted to units of mass/surface (such as ng/cm^2). This value can be then used, if the M_w values of the interacting molecules are known, to estimate the "apparent" stoichiometry of the association. In our case, the L/P molar ratio was calculated. A smaller L/P value indicated more bound protein subunits as the chip-bound amount of lipid was the same in all cases. This last statement was checked using the average molecular weights of each of the lipid compositions used and comparing the expected and observed mass ratios, which were in good agreement in all cases (see section 5.1.3 and Table S1 in paper I).

When the L/P molar ratio was measured using SPR, the overall trend showed that protein binding increased with bilayers having shorter acyl chain lipids. This held true for both Chol-containing and -lacking systems. This trend was almost linear in the Chol-lacking systems. As happened with the anisotropy measurements discussed in the previous section, one of the values stood above what would be expected—the one corresponding to membranes containing di-16:1-PC (Figure 13, panels A and C). Incidentally, this system was also the one that showed higher-than-expected steady-state DPH anisotropy (Figure 39). This suggests that, in addition to bilayer thickness itself, the overall order of the membrane could play a role in membrane binding. To explore this idea, one could plot the values obtained for the L/P ratio as function of the steady-state anisotropy of the corresponding bilayer. If this is done, a linear dependence is obtained for the situations in which Chol-lacking membranes were employed (Figure 40, top panels). If the same is done for the Chol-containing bilayers, the trend is no longer linear (Figure 40, lower panels). Nevertheless, in both cases, these plots are intriguing. In the case where one kept a constant lipid content in the sample, a decreasing L/P molar ratio would indicate an increasing number of membrane-bound protein units. Hence, maximum possible binding would occur as the L/P molar ratio tends to zero. Strictly speaking, and following the above statement, this would mean that an infinite number of proteins has bound each lipid. This has no physical sense, but this hypothetical situation can be related to the effect of membrane-anisotropy on protein binding,

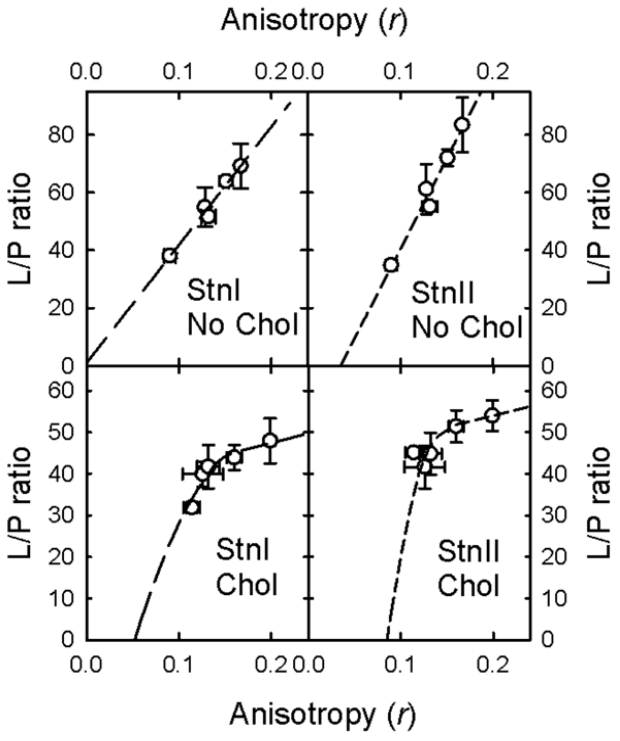

Figure 40. *Plots of the L/P molar ratios obtained from SPR as function of the DPH steady-state anisotropy measured for the same lipid systems. The fits on the top two panels have a R^2 of 0.974 and 0.970 for StnI and StnII, respectively. The lines in the lower panel are only guides to the eye drawn based on the overall trend of the points and not result from fitting.*

Extrapolation from the fits shown in Figure 40 indicates that an L/P molar ratio equal to zero would be reached at $r \approx 0.0$ and $r \approx 0.05$ for StnI and StnII, respectively. Therefore, it could be speculated that in order to achieve maximum possible binding, StnII would be able to overcome the opposing effect of a more ordered membrane. If we consider that the completeness of the pore formation

process (which will be discussed in further detail later) drives membrane binding, it could be said, roughly speaking, that as pores are formed, they leave space for more monomers to bind. This would be expected from the mass action law when applied to a multi-step process. In such case, this ability could be related to the ease by which the N-terminal α-helix is able to penetrate the membrane or, in other words, how easy it is for the membrane to accommodate the helix in its own structure. According to the considerations above, the characteristics of the helix of StnI would be less favorable to that end, at least regarding the initial process of membrane penetration. This could be in fact expected from it having a more polar character than that of StnII (see sequences in Figure 2 and refs. [111, 114]). A similar observation can be made regarding the Chol-containing systems. The presence of Chol, however, would help both proteins in overcoming the energy barrier consequence of lipid order and packing. Possibly, the mechanism could be related to an increased rate of transient void appearance in the membrane, through which the insertion of the helices could be taking place.

Verifying this hypothesis would require a new set of experiments using membrane systems that differed the least possible between one another other than on the acyl chain order of their lipids. If an SPR system capable of maintaining different temperatures was available, the same study could also be performed using a single lipid system at the different temperatures at which its anisotropy had been measured.

7.1.3. How is leakage produced? Comparing calcein and rhodamine 6G

In the sections corresponding to paper III, it has been shown that actinoporins cause the release of LUV-encapsulated probes as a consequence of the process of pore formation rather than through the actual thermodynamically stable pore. Essentially, this would be caused by the insertion of their N-terminal α-helix, since, based on the structure of these proteins, the parts responsible for SM recognition and membrane binding would not reach far enough into the membrane so as to affect both leaflets.

In that same publication, it has also been shown that, at smaller P/L molar ratios, larger leakage is observed when using R6G as the probe instead of calcein. Overall, it might be concluded that R6G experiments are more sensitive. This appears to be obvious when small L/P ratios are used. However, this does not mean that calcein is useless. It just offers a smaller dynamic range than R6G.

Now let us just consider the results from R6G and calcein since H^+ and Tb^{3+} assays were already argued to be not fully comparable due to their potential interactions with the toxins (see section 6.3.2). Since the experiments in paper III were performed with the same protein and always using the same lipid composition, it can be assumed that the membrane perturbations reported for calcein or R6G are the same in all cases.

Considering the results at an P/L molar ratio < 0.0005 from Figure 22a, it can be readily seen that less calcein than R6G is released. This would mean that the number of calcein molecules released per membrane perturbation is smaller, which is also perfectly consistent with the results presented in Figure 22b. In such situations, the release would be controlled by the time for passage that is permitted for each probe, which depends on its molecular characteristics of charge and size as well as the lifetime of the protein-induced membrane perturbations. Dependence on size would be twofold: smaller size entails a larger diffusion coefficient and also a longer time-window during which to pass through (until the membrane "breach" is closed). This last factor would also be affected by charge since short-range electrostatic repulsions would also reduce passage time. Based on this, the molecules that can exit the vesicle when low P/L ratios are used would be those that are within a "diffusible distance" when the membrane breached, being that distance determined by the diffusion coefficient of the probe and its passage time.

When the P/L ratio is larger, however, total release is plateaued. At that point, release is not increased even when the P/L molar ratio is. This could be a consequence of several things. Past ITC experiments have shown that saturation is reached at L/P molar ratios ≥ ~80 (= ~0.0125 P/L molar ratio). In the present leakage experiments, saturation is reached at only a P/L molar ratio of ~0.0005. Therefore, this effect cannot be accounted to no more proteins being incorporated into the membrane after that P/L molar ratio. Another explanation is necessary. One could start from the following. It has been shown that release ceases when pores are formed. This suggests that the faster the pores are formed, the shorter-lived the membrane perturbations are. In other words, the lifetime of the disturbances is inversely proportional to the surface density of toxin monomers, which in turn is proportional to the L/P ratio. Thus, when the amount of toxin used is high enough, only the probe molecules that are in the immediate vicinity of a membrane discontinuity would have time to diffuse through it and leave the vesicle. The consequence of this would be that the effects of probe size and charge are minimized, as is in fact observed experimentally when different probes are compared.

7.1.4. What is sensed by ITC in the case of actinoporins?

ITC quantifies the heat change in the sample as a consequence of sample injection, including that of any reaction or interaction occurring within. Ideally, the sole cause of the temperature change would be the reaction or interaction of interest.[4] Therefore,

[4] This is hardly ever the case. Nevertheless, trivial heat contributions, such as sample dilution, can be accounted for by measuring them separately and subtracting them during data analysis.

regarding actinoporins, it would measure the heat changes due to membrane association, and the subsequent conformational changes. This comprises many different interactions and stages,[5] namely, membrane adsorption and attachment to SM, monomer-monomer interactions, membrane disruption and the rearrangement of lipids, the conformational change of the proteins to form pores, and the associated changes in solvent distribution caused by the variation in the exposed surfaces.

Often, for the sake of explanatory simplicity, the process of pore formation is divided in just two "major" steps: membrane binding, and pore formation. In this sense, it has been said that ITC reflects only the first part of the process, namely, binding, and not the subsequent steps, implicitly assuming that the latter has no effect whatsoever on the thermodynamic constants of the process. This idea might have arisen as follows. In Alegre-Cebollada *et al,* (2008) [107], both StnII-WT and StnII-A10P were characterized using ITC (with DOPC:SM:Chol 1:1:1 vesicles) and hemolysis assays. The ITC isotherms and the thermodynamic parameters of these two proteins were nearly identical, but the hemolytic activity of the mutant was reported to be 0.26 of that of StnII-WT. Since the ITC results were the same, but StnII-A10P was not nearly as hemolytic, and thus presumably not forming pores, ITC was said to report *only* membrane binding.

The ITC characterization of StnII-WT and StnII-A10P was then repeated in García-Linares *et al.* (2015), incorporating the use of POPC:PSM 4:1 vesicles [113]. This time, hemolysis assays were replaced by calcein release experiments. Again, the thermodynamic parameters reported for both proteins were extremely similar, only differing a bit more in the case of Chol-lacking vesicles. This was the calcein release as well. In Chol-containing membranes, StnII-A10P produced essentially *the same* release curves as StnII-WT. While its induced release was reduced in Chol-lacking vesicles, it was still about half of that of the WT protein. Therefore, and according to the calcein release results presented there, StnII-A10P was capable of disrupting those model membranes.

In spite of the calcein release results, it could be argued that StnII-A10P did not form pores, as suggested by the hemolysis assays. This could be the case if the monomers did not fully assemble into a complex and just inserted their helix into the membrane. As mentioned in section 7.1.3, it is extremely unlikely that only SM-recognition and binding could trigger leakage, since the proteins loops responsible for such barely penetrate the outer leaflet of the bilayer. However, in either case, one

[5] The process is artificially divided into stages for clarity. This does not mean that those stages are actually distinguishable from one another in the actual molecular process or that they even occur as such.

would expect the ITC results to differ. Since that did not occur, the most probable scenario would be that StnII-A10P did behave, overall, nearly exactly the same as StnII-WT. The mutation would have had the following two effects: first, hindering membrane penetration in absence of Chol and, second, and most importantly, altering the conformation of the N-terminal α-helices in the final pore assembly. This could narrow the lumen of the pore, hindering cation flow-through. As a consequence, the osmotic shock exerted on the erythrocytes in the hemolysis assays would be greatly reduced. As calcein release experiments reveal, this mutant would still be capable of inducing membrane disruption via the insertion of the α-helix. Nevertheless, the results from paper III suggest that these events are short-lived. Hence, in the case of red blood cells, these may not be enough to cause hemolysis, especially given that the volume of the erythrocytes used for hemolysis is about ~7000 times that of the vesicles typically used for calcein release experiments.[6] Following the discussion in section 7.1.3, only the volume immediately beneath the membrane would be affected by the insertion of the α-helices. Changes in concentration on that fraction of the erythrocyte's content would not be enough to cause them to burst. For this, fully functional pores, which allow for a continuous flow of cations, would be required, such as those of the WT isoform.

Hence, it could be said that ITC does capture contributions from all steps of the process, including pore formation and the associated reorganization of lipids in the membrane. Elucidating what the specific contributions of each sub-process are, given that they could somehow be isolated experimentally, would require the use of a variety of mutants. Such studies might be challenging since they might require high sample concentrations to obtain a detectable signal. However, valuable data would be obtained, increasing the understanding of the process of pore formation. The mutants that come to mind in order to perform such a study would be the following: one whose capability to penetrate the bilayer is, with no doubt, impeded, such as the EqtII-V8C/K69C double mutant [27, 102]; one that does not oligomerize, similar to StnII-G142A, which lost its ability to produce competent oligomerization [179]; and finally one that combines the features of both and could only, in principle, bind to SM. Again, these experiments might be challenging since, given that the process would halt unfinished (the whole point is to hinder pore formation in various ways), monomers would be less prone to bind the bilayer, as expected from the predictions derived from the mass action law.

[6] Sheep erythrocytes have a volume of about 30 fL [243]. Assuming ideal sphericity, vesicles with a diameter of 200 nm would have a volume of ~4.2 aL.

7.1.5. Apparent SPR-ITC disagreement

Based on the above discussion, especially regarding SPR, it could seem that the SPR and ITC results in publication I disagree. SPR reports more binding for thinner membranes by both sticholysins (Figure 13), while ITC shows that the membranes with intermediate thickness are preferred (Figure 14), an observation that is also supported by calcein release experiments (Figure 12). It should be noted, however, that the conditions under which the interaction between sticholysins and LUVs is carried out differ between both methodologies. Not only that, the measured signal arises from different aspects of the interaction. In any case, more binding does not necessarily mean a more productive or affine binding.

In an SPR experiment a constant population of vesicles remains on the chip while a continuous flow of protein maintains the feed of free toxin. Thus, the system is not allowed to equilibrate. Regarding the detection method, SPR senses the presence of protein mass directly. It does not perceive any signal that could originate from protein functionality. As mentioned previously, due to the high affinity binding of actinoporins, a value for the k_{off} could not be retrieved. Hence, in our case, the stoichiometry was measured in place of the affinity constant (which would be calculated from k_{on} and k_{off}). The stoichiometry obtained in this way, that is, by supplying a constant feed of free toxin to system saturation, is related to the maximum capacity of each of the lipid systems to accept toxins. This, in turn, would depend on the effects exerted by the protein on lipid distribution and the arrangement on each particular set of lipids.

On the contrary, the signal sensed by ITC is more complex than that of SPR, as explained in the previous section. Nevertheless, ITC does allow the measurement of the affinity constant directly. Moreover, it also differs from SPR in that, after each injection of the lipid suspension, the system is allowed to equilibrate. Although after each of the first few injections vesicles are in an environment similar to that of SPR, the value of the association constant is determined, essentially, from the heat values obtained when the toxin is no longer in excess and its binding depends most strongly on its affinity for the membrane.

At this point, one could argue, based on this section and the one immediately before, that the affinity constant measured with ITC is not correct. This would be the case only if the ΔH/molecule was not constant. This could be the case if, when the L/P ratio is high enough, not all proteins that bind the membrane and give a measurable signal are able to complete the pore formation process. However, the release results from paper III should be remembered at this point. They show that very small P/L molar ratios are capable of producing probe release, suggesting that at least, most of

the monomers that do bind the membrane are able to produce leakage. Therefore, the ΔH/molecule would be constant (approximately, at least) in each experiment.

7.1.6. Protein shape, α-helix, and stoichiometry

The stoichiometry of sticholysin pores has come up within this text in regard to both paper I, in which it was related to the length of the N-terminal α-helix, and paper IV, which was dedicated entirely to the study this characteristic of the pores of sticholysins. The results of the analyses presented in the two papers agree nicely, both suggesting a stoichiometry of seven or eight monomers per pore as the most likely.

The analysis in paper I was done in a way that might suggest that the length of the N-terminal α-helix, in combination with the thickness of the membrane, might be the determinant of the stoichiometry. This is, however, unlikely. It is more probable that the structure of the β-sandwich is, in fact, the factor that determines the number of monomers per pore. Why? Because its structure is far more complex than that of just the N-terminal α-helix, and it carries out a much more delicate task: the recognition of the head group of SM.

The spatial disposition of the residues required to recognize the SM head group moiety is, *a priori*, much more difficult to achieve than that of an amphipathic α-helix. In other words, once the overall actinoporin structure appeared, the β-sandwich would have been subject to a much stronger selective pressure than the N-terminal α-helix. This can be readily appreciated since it is precisely in the first 30-residue stretch where most differences between actinoporins appear (see Figure 2). While these changes can result in differences in the activity of the toxins [26], they certainly do not unpair it completely, as mutations in the POC-binding site have been shown to do, at least in the absence of Chol [113]. Not only that, but a common mechanism for the appearance of new toxins is the selection of proteins for new, initially similar, tasks, which might change with later specialization [244]. This can occur by random mutation events that, eventually, represent an adaptative advantage for the individuals that possess the mutation. Thus, it is not unlikely that the overall folding motif required for membrane recognition appeared first—associated to a different process but still related to membrane binding and recognition—in the ancestors. The α-helix probably would have been incorporated later as the ancient protein was selected for a toxic functionality. Its length would have been refined later by the evolutionary pressure exerted by the thickness of the membranes that it would act upon. This last part agrees nicely with what was shown in publication I, in which membranes containing di-18:1-PC were, overall, the ones preferred by both sticholysins. The acyl chains of similar lengths as that of the 18:1 acyl chain are precisely the ones most

abundant in many fish species, including the 18:1 acyl chain itself [245]. This study regarding the lipid contents of fish was performed on species from the Mediterranean Sea, where *A. equina*, the sea anemone that produces EqtII (most similar to sticholysins, especially StnI), occurs. These fish are potential prey of sea anemones, and their membranes thus target of actinoporins.

There is still another argument in favor of this point of view. Protein-protein interactions appear to occur, according to the available structures, mainly implying residues located at the β-sandwich, and much less at the α-helix. Therefore, varying stoichiometry would rely on the flexibility of those residues, so that their interactions, which would favor the formation of the complex, could be maintained. This argument also supports the occurrence of higher stoichiometries since the increment in angular displacement that a residue would have to undergo in order to maintain the same interactions is smaller as the number of monomers per pores is increased.

8. CONCLUSIONS

In this thesis, the following aspects of the molecular behavior of sticholysins have been studied: the influence of bilayer thickness on the activity of sticholysins, the relationship between Chol and the activity of these toxins, and the details of the sticholysin-induced permeability of lipid bilayers.

In **paper I**, we determined that sticholysins are more efficient when facing bilayers whose thickness corresponds to that of membranes composed of di-18:1-PC. Our observations and predictions were consistent with the previously measured values of helix tilting and oligomerization numbers. Furthermore, the lipid composition of Mediterranean fish, where *A. equina* (the producer of EqtII) is prevalent, shows a predominance of fatty acids with 16 and 18 carbon atoms [245]. Thus, it appears that the length of the N-terminal α-helix of actinoporins is a result of evolutionary pressure related to the bilayer thickness of the membranes of its preys.

In **paper II**, we determined that the hydroxyl group of Chol was not enough to explain its enhancing effect on the activity of sticholysins, as shown by its comparison with OCer. In fact, Chol induced less acyl chain contacts between SM molecules, as revealed by the experiments with pyr-SM. We showed that StnII was able to change the environment surrounding sterols, using CTL. This fluorescent sterol enabled us as well to show that sterols preferentially partition close to StnII when the toxin is bound to the membrane, particularly next to Trp residues 110 and 114.

In **paper III**, we concluded that the key factor that determines passage through the pores of actinoporins was size. However, we also observed that charge was still important, as revealed by the rates of release of R6G. We determined that the mechanism by which actinoporins cause dye release is, for most assays, mediated by membrane disruption and that passage through the thermodynamically stable pores does not take place for regular, calcein-sized probes.

In **paper IV**, we studied the oligomerization and the stoichiometry of the pores formed by StnI, both on its own and with StnII, and using membranes containing and lacking Chol. We have presented evidence showing that the stoichiometry of the pores is maintained in Chol-containing membranes regardless of the protein composition of the oligomer. Our results also show that StnII promotes the formation of oligomers in solution, an effect that likely aids the recognition and binding of StnI to membranes in which Chol is absent.

9. REFERENCES

1. Eme, L., Spang, A., Lombard, J., Stairs, C.W., Ettema, T.J. (2017). **Archaea and the origin of eukaryotes**. *Nature Reviews Microbiology*, 15 (12), 711.
2. Lesieur, C., Vecseysemjen, B., Abrami, L., Fivaz, M., Vandergoot, F.G. (1997). **Membrane insertion: The strategies of toxins**. *Molecular Membrane Biology*, 14 (2), 45-64.
3. Dal Peraro, M., Van Der Goot, F.G. (2016). **Pore-forming toxins: ancient, but never really out of fashion**. *Nature reviews microbiology*, 14 (2), 77.
4. Parker, M.W., Feil, S.C. (2005). **Pore-forming protein toxins: from structure to function**. *Prog Biophys Mol Biol*, 88 (1), 91-142.
5. Anderluh, G., Lakey, J.H. (2008). **Disparate proteins use similar architectures to damage membranes**. *Trends Biochem Sci*, 33 (10), 482-490.
6. Szczesny, P., Iacovache, I., Muszewska, A., Ginalski, K., Van Der Goot, F.G., Grynberg, M. (2011). **Extending the aerolysin family: from bacteria to vertebrates**. *PLoS One*, 6 (6).
7. Galinier, R., Portela, J., Moné, Y., Allienne, J.F., Henri, H., Delbecq, S., . . . Duval, D. (2013). **Biomphalysin, a new β pore-forming toxin involved in *Biomphalaria glabrata* immune defense against *Schistosoma mansoni***. *PLoS pathogens*, 9 (3).
8. Xiang, Y., Yan, C., Guo, X., Zhou, K., Gao, Q., Wang, X., . . . Zhang, Y. (2014). **Host-derived, pore-forming toxin–like protein and trefoil factor complex protects the host against microbial infection**. *Proc Natl Acad Sci*, 111 (18), 6702-6707.
9. Muller-Eberhard, H.J. (1986). **The membrane attack complex of complement**. *Annual review of immunology*, 4 (1), 503-528.
10. Rivera-de-Torre, E., Martínez-del-Pozo, A., Garb, J.E. (2018). ***Stichodactyla helianthus*' de novo transcriptome assembly: Discovery of a new actinoporin isoform**. *Toxicon*, 150, 105-114.
11. Maček, P. (1992). **Polypeptide cytolytic toxins from sea anemones (Actiniaria)**. *FEMS Microbiol Immunol*, 5 (1-3), 121-129.
12. Anderluh, G., Maček, P. (2002). **Cytolytic peptide and protein toxins from sea anemones (Anthozoa: Actiniaria)**. *Toxicon*, 40 (2), 111-124.
13. Alegre-Cebollada, J., Oñaderra, M., Gavilanes, J.G., Martínez-del-Pozo, A. (2007). **Sea anemone actinoporins: The transition from a folded soluble state to a functionally active membrane-bound oligomeric pore**. *Curr Protein Pept Sci*, 8 (6), 558-572.
14. Caaveiro, J.M., Echabe, I., Gutiérrez-Aguirre, I., Nieva, J.L., Arrondo, J.L., González-Mañas, J.M. (2001). **Differential interaction of equinatoxin II with model membranes in response to lipid composition**. *Biophys J*, 80 (3), 1343-1353.
15. Schön, P., García-Saez, A.J., Malovrh, P., Bacia, K., Anderluh, G., Schwille, P. (2008). **Equinatoxin II permeabilizing activity depends on the presence of sphingomyelin and lipid phase coexistence**. *Biophys J*, 95 (2), 691-698.

16. Barlič, A., Gutiérrez-Aguirre, I., Caaveiro, J.M., Cruz, A., Ruiz-Argüello, M.B., Pérez-Gil, J., González-Mañas, J.M. (2004). **Lipid phase coexistence favors membrane insertion of equinatoxin-II, a pore-forming toxin from *Actinia equina***. *J Biol Chem*, 279 (33), 34209-34216.

17. Varanda, W., Finkelstein, A. (1980). **Ion and nonelectrolyte permeability properties of channels formed in planar lipid bilayer membranes by the cytolytic toxin from the sea anemone, *Stoichactis helianthus***. *J Membr Biol*, 55 (3), 203-211.

18. De los Ríos, V., Mancheño, J.M., Lanio, M.E., Oñaderra, M., Gavilanes, J.G. (1998). **Mechanism of the leakage induced on lipid model membranes by the hemolytic protein sticholysin II from the sea anemone *Stichodactyla helianthus***. *Eur J Biochem*, 252 (2), 284-289.

19. Martínez, D., Otero, A., Álvarez, C., Pazos, F., Tejuca, M., Lanio, M.E., . . . Lissi, E. (2007). **Effect of sphingomyelin and cholesterol on the interaction of St II with lipidic interfaces**. *Toxicon*, 49 (1), 68-81.

20. Bakrač, B., Anderluh, G., **Molecular mechanism of sphingomyelin-specific membrane binding and pore formation by actinoporins**, in: Proteins Membrane Binding and Pore Formation, Springer, 2010, pp. 106-115.

21. Pedrera, L., Fanani, M.L., Ros, U., Lanio, M.E., Maggio, B., Álvarez, C. (2014). **Sticholysin I-membrane interaction: an interplay between the presence of sphingomyelin and membrane fluidity**. *Biochim Biophys Acta (BBA) - Biomembranes*, 1838 (7), 1752-1759.

22. Pedrera, L., Gomide, A.B., Sánchez, R.E., Ros, U., Wilke, N., Pazos, F., . . . Álvarez, C. (2015). **The presence of sterols favors sticholysin I-membrane association and pore formation regardless of their ability to form laterally segregated domains**. *Langmuir*, 31 (36), 9911-9923.

23. Alm, I., García-Linares, S., Gavilanes, J.G., Martínez-del-Pozo, A., Slotte, J.P. (2015). **Cholesterol stimulates and ceramide inhibits sticholysin II-induced pore formation in complex bilayer membranes**. *Biochim Biophys Acta (BBA) - Biomembranes*, 1848, 925-931.

24. García-Linares, S., Palacios-Ortega, J., Yasuda, T., Astrand, M., Gavilanes, J.G., Martínez-del-Pozo, A., Slotte, J.P. (2016). **Toxin-induced pore formation is hindered by intermolecular hydrogen bonding in sphingomyelin bilayers**. *Biochim Biophys Acta (BBA) - Biomembranes*, 1858 (6), 1189-1195.

25. Palacios-Ortega, J., García-Linares, S., Astrand, M., Al Sazzad, M.A., Gavilanes, J.G., Martínez-del-Pozo, A., Slotte, J.P. (2016). **Regulation of Sticholysin II-Induced Pore Formation by Lipid Bilayer Composition, Phase State, and Interfacial Properties**. *Langmuir*, 32 (14), 3476-3484.

26. García-Linares, S., Rivera-de-Torre, E., Morante, K., Tsumoto, K., Caaveiro, J.M., Gavilanes, J.G., . . . Martínez-del-Pozo, Á. (2016). **Differential effect of membrane composition on the pore-forming ability of four different sea anemone actinoporins**. *Biochemistry*, 55 (48), 6630-6641.

27. Wacklin, H.P., Bremec, B.B., Moulin, M., Rojko, N., Haertlein, M., Forsyth, T., . . . Norton, R.S. (2016). **Neutron reflection study of the interaction of the eukaryotic pore-forming actinoporin equinatoxin II with lipid membranes reveals intermediate states in pore formation**. *Biochim Biophys Acta (BBA) - Biomembranes*, 1858 (4), 640-652.

28. Marchioretto, M., Podobnik, M., Dalla Serra, M., Anderluh, G. (2013). **What planar lipid membranes tell us about the pore-forming activity of cholesterol-dependent cytolysins**. *Biophys Chem*, 182, 64-70.

29. Mancheño, J.M., Martín-Benito, J., Martínez-Ripoll, M., Gavilanes, J.G., Hermoso, J.A. (2003). **Crystal and electron microscopy structures of sticholysin II actinoporin reveal insights into the mechanism of membrane pore formation**. *Structure*, 11 (11), 1319-1328.

30. García-Linares, S., Castrillo, I., Bruix, M., Menéndez, M., Alegre-Cebollada, J., Martínez-del-Pozo, A., Gavilanes, J.G. (2013). **Three-dimensional structure of the actinoporin sticholysin I. Influence of long-distance effects on protein function**. *Arch Biochem Biophys*, 532 (1), 39-45.

31. Athanasiadis, A., Anderluh, G., Maček, P., Turk, D. (2001). **Crystal structure of the soluble form of equinatoxin II, a pore-forming toxin from the sea anemone *Actinia equina***. *Structure*, 9 (4), 341-346.

32. Hinds, M.G., Zhang, W., Anderluh, G., Hansen, P.E., Norton, R.S. (2002). **Solution structure of the eukaryotic pore-forming cytolysin equinatoxin II: Implications for pore formation**. *J Mol Biol*, 315 (5), 1219-1229.

33. Mechaly, A.E., Bellomio, A., Morante, K., González-Mañas, J.M., Guerin, D.M. (2009). **Crystallization and preliminary crystallographic analysis of fragaceatoxin C, a pore-forming toxin from the sea anemone *Actinia fragacea***. *Acta Crystallogr Sect F Struct Biol Cryst Commun*, 65 (4), 357-360.

34. Mechaly, A.E., Bellomio, A., Gil-Carton, D., Morante, K., Valle, M., González-Mañas, J.M., Guerin, D.M. (2011). **Structural insights into the oligomerization and architecture of eukaryotic membrane pore-forming toxins**. *Structure*, 19 (2), 181-191.

35. Tanaka, K., Caaveiro, J.M., Morante, K., González-Mañas, J.M., Tsumoto, K. (2015). **Structural basis for self-assembly of a cytolytic pore lined by protein and lipid**. *Nat Commun*, 6 (1), 1-11.

36. Welsh, J.H. (1964). **Composition and mode of action of some invertebrate venoms**. *Annual Review of Pharmacology*, 4 (1), 293-304.

37. Baslow, M.H. (1971). **Marine toxins**. *Annual Review of Pharmacology*, 11 (1), 447-454.

38. Lane, C. (1968). **Toxins of marine origin**. *Annual Review of Pharmacology*, 8 (1), 409-426.

39. Devlin, J.P. (1974). **Isolation and partial purification of hemolytic toxin from sea anemone, *Stoichactis helianthus***. *Journal of pharmaceutical sciences*, 63 (9), 1478-1480.

40. Bernheimer, A.W., Avigad, L.S. (1976). **Properties of a toxin from the sea anemone *Stoichactis helianthus*, including specific binding to sphingomyelin**. *Proc Natl Acad Sci*, 73 (2), 467-471.

41. Linder, R., Bernheimer, A.W. (1978). **Effect on sphingomyelin-containing liposomes of phospholipase D from *Corynebacterium ovis* and the cytolysin from *Stoichactis helianthus***. *Biochim Biophys Acta (BBA) - Biomembranes*, 530 (2), 236-246.

42. Linder, R., Bernheimer, A.W., Kim, K.S. (1977). **Interaction between sphingomyelin and a cytolysin from the sea anemone *Stoichactis helianthus***. *Biochim Biophys Acta (BBA) - Biomembranes*, 467 (3), 290-300.

43. Michaels, D.W. (1979). **Membrane damage by a toxin from the sea anemone *Stoichactis helianthus*. I. Formation of transmembrane channels in lipid bilayers**. *Biochim Biophys Acta (BBA) - Biomembranes*, 555 (1), 67-78.

44. Shin, M.L., Michaels, D.W., Mayer, M.M. (1979). **Membrane damage by a toxin from the sea anemone *Stoichactis helianthus*. II. Effect of membrane lipid composition in a liposome system**. *Biochim Biophys Acta (BBA) - Biomembranes*, 555 (1), 79-88.

45. Kem, W., Doyle, J., Dunn, B., Blumenthal, K., **Purification and Characterization of Sea Anemone (*Stoichactis*) Cytotoxins**, in: Federation Proceedings, vol. 41, Federation Amer Soc Exp Biol 9650 Rockville Pike, Bethesda, MD 20814-3998, 1982, pp. 1643-1643.

46. Blumenthal, K., Kem, W. (1983). **Primary structure of *Stoichactis helianthus* cytolysin III**. *J Biol Chem*, 258 (9), 5574-5581.

47. Kem, W.R., Dunn, B.M. (1988). **Separation and characterization of four different amino acid sequence variants of a sea anemone (*Stichodactyla helianthus*) protein cytolysin**. *Toxicon*, 26 (11), 997-1008.

48. Doyle, J.W., Kem, W.R. (1989). **Binding of a radiolabeled sea anemone cytolysin to erythrocyte membranes**. *Biochim Biophys Acta (BBA) - Biomembranes*, 987 (2), 181-186.

49. Doyle, J.W., Kem, W.R., Vilallonga, F.A. (1989). **Interfacial activity of an ion channel-generating protein cytolysin from the sea anemone *Stichodactyla helianthus***. *Toxicon*, 27 (4), 465-471.

50. Kem, W.R., Parten, B., Pennington, M.W., Price, D.A., Dunn, B.M. (1989). **Isolation, characterization, and amino acid sequence of a polypeptide neurotoxin occurring in the sea anemone *Stichodactyla helianthus***. *Biochemistry*, 28 (8), 3483-3489.

51. Ávila, A., De Acosta, C.M., Lage, A. (1988). **A new immunotoxin built by linking a hemolytic toxin to a monoclonal antibody specific for immature T lymphocytes**. *International journal of cancer*, 42 (4), 568-571.

52. Ávila, A., Mateo Acosta, C.D., Lage, A. (1989). **A carcinoembryonic antigen‐directed immunotoxin built by linking a monoclonal antibody to a hemolytic toxin**. *International journal of cancer*, 43 (5), 926-929.

53. Ferlan, I., Lebez, D. (1974). **Equinatoxin, a lethal protein from *Actinia equina*—I Purification and characterization**. *Toxicon*, 12 (1), 57-58.

54. Sket, D., Drašlar, K., Ferlan, I., Lebez, D. (1974). **Equinatoxin, a lethal protein from *Actinia equina*—II. Pathophysiological action**. *Toxicon*, 12 (1), 63-68.

55. Giraldi, T., Ferlan, I., Romeo, D. (1976). **Antitumour activity of equinatoxin**. *Chemico-biological interactions*, 13 (3-4), 199-203.

56. Ferlan, I., Jackson, K.W. (1983). **Partial amino acid sequence of equinatoxin**. *Toxicon*, 21, 141-144.

57. Maček, P., Lebez, D. (1981). **Kinetics of hemolysis induced by equinatoxin, a cytolytic toxin from the sea anemone *Actinia equina*. Effect of some ions and pH**. *Toxicon*, 19 (2), 233-240.

58. Lafranconi, W.M., Ferlan, I., Russell, F.E., Huxtable, R.J. (1984). **The action of equinatoxin, a peptide from the venom of the sea anemone, *Actinia equina*, on the isolated lung**. *Toxicon*, 22 (3), 347-352.

59. Ho, C., Ko, J., Lue, H., Lee, C., Ferlan, I. (1987). **Effects of equinatoxin on the guinea-pig atrium**. *Toxicon*, 25 (6), 659-664.

60. Maček, P., Lebez, D. (1988). **Isolation and characterization of three lethal and hemolytic toxins from the sea anemone *Actinia equina* L**. *Toxicon*, 26 (5), 441-451.

61. Teng, C.-M., Lee, L.-G., Lee, C.-Y., Ferlan, I. (1988). **Platelet aggregation induced by equinatoxin**. *Thrombosis research*, 52 (5), 401-411.

62. Turk, T., Maček, P., Gubensek, F. (1989). **Chemical modification of equinatoxin II, a lethal and cytolytic toxin from the sea anemone *Actinia equina* L**. *Toxicon*, 27 (3), 375-384.

63. Batista, U., Maček, P., Sedmak, B. (1990). **The cytotoxic and cytolytic activity of equinatoxin II from the sea anemone *Actinia equina***. *Cell Biol Int Rep*, 14 (11), 1013-1024.

64. Zorec, R., Tester, M., Maček, P., Mason, W.T. (1990). **Cytotoxicity of equinatoxin II from the sea anemone *Actinia equina* involves ion channel formation and an increase in intracellular calcium activity**. *J Membr Biol*, 118 (3), 243-249.

65. Belmonte, G., Pederzolli, C., Maček, P., Menestrina, G. (1993). **Pore formation by the sea anemone cytolysin equinatoxin-II in red blood cells and model lipid membranes**. *J Membr Biol*, 131, 11-22.

66. Maček, P., Belmonte, G., Pederzolli, C., Menestrina, G. (1994). **Mechanism of action of equinatoxin II, a cytolysin from the sea anemone *Actinia equina* L. belonging to the family of actinoporins**. *Toxicology*, 87 (1-3), 205-227.

67. Belmonte, G., Menestrina, G., Pederzolli, C., Krizaj, I., Gubensek, F., Turk, T., Maček, P. (1994). **Primary and secondary structure of a pore-forming toxin from the sea anemone, *Actinia equina L.*, and its association with lipid vesicles**. *Biochim Biophys Acta (BBA) - Biomembranes*, 1192, 197-204.

68. Anderluh, G., Pungerear, J., Strukelj, B., Maček, P., Gubensk, F. (1996). **Cloning, sequencing and expression of equinatoxin II**. *Biochem Biophys Res Commun*, 220, 437-442.

69. Morera, V., Gómez, J., Besada, V., Estrada, R., Pons, T., Álvarez, C., . . . Pazos, F. (1994). **Primary structure analysis of the haemolytic polypeptide sticholysin isolated from a sea anemone**.

70. Alvarez, C., Tejuca, M., Morera, V., Besada, V., Pazos, F., Veitia, R., . . . Lanio, M. (1994). **Some characteristics of sticholysin: a novel cytolysin from *Stichodactyla helianthus***. *Adv Mod Biotechnol*, 2, 135-146.

71. Alvarez, C., Tejuca, M., Morera, V., Besada, V., Pazos, F., Lanio, M., Padrón, G. (1996). **Novel primary structure of sticholysin and its interaction with membranes**. *Toxicon*, 3 (34), 301.

72. Tejuca, M., Dalla Serra, M., Ferreras, M., Lanio, M.E., Menestrina, G. (1996). **Mechanism of membrane permeabilization by sticholysin I, a cytolysin isolated from the venom of the sea anemone *Stichodactyla helianthus***. *Biochemistry*, 35 (47), 14947-14957.

73. Bellomio, A., Morante, K., Barlič, A., Gutiérrez-Aguirre, I., Viguera, A.R., González-Mañas, J.M. (2009). **Purification, cloning and characterization of fragaceatoxin C, a novel actinoporin from the sea anemone *Actinia fragacea***. *Toxicon*, 54 (6), 869-880.

74. Vincent, J., Balerna, M., Barhanin, J., Fosset, M., Lazdunski, M. (1980). **Binding of sea anemone toxin to receptor sites associated with gating system of sodium channel in synaptic nerve endings in vitro**. *Proc Natl Acad Sci*, 77 (3), 1646-1650.

75. Barhanin, J., Hugues, M., Schweitz, H., Vincent, J.-P., Lazdunski, M. (1981). **Structure-function relationships of sea anemone toxin II from *Anemonia sulcata***. *J Biol Chem*, 256 (11), 5764-5769.

76. Bernheimer, A.W., Avigad, L.S., Lai, C. (1982). **Purification and properties of a toxin from the sea anemone *Condylactis gigantea***. *Arch Biochem Biophys*, 214 (2), 840-845.

77. Bernheimer, A.W., Avigad, L.S. (1982). **Toxins of the sea anemone *Epiactis prolifera***. *Arch Biochem Biophys*, 217 (1), 174-180.

78. Bernheimer, A.W., Avigad, L.S., Branch, G., Dowdle, E., Lai, C.Y. (1984). **Purification and properties of a toxin from the South African sea anemone, *Pseudactinia varia***. *Toxicon*, 22 (2), 183-191.

79. Bernheimer, A.W., Lai, C.Y. (1985). **Properties of a cytolytic toxin from the sea anemone, *Stoichactis kenti***. *Toxicon*, 23 (5), 791-799.

80. El-Sherif, N., Fozzard, H.A., Hanck, D.A. (1992). **Dose-dependent modulation of the cardiac sodium channel by sea anemone toxin ATXII**. *Circulation Research*, 70 (2), 285-301.

81. Khoo, K.S., Kam, W.K., Khoo, H.E., Gopalakrishnakone, P., Chung, M.C. (1993). **Purification and partial characterization of two cytolysins from a tropical sea anemone, *Heteractis magnifica***. *Toxicon*, 31 (12), 1567-1579.

82. Aneiros, A., García, I., Martínez, J.R., Harvey, A.L., Anderson, A.J., Marshall, D.L., . . . Karlsson, E. (1993). **A potassium channel toxin from the secretion of the sea anemone *Bunodosoma granulifera*. Isolation, amino acid sequence and biological activity**. *Biochim Biophys Acta (BBA) - General Subjects*, 1157 (1), 86-92.

83. Tkacheva, E., Leychenko, E., Monastyrnaya, M., Issaeva, M., Zelepuga, E., Anastuk, S., . . . Kozlovskaya, E. (2011). **New actinoporins from sea anemone *Heteractis crispa*: Cloning and functional expression**. *Biochemistry*, 76 (10), 1131.

84. Norton, R.S., Bobek, G., Ivanov, J.O., Thomson, M., Fiala-Beer, E., Moritz, R.L., Simpson, R.J. (1990). **Purification and characterisation of proteins with cardiac stimulatory and haemolytic activity from the anemone *Actinia tenebrosa***. *Toxicon*, 28 (1), 29-41.

85. Jiang, X., Chen, H., Yang, W., Liu, Y., Liu, W., Wei, J., . . . Xu, A. (2003). **Functional expression and characterization of an acidic actinoporin from sea anemone *Sagartia rosea***. *Biochem Biophys Res Commun*, 312 (3), 562-570.

86. Tejuca, M., Dalla Serra, M., Potrich, C., Álvarez, C., Menestrina, G. (2001). **Sizing the Radius of the Pore Formed in Erythrocytes and Lipid Vesicles by the Toxin Sticholysin I from the Sea Anemone *Stichodactyla helianthus***. *J Membr Biol*, 183 (2), 125-135.

87. Saier Jr, M.H., Reddy, V.S., Tsu, B.V., Ahmed, M.S., Li, C., Moreno-Hagelsieb, G. (2016). **The transporter classification database (TCDB): recent advances**. *Nucleic acids research*, 44 (D1), D372-D379.

88. Iacovache, I., van der Goot, F.G., Pernot, L. (2008). **Pore formation: an ancient yet complex form of attack**. *Biochim Biophys Acta (BBA) - Biomembranes*, 1778 (7-8), 1611-1623.

89. Mueller, M., Grauschopf, U., Maier, T., Glockshuber, R., Ban, N. (2009). **The structure of a cytolytic α-helical toxin pore reveals its assembly mechanism**. *Nature*, 459 (7247), 726-730.

90. Mueller, M., Ban, N. (2010). **Enhanced SnapShot: Pore-forming toxins**. *Cell*, 142 (2), 334, 334 e331.

91. Geny, B., Popoff, M.R. (2006). **Bacterial protein toxins and lipids: pore formation or toxin entry into cells**. *Biol Cell*, 98 (11), 667-678.

92. González, M.R., Bischofberger, M., Pernot, L., van der Goot, F.G., Freche, B. (2008). **Bacterial pore-forming toxins: the (w)hole story?** *Cell Mol Life Sci*, 65 (3), 493-507.

93. Law, R.H., Lukoyanova, N., Voskoboinik, I., Caradoc-Davies, T.T., Baran, K., Dunstone, M.A., . . . Whisstock, J.C. (2010). **The structural basis for membrane binding and pore formation by lymphocyte perforin**. *Nature*, 468 (7322), 447-451.

94. Basulto, A., Pérez, V.M., Noa, Y., Varela, C., Otero, A.J., Pico, M.C. (2006). **Immunohistochemical targeting of sea anemone cytolysins on tentacles, mesenteric filaments and isolated nematocysts of *Stichodactyla helianthus***. *J Exp Zoolog A Comp Exp Biol*, 305 (3), 253-258.

95. Rivera-de-Torre, E., García-Linares, S., Alegre-Cebollada, J., Lacadena, J., Gavilanes, J.G., Martínez-del-Pozo, A. (2016). **Synergistic action of actinoporin isoforms from the same sea anemone species assembled into functionally active heteropores**. *J Biol Chem*, 291 (27), 14109-14119.

96. Wang, Y., Yap, L.L., Chua, K.L., Khoo, H.E. (2008). **A multigene family of *Heteractis* magnificalysins (HMgs)**. *Toxicon*, 51 (8), 1374-1382.

97. Monastyrnaya, M., Leychenko, E., Isaeva, M., Likhatskaya, G., Zelepuga, E., Kostina, E., . . . Kozlovskaya, E. (2010). **Actinoporins from the sea anemones, tropical *Radianthus***

macrodactylus **and northern** ***Oulactis orientalis*****: Comparative analysis of structure-function relationships**. *Toxicon*, 56 (8), 1299-1314.

98. Turk, T. (1991). **Cytolytic toxins from sea anemones**. *Toxin Reviews*, 10 (3), 223-262.

99. De los Ríos, V., Oñaderra, M., Martínez-Ruiz, A., Lacadena, J., Mancheño, J.M., Martínez-del-Pozo, A., Gavilanes, J.G. (2000). **Overproduction in *Escherichia coli* and purification of the hemolytic protein sticholysin II from the sea anemone *Stichodactyla helianthus***. *Protein Expr Purif*, 18 (1), 71-76.

100. The-UniProt-Consortium. (2018). **UniProt: a worldwide hub of protein knowledge**. *Nucleic Acids Research*, 47 (D1), D506-D515.

101. Hoang, Q.T., Cho, S.H., McDaniel, S.F., Ok, S.H., Quatrano, R.S., Shin, J.S. (2009). **An actinoporin plays a key role in water stress in the moss *Physcomitrella patens***. *New Phytol*, 184 (2), 502-510.

102. Hong, Q., Gutiérrez-Aguirre, I., Barlič, A., Malovrh, P., Kristan, K., Podlesek, Z., . . . Anderluh, G. (2002). **Two-step Membrane Binding by Equinatoxin II, a Pore-forming Toxin from the Sea Anemone, Involves an Exposed Aromatic Cluster and a Flexible Helix**. *J Biol Chem*, 277 (44), 41916-41924.

103. Norton, R.S. (2009). **Structures of sea anemone toxins**. *Toxicon*, 54 (8), 1075-1088.

104. Malovrh, P., Viero, G., Serra, M.D., Podlesek, Z., Lakey, J.H., Maček, P., . . . Anderluh, G. (2003). **A novel mechanism of pore formation: membrane penetration by the N-terminal amphipathic region of equinatoxin**. *J Biol Chem*, 278 (25), 22678-22685.

105. Kristan, K., Podlesek, Z., Hojnik, V., Gutiérrez-Aguirre, I., Guncar, G., Turk, D., . . . Anderluh, G. (2004). **Pore Formation by Equinatoxin, a Eukaryotic Pore-forming Toxin, Requires a Flexible N-terminal Region and a Stable b-Sandwich**. *J Biol Chem*, 279 (45), 46509-46517.

106. Alegre-Cebollada, J., Martínez-del-Pozo, A., Gavilanes, J.G., Goormaghtigh, E. (2007). **Infrared spectroscopy study on the conformational changes leading to pore formation of the toxin sticholysin II**. *Biophys J*, 93 (9), 3191-3201.

107. Alegre-Cebollada, J., Cunietti, M., Herrero-Galán, E., Gavilanes, J.G., Martínez-del-Pozo, A. (2008). **Calorimetric scrutiny of lipid binding by sticholysin II toxin mutants**. *J Mol Biol*, 382 (4), 920-930.

108. Pettersen, E.F., Goddard, T.D., Huang, C.C., Couch, G.S., Greenblatt, D.M., Meng, E.C., Ferrin, T.E. (2004). **UCSF Chimera--a visualization system for exploratory research and analysis**. *J Comput Chem*, 25 (13), 1605-1612.

109. Casallanovo, F., de Oliveira, F.J., de Souza, F.C., Ros, U., Martínez, Y., Penton, D., . . . Schreier, S. (2006). **Model peptides mimic the structure and function of the N-terminus of the pore-forming toxin sticholysin II**. *Biopolymers*, 84 (2), 169-180.

110. Lima de Oliveira, A., Maffud Cilli, E., Ros, U., Crusca, E., Jr., Lanio, M.E., Alvarez, C., . . . Spisni, A. (2018). **Insights on the structure-activity relationship of peptides derived from Sticholysin II**. *Peptide Science*, 110 (5), e23097.

111. Ros, U., Pedrera, L., Diaz, D., Karam, J.C., Sudbrack, T.P., Valiente, P.A., . . . Avarez, C. (2012). **The membranotropic activity of N-terminal peptides from the pore-forming**

proteins sticholysin I and II is modulated by hydrophobic and electrostatic interactions as well as lipid composition. *J Biosci*, 36 (5), 781-791.

112. Morante, K., Caaveiro, J.M., Tanaka, K., González-Mañas, J.M., Tsumoto, K. (2015). **A pore-forming toxin requires a specific residue for its activity in membranes with particular physicochemical properties**. *J Biol Chem*, 290 (17), 10850-10861.

113. García-Linares, S., Alm, I., Maula, T., Gavilanes, J.G., Slotte, J.P., Martínez-del-Pozo, A. (2015). **The effect of cholesterol on the long-range network of interactions established among sea anemone Sticholysin II residues at the water-membrane interface**. *Mar Drugs*, 13 (4), 1647-1665.

114. Rivera-de-Torre, E., Palacios-Ortega, J., García-Linares, S., Gavilanes, J.G., Martínez-del-Pozo, A. (2017). **One single salt bridge explains the different cytolytic activities shown by actinoporins sticholysin I and II from the venom of *Stichodactyla helianthus***. *Arch Biochem Biophys*, 636, 79-89.

115. Casallanovo, F., de Oliveira, F.J.F., Souto, A.L.C.F., de Souza, F.C., Cilli, E.M., Martínez, Y., . . . Álvarez, C., **Peptides from the N-terminal domain of a pore-forming toxin, Sticholysin II. Conformation and activity.**, in: 48th Annual Meeting of the Biophysical Society, Biophys J, *Baltimore, MD*, 2004.

116. Ros, U., Souto, A.L., de Oliveira, F.J., Crusca, E., Jr., Pazos, F., Cilli, E.M., . . . Alvarez, C. (2013). **Functional and topological studies with Trp-containing analogs of the peptide StII1-30 derived from the N-terminus of the pore forming toxin sticholysin II: contribution to understand its orientation in membrane**. *Biopolymers*, 100 (4), 337-346.

117. De Planque, M.R., Kruijtzer, J.A., Liskamp, R.M., Marsh, D., Greathouse, D.V., Koeppe, R.E., 2nd, . . . Killian, J.A. (1999). **Different membrane anchoring positions of tryptophan and lysine in synthetic transmembrane a-helical peptides**. *J Biol Chem*, 274 (30), 20839-20846.

118. Alegre-Cebollada, J., Lacadena, V., Oñaderra, M., Mancheño, J.M., Gavilanes, J.G., Martínez-del-Pozo, A. (2004). **Phenotypic selection and characterization of randomly produced non-haemolytic mutants of the toxic sea anemone protein sticholysin II**. *FEBS Lett*, 575 (1-3), 14-18.

119. Anderluh, G., Razpotnik, A., Podlesek, Z., Maček, P., Separovic, F., Norton, R.S. (2005). **Interaction of the eukaryotic pore-forming cytolysin equinatoxin II with model membranes: ^{19}F NMR studies**. *J Mol Biol*, 347 (1), 27-39.

120. Bakrač, B., Gutierrez-Aguirre, I., Podlesek, Z., Sonnen, A.F., Gilbert, R.J., Maček, P., . . . Anderluh, G. (2008). **Molecular determinants of sphingomyelin specificity of a eukaryotic pore-forming toxin**. *J Biol Chem*, 283 (27), 18665-18677.

121. Pardo-Cea, M.A., Alegre-Cebollada, J., Martínez-del-Pozo, A., Gavilanes, J.G., Bruix, M. (2010). **^{1}H, ^{13}C, and ^{15}N NMR assignments of StnII-Y111N, a highly impaired mutant of the sea anemone actinoporin Sticholysin II**. *Biomol NMR Assign*, 4 (1), 69-72.

122. Pardo-Cea, M.A., Castrillo, I., Alegre-Cebollada, J., Martínez-del-Pozo, A., Gavilanes, J.G., Bruix, M. (2011). **Intrinsic local disorder and a network of charge-charge**

interactions are key to actinoporin membrane disruption and cytotoxicity. *FEBS J*, 278 (12), 2080-2089.

123. Maula, T., Isaksson, Y.J., García-Linares, S., Niinivehmas, S., Pentikainen, O.T., Kurita, M., . . . Slotte, J.P. (2013). **2NH and 3OH are crucial structural requirements in sphingomyelin for sticholysin II binding and pore formation in bilayer membranes**. *Biochim Biophys Acta (BBA) - Biomembranes*, 1828 (5), 1390-1395.

124. Bakrač, B., Kladnik, A., Maček, P., McHaffie, G., Werner, A., Lakey, J.H., Anderluh, G. (2010). **A toxin-based probe reveals cytoplasmic exposure of golgi sphingomyelin**. *J Biol Chem*, 285 (29), 22186-22195.

125. Yeagle, P.L. 2004. **The structure of biological membranes**, CRC press.

126. Yeagle, P.L. 2016. **The membranes of cells**, Academic Press.

127. Tanford, C. (1978). **The hydrophobic effect and the organization of living matter**. *Science*, 200 (4345), 1012-1018.

128. Voelker, D.R., **Lipid assembly into cell membranes**, in: Biochemistry of Lipids, Lipoproteins and Membranes, Elsevier, 2008, pp. 441-484.

129. Nyholm, T.K., Lindroos, D., Westerlund, B., Slotte, J.P. (2011). **Construction of a DOPC/PSM/cholesterol phase diagram based on the fluorescence properties of trans-parinaric acid**. *Langmuir*, 27 (13), 8339-8350.

130. Björkqvist, Y.J., Nyholm, T.K., Slotte, J.P., Ramstedt, B. (2005). **Domain formation and stability in complex lipid bilayers as reported by cholestatrienol**. *Biophys J*, 88 (6), 4054-4063.

131. Engberg, O., Yasuda, T., Hautala, V., Matsumori, N., Nyholm, T.K., Murata, M., Slotte, J.P. (2016). **Lipid Interactions and Organization in Complex Bilayer Membranes**. *Biophys J*, 110 (7), 1563-1573.

132. Klose, C., Ejsing, C.S., García-Sáez, A.J., Kaiser, H.-J., Sampaio, J.L., Surma, M.A., . . . Simons, K. (2010). **Yeast lipids can phase-separate into micrometer-scale membrane domains**. *J Biol Chem*, 285 (39), 30224-30232.

133. De Almeida, R.F., Fedorov, A., Prieto, M. (2003). **Sphingomyelin-Phosphatidylcholine-Cholesterol phase diagram: boundaries and composition of lipid rafts**. *Biophys J*, 85 (4), 2406-2416.

134. De Almeida, R.F., Loura, L.M., Fedorov, A., Prieto, M. (2005). **Lipid rafts have different sizes depending on membrane composition: a time-resolved fluorescence resonance energy transfer study**. *J Mol Biol*, 346 (4), 1109-1120.

135. Nyholm, T.K., Nylund, M., Slotte, J.P. (2003). **A calorimetric study of binary mixtures of dihydrosphingomyelin and sterols, sphingomyelin, or phosphatidylcholine**. *Biophys J*, 84 (5), 3138-3146.

136. Cooper, G.M., Hausman, R., **A molecular approach**, in: The Cell., Sunderland, MA: Sinauer Associates, 2000.

137. Van Meer, G., Voelker, D.R., Feigenson, G.W. (2008). **Membrane lipids: where they are and how they behave**. *Nature reviews: Molecular cell biology*, 9 (2), 112-124.

138. Cevc, G. (1987). **How membrane chain melting properties are regulated by the polar surface of the lipid bilayer**. *Biochemistry*, 26 (20), 6305-6310.

139. Cevc, G., Watts, A., Marsh, D. (1981). **Titration of the phase transition of phosphatidylserine bilayer membranes. Effects of pH, surface electrostatics, ion binding, and head-group hydration**. *Biochemistry*, 20 (17), 4955-4965.

140. Jouhet, J. (2013). **Importance of the hexagonal lipid phase in biological membrane organization**. *Frontiers in plant science*, 4, 494.

141. Kumar, V. (1991). **Complementary molecular shapes and additivity of the packing parameter of lipids**. *Proc Natl Acad Sci*, 88 (2), 444-448.

142. Yeagle, P.L. (1985). **Cholesterol and the cell membrane**. *Biochim Biophys Acta (BBA) - Reviews on Biomembranes*, 822 (3-4), 267-287.

143. Shieh, H.-S., Hoard, L., Nordman, C. (1981). **The structure of cholesterol**. *Acta Crystallographica Section B: Structural Crystallography Crystal Chemistry*, 37 (8), 1538-1543.

144. Sankaram, M.B., Thompson, T.E. (1990). **Modulation of phospholipid acyl chain order by cholesterol. A solid-state deuterium nuclear magnetic resonance study**. *Biochemistry*, 29 (47), 10676-10684.

145. Lönnfors, M., Doux, J.P., Killian, J.A., Nyholm, T.K., Slotte, J.P. (2011). **Sterols Have Higher Affinity for Sphingomyelin than for Phosphatidylcholine Bilayers even at Equal Acyl-Chain Order**. *Biophys J*, 100 (11), 2633-2641.

146. Slotte, J.P. (2016). **The importance of hydrogen bonding in sphingomyelin's membrane interactions with co-lipids**. *Biochim Biophys Acta (BBA) - Biomembranes*, 1858 (2), 304-310.

147. Ramstedt, B., Slotte, J.P. (2002). **Membrane properties of sphingomyelins**. *FEBS Lett*, 531 (1), 33-37.

148. Jain, M.K., Wagner, R.C., **Introduction to biological membranes**, in, Wiley New York, 1988.

149. Silvius, J.R., Delgiudice, D., Lafleur, M. (1996). **Cholesterol at different bilayer concentrations can promote or antagonize lateral segregation of phospholipids of differing acyl chain length**. *Biochemistry*, 35 (48), 15198-15208.

150. Valcarcel, C.A., Dalla Serra, M., Potrich, C., Bernhart, I., Tejuca, M., Martínez, D., . . . Menestrina, G. (2001). **Effects of lipid composition on membrane permeabilization by sticholysin I and II, two cytolysins of the sea anemone *Stichodactyla helianthus***. *Biophys J*, 80 (6), 2761-2774.

151. Alegre-Cebollada, J., Rodríguez-Crespo, I., Gavilanes, J.G., Martínez-del-Pozo, A. (2006). **Detergent-resistant membranes are platforms for actinoporin pore-forming activity on intact cells**. *FEBS J*, 273 (4), 863-871.

152. Bakrač, B., Anderluh, G. (2009). **Molecular mechanism of sphingomyelin-specific membrane binding and pore formation by actinoporins**. *Avd Exp Med Biol*, 677, 106-115.

153. Rojko, N., Dalla Serra, M., Maček, P., Anderluh, G. (2016). **Pore formation by actinoporins, cytolysins from sea anemones**. *Biochim Biophys Acta (BBA) - Biomembranes*, 1858 (3), 446-456.

154. Martínez, D., Campos, A.M., Pazos, F., Álvarez, C., Lanio, M.E., Casallanovo, F., . . . Lissi, E. (2001). **Properties of St I and St II, two isotoxins isolated from *Stichodactyla helianthus*: a comparison**. *Toxicon*, 39 (10), 1547-1560.

155. Busto, J.V., Fanani, M.L., De Tullio, L., Sot, J., Maggio, B., Goni, F.M., Alonso, A. (2009). **Coexistence of immiscible mixtures of palmitoylsphingomyelin and palmitoylceramide in monolayers and bilayers**. *Biophys J*, 97 (10), 2717-2726.

156. Castro, B.M., de Almeida, R.F., Silva, L.C., Fedorov, A., Prieto, M. (2007). **Formation of ceramide/sphingomyelin gel domains in the presence of an unsaturated phospholipid: a quantitative multiprobe approach**. *Biophys J*, 93 (5), 1639-1650.

157. Chiantia, S., Kahya, N., Ries, J., Schwille, P. (2006). **Effects of ceramide on liquid-ordered domains investigated by simultaneous AFM and FCS**. *Biophys J*, 90 (12), 4500-4508.

158. Meinardi, E., Florin-Christensen, M., Paratcha, G., Azcurra, J.M., Florin-Christensen, J. (1995). **The molecular basis of the self/nonself selectivity of a coelenterate toxin**. *Biochem Biophys Res Commun*, 216 (1), 348-354.

159. Anderluh, G., Podlesek, Z., Maček, P. (2000). **A common motif in proparts of Cnidarian toxins and nematocyst collagens and its putative role**. *Biochim Biophys Acta (BBA) - Protein Structure Molecular Enzymology*, 1476 (2), 372-376.

160. Meinardi, E., Azcurra, J.M., Florin-Christensen, M., Florin-Christensen, J. (1994). **Coelenterolysin: a hemolytic polypeptide associated with the coelenteric fluid of sea anemones**. *Comparative Biochemistry Physiology Part B: Comparative Biochemistry*, 109 (1), 153-161.

161. Hori, T., Nozawa, Y., **Phosphonolipids**, in: New comprehensive biochemistry, vol. 4, Elsevier, 1982, pp. 95-128.

162. Hilderbrand, R.L., Henderson, T.O., **Phosphonic acids in nature**, in: The role of phosphonates in living systems, 1983, pp. 5-30.

163. Simon, G., Rouser, G. (1967). **Phospholipids of the sea anemone: Quantitative distribution; absence of carbon - phosphorus linkages in glycerol phospholipids; structural elucidation of ceramide aminoethylphosphonate**. *Lipids*, 2 (1), 55-59.

164. Joseph, J.D. (1979). **Lipid composition of marine and estuarine invertebrates: Porifera and Cnidaria**. *Progress in lipid research*, 18 (1), 1-30.

165. Nelson, M.M., Phleger, C.F., Mooney, B.D., Nichols, P.D. (2000). **Lipids of gelatinous Antarctic zooplankton: Cnidaria and Ctenophora**. *Lipids*, 35 (5), 551-559.

166. Meneses, P., Navarro, N. (1992). **^{31}P NMR phospholipid profile study of seven sea anemone species**. *Comparative Biochemistry Physiology Part B: Comparative Biochemistry*, 102 (2), 403-407.

167. Huang, J., Buboltz, J.T., Feigenson, G.W. (1999). **Maximum solubility of cholesterol in phosphatidylcholine and phosphatidylethanolamine bilayers**. *Biochim Biophys Acta (BBA) - Biomembranes*, 1417 (1), 89-100.

168. Björkbom, A., Róg, T., Kaszuba, K., Kurita, M., Yamaguchi, S., Lönnfors, M., . . . Slotte, J.P. (2010). **Effect of Sphingomyelin Headgroup Size on Molecular Properties and Interactions with Cholesterol**. *Biophys J*, 99 (10), 3300-3308.

169. Jaikishan, S., Björkbom, A., Slotte, J.P. (2010). **Sphingomyelin analogs with branched N-acyl chains: the position of branching dramatically affects acyl chain order and sterol interactions in bilayer membranes**. *Biochim Biophys Acta (BBA) - Biomembranes*, 1798 (10), 1987-1994.

170. Feinstein, M., Fernandez, S., Sha'Afi, R. (1975). **Fluidity of natural membranes and phosphatidylserine and ganglioside dispersions: Effects of local anesthetics, cholesterol and protein**. *Biochim Biophys Acta (BBA) - Biomembranes*, 413 (3), 354-370.

171. Aittoniemi, J., Rog, T., Niemelä, P., Pasenkiewicz-Gierula, M., Karttunen, M., Vattulainen, I. (2006). **Tilt: major factor in sterols' ordering capability in membranes**. *The Journal of Physical Chemistry B*, 110 (51), 25562-25564.

172. Róg, T., Pasenkiewicz-Gierula, M. (2006). **Cholesterol-sphingomyelin interactions: a molecular dynamics simulation study**. *Biophys J*, 91 (10), 3756-3767.

173. Bruzik, K.S., Sobon, B., Salamonczyk, G.M. (1990). **Nuclear magnetic resonance study of sphingomyelin bilayers**. *Biochemistry*, 29 (16), 4017-4021.

174. Cosentino, K., Ros, U., García-Sáez, A.J. (2016). **Assembling the puzzle: Oligomerization of a-pore forming proteins in membranes**. *Biochim Biophys Acta (BBA) - Biomembranes*, 1858 (3), 457-466.

175. Álvarez, C., Mancheño, J.M., Martínez, D., Tejuca, M., Pazos, F., Lanio, M.E. (2009). **Sticholysins, two pore-forming toxins produced by the Caribbean sea anemone *Stichodactyla helianthus*: Their interaction with membranes**. *Toxicon*, 54 (8), 1135-1147.

176. Martínez, D., Álvarez, C., Tejuca, M., Pazos, F., Valle, A., Calderón, L., . . . Lanio, M.E. (2006). **Los lípidos de la membrana actúan como moduladores de la actividad permeabilizante de Sticholisina II, una toxina formadora de poros con aplicaciones biomédicas.** *Biología Aplicada*, 23 (3), 251-254.

177. Anderluh, G., Dalla Serra, M., Viero, G., Guella, G., Maček, P., Menestrina, G. (2003). **Pore formation by equinatoxin II, a eukaryotic protein toxin, occurs by induction of nonlamellar lipid structures**. *J Biol Chem*, 278 (46), 45216-45223.

178. Ruoslahti, E. (1988). **Fibronectin and its receptors**. *Annual review of biochemistry*, 57 (1), 375-413.

179. García-Linares, S., Richmond, R., García-Mayoral, M.F., Bustamante, N., Bruix, M., Gavilanes, J.G., Martínez-del-Pozo, A. (2014). **The sea anemone actinoporin (Arg-Gly-Asp) conserved motif is involved in maintaining the competent oligomerization state of these pore-forming toxins**. *FEBS J*, 281 (5), 1465-1478.

180. Tanaka, K., Caaveiro, J.M.M., Morante, K., Tsumoto, K. (2017). **Haemolytic actinoporins interact with carbohydrates using their lipid-binding module**. *Philos Trans R Soc Lond B Biol Sci*, 372 (1726), 20162016.

181. García-Linares, S., Rivera-de-Torre, E., Palacios-Ortega, J., Gavilanes, J.G., Martínez-del-Pozo, A., **The metamorphic transformation of a water-soluble monomeric protein into an oligomeric transmembrane pore**, in: Iglič, A., Rappolt, M., García-Sáez, A.J. (Eds.) Advances in Biomembranes and Lipid Self-Assembly, vol. 26, 2017, pp. 51-97.

182. García-Ortega, L., Alegre-Cebollada, J., García-Linares, S., Bruix, M., Martínez-del-Pozo, A., Gavilanes, J.G. (2011). **The behavior of sea anemone actinoporins at the water-membrane interface**. *Biochim Biophys Acta (BBA) - Biomembranes*, 1808 (9), 2275-2288.

183. Castrillo, I., Araujo, N.A., Alegre-Cebollada, J., Gavilanes, J.G., Martínez-del-Pozo, A., Bruix, M. (2010). **Specific interactions of sticholysin I with model membranes: an NMR study**. *Proteins*, 78 (8), 1959-1970.

184. De los Ríos, V., Mancheño, J.M., Martínez-del-Pozo, A., Alfonso, C., Rivas, G., Oñaderra, M., Gavilanes, J.G. (1999). **Sticholysin II, a cytolysin from the sea anemone *Stichodactyla helianthus*, is a monomer-tetramer associating protein**. *FEBS Lett*, 455 (1-2), 27-30.

185. Morante, K., Bellomio, A., Gil-Carton, D., Redondo-Morata, L., Sot, J., Scheuring, S., . . . Caaveiro, J.M.M. (2016). **Identification of a Membrane-bound Prepore Species Clarifies the Lytic Mechanism of Actinoporins**. *Journal of Biological Chemistry*, 291 (37), 19210-19219.

186. Rojko, N., Kristan, K.C., Viero, G., Zerovnik, E., Maček, P., Dalla Serra, M., Anderluh, G. (2013). **Membrane damage by an a-helical pore-forming protein, Equinatoxin II, proceeds through a succession of ordered steps**. *J Biol Chem*, 288 (33), 23704-23715.

187. Subburaj, Y., Ros, U., Hermann, E., Tong, R., García-Sáez, A.J. (2015). **Toxicity of an a-pore-forming toxin depends on the assembly mechanism on the target membrane as revealed by single-molecule imaging**. *J Biol Chem*, 290 (8), 4856-4865.

188. Valle, A., Lopez-Castilla, A., Pedrera, L., Martinez, D., Tejuca, M., Campos, J., . . . Schreier, S. (2011). **Cys mutants in functional regions of Sticholysin I clarify the participation of these residues in pore formation**. *Toxicon*, 58 (1), 8-17.

189. Martín-Benito, J., Gavilanes, F., de Los Ríos, V., Mancheño, J.M., Fernández, J.J., Gavilanes, J.G. (2000). **Two-dimensional crystallization on lipid monolayers and three-dimensional structure of sticholysin II, a cytolysin from the sea anemone *Stichodactyla helianthus***. *Biophys J*, 78 (6), 3186-3194.

190. Rojko, N., Cronin, B., Danial, J.S., Baker, M.A., Anderluh, G., Wallace, M.I. (2014). **Imaging the lipid-phase-dependent pore formation of equinatoxin II in droplet interface bilayers**. *Biophys J*, 106 (8), 1630-1637.

191. Antonini, V., Perez-Barzaga, V., Bampi, S., Penton, D., Martinez, D., Dalla Serra, M., Tejuca, M. (2014). **Functional Characterization of Sticholysin I and W111C Mutant Reveals the Sequence of the Actinoporin's Pore Assembly**. *PLoS One*, 9 (10), e110824.

192. Baker, M.A., Rojko, N., Cronin, B., Anderluh, G., Wallace, M.I. (2014). **Photobleaching Reveals Heterogeneous Stoichiometry for Equinatoxin II Oligomers**. *Chembiochem*, 15 (14), 2139-2145.

193. Kristan, K., Viero, G., Maček, P., Dalla Serra, M., Anderluh, G. (2007). **The equinatoxin N-terminus is transferred across planar lipid membranes and helps to stabilize the transmembrane pore**. *FEBS J*, 274 (2), 539-550.

194. Cohen, R., Barenholz, Y., Gatt, S., Dagan, A. (1984). **Preparation and characterization of well defined D-*erythro* sphingomyelins**. *Chemistry and physics of lipids*, 35 (4), 371-384.

195. Fischer, R.T., Stephenson, F.A., Shafiee, A., Schroeder, F. (1984). **$\Delta^{5,7,9(11)}$-Cholestatrien-3β-ol: A fluorescent cholesterol analogue**. *Chemistry and physics of lipids*, 36 (1), 1-14.

196. Térová, B., Slotte, J.P., Nyholm, T.K. (2004). **Miscibility of acyl-chain defined phosphatidylcholines with N-palmitoyl sphingomyelin in bilayer membranes**. *Biochim Biophys Acta*, 1667 (2), 182-189.

197. Alegre-Cebollada, J., Clementi, G., Cunietti, M., Porres, C., Oñaderra, M., Gavilanes, J.G., Martínez-del-Pozo, A. (2007). **Silent mutations at the 5'-end of the cDNA of actinoporins from the sea anemone *Stichodactyla helianthus* allow their heterologous overproduction in *Escherichia coli***. *J Biotechnol*, 127 (2), 211-221.

198. García-Linares, S., Maula, T., Rivera-de-Torre, E., Gavilanes, J.G., Slotte, J.P., Martínez-del-Pozo, A. (2016). **Role of the tryptophan residues in the specific interaction of the sea anemone *Stichodactyla helianthus*'s actinoporin Sticholysin II with biological membranes**. *Biochemistry*, 55 (46), 6406-6420.

199. Ho, S.F., Hunt, H.D., Horton, R.M., Pullen, J.K. and Pease, L.R. (1989). **Site-directed mutagenesis by overlap extension using the polymerase chain reaction**. *Gene*, 77 (1), 51-59.

200. Lakowicz, J.R. 2006. **Principles of fluorescence spectroscopy**, Springer Science & Business Media.

201. Melo, A.M., Fedorov, A., Prieto, M., Coutinho, A. (2014). **Exploring homo-FRET to quantify the oligomer stoichiometry of membrane-bound proteins involved in a cooperative partition equilibrium**. *Physical Chemistry Chemical Physics*, 16 (34), 18105-18117.

202. Valeur, B., Berberan-Santos, M.N., **Molecular Fluorescence, Principles and Applications**, in, Wiley-VCH Verlag GmbH & Co. KGaA, 2012.

203. Wimley, W.C. (2015). **Determining the Effects of Membrane-Interacting Peptides on Membrane Integrity**. *Methods Mol Biol*, 1324, 89-106.

204. Rouser, G., Fkeischer, S., Yamamoto, A. (1970). **Two dimensional thin layer chromatographic separation of polar lipids and determination of phospholipids by phosphorus analysis of spots**. *Lipids*, 5 (5), 494-496.

205. Andersson, A., Danielsson, J., Gräslund, A., Mäler, L. (2007). **Kinetic models for peptide-induced leakage from vesicles and cells**. *Eur Biophys J*, 36 (6), 621-635.

206. Schroeder, F., Nemecz, G., Gratton, E., Barenholz, Y., Thompson, T.E. (1988). **Fluorescence properties of cholestatrienol in phosphatidylcholine bilayer vesicles**. *Biophys Chem*, 32 (1), 57-72.

207. Davenport, L., Dale, R.E., Bisby, R.H., Cundall, R.B. (1985). **Transverse location of the fluorescent probe 1,6-diphenyl-1,3,5-hexatriene in model lipid bilayer membrane systems by resonance excitation energy transfer**. *Biochemistry*, 24 (15), 4097-4108.

208. Heymann, J.B., Zakharov, S.D., Zhang, Y.L., Cramer, W.A. (1996). **Characterization of electrostatic and nonelectrostatic components of protein membrane binding interactions**. *Biochemistry*, 35, 2717-2725.

209. Hille, J.D., Donne-Op den Kelder, G.M., Sauve, P., De Haas, G.H., Egmond, M.R. (1981). **Physicochemical studies on the interaction of pancreatic phospholipase A2 with a micellar substrate analog**. *Biochemistry*, 20 (14), 4068-4073.

210. Wiseman, T., Williston, S., Brandts, J.F., Lin, L.-N. (1989). **Rapid measurement of binding constants and heats of binding using a new titration calorimeter**. *Analytical biochem*, 179 (1), 131-137.

211. Hresko, R.C., Sugar, I.P., Barenholz, Y., Thompson, T.E. (1986). **Lateral distribution of a pyrene-labeled phosphatidylcholine in phosphatidylcholine bilayers: fluorescence phase and modulation study**. *Biochemistry*, 25 (13), 3813-3823.

212. Hresko, R.C., Sugar, I.P., Barenholz, Y., Thompson, T.E. (1987). **The lateral distribution of pyrene-labeled sphingomyelin and glucosylceramide in phosphatidylcholine bilayers**. *Biophys J*, 51 (5), 725-733.

213. Jones, M.E., Lentz, B.R. (1986). **Phospholipid lateral organization in synthetic membranes as monitored by pyrene-labeled phospholipids: effects of temperature and prothrombin fragment 1 binding**. *Biochemistry*, 25 (3), 567-574.

214. Kullberg, A., Ekholm, O.O., Slotte, J.P. (2016). **Miscibility of Sphingomyelins and Phosphatidylcholines in Unsaturated Phosphatidylcholine Bilayers**. *Biophys J*, 109 (9), 1907-1916.

215. Wang, T.Y., Silvius, J.R. (2003). **Sphingolipid partitioning into ordered domains in cholesterol-free and cholesterol-containing lipid bilayers**. *Biophys J*, 84 (1), 367-378.

216. Koivusalo, M., Alvesalo, J., Virtanen, J.A., Somerharju, P. (2004). **Partitioning of pyrene-labeled phospho- and sphingolipids between ordered and disordered bilayer domains**. *Biophys J*, 86 (2), 923-935.

217. Holt, A., de Almeida, R.F., Nyholm, T.K., Loura, L.M., Daily, A.E., Staffhorst, R.W., . . . Killian, J.A. (2008). **Is there a preferential interaction between cholesterol and tryptophan residues in membrane proteins?** *Biochemistry*, 47 (8), 2638-2649.

218. Runnels, L.W., Scarlata, S.F. (1995). **Theory and application of fluorescence homotransfer to melittin oligomerization**. *Biophys J*, 69, 1569-1583.

219. Kristan, K.C., Viero, G., Dalla Serra, M., Maček, P., Anderluh, G. (2009). **Molecular mechanism of pore formation by actinoporins**. *Toxicon*, 54 (8), 1125-1134.

220. Lewis, B.A., Engelman, D.M. (1983). **Lipid bilayer thickness varies linearly with acyl chain length in fluid phosphatidylcholine vesicles**. *J Mol. Biol.*, 166 (2), 211-217.

221. Marsh, D. (1999). **Thermodynamic analysis of chain-melting transition temperatures for monounsaturated phospholipid membranes: dependence on *cis*-monoenoic double bond position**. *Biophys J*, 77 (2), 953-963.

222. Wang, Z.-q., Lin, H., Li, S., Huang, C.-H. (1994). **Calorimetric studies and molecular mechanics simulations of monounsaturated phosphatidylethanolamine bilayers**. *J Biol Chem*, 269 (38), 23491-23499.

223. Stockton, G.W., Smith, I.C. (1976). **A deuterium nuclear magnetic resonance study of the condensing effect of cholesterol on egg phosphatidylcholine bilayer membranes. I. Perdeuterated fatty acid probes**. *Chem Phys Lipids*, 17 (2-3), 251-263.

224. Kučerka, N., Nieh, M.-P., Pencer, J., Sachs, J.N., Katsaras, J. (2009). **What determines the thickness of a biological membrane**. *J Gen Physiol Biophys*, 28 (2), 117-125.

225. Seelig, J. (1997). **Titration calorimetry of lipid-peptide interactions**. *Biochim Biophys Acta (BBA) - Reviews on Biomembranes*, 1 (1331), 103-116.

226. Nyholm, T.K., Grandell, P.-M., Westerlund, B., Slotte, J.P. (2010). **Sterol affinity for bilayer membranes is affected by their ceramide content and the ceramide chain length**. *Biochim Biophys Acta (BBA) - Biomembranes*, 1798 (5), 1008-1013.

227. Westerlund, B., Grandell, P.-M., Isaksson, Y.J.E., Slotte, J.P. (2010). **Ceramide acyl chain length markedly influences miscibility with palmitoyl sphingomyelin in bilayer membranes**. *Eur Biophys J*, 39 (8), 1117-1128.

228. Eftink, M.R., **Fluorescence quenching reactions**, in: Biophysical and biochemical aspects of fluorescence spectroscopy, Springer, 1991, pp. 1-41.

229. Morante, K., Caaveiro, J.M., Viguera, A.R., Tsumoto, K., González-Mañas, J.M. (2015). **Functional characterization of Val60, a key residue involved in the membrane-oligomerization of fragaceatoxin C, an actinoporin from *Actinia fragacea***. *FEBS Lett*, 589 (15), 1840-1846.

230. Carretero, G.P.B., Vicente, E.F., Cilli, E.M., Alvarez, C.M., Jenssen, H., Schreier, S. (2018). **Dissecting the mechanism of action of actinoporins. Role of the N-terminal amphipathic alpha-helix in membrane binding and pore activity of sticholysins I and II**. *PLoS One*, 13 (8), e0202981.

231. Soto, C., Del Valle, A., Valiente, P.A., Ros, U., Lanio, M.E., Hernandez, A.M., Alvarez, C. (2017). **Differential binding and activity of the pore-forming toxin sticholysin II in model membranes containing diverse ceramide-derived lipids**. *Biochimie*, 138, 20-31.

232. Ros, U., Carretero, G.P.B., Paulino, J., Crusca, E., Jr., Pazos, F., Cilli, E.M., . . . Alvarez, C. (2019). **Self-association and folding in membrane determine the mode of action of peptides from the lytic segment of sticholysins**. *Biochimie*, 156, 109-117.

233. Mesa-Galloso, H., Delgado-Magnero, K.H., Cabezas, S., Lopez-Castilla, A., Hernandez-Gonzalez, J.E., Pedrera, L., . . . Valiente, P.A. (2017). **Disrupting a key hydrophobic pair in the oligomerization interface of the actinoporins impairs their pore-forming activity**. *Protein Sci*, 26 (3), 550-565.

234. Laborde, R.J., Sanchez-Ferras, O., Luzardo, M.C., Cruz-Leal, Y., Fernandez, A., Mesa, C., . . . Lanio, M.E. (2017). **Novel Adjuvant Based on the Pore-Forming Protein**

Sticholysin II Encapsulated into Liposomes Effectively Enhances the Antigen-Specific CTL-Mediated Immune Response. *J Immunol*, 198 (7), 2772-2784.

235. Marcus, Y. (2012). **Volumes of aqueous hydrogen and hydroxide ions at 0 to 200 °C**. *J Chem Phys*, 137 (15), 154501.

236. Alvarez, C., Casallanovo, F., Shida, C.S., Nogueira, L.V., Martínez, D., Tejuca, M., . . . Schreier, S. (2003). **Binding of sea anemone pore-forming toxins sticholysins I and II to interfaces-Modulation of conformation and activity, and lipid-protein interaction**. *Chem Phys Lipids*, 122 (1-2), 97-105.

237. Tamba, Y., Ariyama, H., Levadny, V., Yamazaki, M. (2010). **Kinetic pathway of antimicrobial peptide magainin 2-induced pore formation in lipid membranes**. *J Phys Chem B*, 114 (37), 12018-12026.

238. Mustafa, M.B., Tipton, D.L., Barkley, M.D., Russo, P.S., Blum, F.D. (1993). **Dye Diffusion in Isotropic and Liquid-Crystalline Aqueous (Hydroxypropyl)Cellulose**. *Macromolecules*, 26 (2), 370-378.

239. Müller, C.B., Loman, A., Pacheco, V., Koberling, F., Willbold, D., Richtering, W., Enderlein, J. (2008). **Precise measurement of diffusion by multi-color dual-focus fluorescence correlation spectroscopy**. *EPL (Europhys Lett)*, 83 (4), 46001.

240. Šuput, D. (1986). **Effects of Equinatoxin on the membrane of skeletal-muscle fiber**. *Period. Biol.*, 88 (2), 210-211.

241. Krauson, A.J., He, J., Wimley, W.C. (2012). **Determining the mechanism of membrane permeabilizing peptides: identification of potent, equilibrium pore-formers**. *Biochim Biophys Acta (BBA) - Biomembranes*, 1818 (7), 1625-1632.

242. Krauson, A.J., He, J., Wimley, W.C. (2012). **Gain-of-function analogues of the pore-forming peptide melittin selected by orthogonal high-throughput screening**. *J Am Chem Soc*, 134 (30), 12732-12741.

243. Mock, D.M., Matthews, N.I., Strauss, R.G., Burmeister, L.F., Schmidt, R., Widness, J.A. (2009). **Red blood cell volume can be independently determined in vitro using sheep and human red blood cells labeled at different densities of biotin**. *J Transfusion*, 49 (6), 1178-1185.

244. Calvete, J.J. (2017). **Venomics: integrative venom proteomics and beyond**. *Biochem. J.*, 474 (5), 611-634.

245. Prato, E., Biandolino, F. (2012). **Total lipid content and fatty acid composition of commercially important fish species from the Mediterranean, Mar Grande Sea**. *Food Chemistry*, 131 (4), 1233-1239.

10. APPENDIX

10.1. Excitation anisotropy spectrum of ATTO-488

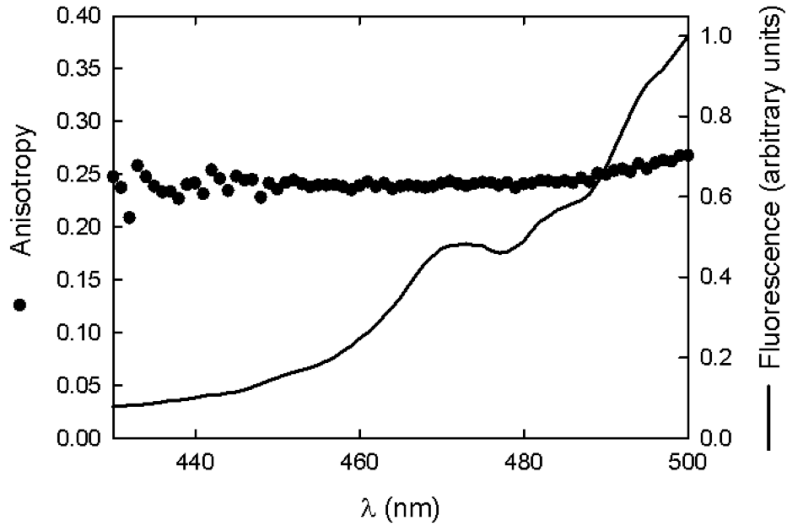

Figure A1. *Excitation anisotropy spectrum (solid circles) and excitation intensity spectrum (solid line) of ATTO-488 in 87% glycerol (v/v) at room temperature using 520 nm for emission wavelength. Notice that the values agree nicely with the* r*(0) values obtained in the anisotropy decays measured for ATTO-labeled StnI (the resolution of the instrument did not allow to resolve the r(0) value for the free label).*

10.2. Structural characterization of StnI-T43C

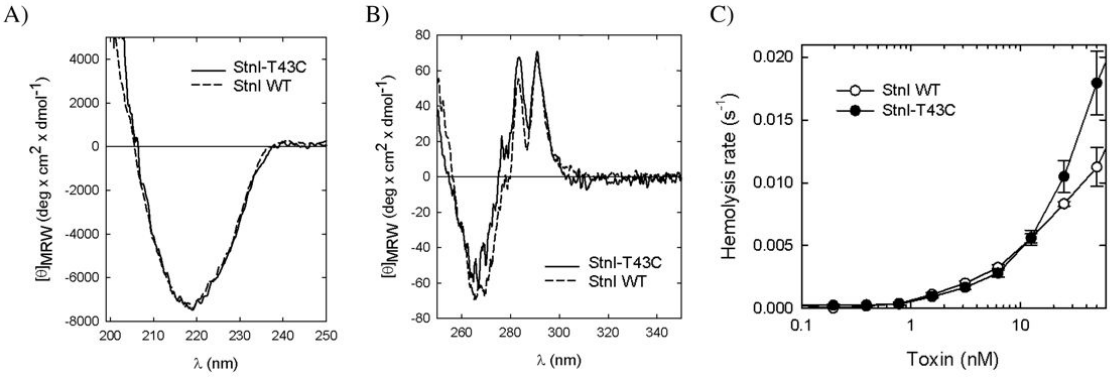

Figure A2. A) *Far-UV circular dichroism of the mutant (solid line) and StnI-WT (dashed line).* **B)** *Near-UV circular dichroism of the mutant (solid line) and StnI-WT (dashed line).* **C)** *Hemolysis rates of erythrocyte preparations when exposed to the indicated concentrations of StnI-WT (open circles) or StnI-T43C (solid circles).*

10.3. Mutated position of StnI-T43C

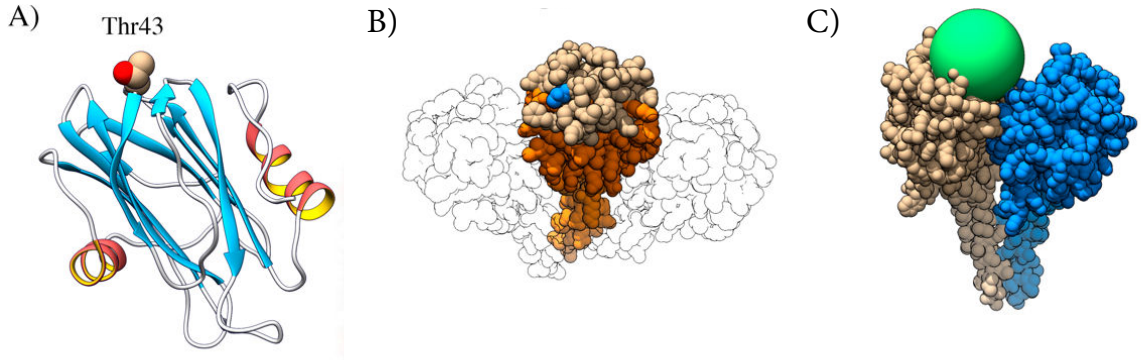

Figure A3. A) *Three-dimensional structure of StnI with Thr43 shown as spheres.* **B)** *Three StnI monomers (as spheres) arranged according to the octameric structure of FraC, showing the position of Thr43 in blue. Residues in orange were considered to be especially relevant for StnI functionality, and hence should preferably not be mutated.* **C)** *Two StnI-monomers arranged as in B, with a green sphere representing the maximum possible reach of the fluorescent labels used. It can be readily seen that the label will hardly interfere with the interaction with the neighboring monomer.*

10.4. Python program used to predict FRET efficiencies in the pores of sticholysins as a function of acceptor percentage in the sample

```
#!/usr/bin/env python3
# -*- coding: utf-8 -*-
"""
Last version. Included on this file on Thu Jun 11 13:17:34 2020
@author: Juan Palacios Ortega
Separation of the comments on the program has been adjusted for better display when
printed with this thesis
"""
import matplotlib.pyplot as plt
import numpy as np
from itertools import combinations as cmb

# General parametes & adjustments

r_mm = 29.0          # Distance between labelled positions
R0DD = 00.0          # R0 for D-D transfer; = 0.0 for D-D not affecting signal
R0DA = 63.8          # R0 for D-A transfer
t_D  = 4.1           # Average lifetime of the donor
ktd  = 1/t_D         # Decay rate of the D

fD   = 5             # Fraction of D, usually constant; max 100-fA

stoich = list(range(11,1,-1)) # Stoichiometries; as range(max,min-1,interval)

breakdown = 0        # Prints number of combinations for a stoich.
roff      = 10.0     # Distance from prot. center to label
aloff = np.pi/180*66 # Angle of the offset relative to line to oligomer center

#Output options
plotter = 0          # Show the plots of the oligomers
labs    = 0          # Show the distance labels
labs_c  = 0          # Show the distance to the center
```

```
rel_siz = 0          # Plot olig. so that 1 unit is NOT same in all (if == 1)
save_drw= 0          # Saves the schemes of the oligomers

sel_fA  = 0.06       # fA at which to plot FRET(stoich)
subdiv  = 4          # Resolution on x axis of the final traces is 1/subdiv

#-------------------------------------------------------------------------
finalE = [184]
for N in stoich:
    # Geometrical calculations

    Cn   = r_mm/(2*np.sin(np.pi/N))        # Distance to the center
    Cn   = np.sqrt((Cn+roff*np.cos(aloff))\
           **2+(roff*np.sin(aloff))**2)   # Distance to center from fluorophore
    ri   = [0]              # Distances from 0 to i, calculated in the next loop
    ralf = [0]

    for i in range(1,N):
        ri.append(2*Cn*np.sin((np.pi*i)/N))
        ralf.append(2*np.pi*(i)/N)

#=========================================================================
# Plot of the oligomers

    x    = []              # Stores x coordinates of the poligon
    y    = []              # Stores y cooridnates of the poligon

    for j in ralf:         # Loop to calculate x,y coordinates
        if rel_siz == 1:
            x.append(np.cos(j)*Cn)
            y.append(np.sin(j)*Cn)
        else:
            x.append(np.cos(j)*Cn)
            y.append(np.sin(j)*Cn)

    x.append(x[0])         # Adds first to have the last line in the diagram
    y.append(y[0])

    if N == max(stoich):
        xm   = max(x)*1.2  # Adjust the maximum values of the axis
        ym   = max(y)*1.2

        if xm > ym:
            ym = xm
        else:
            xm = ym

        if ym < 0.02:
            ym = 1.2
            xm = ym

    fig  = plt.figure(figsize = [6,6])     # Creates the plot

    plt.plot(x,y, 'k:')                    # Plots the exterior line
    plt.plot(x,y, 'o', markersize = 10, color = 'none', \
             mec = 'k', mew = 2)           # Plots the points in the vertices

    for j in range(1,int(N/2+1)):          # Loop that plots the non-symmetric ri and
the values of the distances
        plt.plot([x[0],x[j]],[y[0],y[j]],'b--', lw = 2, dashes = [5,2*j])
        if labs == 1:
            plt.text((x[0]+x[j]*1.3)/2,(y[0]+y[j]*1.25)/2,\
                 'r'+str(j)+' = '+str(ri[j])[:5], fontsize = 12, color = 'b')

    plt.plot([x[N-1],0],[y[N-1],0],'r-.', lw = 2)   # Plot of the line to the center
    if labs_c == 1:
        plt.text(x[N-1]/2,y[N-1]*1.1/2,'$C_n $= '+str(Cn)[:5]+' Å',\
             fontsize = 15, color = 'r')           # Plot of the distance to the center

    for j in range(len(x)-1):                      # Plot of subunit numbering
        plt.text(x[j]*1.4,y[j]*1.4,str(j+1), fontsize = 15)
```

```
    ax = plt.gca()                                  # Adjustments of the axis
    ax.set_xlim([-xm,xm])
    ax.set_ylim([-ym,ym])
    ax.axis('off')

    if save_drw == 1:
        plt.savefig(str(N)+'mer_Distances.png',\
                            transparent = True,dpi = 150)
        plt.savefig(str(N)+'mer_Distances.pdf',dpi = 150)
    if plotter == 1:
        plt.show()
    plt.close()

#=====================================================================
# Combinatorial calculations
# We consider that a donor is always placed at a fixed position (1) of the oligomer.
That way, redundances due to rotational symmetry are avoided

    combs = {}          # Dict. for the combinations. Name is COMBinationS

    for D in range(1,N+1):     # Loop that creates "all" the combinations
        combs[D] = {}  # Dict. for all the combinations for each number of Ds

        if D == 1:   # The possible donor combinations, NOT having 1 fixed
            d = list(cmb(range(0,1),D))
        elif D == N:
            d = tuple(range(N))
            combs[D][0] = d
        else:
            d = list(cmb(range(0,N),D))
# Combinations of A, removes the redundances, inforces the "1 fixed" rule
        for A in range(1,N-D+1):
            combs[D][A] = []
            a = list(cmb(range(N),A))
            for i in d:
                for m in a:
                    if 0 in i:
                        U = True
                        for j in i:
                            if j not in m:
                                continue
                            else:
                                U = False
                        if U:
                            combs[D][A].append((i,m))

    ck = list(combs.keys())
    for i in ck:      # Loop to get the combinations for the donors if A = 0
        if i < N:
            varl = []
            vark = list(combs[i].keys())
            for j in vark:
                if j == max(ck)-i:
                    for k in combs[i][j]:
                        if type(k) is tuple:
                            varl.append(tuple(k[0]))
                    combs[i][0] = varl

    combs[0] = {}
    for i in ck:            # Loop to get the combinations of A when D = 0
        combs[0][i] = combs[i][0]

    combs[0][0] = ['none']  # Definition, D & A = 0, all are empty

    ck = list(combs.keys()) # Update of the dict. key list

    if breakdown == 1:
        suma = 0            # Counting combinations produced; check point
        for i in ck:
            for j in combs[i]:
```

```
                if type(combs[i][j]) is list:
                    print(i, 'D ',j,'A ->\t',\
                          len(combs[i][j]),'\tcombinations')
                    suma += len(combs[i][j])
                else:
                    print(i, 'D ',j,'A ->\t 1\tcombinations')
                    suma += 1

        print('Total    ->\t',suma,'combinations\n')

#=============================================================================
    rate_comp = {}          # Stores transfer rates for each configuration
    for i in ck:
        rate_comp[i] = {}
        for j in combs[i]:
            rate_comp[i][j] = []
            for k in combs[i][j]:
                if i != ck[-1]:
                    if type(k) is tuple:
# This "if" calculates them for the combinations that A != 0
                        if type(k[0]) is tuple:
                            rates = 0
                            for m in k[1]:
                                rates += ktd*(R0DA/ri[m])**6
                            for m in k[0]:
# This "if" takes into account D-D transfer, if it is possible (D>1)
                                if m != 0:
                                    rates += ktd*(R0DD/ri[m])**6
                            rate_comp[i][j].append(rates)
                        if type(k[0]) is not tuple:   # Same for A = 0
                            rates = 0
                            for m in k:
                                if m != 0:
                                    rates += ktd*(R0DD/ri[m])**6
                            rate_comp[i][j].append(rates)

    rates = 0
    if N > 2:
        for i in ck:    # Same for D = N
            rates += ktd*(R0DD/ri[m])**6
        rate_comp[N][0].append(rates)

#_____________________________________________________________
    E_vals = {}

    for i in ck:
        E_vals[i] = {}
        for j in rate_comp[i]:
            E = 0
            rounds = 0
            for k in rate_comp[i][j]:
                E += k/(k+ktd)
                rounds += 1
            if rounds != 0:
                E_vals[i][j] = []
                E_vals[i][j].append(E/rounds)

#=============================================================================

    fact = {}
    for i in ck:
        fact[i] = np.math.factorial(i)

    emp_combs = {}
    for i in ck:
        emp_combs[i] = {}
        if i != 0:
            for j in E_vals[i]:
                emp_combs[i][j] = int(fact[N-1]/\
                                  (fact[i-1]*fact[j]*fact[N-i-j]))
```

```
    fA   = np.arange(0,subdiv*100-subdiv*fD,1)/(100*subdiv) # Fraction of A, usually
variable; max 100-fD

    finalE[N] = []

    for u in range(len(fA)):
        value  = 0
        wei_E = {}
        tot = 0

        for i in emp_combs:
            wei_E[i] = {}
            for j in emp_combs[i]:
                wei_E[i][j] = emp_combs[i][j]*(fD/100)**(i-1)\
                              *fA[u]**j*(1-(fD/100)-fA[u])**(N-i-j)
                tot += wei_E[i][j]

        for i in E_vals:
            for j in E_vals[i]:
                value += E_vals[i][j][0]*wei_E[i][j]

        finalE[N].append(value)

# Plot of the results
fig_Es = plt.figure(figsize = [6,6])
for N in finalE:
    plt.plot(fA,finalE[N])

ax = plt.gca()
ax.set_xlim([0,1])
ax.set_ylabel('FRET Efficiency')
ax.set_ylim([0,1])
ax.set_xlabel('Fraction of acceptor')
ax.tick_params(axis = 'both',direction = 'in', top = True,right=True)

fA_plt = int(np.where(fA == sel_fA)[0])

fig_Egx = plt.figure(figsize = [4,4])
for N in finalE:
    plt.plot(N,finalE[N][fA_plt],'ko')

ax2 = plt.gca()
ax2.set_title('FRET efficiency at $f_A =$'+str(fA[fA_plt]))
ax2.set_ylabel('FRET efficiency')
ax2.set_xlabel('Stoichiometry')
ax2.tick_params(axis = 'both',direction = 'in', top = True,right=True)

# Export the results to a .txt file in the current folder
with open('Predicts.txt','w') as f:
    f.write('\t')
    for N in finalE:
        f.write(str(N)+'\t')
    f.write('\n')
    for i in range(len(finalE[2])):
        f.write(str(fA[i]).replace('.',',')+'\t')
        for N in finalE:
            f.write(str(finalE[N][i])[:7].replace('.',',')+'\t')
        f.write('\n')
```

11. ORIGINAL PUBLICATIONS

Paper I is reprinted with permission from Palacios-Ortega, J., García-Linares, S., Rivera-de-Torre, E., Gavilanes, J. G., Martínez-del-Pozo, A., & Slotte, J. P. (2017). **Differential effect of bilayer thickness on sticholysin activity**. *Langmuir*, 33(41), 11018-11027.
https://doi.org/10.1021/acs.langmuir.7b01765

Paper II is reprinted with permission from Palacios-Ortega, J., García-Linares, S., Rivera-de-Torre, E., Gavilanes, J. G., Martínez-del-Pozo, Á., & Slotte, J. P. (2019). **Sticholysin, sphingomyelin, and cholesterol: a closer look at a tripartite interaction**. *Biophysical journal*, 116(12), 2253-2265.
https://doi.org/10.1016/j.bpj.2019.05.010

Paper III is reprinted with permission from Palacios-Ortega, J., Rivera-de-Torre, E., Gavilanes, J. G., Slotte, J. P., & Martínez-del-Pozo, Á. (2020). **Evaluation of different approaches used to study membrane permeabilization by actinoporins on model lipid vesicles**. *Biochimica et Biophysica Acta (BBA)-Biomembranes*, 1862(9), 183311.
https://doi.org/10.1016/j.bbamem.2020.183311

Paper IV is reprinted with permission from Palacios-Ortega, J., Rivera-de-Torre, E., García-Linares, S., Gavilanes, J. G., Martínez-del-Pozo, Á., & Slotte, J. P. (2021). **Oligomerization of Sticholysins from Förster Resonance Energy Transfer**. *Biochemistry*, 60(4), 314-323.
https://pubs.acs.org/doi/abs/10.1021/acs.biochem.0c00840

LANGMUIR Article
Cite This: Langmuir 2017, 33, 11018-11027 pubs.acs.org/Langmuir

Differential Effect of Bilayer Thickness on Sticholysin Activity

Juan Palacios-Ortega,[†,‡] Sara García-Linares,[†,‡] Esperanza Rivera-de-Torre,[†] José G. Gavilanes,[†] Álvaro Martínez-del-Pozo,*[,†] and J. Peter Slotte*[,‡]

[†]Departamento de Bioquímica y Biología Molecular I, Universidad Complutense, Madrid 28040, Spain
[‡]Biochemistry, Faculty of Science and Engineering, Åbo Akademi University, 20500 Turku, Finland

Supporting Information

ABSTRACT: In this study, we examined the influence of bilayer thickness on the activity of the actinoporin toxins sticholysin I and II (StnI and StnII) at 25 °C. Bilayer thickness was varied using dimonounsaturated phosphatidylcholine (PC) analogues (with 14:1, 16:1, 18:1, 20:1, and 22:1 acyl chains). In addition, *N*-14:0-sphingomyelin (SM) was always included because StnI and StnII are SM specific. Cholesterol was also incorporated as indicated. In cholesterol-free large unilamellar vesicles (LUVs) the PC:SM molar ratio was 4:1, and when cholesterol was included, the complete molar ratio was 4:1:0.5 (PC:SM:cholesterol, respectively). Stn toxins promote bilayer leakage through pores formed by oligomerized toxin monomers. Initial calcein leakage was moderately dependent on bilayer PC acyl chain length (and thus bilayer thickness), with higher rates observed with di-16:1 and di-18:1 PC bilayers. In the presence of cholesterol, the maximum rates of calcein leakage were observed in di-14:1 and di-16:1 PC bilayers. Using isothermal titration calorimetry to study the Stn−LUV interaction, we observed that the bilayer affinity constant (K_a) peaked with LUVs containing di-18:1 PC, and was lower in shorter and longer PC acyl chain bilayers. The presence of cholesterol increased the binding affinity approximately 30-fold at the optimal bilayer thickness (di-18:1-PC). We conclude that bilayer thickness affects both functional and conformational aspects of Stn membrane binding and pore formation. Moreover, the length of the actinoporins' N-terminal α-helix, which penetrates the membrane to form a functional pore, appears to be optimal for the membrane thickness represented by di-18:1 PC.

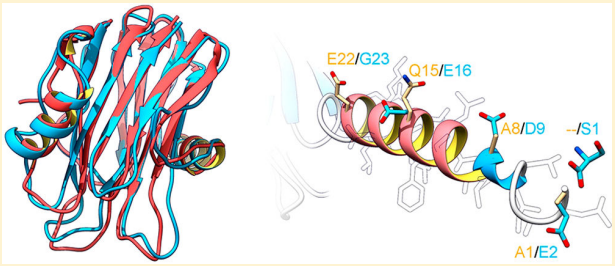

Lipid bilayers are one of the few structures found in all known living organisms. They provide the compartmentalization required for regulated molecular interactions. They also form the boundary that constitutes the first line of cellular defense against extracellular compounds. Because of this extracellular exposure, all membrane components are subject to a very strong selective pressure.[1] If enough generations of a species experience a similar environment, all their constituents are optimized for specific tasks under those given conditions.

Bilayer thickness has been recognized as a key membrane property regulating the activity of intrinsic membrane proteins.[2,3] A mismatch in length between the hydrophobic part of a protein and hydrophobic thickness of the bilayer can cause conformational alterations in either or both of them: transmembrane protein segments may tilt or kink, and membrane lipids might stretch or fold in order to completely avoid either protein or lipid hydrophobic exposure. Rhodopsin, for example, is known to increase its helical content in the presence of thicker bilayers, but in doing so, its activity changes.[4−6] Another example is MscL, a mechanosensitive channel found in *Escherichia coli*. Conformational changes favor its opening in thin bilayers and its closure in thicker bilayers.[7,8] Protein sensitivity to bilayer thickness can be such that some proteins, such as DesK in *Bacillus subtilis*, detect thickness changes caused by temperature-dependent phase states of lipids.[9,10] Thus, the activities of many intrinsic proteins are dependent on bilayer thickness.

Because of their universality and exposure to extracellular compounds, lipid membranes are also an exceptional target for toxins. In fact, pore forming toxins (PFTs) are widely found in nature. One well-known example is the human membrane attack complex, a part of the complement system, which participates in the nonadaptive immune response.[11,12] Some other extensively studied examples are cytolysin A in *E. coli*, α-hemolysin in *Staphylococcus aureus*, lysenin in *Eisenia fetida*, or actinoporins in sea anemones. Actinoporins constitute a widely studied family of α-PFTs that comprise approximately 175 amino acids, and bind to lipid membranes via sphingomyelin (SM) recognition.[13−18] Their well-known three-dimensional water-soluble structure consists of a β-sandwich flanked by two α-helices, one of which is at the N-terminal end of the structure (Figure 1).[20−26] This helix is a key component because it extends and penetrates the membrane to form the functional pore. In fact, it displays longitudinal amphipathicity in order to

Received: May 26, 2017
Revised: September 20, 2017
Published: September 21, 2017

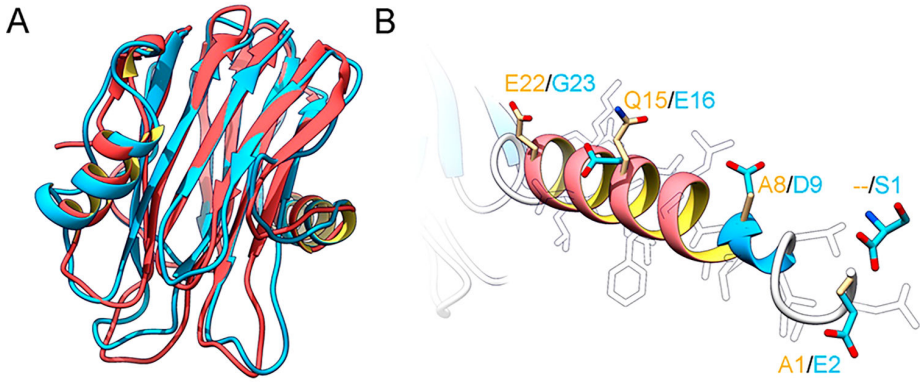

Figure 1. (A) Structural diagram showing the superposition of the three-dimensional structures of StnI (blue PDB 2KS4) and StnII (red, PDB 1GWY) water-soluble monomers. (B) Three-dimensional structure modeling of the extended N-terminal α-helix of both actinoporins. The side-chains of residues differing between both proteins are shown in color (blue for StnI and tan for StnII); other side-chain residues appear in white. Polar residues in blue would be facing the lumen of the pore. These representations were made using USCF Chimera.[19]

line the wall of the pore that is in contact with both the acyl carbon chains of lipids and the lumen.[27−32]

All actinoporins share at least ∼60% sequence identity,[22] but most relevant differences among them appear to be concentrated in the aforementioned N-terminal helix, which differs not only in sequence, but also in its length (Figure 1B). However, these differences are small, at no more than 1−3 residues in most cases. Considering that some proteins are capable of detecting bilayer thickness changes, these differences in actinoporin lengths might reflect the diversity of their targets in terms of bilayer thicknesses. Since actinoporin-producing sea anemones are widely distributed, each sea anemone−prey/attacker tandem would be exposed to different environmental conditions such as temperature and salinity. Consequently, slightly different bilayers could have been evolutionarily selected as optimal operating barriers in the potential prey/attacker, and best matching actinoporins in the coexisting anemones.

In the present study, we tested sticholysins I and II (StnI and StnII), two actinoporins produced by the Caribbean sea anemone *Stichodactyla helianthus*. StnI and StnII are quite similar, displaying a > 90% sequence identity and almost identical three-dimensional structure (Figure 1A). However, they show distinct hemolytic activity and differences in the hydrophobic character of their N-terminal α-helices.[33] In addition, the StnI α-helix is one residue longer (Figure 1B). Both actinoporins were assayed against model lipid bilayers of different thicknesses. Dimonounsaturated acyl chain-phosphatidylcholines (D(X)PC), where X indicates the variable acyl chain, were employed as the main component affecting bilayer thickness. We used 14:0-SM to facilitate membrane recognition by the actinoporins. We specifically selected 14:0-SM to ensure that no gel phase was formed at the experimental temperature (T_m of 14:0-SM is 27 °C (data not shown), and experiments were carried out at 25 °C). We also evaluated the effect of cholesterol in these systems, since cholesterol is also known to affect bilayer thickness.[34] Interactions between StnI−StnII and bilayers were assessed in terms of the ability of the sticholysins to bind to the bilayers and cause bilayer permeabilization, which was measured by calcein leakage. Surface plasmon resonance (SPR) and isothermal titration calorimetry (ITC) were used to study the Stn−bilayer interaction in more detail. We observed that both sticholysins could act more efficiently on bilayers prepared from di-16:1-PC or di-18:1-PC than on bilayers made from shorter or longer PC acyl chain analogues. Cholesterol markedly increased the affinity of sticholysins for large unilamellar vesicles (LUVs), especially those prepared from di-18:1-PC.

MATERIALS AND METHODS

Materials. Calcein and cholesterol were obtained from Sigma-Aldrich (St. Louis, MO, USA). The following were obtained from Avanti Polar Lipids (Alabaster, AL, USA): 1,2-dimyristoleoyl-*sn*-glycero-3-phosphocholine (di-14:1-PC); 1,2-dipalmitoleoyl-*sn*-glycero-3-phosphocholine (di-16:1-PC); 1,2-dioleoyl-*sn*-glycero-3-phosphocholine (di-18:1-PC); 1,2-dieicosenoyl-*sn*-glycero-3-phosphocholine (di-20:1-PC); and 1,2-erucoyl-*sn*-glycero-3-phosphocholine (di-22:1-PC). We synthesized 14:0-SM from 14:0 fatty acid and lyso SM (Avanti Polar Lipids), with *N*,*N*′-dicyclohexylcarbodiimide (Sigma-Aldrich) as a catalyst.[35]

Steady-State Fluorescence Anisotropy Measurements. Steady-state fluorescence anisotropy measurements were performed on a SLM Aminco 8000 spectrofluorimeter (Aminco International, Inc., Rochester, NY) working in the T-format. Multilamellar bilayer vesicles were prepared using DPH (diphenylhexatriene) concentration of 1 mol %. The DPH anisotropy was measured in vesicles containing D(X)PC/14:0-SM 4:1 molar ratio or D(X)PC/14:0-SM/Chol 4:1:0.5 molar ratios. For DPH anisotropy measurements the emission and excitation slits were set to 4 nm. The temperature was controlled by a Peltier element with a temperature probe submerged in the cell of reference. The samples were heated from 10 to 50 °C constantly stirred. DPH was excited at 360 nm and the emission was detected at 430 nm. The anisotropy was calculated as described in Lakowicz.[36]

Calcein Release from LUVs. Calcein-entrapped LUVs were prepared by extrusion through 200 nm polycarbonate filters at 60 °C. The composition of the employed LUVs is indicated in each figure. Calcein was encapsulated in Tris buffer (10 mM Tris, 140 mM NaCl, pH 7.4) containing 100 mM calcein. The detailed method for preparation of calcein-entrapped LUVs has been previously described.[37] The LUVs were used for permeabilization studies within 8 h of their preparation. The concentration of LUV-forming lipid molecules during the calcein-leakage experiments was 7.5 μM. The emission was recorded at 550 nm at a steady temperature (25 °C), as a function of time. The excitation wavelength was 480 nm. Fluorescence emission was measured using a PTI Quanta-Master spectrofluorimeter (Photon Technology International, Inc., Birmingham, NJ, USA) or an SLM Aminco 8000 spectrofluorimeter (Aminco International, Inc., Rochester, NY, USA). To confirm the absence of spontaneous leakage, we recorded the fluorescence emission of each sample for 3−5 min before adding the toxin. All samples generated a steady signal level, indicating intact vesicles. The percentage of calcein released was determined on the basis of maximum release induced by the addition

DOI: 10.1021/acs.langmuir.7b01765
Langmuir 2017, 33, 11018−11027

of 10 μL of 10% Triton X-100 (Sigma-Aldrich), to reach a final concentration of 0.05% v/v, which resulted in LUV disintegration.

Surface Plasmon Resonance Measurements. Stn−LUV association on coated gold chips was examined as previously described.[37] LUVs with the indicated lipid composition were prepared in Tris buffer by extrusion through 100 nm polycarbonate filters at 60 °C. The experiment was performed at 25 °C using a BioNavis SPR Navi 200 instrument (BioNavis Ltd., Tampere, Finland). The sensor gold chip was coated with a carboxymethylated dextran layer previously treated with *N*-hydroxysuccinimide and *N*-ethyl-*N*′-(dimethylaminopropyl)-carbodiimide to activate the surface for capturing phospholipid membranes. All solutions used for SPR were filtered through 0.2 μm membrane filters, and degassed with bath sonication before use. Tris buffer was used as the running buffer, at a flow rate of 5 μL/min. First, the chip surface was cleaned with two injections of 10 mM 3-[(3-cholamidopropyl)- dimethylammonio]-1-propanesulfonate (CHAPS). Then, extruded LUVs (0.5 mM lipid concentration) were applied on the surface (10 min injection), and the excess was removed by an injection of 50 mM NaOH (2 min). Bovine serum albumin (Sigma-Aldrich; 0.1 mg/mL, 2 min injection) was used to ensure that the chip was completely covered with LUVs. Finally, StnI or StnII (4.0 μM; 125:1 lipid:protein molar ratio) was applied for 10 min, after which buffer alone was injected for 2 min to study toxin dissociation. The chip was regenerated with CHAPS as in the beginning of the experiment.

K_{on} and K_{off} constants cannot be calculated for Stn−membrane systems by using SPR, since sticholysins cannot be substantially removed from supported bilayers. However, SPR can be used to estimate system saturation. In the present case, differential binding behavior does not reflect differential membrane recognition because the surface of all vesicles was approximately the same in every case. It is however possible to measure a maximum value of stoichiometry. Within that idea, the lipid:protein molar ratio was calculated using ng/cm^2 values once the SPR sensogram signal reached steady levels (580 s for lipid samples and 500 s for protein samples), given that the average molecular weight for each lipid mixture, as well the molecular weight of proteins, were known.

Isothermal Titration Calorimetry. The interaction between sticholysins and LUVs prepared from D(X)PC and 14:0-SM (4:1 molar ratio, 100 nm diameter) or D(X)PC, 14:0-SM, and cholesterol (4:1:0.5 molar ratio, 100 nm diameter) was measured by ITC as previously described,[28] using a VP-ITC calorimeter (Malvern MicroCal, Worcestershire, U.K.). Briefly, 1.0−4.0 μM protein solutions were titrated by injection of 20 μL aliquots of lipid suspensions (phospholipid concentration of 0.5−4.0 mM) at a constant temperature of 25 °C. The buffer employed consisted of 10 mM Tris, 100 mM NaCl, and 1 mM EDTA (pH 7.4). Binding isotherms were adjusted according to a model in which the protein binds to a membrane involving *n* lipid molecules, as described previously.[28]

RESULTS

Bilayer Characterization and Stn-Induced Calcein Release. In order to measure the permeabilization capacity of sticholysins in bilayers made of D(X)PC and 14:0-SM, we measured the release of calcein from dye-entrapped LUVs exposed to increasing concentrations of StnI and StnII. To confirm the absence of a gel phase in the bilayers examined at the experimental temperature, we measured the steady-state anisotropy of bilayers prepared from acyl chain PC analogues together with 14:0-SM (4:1 molar ratio). As shown in Figure S1, the DPH anisotropy/temperature function showed a smooth temperature-induced decline without apparent phase transition for all the bilayer compositions used in this study, whether cholesterol was present or not. Thus, we confirmed that no phase transition occurred in any of the D(X)PC/14:0-SM bilayers at 25 °C, the temperature at which all further experiments were conducted. The acyl chain order, as determined from DPH anisotropy measurements, was plotted as a function of PC acyl chain length at 25 °C, and the results shown in Figure S2 suggest that the acyl chain order increased linearly with increasing PC acyl chain length, and that the ordering effect of cholesterol was modest.

The initial release of calcein from LUVs containing PCs with variable acyl chain lengths was first determined for either StnI or StnII in the absence of cholesterol (Figure S3 shows raw data for calcein release during the first 100 s of toxin exposure, and Figure S4 show calculated initial release rates). We found that at saturating protein concentrations (protein/lipid ratio of 1/125) initial calcein release was fastest for di-16:1-PC and di-18:1-PC bilayers (Figure 2), and slower in bilayers having

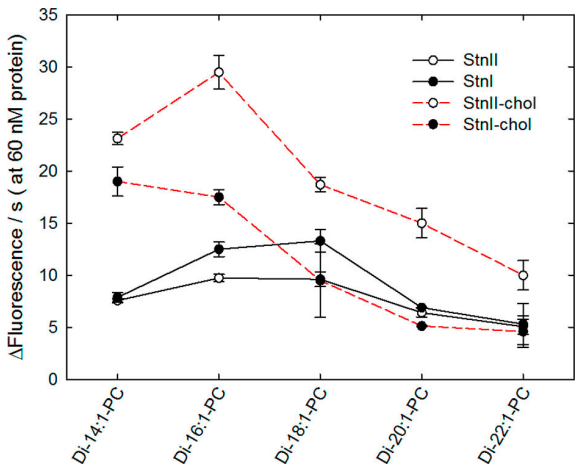

Figure 2. Initial rates of calcein release. The rates of calcein release for 60 nM StnI or StnII were calculated as normalized fluorescence units per second. Vesicles were composed of D(X)PC/14:0-SM at a 4:1 molar ratio, or D(X)PC/14:0-SM/cholesterol at a 4:1:0.5 molar ratio. Lipid concentration was 2.5 μM in all experiments. Values are averages ± standard error of the mean (SEM) for $n = 2$.

shorter (di-14:1-PC) or longer acyl chain PCs (di-20:1-PC and di-22:1-PC). This finding was true for both StnI and StnII, although initial calcein release rates were slightly higher with StnI than with StnII. These results suggest that bilayer permeabilization by sticholysins is affected by the target membrane thickness. Since cholesterol is known to both enhance bilayer permeabilization by sticholysins, and increase bilayer thickness (and acyl chain order), we next examined initial calcein release induced by StnI and StnII in D(X)PC/14:0-SM bilayers containing cholesterol (4:1:0.5 molar ratio). First, we noted that cholesterol increased the permeabilization activity of StnII more than that of StnI (Figure 2). This effect has been reported previously.[22] Second, we noted that for StnI, calcein leakage rate was approximately the same in di-14:1-PC and di-16:1-PC bilayers, and lower in longer acyl chain PC bilayers. For StnII, the highest bilayer permeabilization was seen with di-16:1-PC bilayers, followed by di-14:1-PC and the longer acyl chain PC bilayers (Figure 2). The initial calcein release data for different toxin concentrations are presented in Figure S4, and show similar trends as displayed in Figure 2 for 60 nM toxin. The average total calcein release percentage was 60−80% under the experimental conditions, and showed no correlation with PC acyl chain length (data not shown). Taken together, these results suggest that bilayer thickness moderately affected initial calcein release rates, and that cholesterol

DOI: 10.1021/acs.langmuir.7b01765
Langmuir 2017, 33, 11018−11027

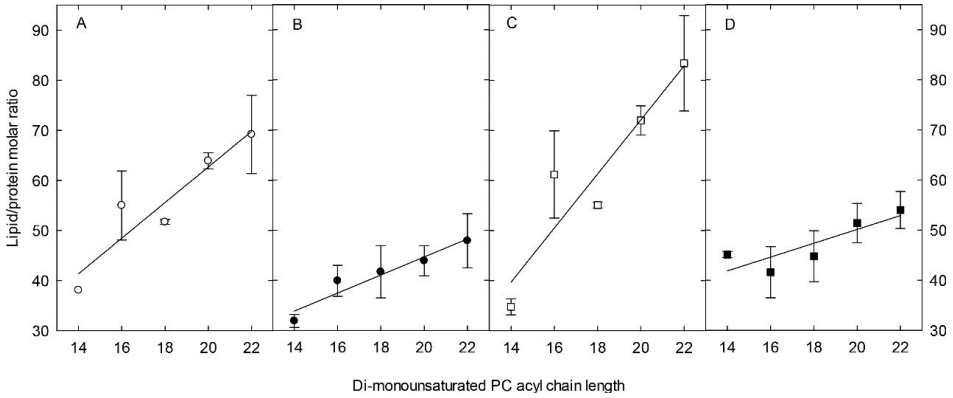

Figure 3. SPR data for Stn binding to supported vesicles. The lipid:protein molar ratio is plotted against the bilayer PC acyl chain length. The lipid:protein molar ratio was calculated using ng/cm^2 values once the SPR sensogram signal reached steady levels (580 s for lipid samples and 500 s for protein samples), given that the average molecular weight for each lipid mixture, as well the molecular weight of proteins, are known. Panels A and B show data for StnI, and panels C and D show data for StnII. Filled symbols depict conditions where LUVs also contained cholesterol.

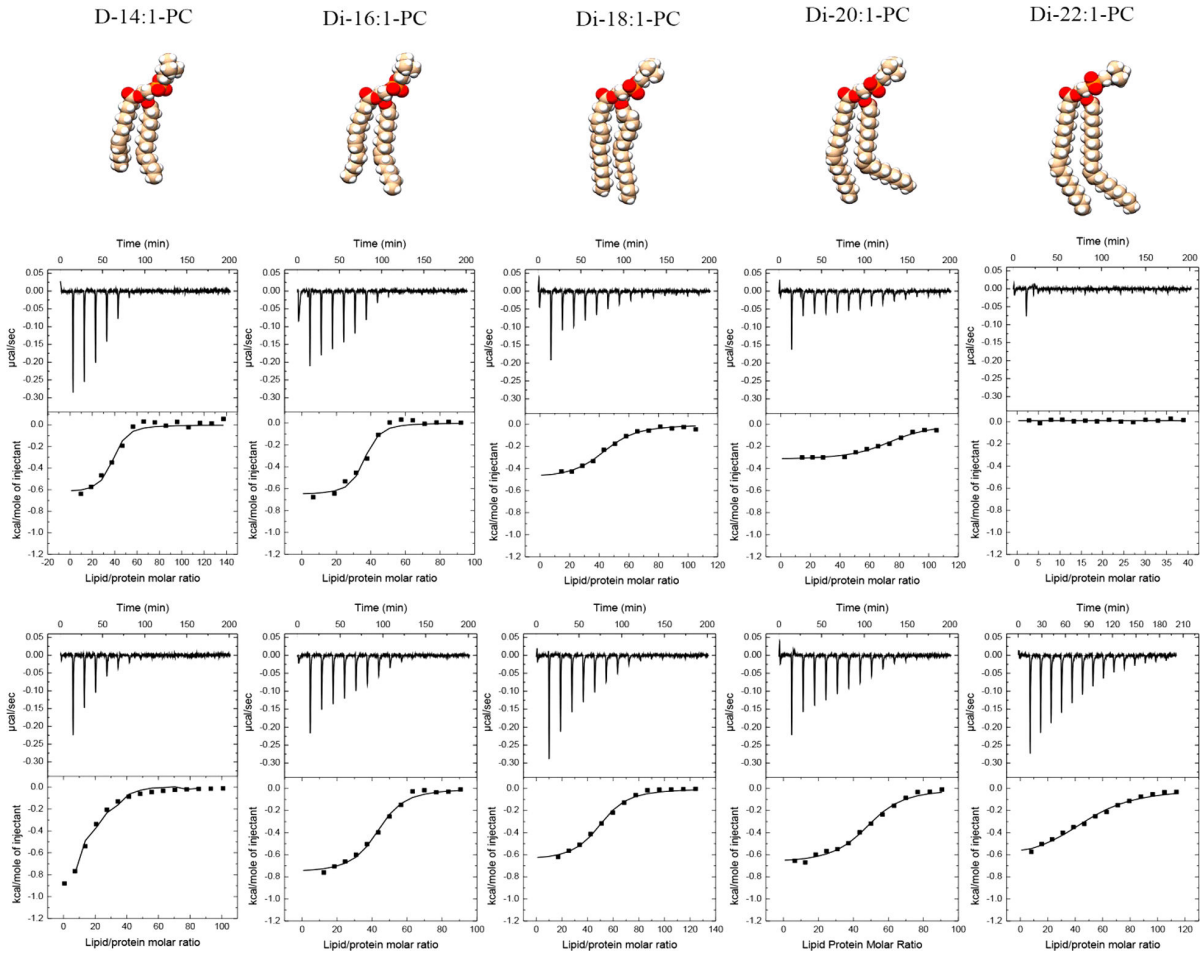

Figure 4. ITC results. Thermograms reflecting the heat released following the interaction of StnI (upper row) and StnII (lower row) with vesicles composed of the indicated PC species plus 14:0-SM at a 4:1 molar ratio.

appeared to affect the sensitivity of sticholysins to a small extent, without dramatically affecting the bilayer thickness optima.

Association of Stn with LUVs as Determined by SPR Measurements. To obtain further information about the interactions of StnI and StnII with lipid bilayers made from PCs with varying acyl chain length, we coated appropriately activated SPR gold chips with LUVs prepared from the acyl chain analogues of PCs together with 14:0-SM (4:1 molar ratio) in the absence or presence of cholesterol (4:1:0.5 molar ratio). The toxin-containing buffer (5 μM toxin) was allowed to flow over the SPR chip with LUVs, and the SPR response was

DOI: 10.1021/acs.langmuir.7b01765
Langmuir 2017, 33, 11018−11027

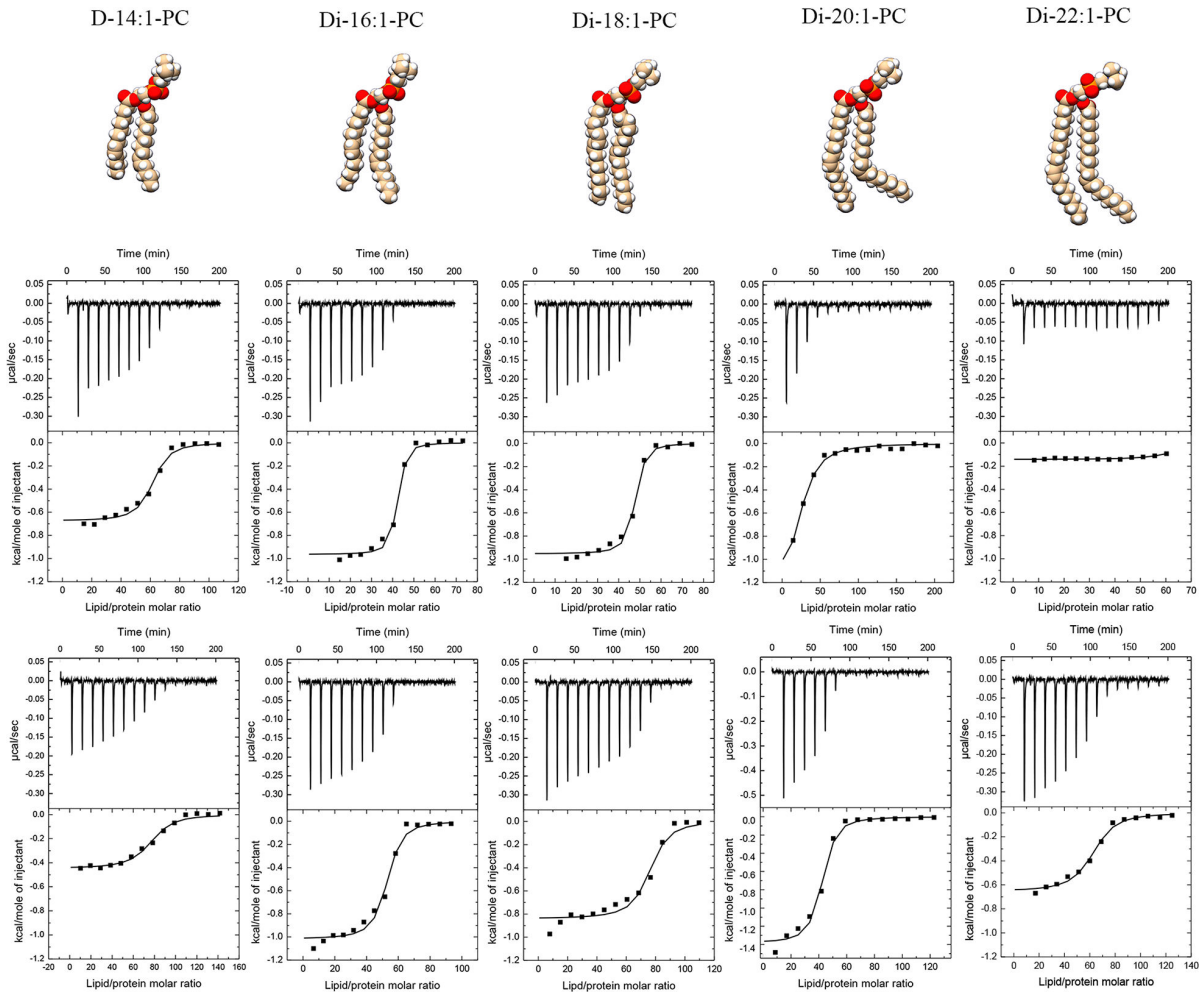

Figure 5. ITC results. Thermograms accounting for the heat released following the interaction of StnI (upper row) and StnII (lower row) with vesicles composed of the indicated PC species plus 14:0-SM and cholesterol at a 4:1:0.5 molar ratio.

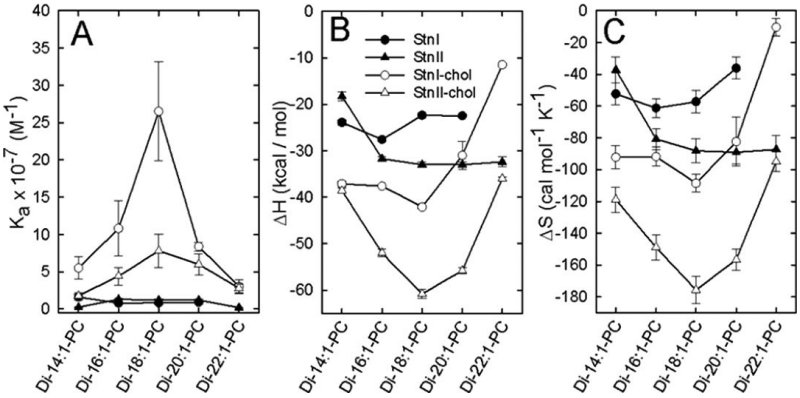

Figure 6. Affinity of Stn binding to LUVs with different compositions, and thermodynamic parameters for the associations. Panel A shows the K_a values were obtained from ITC measurements (see total data compilation in Table S3, curve identification as shown in panel B). In panel B the enthalpy of Stn/LUV association as a function of LUV composition is shown. In panel C the entropy of Stn/LUV association as a function of LUV composition is shown (line identifications as in panel B). Each value is the average ± standard deviation for n = 3.

registered at 25 °C as a function of time and LUV lipid composition. Before the actual toxin experiments were conducted, we ascertained that coverage of LUVs on the SPR chips was equal for all PC analogues (theoretical versus actual mass ratio on chips—see Table S1). The measured mass ratio matched the calculated theoretical mass ratio for all PC acyl chain analogues, and thus confirmed that each toxin was exposed to an equal amount of lipids during SPR analysis.

DOI: 10.1021/acs.langmuir.7b01765
Langmuir 2017, 33, 11018−11027

The SPR sensograms (Figure S5) show that after injection of StnI or StnII over the LUV-covered chips, the response curve showed saturation for most of the compositions after approximately 100−200 s of toxin flow (the exception was chips containing di-14:1-PC/14:0-SM and StnI in the absence or presence of cholesterol). From the sensograms, we calculated the lipid:protein ratios at the obtained steady state level (500 s), which are shown in Figure 3. According to these data, for the cholesterol-free bilayers (Figure 3A,C for StnI and StnII, respectively), the highest binding of toxin to LUV-covered chips was for the di-14:1-PC bilayers (lowest lipid:protein ratio), and the binding of toxin to LUVs decreased in a somewhat linear fashion as the bilayer PC acyl chain became longer. Both StnI and StnII behaved similarly. Cholesterol moderately enhanced toxin binding to LUV-covered SPR chips (Figure 3B,D for StnI and StnII, respectively). For detailed SPR results, please refer to Supporting Table S2. Taken together, the SPR data suggest that toxin binding to LUVs is linearly dependent on PC acyl chain length.

Thermodynamic Analysis of Stn/LUV Interaction. To complement the SPR analysis, we also performed ITC analysis of the interaction of StnI or StnII with LUVs containing D(X)PC/14:0-SM with cholesterol (4:1:0.5 molar ratio) or without it (4:1 molar ratio). In these experiments, LUVs were repeatedly injected into a toxin solution in the ITC cell, until toxin binding to LUVs became saturated. ITC thermograms are shown in Figures 4 and 5 for cholesterol-free and cholesterol-containing systems, respectively. The binding affinity (K_a) of toxins to LUVs made from different PC analogues is shown in Figure 6A as a function of toxin type and PC acyl chain length. Preliminary analysis of StnI binding to LUVs without cholesterol suggested that the K_a was slightly higher for LUVs containing di-14:1-PC than for bilayers made from longer acyl chain PCs (Figure 6A). Notably StnI interaction with LUVs prepared from di-22:1-PC in the cholesterol-free bilayers was below the detection limits of the experiment. In the absence of cholesterol, the highest K_a values for StnII binding were observed with LUVs prepared from di-18:1-PC to di-20:1-PC, and binding affinity was lower with di-14:1-PC and di-22:1-PC LUVs. In the presence of cholesterol in the bilayers, the binding affinity (K_a) increased markedly, with the highest K_a observed for LUVs containing di-18:1-PC, and lower values observed for shorter or longer acyl chain PC LUVs, irrespective of toxin type (Figure 6A). In addition, binding affinities in the presence of cholesterol were markedly higher with StnI than with StnII for all LUV types Both ΔH and ΔS contributions varied with PC acyl chain length. The binding enthalpy of StnI−LUV interactions in the absence of cholesterol was highest (exothermic) for the StnI−di-16:1-PC LUV interaction, and decreased for interactions with longer acyl chain PC LUVs (Figure 6B). The binding enthalpy for StnII−LUV interactions was lowest with the shortest PC analogue used, and increased substantially as the acyl chain length of the PCs increased. Addition of cholesterol to the LUVs made the ΔH more dependent on PC acyl chain length with regard to toxin binding, and the highest binding enthalpy for both toxins was observed with LUVs prepared from di-18:1-PC (Figure 6B). Changes in binding entropy (ΔS) for both toxins followed a very similar trend to that observed for binding enthalpy (ΔH) (Figure 6C), thus confirming that the toxin/LUV interactions were enthalpy-driven.[28] These results may seem unexpected for hydrophobic interactions, but, in addition to being the norm in actinoporins,[28] they have been observed for other proteins that penetrate into the membrane rather than remaining superficially adsorbed.[38] Accordingly, they have been interpreted as the measured binding enthalpy representing the van-der-Waals interaction energy between the hydrophobic residues of the proteins and the inner core of the lipid bilayer, while the loss of the hydration shell upon entering the bilayer would be compensated by an increased hydration of the lipid−water interface.[38] The information obtained from the ITC analysis of toxin binding to LUVs suggests that interactions with di-18:1-PC LUVs were favored, especially in the presence of cholesterol.

DISCUSSION

The general mechanism by which actinoporins (including StnI and StnII) interact with bilayer membranes to form pore structures is known.[18,39] These proteins remain stably folded and soluble in aqueous solution, but upon interaction with lipid membranes containing SM, they bind to the bilayer surface, extend their N-terminal α-helix, and become oligomeric integral membrane structures by inserting this amphipathic helix within the membrane core.[16,27−32,40−43] This results in the formation of a pore that leads to cell death by inducing osmotic shock. The Stn−SM interaction is stabilized by the binding of the SM headgroup to the POC (phosphocholine binding) site of the toxin; the interaction is further stabilized by the interaction of selected tyrosine and other amino acid residues with 2HN and 3OH of the SM interfacial region.[37,44,45] Most-accepted models explaining the mechanism of actinoporin pore formation assume that toxin dimerization after binding to bilayer membranes is an important intermediate step leading to the formation of different oligomeric species, including at least dimers, tetramers, and hexamers.[42,46−50] The structure of the final pore is not yet completely defined. The existence of a tetrameric toroidal structure has been shown by different methods, and this structure would explain why actinoporin pores are less stable than pores generated by other α-PFTs.[27] However, an octameric nontoroidal structure has also been crystallized,[26] although this "hybrid pore" would still be composed of both protein and lipids. Another aspect of the mechanism that requires further clarification is the state at which helices transfer to the bilayer and across the membrane to form a functional pore; the existence of nonconducive "pre-pore" structures remains controversial.[25,41,42] The existence of all these steps between membrane association and pore formation indicates that bilayer properties affect not only initial membrane binding and SM recognition, but also diffusion of monomers in the plane of the bilayer. The translocation of the N-terminal α-helix across the membrane bilayer is also likely to be influenced by lipid interactions and acyl chain length (i.e., bilayer thickness). Lastly, it is likely that fully functional pores are optimally formed only in bilayers of a specific thickness, which is dictated by the length and properties of the N-terminal α-helix.

For a better understanding of Stn−bilayer interactions as the bilayer PC acyl chains vary in length, we must first understand the properties of bilayers prepared from different dimonounsaturated PC analogues. As the PC chain length increases, so does the bilayer thickness[51] and acyl chain order (Figure S2). The relationship between thickness and acyl chain length is known to be linear.[51] However, the acyl chain length also potentially affects bilayer elasticity[52] and clearly affects acyl chain order (Figure S2), as more possibilities for attractive van der Waals

DOI: 10.1021/acs.langmuir.7b01765
Langmuir 2017, 33, 11018−11027

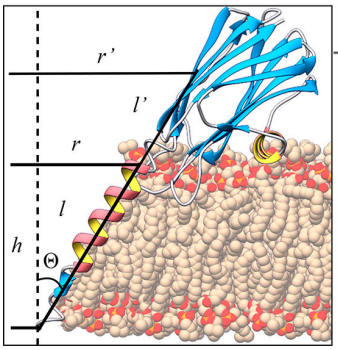

Pure lipid	Experimental h (Å)	Theoretical Θ	Estimated r' (Å)	Estimated nº of monomers/pore
Di-14:1-PC	31,00	46,46	41,9	10,2
Di-16:1-PC	34,50	39,94	37,1	9,0
Di-18:1-PC	38,00	32,39	30,9	7,5
Di-20:1-PC	41,50	22,75	22,3	5,4
Di-22:1-PC	45,00	0,00	0,0	0,0

Figure 7. Theoretical estimations of possible bilayer thickness-dependent pore parameters. In the scheme, h indicates the bilayer thickness between phosphate groups, r is the radius of the pore at the end of the helix, l is the theoretical length of the helix (1.5 Å/residue × 30 residues = 45 Å) and Θ is the angle formed by the helix and the bilayer normal. Also, $l + l'$, which was estimated manually on PDB 4TSY (FraC pore) using UCSF Chimera,[19] was 57.8 Å, which was used to calculate r'. In addition, the width of a monomer was estimated at the position indicated by the intersection of r' and l' (25.8 Å). These last data were used to calculate approximately the possible number of monomers per pore in each condition. Experimental values of h were from a previous report.[51] The experimental Θ value for StnII in dioleoyl-PC:SM:cholesterol 1:1:1 molar ratio bilayers is ~31°,[27] which is very close to the predicted value for di(18:1-PC bilayers), 32.39°. Furthermore, the prediction presented here for the number of proteins per pore in di-18:1-PC bilayers agrees with strong experimental evidence indicating that the preferred stoichiometry of the pore structure is eight monomers.

forces exists in longer chain PC bilayers than in shorter chain PC bilayers.[53] Furthermore, the position of the single *cis* double bond varies as the dimonounsaturated PC acyl chain length increases, changing from Δ^9 (14:1, 16:1, 18:1) to Δ^{11} (20:1) and Δ^{13} (22:1). The more distal the double bond is from the water−lipid interface, the more ordered the proximal acyl chain portion is likely to be.[54,55] We did not observe a gel−liquid crystalline phase transition in the di-22:1-PC bilayer system, indicating that the acyl chains did not become gel-like in packing. In bilayers with disordered acyl chains, cholesterol increases the acyl chain order because cholesterol−acyl chain interactions increase the ratio of trans:gauche isomers among the C−C single bonds.[56] Cholesterol is also known to favor interactions with saturated SM over interactions with unsaturated PCs,[57] and therefore a large fraction of cholesterol is probably associated with 14:0-SM in our cholesterol-containing bilayer systems. However, some cholesterol is still likely to interact with the monounsaturated PC analogues, and in doing so, increase the acyl chain order (especially for di-22:1-PC, Figure S2) and length.[58]

With these bilayer properties in mind, we can try to understand how they may affect Stn interactions with membranes, and subsequent pore formation. In the present study, we can assume that the chemical nature of the interfacial region is similar for all acyl chain PC analogues. However, the lateral distribution of 14:0-SM and the overall packing at the interface is likely to be different with LUVs prepared from different PC analogues (Figure S2). These differences are probably accentuated when cholesterol is included in the bilayers because 14:0-SM segregation is enhanced by cholesterol, and acyl chain packing is increased.[59] Furthermore, though still a matter of study, it is well-known that cholesterol facilitates the activity of actinoporins, as stated above and shown in this study, and that its presence is required for actinoporin insertion into the core of the membrane.[60] However, the presence of cholesterol increased the bilayer affinity (K_a) of Stn by a factor of approximately 30 (Figure 6A), but its effects on acyl chain order or bilayer thickness were only moderate. Thus, it is likely that the effects of cholesterol on the membrane binding and oligomerization of Stn are more specific, and unrelated to acyl chain order or bilayer thickness.

When bilayer permeabilization was measured using calcein release from dye-entrapped LUVs, typically only 60−80% of the LUV calcein content was released during a 20 min experiment (Figures S4 and 5), suggesting that pores are formed initially, but eventually become nonconducive. One cannot fully discard, however, nonhomogenous binding or the presence multilamellar vesicles to explain this effect. This behavior consistently takes place with actinoporins.[22,61] Therefore, measurement of initial calcein release might be more relevant for examining how Stns induce leakage in different types of LUVs because it contains information about both kinetic and pore-forming proficiency.[22] The initial leakage rates were affected by PC acyl chain length, with faster rates observed with intermediate acyl chain length PCs. This finding suggest that the transbilayer penetration of the N-terminal α-helix (required for permeabilization) was affected more by bilayer thickness than by bilayer acyl chain order. Compared with the cholesterol-free system, the presence of cholesterol in the LUVs caused maximal calcein leakage from shorter PC analogues. A simple interpretation would be that cholesterol affected bilayer thickness, and shifted the optimal bilayer thickness for Stn-induced calcein release from 16:1 and 18:1 chains in the absence of cholesterol to 14:1 and 16:1 chains in the presence of cholesterol. However, when the Stn−bilayer association was measured using SPR, we observed a linear relationship between Stn binding to supported LUVs and bilayer thickness, with less membrane binding to longer acyl chain PC (thicker) bilayers. SPR data showed no apparent preference of Stn binding to intermediate thickness bilayers, as suggested by calcein leakage experiments. However, the Stn−bilayer binding measured by SPR appeared to correlate with lateral packing in the bilayer, as affected by the PC acyl chains (Figure S2). However, calcein leakage is a functional assay, whereas SPR is not, and in the conditions used, SPR mostly reveals maximum possible toxin association with LUVs on the supported SPR chips. The immobilized LUVs may behave differently from freely diffusing LUVs in solution (as in calcein leakage), possibly explaining the different PC acyl chain length dependence of Stn−LUV

DOI: 10.1021/acs.langmuir.7b01765
Langmuir 2017, 33, 11018−11027

interactions. Interestingly, ITC analysis of toxin−LUV interactions revealed a clear relationship between K_a and LUV PC acyl chain length. Maximal K_a was seen with di-18:1-PC bilayers, in both the absence and presence of cholesterol. While the presence of cholesterol did not affect the K_a profile, it resulted in a marked increase in the absolute K_a, which is consistent with previous reports on the effect of cholesterol on Stn activity.[62] This finding further suggests that the effect of cholesterol on Stn−membrane association is not related to effects of cholesterol on membrane thickness or acyl chain order, which are linear with PC acyl chain length, but may instead relate to a variety of complex effects of cholesterol on the membrane and on/or SM recognition by Stn.[22,45,63] Since the highest K_a was observed with di-18:1-PC, this bilayer probably has the most optimal thickness and other properties to allow for best Stn binding, oligomerization, and subsequent pore formation. Since Stn pore formation appears to be affected by bilayer thickness, and since some calcein leakage was observed with all bilayer thicknesses used in the study, either pore assembly (oligomerization) or pore structure (number of monomers, or orientation of monomers in the pore) is affected by bilayer thickness, possibly in the manner depicted in Figure 7. According to the simple geometric calculations presented in Figure 7, a pore with approximately eight monomers (currently believed to be the monomer number in actinoporin pores that are more thermodynamically stable) could be formed in bilayers with a thickness formed by di-18:1-PC, consistent with our thermodynamic measurements. In thicker or thinner bilayers, the pore composition is likely to differ from the octamer structure, and the N-terminal α-helix angle with regard to the bilayer normal (Φ) would change and probably assume more unfavorable orientations.

SUMMARY AND CONCLUSIONS

In conclusion, we found that membrane binding (directly) and subsequent pore formation (indirectly) of Stn appears to be optimal in bilayers with a thickness represented by di-18:1-PC. This is not surprising considering that PCs with C18 acyl chain length dominate in most bilayer membranes of Stn targets. Interestingly, lipid content analysis of different Mediterranean fish revealed a high predominance of C18 and C16 fatty acids.[64] The relationship between Stn function and optimal bilayer thickness is likely to be a result of evolutionary pressure, and is probably manifested via the length of the crucial N-terminal α-helix.

ASSOCIATED CONTENT

Supporting Information

The Supporting Information is available free of charge on the ACS Publications website at DOI: 10.1021/acs.langmuir.7b01765.

DPH anisotropy versus temperature for bilayers prepared from all PC acyl chain analogues (Figure S1); DPH anisotropy at 25 °C as a function of PC acyl chain length (Figure S2); representative kinetic calcein release traces at 10 nM protein concentration (Figure S3); initial calcein release rates as a function of Stn concentration (Figure S4); calculation of theoretical and observed mass ratio of vesicles in SPR chips, as a function of PC acyl chain length (Table S1); SPR response information following Stn−LUV interaction (Table S2); SPR response curves of Stn binding to LUVs prepared from different PC acyl chain analogues, as a function of time (Figure S5); thermodynamic parameters from ITC experiments investigating Stn−LUV interactions (Table S3) (PDF)

AUTHOR INFORMATION

Corresponding Authors

*Address: Departamento de Bioquímica y Biología Molecular I, Universidad Complutense Madrid, Spain. E-mail: alvaromp@quim.ucm.es (A.M.-d.-P.).

*Address: Biochemistry, Faculty of Sciences and Engineering, Åbo Akademi University, Turku, Finland. E-mail: jpslotte@abo.fi (J.P.S.).

ORCID

Juan Palacios-Ortega: 0000-0002-4629-0221

Álvaro Martínez-del-Pozo: 0000-0003-0043-5939

J. Peter Slotte: 0000-0002-4850-5759

Notes

The authors declare no competing financial interest.

ACKNOWLEDGMENTS

We thank Anna Möuts, M.Sc., for help with some control experiments. This work was funded by grants from the Academy of Finland, the Sigrid Juselius Foundation, the Ella and Georg Ehrnrooth Foundation, and the Magnus Ehrnrooth Foundation to J.P.S. An FPU fellowship was granted to S.G.-L., and a UCM-Banco Santander fellowship was granted to E.R.-d.-T.

ABBREVIATIONS

di-14:1-PC, 1,2-dimyristoleoyl-*sn*-glycero-3-phosphocholine; di-16:1-PC, 1,2-dipalmitoleoyl-*sn*-glycero-3-phosphocholine; di-18:1-PC, 1,2-dioleoyl-*sn*-glycero-3-phosphocholine; di-20:1-PC, 1,2-dieicosenoyl-*sn*-glycero-3-phosphocholine; di-22:1-PC, 1,2-erucoyl-*sn*-glycero-3-phosphocholine; D(X)PC, phosphatidylcholine with variable acyls chain length (X); DPH, diphenylhexatriene; ITC, isothermal titration calorimetry; LUV, large unilamellar vesicle; 14:0-SM, myristoyl sphingomyelin; PFT, pore-forming toxin; SM, sphingomyelin; SPR, surface plasmon resonance; StnI, sticholysin I; StnII, sticholysin II; Stn, sticholysin; T_m, transition temperature

REFERENCES

(1) Sojo, V.; Dessimoz, C.; Pomiankowski, A.; Lane, N. Membrane proteins are dramatically less conserved than water-soluble proteins across the tree of life. *Mol. Biol. Evol.* **2016**, *33*, 2874−2884.

(2) Cybulski, L. E.; de Mendoza, D. Bilayer hydrophobic thickness and integral membrane protein function. *Curr. Protein Pept. Sci.* **2011**, *12*, 760−766.

(3) Nyholm, T. K.; Ozdirekcan, S.; Killian, J. A. How protein transmembrane segments sense the lipid environment. *Biochemistry* **2007**, *46*, 1457−1465.

(4) Baldwin, P. A.; Hubbell, W. L. Effects of lipid environment on the light-induced conformational changes of rhodopsin. 2. Roles of lipid chain length, unsaturation, and phase state. *Biochemistry* **1985**, *24*, 2633−2639.

(5) Botelho, A. V.; Huber, T.; Sakmar, T. P.; Brown, M. F. Curvature and hydrophobic forces drive oligomerization and modulate activity of rhodopsin in membranes. *Biophys. J.* **2006**, *91*, 4464−4477.

(6) Brown, M. F. Influence of nonlamellar-forming lipids on rhodopsin. *Curr. Top. Membr.* **1997**, *44*, 285−356.

DOI: 10.1021/acs.langmuir.7b01765
Langmuir 2017, 33, 11018−11027

(7) Chang, G.; Spencer, R. H.; Lee, A. T.; Barclay, M. T.; Rees, D. C. Structure of the MscL homolog from Mycobacterium tuberculosis: a gated mechanosensitive ion channel. *Science* **1998**, *282*, 2220−2226.
(8) Perozo, E.; Kloda, A.; Cortes, D. M.; Martinac, B. Physical principles underlying the transduction of bilayer deformation forces during mechanosensitive channel gating. *Nat. Struct. Biol.* **2002**, *9*, 696−703.
(9) Aguilar, P. S.; Hernandez-Arriaga, A. M.; Cybulski, L. E.; Erazo, A. C.; de Mendoza, D. Molecular basis of thermosensing: a two-component signal transduction thermometer in Bacillus subtilis. *EMBO journal* **2001**, *20*, 1681−1691.
(10) Mansilla, M. C.; Cybulski, L. E.; Albanesi, D.; de Mendoza, D. Control of membrane lipid fluidity by molecular thermosensors. *Journal of bacteriology* **2004**, *186*, 6681−6688.
(11) Merle, N. S.; Church, S. E.; Fremeaux-Bacchi, V.; Roumenina, L. T. Complement system part I−molecular mechanisms of activation and regulation. *Front. Immunol.* **2015**, *6*, 262.
(12) Merle, N.; Noe, R.; Halbwachs-Mecarelli, L.; Fremeaux-Bacchi, V.; Roumenina, L. Complement system part II: role in immunity. *Front. Immunol.* **2015**, *6*, 257.
(13) Alegre-Cebollada, J.; Oñaderra, M.; Gavilanes, J. G.; Martínez-del-Pozo, Á. Sea anemone actinoporins: the transition from a folded soluble state to a functionally active membrane-bound oligomeric pore. *Curr. Protein Pept. Sci.* **2007**, *8*, 558−572.
(14) Anderluh, G.; Macek, P. Cytolytic peptide and protein toxins from sea anemones (Anthozoa: Actiniaria). *Toxicon* **2002**, *40*, 111−124.
(15) Bakrac, B.; Gutierrez-Aguirre, I.; Podlesek, Z.; Sonnen, A. F.; Gilbert, R. J.; Macek, P.; Lakey, J. H.; Anderluh, G. Molecular determinants of sphingomyelin specificity of a eukaryotic pore-forming toxin. *J. Biol. Chem.* **2008**, *283*, 18665−18677.
(16) Bakrac, B.; Anderluh, G. Molecular mechanism of sphingomyelin-specific membrane binding and pore formation by actinoporins. *Adv. Exp. Med. Biol.* **2010**, *677*, 106−115.
(17) Macek, P. Polypeptide cytolytic toxins from sea anemones (*Actiniaria*). *FEMS Microbiol. Lett.* **1992**, *105*, 121−129.
(18) Rojko, N.; Dalla Serra, M.; Macek, P.; Anderluh, G. Pore formation by actinoporins, cytolysins from sea anemones. *Biochim. Biophys. Acta, Biomembr.* **2016**, *1858*, 446−456.
(19) Pettersen, E. F.; Goddard, T. D.; Huang, C. C.; Couch, G. S.; Greenblatt, D. M.; Meng, E. C.; Ferrin, T. E. UCSF Chimera—a visualization system for exploratory research and analysis. *J. Comput. Chem.* **2004**, *25*, 1605−1612.
(20) Athanasiadis, A.; Anderluh, G.; Macek, P.; Turk, D. Crystal structure of the soluble form of equinatoxin II, a pore-forming toxin from the sea anemone Actinia equina. *Structure* **2001**, *9*, 341−346.
(21) Castrillo, I.; Araujo, N. A.; Alegre-Cebollada, J.; Gavilanes, J. G.; Martínez-Del-Pozo, A.; Bruix, M. Specific interactions of sticholysin I with model membranes: an NMR study. *Proteins: Struct., Funct., Genet.* **2010**, *78*, 1957−1970.
(22) Garcia-Linares, S.; Rivera-de-Torre, E.; Morante, K.; Tsumoto, K.; Caaveiro, J. M.; Gavilanes, J. G.; Slotte, J. P.; Martínez-del-Pozo, Á. Differential effect of membrane composition on the pore−forming ability of four different sea anemone actinoporins. *Biochemistry* **2016**, *55*, 6630−6641.
(23) Hinds, M. G.; Zhang, W.; Anderluh, G.; Hansen, P. E.; Norton, R. S. Solution Structure of the Eukaryotic Pore-forming Cytolysin Equinatoxin II: Implications for Pore Formation. *J. Mol. Biol.* **2002**, *315*, 1219−1229.
(24) Mancheno, J. M.; Martin-Benito, J.; Martinez-Ripoll, M.; Gavilanes, J. G.; Hermoso, J. A. Crystal and electron microscopy structures of sticholysin II actinoporin reveal insights into the mechanism of membrane pore formation. *Structure* **2003**, *11*, 1319−1328.
(25) Mechaly, A. E.; Bellomio, A.; Gil-Cartón, D.; Morante, K.; Valle, M.; González-Mañas, J. M.; Guérin, D. M. Structural insights into the oligomerization and architecture of eukaryotic membrane pore-forming toxins. *Structure* **2011**, *19*, 181−191.
(26) Tanaka, K.; Caaveiro, J. M.; Morante, K.; González-Mañas, J. M.; Tsumoto, K. Structural basis for self-assembly of a cytolytic pore lined by protein and lipid. *Nat. Commun.* **2015**, *6*, 6337.
(27) Alegre-Cebollada, J.; Martinez del Pozo, A.; Gavilanes, J. G.; Goormaghtigh, E. Infrared spectroscopy study on the conformational changes leading to pore formation of the toxin sticholysin II. *Biophys. J.* **2007**, *93*, 3191−3201.
(28) Alegre-Cebollada, J.; Cunietti, M.; Herrero-Galan, E.; Gavilanes, J. G.; Martinez-Del-Pozo, A. Calorimetric scrutiny of lipid binding by sticholysin II toxin mutants. *J. Mol. Biol.* **2008**, *382*, 920−930.
(29) Anderluh, G.; Dalla Serra, M.; Viero, G.; Guella, G.; Macek, P.; Menestrina, G. Pore formation by equinatoxin II, a eukaryotic protein toxin, occurs by induction of nonlamellar lipid structures. *J. Biol. Chem.* **2003**, *278*, 45216−45223.
(30) García-Linares, S.; Richmond, R.; García-Mayoral, M. F.; Bustamante, N.; Bruix, M.; Gavilanes, J. G.; Martínez-Del-Pozo, A. The sea anemone actinoporin (Arg-Gly-Asp) conserved motif is involved in maintaining the competent oligomerization state of these pore-forming toxins. *FEBS J.* **2014**, *281*, 1465−1478.
(31) Kristan, K. C.; Viero, G.; Dalla Serra, M.; Macek, P.; Anderluh, G. Molecular mechanism of pore formation by actinoporins. *Toxicon* **2009**, *54*, 1125−1134.
(32) Malovrh, P.; Viero, G.; Serra, M. D.; Podlesek, Z.; Lakey, J. H.; Macek, P.; Menestrina, G.; Anderluh, G. A novel mechanism of pore formation: membrane penetration by the N-terminal amphipathic region of equinatoxin. *J. Biol. Chem.* **2003**, *278*, 22678−22685.
(33) Ros, U.; Rodriguez-Vera, W.; Pedrera, L.; Valiente, P. A.; Cabezas, S.; Lanio, M. E.; Garcia-Saez, A. J.; Alvarez, C. Differences in activity of actinoporins are related with the hydrophobicity of their N-terminus. *Biochimie* **2015**, *116*, 70−78.
(34) Yeagle, P. L. Modulation of Membrane Function by Cholesterol. *Biochimie* **1991**, *73*, 1303−1310.
(35) Cohen, R.; Barenholz, Y.; Gatt, S.; Dagan, A. Preparation and characterization of well defined D-*erythro* sphingomyelins. *Chem. Phys. Lipids* **1984**, *35*, 371−384.
(36) Lakowicz, J. R. *Principles of Fluorescence Spectroscopy*; Kluwer Academic/Plenum Publishers: New York, 1999.
(37) Maula, T.; Isaksson, Y. J. E.; Garcia-Linares, S.; Niinivehmas, S.; Pentikainen, O. T.; Kurita, M.; Yamaguchi, S.; Yamamoto, T.; Katsumura, S.; Gavilanes, J. G.; Martinez-Del-Pozo, A.; Slotte, J. P. 2NH and 3OH are crucial strctural requirements in sphingomyelin for sticholysin II binding and pore formation in bilayer membranes. *Biochim. Biophys. Acta, Biomembr.* **2013**, *1828*, 1390−1395.
(38) Seelig, J. Titration calorimetry of lipid-peptide interactions. *Biochim. Biophys. Acta, Rev. Biomembr.* **1997**, *1331*, 103−116.
(39) Garcia-Ortega, L.; Alegre-Cebollada, J.; Garcia-Linares, S.; Bruix, M.; Martinez-Del-Pozo, A.; Gavilanes, J. G. The behavior of sea anemone actinoporins at the water-membrane interface. *Biochim. Biophys. Acta, Biomembr.* **2011**, *1808*, 2275−2288.
(40) Bakrac, B.; Gutiérrez-Aguirre, I.; Podlesek, Z.; Sonnen, A. F.-P.; Gilbert, R. J.; Macek, P.; Lakey, J. H.; Anderluh, G. Molecular determinants of sphingomyelin specificity of a eukaryotic pore-forming toxin. *J. Biol. Chem.* **2008**, *283*, 18665−18677.
(41) Morante, K.; Bellomio, A.; Gil-Carton, D.; Redondo-Morata, L.; Sot, J.; Scheuring, S.; Valle, M.; Gonzalez-Manas, J. M.; Tsumoto, K.; Caaveiro, J. M. Identification of a Membrane-bound Prepore Species Clarifies the Lytic Mechanism of Actinoporins. *J. Biol. Chem.* **2016**, *291*, 19210−19219.
(42) Rojko, N.; Kristan, K. C.; Viero, G.; Zerovnik, E.; Macek, P.; Dalla Serra, M.; Anderluh, G. Membrane damage by an alpha-helical pore-forming protein, Equinatoxin II, proceeds through a succession of ordered steps. *J. Biol. Chem.* **2013**, *288*, 23704−23715.
(43) Tanaka, K.; Caaveiro, J. M.; Tsumoto, K. Bidirectional Transformation of a Metamorphic Protein between the Water-Soluble and Transmembrane Native States. *Biochemistry* **2015**, *54*, 6863−6866.
(44) Garcia-Linares, S.; Palacios-Ortega, J.; Yasuda, T.; Astrand, M.; Gavilanes, J. G.; Martinez-Del-Pozo, A.; Slotte, J. P. Toxin-induced pore formation is hindered by intermolecular hydrogen bonding in

DOI: 10.1021/acs.langmuir.7b01765
Langmuir 2017, 33, 11018−11027

sphingomyelin bilayers. *Biochim. Biophys. Acta, Biomembr.* **2016**, *1858*, 1189−1195.
(45) Palacios-Ortega, J.; Garcia-Linares, S.; Astrand, M.; Al Sazzad, M. A.; Gavilanes, J. G.; Martinez-Del-Pozo, A.; Slotte, J. P. Regulation of Sticholysin II-Induced Pore Formation by Lipid Bilayer Composition, Phase State, and Interfacial Properties. *Langmuir* **2016**, *32*, 3476−3484.
(46) Antonini, V.; Perez-Barzaga, V.; Bampi, S.; Penton, D.; Martinez, D.; Dalla Serra, S. M.; Tejuca, M. Functional characterization of sticholysin I and W111C mutant reveals the sequence of the actinoporin's pore assembly. *PLoS One* **2014**, *9*, e110824.
(47) Baker, M. A.; Rojko, N.; Cronin, B.; Anderluh, G.; Wallace, M. I. Photobleaching reveals heterogeneous stoichiometry for equinatoxin II oligomers. *ChemBioChem* **2014**, *15*, 2139−2145.
(48) Cosentino, K.; Ros, U.; Garcia-Saez, A. J. Assembling the puzzle: Oligomerization of alpha-pore forming proteins in membranes. *Biochim. Biophys. Acta, Biomembr.* **2016**, *1858*, 457−466.
(49) Rojko, N.; Cronin, B.; Danial, J. S.; Baker, M. A.; Anderluh, G.; Wallace, M. I. Imaging the lipid-phase-dependent pore formation of equinatoxin II in droplet interface bilayers. *Biophys. J.* **2014**, *106*, 1630−1637.
(50) Subburaj, Y.; Ros, U.; Hermann, E.; Tong, R.; Garcia-Saez, A. J. Toxicity of an alpha-pore-forming toxin depends on the assembly mechanism on the target membrane as revealed by single molecule imaging. *J. Biol. Chem.* **2015**, *290*, 4856−4865.
(51) Lewis, B. A.; Engelman, D. M. Lipid bilayer thickness varies linearly with acyl chain length in fluid phosphatidylcholine vesicles. *J. Mol. Biol.* **1983**, *166*, 211−217.
(52) Rawicz, W.; Olbrich, K. C.; McIntosh, T.; Needham, D.; Evans, E. Effect of chain length and unsaturation on elasticity of lipid bilayers. *Biophys. J.* **2000**, *79*, 328−339.
(53) Smaby, J. M.; Brockman, H. L.; Brown, R. E. Cholesterol's interfacial interactions with sphingomyelins and phosphatidylcholines: hydrocarbon chain structure determines the magnitude of condensation [published erratum appears in Biochemistry 1997 Feb 25;36(8):2338]. *Biochemistry* **1994**, *33*, 9135−42.
(54) Wang, Z. Q.; Lin, H. N.; Li, S.; Huang, C. H. Calorimetric studies and molecular mechanics simulations of monounsaturated phosphatidylethanolamine bilayers. *J. Biol. Chem.* **1994**, *269*, 23491−23499.
(55) Marsh, D. Thermodynamic analysis of chain-melting transition temperatures for monounsaturated phospholipid membranes: dependence on cis-monoenoic double bond position. *Biophys. J.* **1999**, *77*, 953−963.
(56) Stockton, G. W.; Smith, I. C. A deuterium nuclear magnetic resonance study of the condensing effect of cholesterol on egg phosphatidylcholine bilayer membranes. I. Perdeuterated fatty acid probes. *Chem. Phys. Lipids* **1976**, *17*, 251−263.
(57) Lonnfors, M.; Doux, J. P.; Killian, J. A.; Nyholm, T. K.; Slotte, J. P. Sterols Have Higher Affinity for Sphingomyelin than for Phosphatidylcholine Bilayers even at Equal Acyl-Chain Order. *Biophys. J.* **2011**, *100*, 2633−2641.
(58) Kucerka, N.; Nieh, M. P.; Pencer, J.; Sachs, J. N.; Katsaras, J. What determines the thickness of a biological membrane. *Gen. Physiol. Biophys.* **2009**, *28*, 117−125.
(59) Engberg, O.; Nurmi, H.; Nyholm, T. K.; Slotte, J. P. Effects of cholesterol and saturated sphingolipids on acyl chain order in 1-palmitoyl-2-oleoyl-sn-glycero-3-phosphocholine bilayers–a comparative study with phase-selective fluorophores. *Langmuir* **2015**, *31*, 4255−4263.
(60) Wacklin, H. P.; Bremec, B. B.; Moulin, M.; Rojko, N.; Haertlein, M.; Forsyth, T.; Anderluh, G.; Norton, R. S. Neutron reflection study of the interaction of the eukaryotic pore-forming actinoporin equinatoxin II with lipid membranes reveals intermediate states in pore formation. *Biochim. Biophys. Acta, Biomembr.* **2016**, *1858*, 640−652.
(61) Rivera-de-Torre, E.; Garcia-Linares, S.; Alegre-Cebollada, J.; Lacadena, J.; Gavilanes, J. G.; Martinez-Del-Pozo, A. Synergistic Action of Actinoporin Isoforms from the Same Sea Anemone Species Assembled into Functionally Active Heteropores. *J. Biol. Chem.* **2016**, *291*, 14109−14119.
(62) De Los Rios, V.; Mancheno, J. M.; Lanio, M. E.; Onaderra, M.; Gavilanes, J. G. Mechanism of the leakage induced on lipid model membranes by the hemolytic protein sticholysin II from the sea anemone Stichodactyla helianthus. *Eur. J. Biochem.* **1998**, *252*, 284−289.
(63) Pedrera, L.; Gomide, A. B.; Sanchez, R. E.; Ros, U.; Wilke, N.; Pazos, F.; Lanio, M. E.; Itri, R.; Fanani, M. L.; Alvarez, C. The presence of sterols favors sticholysin I-membrane association and pore formation regardless of their ability to form laterally segregated domains. *Langmuir* **2015**, *31*, 9911−9923.
(64) Prato, E.; Biandolino, F. Total lipid content and fatty caid composition of commercially important fish species from the Mediterranean, Mar Grande Sea. *Food Chem.* **2012**, *131*, 1233−9.

DOI: 10.1021/acs.langmuir.7b01765
Langmuir 2017, 33, 11018−11027

Supplemental File

DIFFERENTIAL EFFECT OF BILAYER THICKNESS ON STICHOLYSIN ACTIVITY

Juan Palacios-Ortega[†,‡], Sara García-Linares[†,‡], Esperanza Rivera-de-Torre[†], José G. Gavilanes[†], Álvaro Martínez-del-Pozo[†], J. Peter Slotte[‡].

[†]Departamento de Bioquímica y Biología Molecular I, Universidad Complutense Madrid (Spain).

[‡]Biochemistry, Faculty of Science and Engineering, Åbo Akademi University, Turku, Finland.

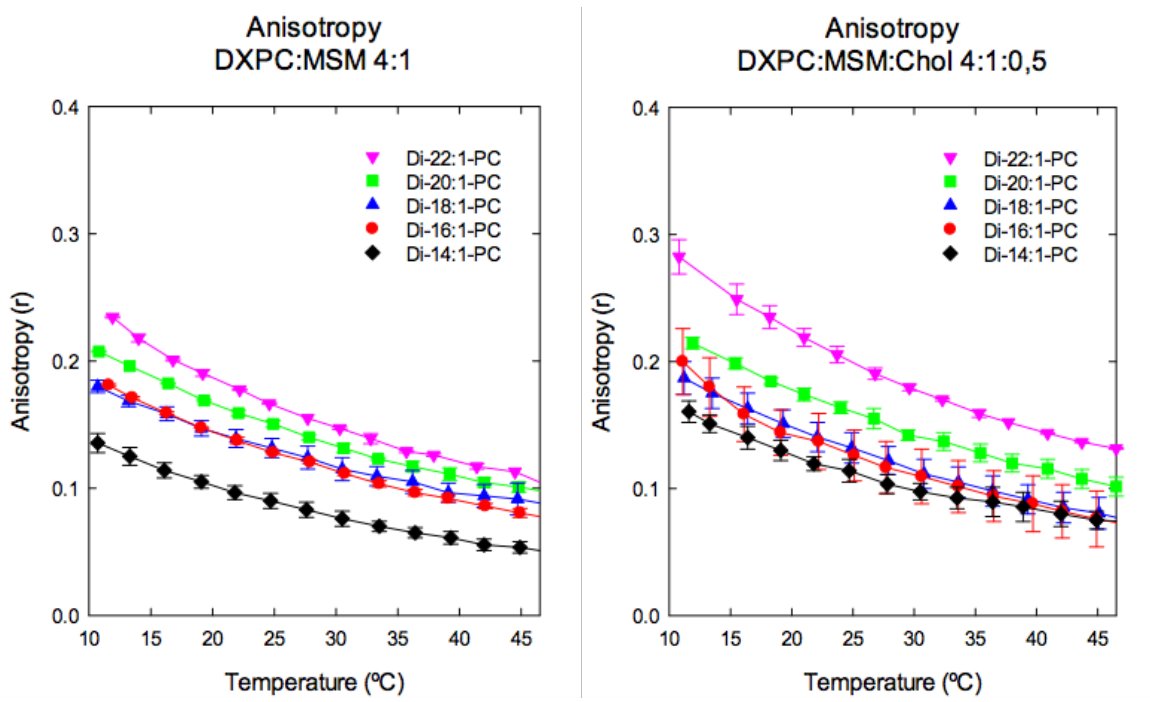

Figure S1. DPH anisotropy measurement for bilayers composed of D(X)PC, 14:0-SM, and cholesterol at indiated proportions. Anisotropy was recorded as a function of temperature between 10 and 45 ^{o}C. Each value is the average $\pm$ SEM for n=2.

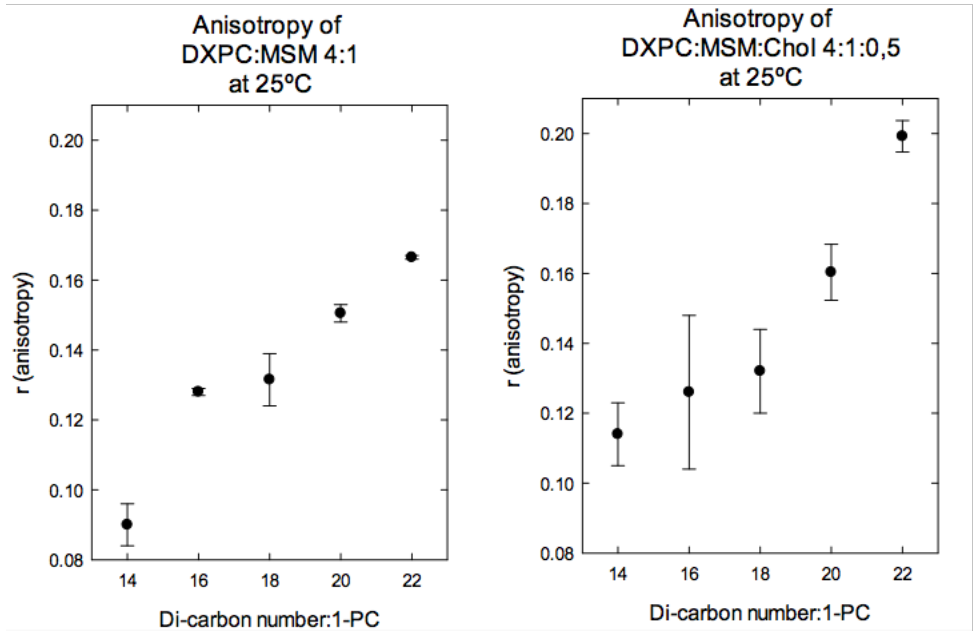

Figure S2. The anisotropy values measured at 25 ^{o}C for each bilayer composition as a function of PC acyl chain length. Anisotropy values from cholesterol-free bilayers are shown in the left panel, and values from bilayers containing cholesterol shown in the right panel, as indicated. Each value is the average $\pm$ SEM for n=2.

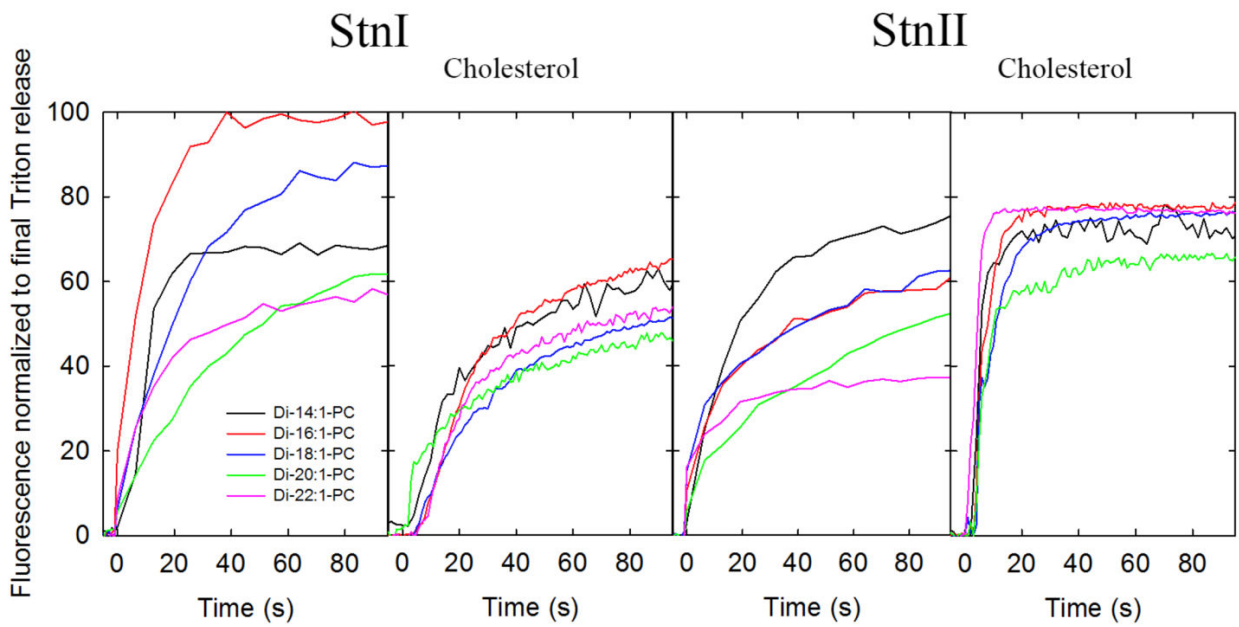

Figure S3. Representative calcein release kinetic traces at 10 nM toxin during the first 100 s of the experiments. Toxin employed and cholesterol presence are indicated in the figure. Black lines indicate vesicles containing Di-14:1-PC; red lines, Di-16:1-PC; blue lines, Di-18:1-PC; green lines, Di-20:1-PC; pink lines, Di-22:1-PC

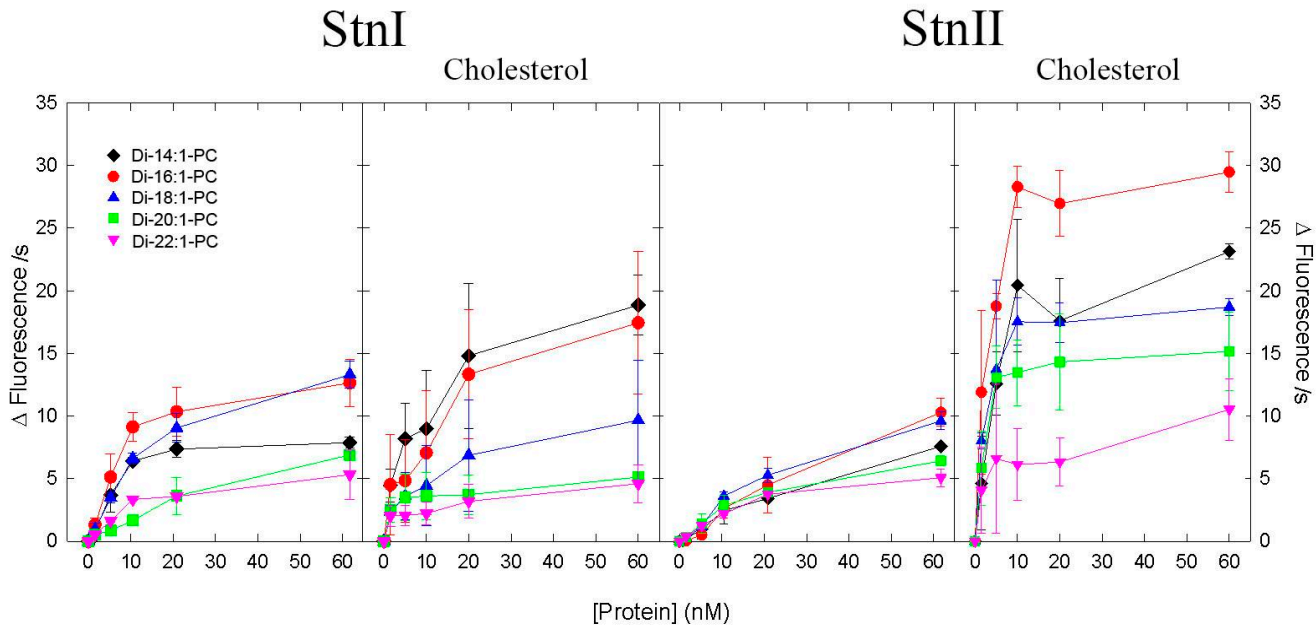

Figure S4. Initial calcein release rates. The calcein release rates were calculated as normalized units of fluorescence per second. Vesicles were composed of D(X)PC/14:0-SM 4:1 molar ratio, or D(X)PC/14:0-SM:chol 4:1:0.5 molar ratio were the presence of cholesterol is indicated. Lipid concentration was 2.5 μM in all cases. Values are averages $\pm$ SEM from n=2.

Table S1. Calculations of the mass ratio of the vesicles. Analysis performed in order to confirm that the number of vesicles used in each assay was essentially constant, ruling out differential vesicle-to-chip binding due to different lipidic composition, as well as different sample concentration. This procedure was performed separately for the vesicles containing and lacking cholesterol. In each case, the theoretical mass ratio was calculated dividing the average M_W per lipid molecule of each mixture by the MW of the di-14:1-PC containing mixture. The same procedure, using ng of bound vesicles per cm^2, was used to estimate the experimental value. Each experimental value is average $\pm$ SEM for n=2.

Lipid mixture	Average MW per lipid (g/mol)	Theoretical mass ratio	SPR response at final time (580 s, ng/cm^2)	Experimental mass ratio
di-14:1-PC:14:1-SM 4:1	674.22	1.000	289.62 ± 2.05	1.00 ± 0.01
di-16:1-PC: 14:1-SM 4:1	719.10	1.067	301.56 ± 5.97	1.04 ± 0.02
di-18:1-PC: 14:1-SM 4:1	763.98	1.133	330.54 ± 8.85	1.14 ± 0.03
di-20:1-PC: 14:1-SM 4:1	808.42	1.199	350.71 ± 6.46	1.21 ± 0.02
di-22:1-PC: 14:1-SM 4:1	853.76	1.266	361.13 ± 5.41	1.25 ± 0.02
di-14:1-PC: 14:1-SM:chol 4:1:0.5	648.07	1.000	264.04 ± 2.00	1.00 ± 0.01
di-16:1-PC: 14:1-SM:chol 4:1:0.5	688.88	1.063	268.22 ± 3.37	1.02 ± 0.01
di-18:1-PC: 14:1-SM:chol 4:1:0.5	729.68	1.126	329.90 ± 0.16	1.25 ± 0.01
di-20:1-PC: 14:1-SM:chol 4:1:0.5	770.08	1.188	322.16 ± 1.32	1.22 ± 0.01
di-22:1-PC: 14:1-SM:chol 4:1:0.5	811.29	1.252	359.93 ± 6.57	1.36 ± 0.03

Table S2. SPR response to Stn binding. SPR responses of supported vesicles of the indicated composition exposed to a constant flow of solutions containing equal amounts of each of the toxins. Both lipid vesicles and Stn-bound curves allow for the estimation of the parameter n_{SPR}, which is the number of lipid molecules per protein monomer. Each value is average ± SEM for n = 2.

Lipid Composition	StnI		StnII	
	SPR response at 500 s (ng/cm^2)	n_{SPR}	SPR response at 500 s (ng/cm^2)	n_{SPR}
di-14:1-PC:14:1-SM 4:1	202.75 ± 12.14	38.1 ± 0.9	214.37 ± 11.16	34.8 ± 1.6
di-16:1-PC: 14:1-SM 4:1	164.73 ± 7.29	55.0 ± 6.8	145.85 ± 5.34	61.2 ± 8.7
di-18:1-PC: 14:1-SM 4:1	155.42 ± 12.89	51.7 ± 0.5	136.82 ± 8.94	55.1 ± 0.6
di-20:1-PC: 14:1-SM 4:1	125.41 ± 5.48	63.9 ± 1.6	109.11 ± 0.44	72.0 ± 2.9
di-22:1-PC: 14:1-SM 4:1	122.63 ± 12.90	69.2 ± 7.8	99.03 ± 9.71	83.4 ± 9.5
di-14:1-PC: 14:1-SM:chol 4:1:0.5	248.28 ± 2.18	31.9 ± 1.3	175.99 ± 5.03	45.1 ± 0.6
di-16:1-PC: 14:1-SM:chol 4:1:0.5	169.76 ± 3.66	39.9 ± 3.1	162.45 ± 6.66	41.6 ± 5.1
di-18:1-PC: 14:1-SM:chol 4:1:0.5	175.55 ± 3.32	41.7 ± 5.2	166.90 ± 0.15	44.8 ± 5.1
di-20:1-PC: 14:1-SM:chol 4:1:0.5	167.01 ± 3.14	43.9 ± 3.0	144.16 ± 4.51	51.4 ± 3.9
di-22:1-PC: 14:1-SM:chol 4:1:0.5	156.02 ± 0.07	47.9 ± 5.4	138.88 ± 0.53	54.0 ± 3.7

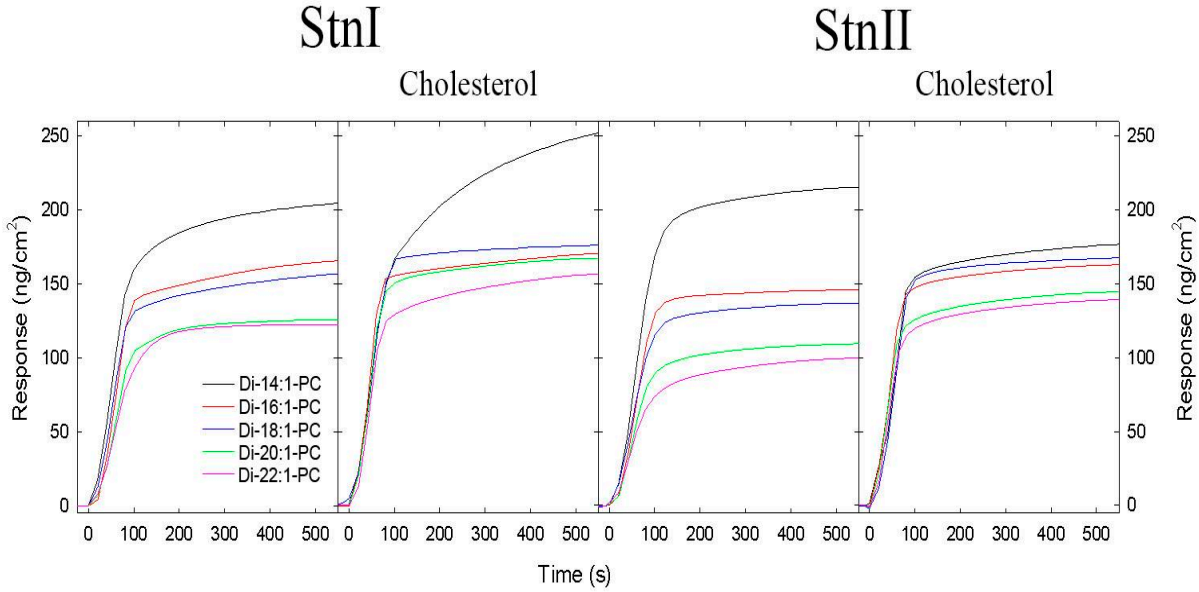

Figure S5. SPR response to Stns binding to supported vesicles. SRP sensograms of Stn binding to supported vesicles composed of D(X)PC/14:0-SM 4:1 molar ratio or D(X)PC/14:0-SM:chol 4:1:0.5 molar ratio. The acyl chain of the PC species, X, employed in each case is indicated in the figure. Curves are representative traces from two experiments.

Table S3. ITC results. Thermodynamic parameters for interaction of each Stn with vesicles composed of D(X)PC/14:0-SM 4:1 molar ratio and D(X)PC/14:0-SM:chol 4:1:0.5 molar ratio. Binding isotherms were adjusted to a previously described model in which each proteins bound to the membrane affects *n* lipid molecules. K_a is the affinity constant calculated as described in (1). The interaction between StnI and the di-22:1-PC/14:0-SM 4:1 molar ratio vesicles was weak and could not be measured within the values of parameter *c* (1 - 1000), being $c = (K_a\ [Protein])$, required for proper curve fitting. Each value average ± SEM for n=2.

	Toxin	PC species	[Lipid] (mM)	[Stn] (μM)	n_{ITC}	$K_a \times 10^{-7}$ (M^{-1})	ΔG (kcal / mol)	ΔH (kcal / mol)	ΔS (cal mol^{-1} K^{-1})
Without cholesterol	StnI	Di-14:1-PC	1.00	1.5	47.0 ± 1.2	1.6 ± 0.4	-7.8 ± 1.4	-23.9 ± 0.6	-52.3 ± 6.9
		Di-16:1-PC	0.65	1.5	34.0 ± 0.5	0.79 ± 0.08	-8.0 ± 1.4	-27.3 ± 0.4	-61.2 ± 6.0
		Di-18:1-PC	0.70	1.5	42.6 ± 1.0	0.82 ± 0.15	-7.3 ± 1.5	-22.4 ± 0.5	-57.2 ± 7.1
		Di-20:1-PC	0.72	1.5	69.5 ± 1.3	0.91 ± 0.25	-7.2 ± 1.4	-22.5 ± 0.4	-36.1 ± 7.0
		Di-22:1-PC	1.05	4.0	-	-	-	-	-
	StnII	Di-14:1-PC	0.70	1.5	24.3 ± 1.5	0.23 ± 0.05	-7.0 ± 1.1	-18.3 ± 1.0	-37.2 ± 8.1
		Di-16:1-PC	0.62	1.5	44.2 ± 0.6	1.3 ± 0.2	-7.7 ± 1.5	-31.7 ± 0.4	-80.8 ± 6.5
		Di-18:1-PC	0.75	1.5	45.2 ± 0.8	1.2 ± 0.2	-7.5 ± 1.5	-33.0 ± 0.6	-88.1 ± 7.5
		Di-20:1-PC	0.60	1.5	45.9 ± 0.8	1.2 ± 0.2	-7.5 ± 1.5	-33.0 ± 0.6	-89.0 ± 7.5
		Di-22:1-PC	1.38	3.6	45.4 ± 1.5	0.18 ± 0.03	-6.4 ± 1.5	-32.4 ± 1.1	-87.3 ± 8.7
With cholesterol	StnI	Di-14:1-PC	0.73	1.5	57.9 ± 0.9	5.5 ± 1.5	-8.3 ± 1.5	-37.1 ± 0.6	-92.1 ± 7.2
		Di-16:1-PC	0.77	1.5	41.2 ± 0.4	10.8 ± 3.7	-9.1 ± 1.5	-37.6 ± 0.3	-91.7 ± 6.1
		Di-18:1-PC	0.51	1.5	39.7 ± 0.3	26.5 ± 6.6	-9.4 ± 1.4	-42.1 ± 0.3	-108.5 ± 5.7
		Di-20:1-PC	0.93	1.5	22.9 ± 2.2	8.3 ± 0.6	-7.8 ± 1.3	-31.0 ± 3.0	-82.4 ± 15.4
		Di-22:1-PC	1.1	4.0	52.4 ± 0.9	3.0 ± 0.9	-8.0 ± 1.5	- 11.5 ± 0.2	-10.3 ± 5.7
	StnII	Di-14:1-PC	0.73	1.5	75.2 ± 1.2	1.8 ± 0.4	-7.6 ± 1.7	-38.6 ± 0.6	-118.9 ± 8.0
		Di-16:1-PC	0.62	1.5	49.9 ± 0.8	4.4 ± 1.2	-8.4 ± 1.5	-52.0 ± 0.8	-148.8 ± 8.0
		Di-18:1-PC	0.75	1.5	67.4 ± 1.1	7.8 ± 2.2	-8.4 ± 1.6	-60.8 ± 1.0	-175.7 ± 8.7
		Di-20:1-PC	0.84	1.5	37.8 ± 0.4	6.0 ± 1.4	-8.7 ± 1.4	-55.8 ± 0.6	-156.6 ± 6.8
		Di-22:1-PC	1.14	2	43.8 ± 0.5	2.8 ± 0.6	-8.3 ± 1.5	-36.0 ± 0.4	-94.9 ± 6.4

Reference:

1. Alegre-Cebollada,J., Cunietti, M., Herrero-Galán, E., Gavilanes,J.G., and Martínez-del-Pozo, A. Calorimetric scrutiny of lipid binding by sticholysin II toxin mutants, J Mol Biol, **2008**, 382 920-930.

Please cite this article in press as: Palacios-Ortega et al., Sticholysin, Sphingomyelin, and Cholesterol: A Closer Look at a Tripartite Interaction, Biophysical Journal (2019), https://doi.org/10.1016/j.bpj.2019.05.010

Biophysical *Journal*
Article

Biophysical Society

Sticholysin, Sphingomyelin, and Cholesterol: A Closer Look at a Tripartite Interaction

Juan Palacios-Ortega,[1,2] Sara García-Linares,[1] Esperanza Rivera-de-Torre,[1] José G. Gavilanes,[1] Álvaro Martínez-del-Pozo,[1,*] and J. Peter Slotte[2,*]
[1]Departamento de Bioquímica y Biología Molecular, Universidad Complutense, Madrid, Spain and [2]Biochemistry, Faculty of Science and Engineering, Åbo Akademi University, Turku, Finland

ABSTRACT Actinoporins are a group of soluble toxic proteins that bind to membranes containing sphingomyelin (SM) and oligomerize to form pores. Sticholysin II (StnII) is a member of the actinoporin family produced by *Stichodactyla helianthus*. Cholesterol (Chol) is known to enhance the activity of StnII. However, the molecular mechanisms behind this activation have remained obscure, although the activation is not Chol specific but rather sterol specific. To further explore how bilayer lipids affect or are affected by StnII, we have used a multiprobe approach (fluorescent analogs of both Chol and SM) in combination with a series of StnII tryptophan (Trp) mutants to study StnII/bilayer interactions. First, we compared StnII bilayer permeabilization in the presence of Chol or oleoyl-ceramide (OCer). The comparison was done because both Chol and OCer have a 1-hydroxyl, which helps to orient the molecule in the bilayer (although OCer has additional polar functional groups). Both Chol and OCer also have increased affinity for SM, which StnII may recognize. However, our results show that only Chol was able to activate StnII-induced bilayer permeabilization; OCer failed to activate it. To further examine possible Chol/StnII interactions, we measured Förster resonance energy transfer between Trp in StnII and cholestatrienol, a fluorescent analog of Chol. We could show higher Förster resonance energy transfer efficiency between cholestatrienol and Trps in position 100 and 114 of StnII when compared to three other Trp positions further away from the bilayer binding region of StnII. Taken together, our results suggest that StnII was able to attract Chol to its vicinity, maybe by showing affinity for Chol. SM interactions are known to be important for StnII binding to bilayers, and Chol is known to facilitate subsequent permeabilization of the bilayers by StnII. Our results help to better understand the role of these important membrane lipids for the bilayer properties of StnII.

SIGNIFICANCE Sticholysin II (StnII) is a pore-forming toxin that interacts with sphingomyelin in target membranes. Cholesterol (Chol) is known to modulate pore formation. In our study, we examine in detail the molecular interactions between StnII and both pyrene-sphingomyelin and cholestatrienol, a fluorescent Chol analog. We show that both lipids interact with StnII in the bilayer. Using tryptophan mutants of StnII, we also obtained information about which tryptophan residues Chol preferentially interacted with. Our findings provide new, to our knowledge, details on the process of StnII pore formation as influenced by sphingomyelin and Chol.

INTRODUCTION

Pore-forming toxins (PFTs) constitute an important family of membrane-binding proteins. In solution, PFTs are monomeric and behave like globular proteins, with a defined stable conformation. When PFTs encounter membranes with certain lipid compositions, these proteins are capable of forming pores that cause an osmotic shock in the targeted cells (1,2). The proteins undergo a molecular metamorphosis that allows the PFTs not only to bind but also to oligomerize and transform into integral membrane proteins. Therefore, these proteins are also called metamorphic or amphitropic proteins because of this dual behavior (3–6). PFTs can assemble into structures inserted across the bilayer to form pores. This process occurs without covalent modification of the polypeptides involved but also without coupling to any other chemical reaction, although the overall process must be thermodynamically favorable. Taken together, these facts suggest that this family of proteins constitutes a very good model for studying the molecular

Submitted March 15, 2019, and accepted for publication May 10, 2019.

*Correspondence: alvaromp@ucm.es or jpslotte@abo.fi

Sara García-Linares's present address is Cell Biology Department, Harvard Medical School, Boston, Massachusetts.

Editor: Tommy Nylander.

https://doi.org/10.1016/j.bpj.2019.05.010

Please cite this article in press as: Palacios-Ortega et al., Sticholysin, Sphingomyelin, and Cholesterol: A Closer Look at a Tripartite Interaction, Biophysical Journal (2019), https://doi.org/10.1016/j.bpj.2019.05.010

mechanisms that allow the transition from an aqueous medium to the hydrophobic environment of biological membranes. Sea anemone actinoporins are PFTs that are an optimal system of study, given their structural and functional features (6–8).

Actinoporins constitute multigenic families that have been detected in more than 20 sea anemone species (6,9–11). However, only four species have been characterized in great detail. They are sticholysins I and II (StnI and StnII, respectively) from *Stichodactyla helianthus* (6–8), equinatoxin II from *Actinia equina* (11,12), and fragaceatoxin C (FraC) from *A. fragacea* (13). All show very similar amino-acid sequences and almost identical monomeric and water-soluble three-dimensional structures (14–19), displaying a β-sandwich motif composed of 10−12 β-strands flanked by two α-helices that interact with both sides of the β-sandwich (Fig. 1 *A*) (14–19). One of these helices (α1) is located at the N-terminal end, and it is responsible for the function of the protein. After binding to the membrane, the helix extends to the first 30 residues and inserts into the membrane to form the walls of the pore (Fig. 1 *B*) (14,20–26).

The incorporation of actinoporin into the membrane and the subsequent pore formation depend largely on the composition of the lipid bilayer and physicochemical properties (12,24,27–35). Sphingomyelin (SM) is required (30,36–38), but other conditions in the bilayer membrane (such as the presence of sterols, the coexistence of various phases or domains, lateral packing, fluidity, membrane thickness, and the strength of the interfacial hydrogen bonding network) have a strong influence on the pore-forming ability of the proteins (24,25,30,32–35,39–45). In this context, cholesterol (Chol) greatly influences the pore-forming mechanism considered as a whole (24,25,32,35,44–48). However, the specific role of Chol remains elusive.

It has been shown that in some conditions, the Chol-induced formation of lipid phase boundaries may enhance pore formation by actinoporins (40,41,43,49). However, using 18:1-SM (OSM) bilayers, we have also shown that StnII does not require those phase boundaries for pore formation (24). The results also suggested that as the lateral packing among the SM chains became tighter and the strength of the hydrogen bonds increased, pore formation was hindered (24,34). It has also been observed that fatty acid alcohols (50) and even benzyl alcohol (24) facilitate pore formation by actinoporins. It was proposed that these alcohols interfere with intermolecular hydrogen bonding among SMs, lowering the energy barrier for the diffusion of monomeric actinoporins and oligomerization to constitute a pore (24,34,50). Further confirmation of the hypothesis involving hydrogen bonding arose from the observation that the presence of dihydro-SMs (which lack the *trans* Δ^4 double bond of the long-chain base) (34) strongly impaired toxin binding and pore formation. This effect of establishing a tighter hydrogen bonding network was easily reverted by the presence of Chol. It has been established that many different Chol analogs have a very strong effect on the functionality of actinoporins, facilitating actinoporin-induced membrane permeabilization (24). Given that all the sterols assayed had a 3β-OH group in common, these results seemed to confirm the hypothesis about the strong influence of intermolecular hydrogen bonding in SM bilayers (34) without disregarding the other possibilities of sterols influencing membrane fluidity and SM clustering. Furthermore, Chol appears to affect the SM phosphocholine headgroup orientation and dynamics similarly as seen with glycerophospholipids (51–54), which could facilitate the interaction between actinoporins and SM. Finally, some authors have also suggested that Chol is required for the insertion of the N-terminal α-helix of equinatoxin II into the core of the membrane, enabling the constitution of a fully functional pore (46).

Among all well-known actinoporins, StnII seems to be especially sensitive to the presence of Chol (35). Therefore, in this work, we examined this actinoporin with the aim of shedding further light on our understanding of the role of Chol in pore formation. The results support the need for preferred SM distribution in the membrane for optimal pore formation and the role of Chol in facilitating this distribution. Using a set of tryptophan (Trp) mutants, we also show the specific approach of StnII to Chol in the pore structures.

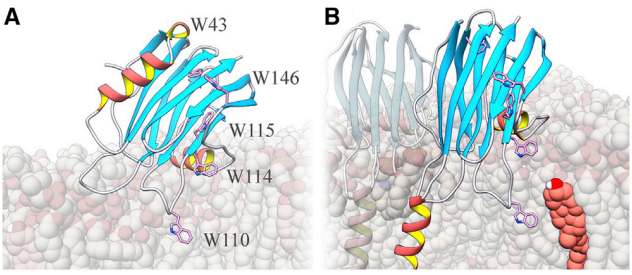

FIGURE 1 Cartoon representation of the expected orientation within the membrane of monomeric StnII (*A*) and its presumed membrane conformation when making an oligomeric pore (*B*). The location and side chains of all its Trp residues are also shown and are in purple. The diagram was constructed using the atomic coordinates deposited in the Protein Data Bank (PDB) for monomeric StnII (PDB: 1GWY) (14) and FraC octameric pores (PDB: 4TSY) (19). A Chol molecule (*salmon*) is highlighted in the membrane. The image was generated with Chimera (93). To see this figure in color, go online.

MATERIALS AND METHODS

Materials

Calcein and Chol were obtained from Sigma-Aldrich (St. Louis, MO). Egg sphingomyelin (eSM), 1,2-dioleoyl-*sn*-glycero-3-phosphocholine (DOPC), 1-palmitoyl-2-oleoyl-*sn*-glycero-3-phosphocholine (POPC), and 1-palmitoyl-2-(7-doxyl)-stearoyl-phosphatidylcholine (7-SLPC) were obtained from Avanti Polar Lipids (Alabaster, AL). Palmitoyl SM (PSM) was isolated from eSM with preparative high-pressure liquid chromatography, as described previously (55). N-C10-pyrene-D-*erythro*-sphingomyelin

Please cite this article in press as: Palacios-Ortega et al., Sticholysin, Sphingomyelin, and Cholesterol: A Closer Look at a Tripartite Interaction, Biophysical Journal (2019), https://doi.org/10.1016/j.bpj.2019.05.010

(Pyr-SM), oleoyl-ceramide (OCer), and cholestatrienol (CTL) were synthesized and purified in-house using published procedures (56). Wild-type StnII and the different Trp mutants employed were produced in *Escherichia coli* RB791 and purified to homogeneity as described previously (57,58).

Preparation of vesicles

Briefly, vesicles were made by extruding resuspended dried lipid films as described previously (24–26,34). Lipid films were made from a methanol mixture of the desired lipids dried under nitrogen flow. This film was later kept in a vacuum for at least 2 h to ensure complete elimination of the organic solvent. Specific details for each set of experiments are provided in the following sections.

Release of calcein from large unilamellar vesicles

Calcein-entrapped large unilamellar vesicles (LUVs) were prepared from different lipids by extrusion through 200 nm filters at 60°C as previously described (38). The buffer used was Tris buffer (10 mM Tris, 140 mM NaCl (pH 7.4)) containing calcein at 100 mM. The LUVs were used for permeabilization studies within 8 h. The specific compositions of the LUVs are indicated in the corresponding sections or figure legends. The LUV and StnII concentrations during the calcein leakage experiments were 2.5 μM and 20 nM, respectively, unless otherwise indicated. Emission at 550 nm was followed at 23°C as a function of time (the excitation wavelength was 480 nm). Fluorescence emission was measured in a FLUOstar OPTIMA microplate reader (BMG-Labtech, Ortenberg, Germany). The fraction of calcein released was determined based on the maximal calcein release that was induced by LUV disintegration using 10% Triton X-100. To ensure that no spontaneous leakage occurred, the emission was measured for each sample for 3−5 min before the toxin was added. A steady signal level, indicating intact vesicles, was observed for all samples.

Measurement of the excimer/monomer ratio of Pyr-SM in bilayer systems

For measurement of the excimer/monomer (E/M) ratio, POPC:PSM:Pyr-SM (5:3:2), POPC:PSM:Pyr-SM:Chol (5:3:2:1), or POPC:PSM:Pyr-SM:OCer (5:3:2:1) LUVs were prepared. The experiments were carried out at 23°C. The final E/M ratio was determined 10 min after StnII was added. The initial E/M ratio also recorded. The final phospholipid concentration was around 1.0 μM in all experiments shown. The exact value was quantified a posteriori with phosphorous determination, using Rouser's method (59), and was then taken into account to calculate the respective protein/lipid molar ratios. Pyr-SM was excited at 345 nm; the monomer emission was read at 392 nm, whereas the excimer emission was monitored at 480 nm. These, as well as subsequently referred to steady-state fluorescence measurements, were made using a PTI Quanta- Master spectrofluorimeter (Photon Technology International, Birmingham, NJ).

Analysis of CTL fluorescence emission in presence of phase-selective quencher

The steady-state fluorescence emissions were measured essentially as described previously (35,58,60–64). Briefly, 7-SLPC is a phosphatidylcholine analog that contains one bulky doxyl group in the *sn*-2 acyl chain. The doxyl group acts as the collisional quencher for CTL. Because of the bulkiness of the doxyl group, 7-SLPC is largely excluded from the ordered domains in the bilayer and instead is enriched in the liquid-disordered phase of the membrane. For that reason, the membrane compositions used for the samples aimed to monitor the quenched emission intensity (F) were POPC:7-SLPC:PSM:CTL 50:30:20:5 and POPC:7-SLPC:PSM:CTL 30:20:50:5. That way, two different conditions were tested: one in which most CTL would be already protected from the quencher by partitioning into the ordered domain (induced by the high amount of PSM) and one in which the extension of the ordered domain was smaller and CTL would be more accessible to 7-SLPC. To measure the emission in the absence of a quencher, 7-SLPC was replaced by POPC in all samples from which unquenched emission intensity was measured (F_0). All other components were kept constant. The CTL content was kept slightly below 5 mol% to avoid self-quenching (65). Emission at 400 nm was continuously recorded using 310 nm as the excitation wavelength. This value was selected to achieve the maximal excitation of CTL while simultaneously avoiding significant excitation of the Trp residues of the proteins. Any Trp-derived emission was subtracted before the subsequent calculations. The lipid concentration was always around 1 μM in all samples. The exact value was determined a posteriori as described above (59). Different amounts of toxin were added after 100 s of a steady signal level of the CTL emission was recorded. The emission increased and reached a plateau after the toxin was added within less than 100 s in all assays.

StnII-induced protection of CTL from 7-SLPC-induced quenching was determined by obtaining the F/F_0 ratios of each pair of comparable samples at all times. The toxin was added to the F and F_0 samples to compare the effect of StnII on CTL in the presence and absence of 7-SLPC. $\Delta(F/F_0)$ after the toxin was added was calculated to show the decreased exposure of CTL to the quencher in the presence of the actinoporin, as well as the larger increased quantum yield of CTL when 7-SLPC was present in the membrane.

Fluorescence emission from the proteins assayed in the presence of lipid vesicles

The fluorescence emission of the different StnII variants was recorded between 280 and 500 nm. Excitation was set to 260 nm to minimize the direct contributions of CTL in the emission (see the following section). The StnII concentration was 200 nM. Emission spectra were recorded repeatedly after every four additions (two in the final step) of small aliquots of vesicles, each addition giving an increment of 1.3 μM lipid concentration, up to a final lipid concentration of 18.5 μM (92.6 L/P ratio). Equivalent samples, in the absence of the toxin, were used to correct for light scattering contributions to the final emission. The areas used to calculate the relative quantum yield were obtained by numerical integration of the recorded spectra. The lipid composition employed was DOPC:eSM:Chol 1:1:1 to ensure binding of the Trp mutants, given that some show low affinity to vesicles containing a lower percentage of Chol (58).

Measurements of Förster resonance energy transfer from StnII to CTL

The StnII and CTL fluorescence emissions were recorded as described in the previous section. The vesicles had the following composition: DOPC:eSM:sterol (1:1:1), where sterol stands for the total amount of Chol + CTL. The mol% of CTL was increased while the amount of Chol was reduced to keep the sterol mol% constant in the membrane. An equivalent sample, without protein added, was used in all experiments to obtain the background contribution of CTL and light scattering. The Förster resonance energy transfer (FRET) efficiencies were calculated by adjusting the emission of the corresponding toxin in the presence of an equivalent amount of DOPC:eSM:Chol (1:1:1) membranes to that of the same toxin in the presence of membranes that contained CTL. The adjustment was performed by nonlinear least-squares fit of the emission between 325 and 340 nm, which contains only the Trp emission. Subtraction of the fitted spectra from the spectra recorded in the presence of CTL yielded the contribution of CTL to the final emission. A very small peak centered between 300 and 310 nm, corresponding to the unquenched Tyr emission in the presence of

CTL, was also obtained. The energy transfer efficiency was calculated as the factor needed to adjust the unquenched spectra to the quenched spectra.

Preferential distribution of CTL around StnII was determined using the StnII mutant StnII W43/110/114/115F, which contains only a single Trp residue (58), according to a model previously described (66,67). The FRET efficiencies were calculated as specified in the previous paragraph. The fluorescence emission decay was measured using a FluoTime 100 spectrofluorimeter with a TimeHarp260 pico time-correlated single-photon-counting module (PicoQuant, Berlin, Germany). The *trans* parinaric acid was excited with a 297 ± 10 nm light-emitting diode laser source (PLS300; PicoQuant), and the emission was collected through a 435/40 nm single-bandpass filter. Fluorescence decays were recorded at 23°C (temperature controlled by water bath) with constant stirring during measurements. Data were analyzed using FluoFit Pro software obtained from PicoQuant.

According to the location of the Trp146 residue in the three-dimensional structure of StnII, and the expected orientation of the protein in the membrane based on previously obtained oligomeric structures (19), the energy transfer to the *trans* leaflet can be considered negligible. Because of the particular geometric configuration of the StnII-membrane system and the position of Trp146 in the system, we used only the part of the model that describes the FRET to acceptors in the *trans* leaflet to predict the effective FRET from that Trp residue to the CTL molecules in the *cis* leaflet of the membrane. The fundamental reason is that in this model, the part that models the FRET to the *cis* leaflet accounts for the FRET from donors to acceptors in the same diffusion plane, whereas the part that describes the FRET to the *trans* leaflet accounts for the FRET from donors to acceptors that are in a separate, parallel diffusion plane. Briefly, the model is used to calculate what the efficiency of the energy transfer would be for a given donor-acceptor pair that is unlinked and randomly distributed in the membrane according to the Förster distance (R_0) of the pair, the exclusion radius of the acceptor around the donor (R_e), the surface density of the acceptor in the membrane (n), and the distance between the diffusion planes of the donors and the acceptors (h).

The Förster distance of this particular FRET pair was calculated as described (68), using the following expression:

$$R_0 = 0.2108\left(\kappa^2 n^{-4} Q_D J(\lambda)\right)^{1/6}, \quad (1)$$

which yields the Förster distance in Å and where κ^2 is the orientation factor, n is the refractive index, Q_D is the quantum yield of the donor, and $J(\lambda)$ is the overlap integral between the donor's emission spectra and the acceptor's absorption spectra. The orientation factor κ^2 was considered to be 2/3, which represents the dynamic isotropic limit. This value is often used for experiments in membranes (69,70). The refractive index n was set to 1.39, which is the average between n_{water} and the estimated values for $n_{membrane}$. The use of n_{water} represented an increase of only ~3% in the Förster distance. The quantum yield of Trp146 was assumed to be 0.14, which is the quantum yield of Trp in water (71). Variations of the Q_D value down to 0.1 or up to 0.2 represented only an approximate 6% change compared to the value used for Q_D (0.14) in the final R_0 value. The overlap integral $J(\lambda)$ was calculated as

$$J(\lambda) = \int_0^\infty F_D(\lambda)\varepsilon_A(\lambda)\lambda^4 d\lambda, \quad (2)$$

where F_D is the donor's emission spectra with its area normalized to 1 and ε_A is the acceptor's absorption spectra in M^{-1} cm^{-1} units. The R_0 value was 22.9 Å.

The time-dependent probability of remaining unquenched of the donor decay in the presence of unlinked, randomly distributed acceptors in a separate diffusion plane was derived in (72):

$$\rho_{cis'}(t) = exp\left(-2\pi h^2 m \int_0^\omega \left\{1 - exp\left[-\left(\frac{R_0}{R_e}\right)^6 \times \left(\frac{t}{\langle\tau\rangle}\right)\alpha^6\right]\right\}\alpha^{-3} d\alpha\right), \quad (3)$$

where h is the distance between the diffusion planes of the donors and acceptors, m is the surface density of the acceptor, and R_e is the exclusion radius between the donor and the acceptor's projection in the donor diffusion plane. The topological parameter α is defined as $\alpha = h/\sqrt{h^2 + r^2}$, where r is the distance between the donor and the projection of the acceptor in the donor's diffusion plane. The parameter ω is a particular case of α at which $r = R_e$, which is the maximal possible value of α.

According to the published structure of the FraC pore (18), h was considered to be 26–28 Å from the equivalent Trp to Trp146 to the location of Chol molecules in a bilayer. For the exclusion distance R_e, a range of possible values were considered, including the extreme case of 0 Å, which would indicate that the acceptor was located right below the donor. The surface density of CTL (m) in the bilayer was calculated from its mole fraction in the bilayer using areas per lipid molecule of 48 $Å^2$ for POPC in the presence of 0.3 mol% of sterol (73), 47.4 $Å^2$ for PSM (74), and 37.7 $Å^2$ for CTL (67,73).

The decay of the donor in the presence of the acceptor in the *cis* leaflet is given by $I_{DA}(t) = I_D(t)\rho_{cis'}(t)$. The theoretical FRET efficiency is then calculated as

$$E = 1 - \frac{\int_0^\infty I_D(t)\rho_{cis'}(t)dt}{\int_0^\infty I_D(t)dt}, \quad (4)$$

where $I_D(t)$ represents the decay of the donor in the absence of the acceptor. For randomly distributed donors and acceptors, experimental results would lie on the theoretically predicted line. However, if the acceptor is preferentially distributed near the donor, the observed FRET efficiencies would be greater than the theoretical values as if the R_0 were larger, although what actually happens is that the average donor-acceptor distance is smaller than expected for a random distribution. The same reasoning, with opposite effects, is valid for acceptors that are excluded from the vicinity of the donor.

RESULTS

StnII causes similar Pyr-SM declustering regardless of the presence of Chol or OCer

Clustering of pyrene-labeled lipids between different bilayer domains can be studied by measuring the pyrene E/M emission ratio (75–77). Therefore, Pyr-SM was employed to study the effect of StnII on SM cluster dispersion. In addition to using Chol, we opted to also test OCer for the following reasons. OCer is a lipid that, like Chol, is prone to interact with SM. The unsaturation in the acyl chain of this ceramide species prevents it, however, from forming gel phases in the range of temperatures that were used. This is particularly important because, as has been shown before (45), gel phase formation hinders the activity of StnII. OCer displays two molecular features that are of interest for the work presented herein: first, its mentioned ability

Please cite this article in press as: Palacios-Ortega et al., Sticholysin, Sphingomyelin, and Cholesterol: A Closer Look at a Tripartite Interaction, Biophysical Journal (2019), https://doi.org/10.1016/j.bpj.2019.05.010

to interact with SM without forming gel phases (24,34), and second, the presence of its interfacial hydroxyl group. This (C1)OH is in a similar location relative to the membrane to that of Chol. By comparing the effect of OCer and Chol on StnII behavior, we aimed to ascertain whether either of these characteristics are the ones that influence Chol's property as a StnII activator.

It is known that SM molecules tend to cluster in equimolecular mixtures of POPC (78). As shown in Fig. 2, a high E/M ratio value of 3.45 was obtained in these conditions. The inclusion of OCer or Chol in the vesicles resulted in a considerable reduction in the ratio. The values decreased to 2.78 and 2.38 in the vesicles containing 9.1 mol% of OCer or Chol, respectively (Fig. 2). This result shows that both lipids can intercalate among SM molecules, thus diminishing the direct Pyr-Pyr interactions that result in excimer emission. Accordingly, Chol would be a slightly better intercalator than OCer. This result might also be related to the documented (24,25,32,35,43–49) improvement in StnII activity observed in the presence of Chol.

Addition of StnII also resulted in a further decrease in the E/M ratio, although the decrease followed a protein concentration dependence that was practically independent of the presence of OCer or Chol (Fig. 2). Thus, the StnII-induced reduction in Pyr-Pyr contacts could be caused by StnII itself intercalating some residue between the Pyr groups or by StnII-induced intercalation of other lipids among the Pyr-SMs.

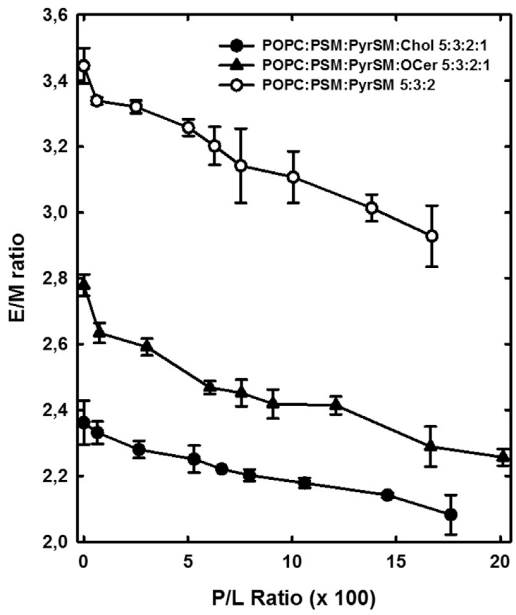

FIGURE 2 The Pyr-SM E/M ratio as a function of various StnII concentrations. POPC:PSM:Pyr-SM (5:3:2) (○), POPC:PSM:Pyr-SM:OCer (5:3:2:1) (▲), or POPC:PSM:Pyr-SM:Chol (5:3:2:1) (●) LUVs were employed at a final phospholipid concentration of 1 μM (approximate). The final stable E/M ratio was determined at 23°C, 10 min after the addition of the protein. Pyr-SM was excited at 345 nm; the monomer emission was read at 392 nm, and the excimer emission was monitored at 480 nm. Each value is the average mean ± standard error (SE) (n = 2–3).

Chol is a better enhancer of the activity of StnII than OCer

One of the questions that remains unsolved is whether the Chol-enhancing effect of actinoporin action (24,25,32,35,43–49) is a major consequence of the formation of lipid boundaries within the membrane because of the existence of liquid-ordered (L_o) phases or whether it is the result of other effects of Chol. As stated in the Introduction, it has been shown that lateral packing or clustering of SM is important (as also observed in this work; see Fig. 2) and how distortion of the SM hydrogen bonding network has a profound effect on actinoporin activity (24,34,50). To further test this hypothesis, calcein leakage experiments were carried out. We first used DOPC:SM (80:20) LUVs that contained increasing amounts of either Chol or OCer. Both lipids showed a high affinity for SM, intercalating between SM molecules (Fig. 2), and contained a hydroxyl group whose location at the bilayer/aqueous interphase was similar. It is possible that this interfacial hydroxyl can distort the intermolecular hydrogen bonding network of SMs. OCer, however, did not participate in creating defined liquid-ordered domains with SM as Chol can do (79).

As seen in Fig. 3, Chol greatly increased the release rates for calcein even when present at a low percentage. The effective Chol concentration was probably below the threshold needed for the formation of Chol-induced lipid domains (80). However, OCer failed to activate StnII-induced release of calcein (Fig. 3). The effect of Chol was noticeably more pronounced, perhaps because of its

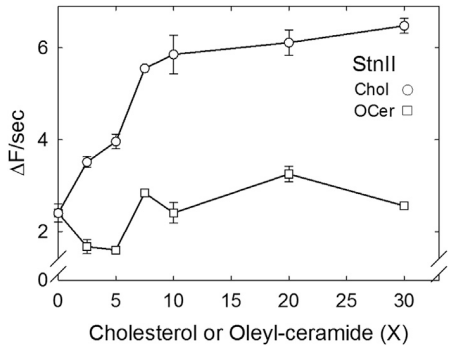

FIGURE 3 Maximal rates of StnII induced the release of calcein entrapped in DOPC:SM:X (80:20:X) LUVs, containing different amounts (X) of Chol (○) or OCer (□). The StnII concentration was 10 nM in all experiments, and the protein/lipid molar ratio was maintained at 0.09. Calcein-entrapped vesicles were prepared via extrusion, and release was measured at 23°C. All intensities were normalized. The maximal rate of release (ΔF/s was measured as the initial slope of the leakage curves) was measured by comparison with protein-free samples to which Triton X-100 was added to a final concentration of 0.05% v/v to induce LUV disintegration. The results shown are representative of three independent experiments. Each value is the average mean ± SE (n = 3).

Please cite this article in press as: Palacios-Ortega et al., Sticholysin, Sphingomyelin, and Cholesterol: A Closer Look at a Tripartite Interaction, Biophysical Journal (2019), https://doi.org/10.1016/j.bpj.2019.05.010

particular structure. Interestingly, at 20 mol% Chol, at which the L_d/S_o phase boundary appears, no further increase in Chol-promoted activation was observed. In both cases, these enhancing effects became stable when the proportions employed were 80:20:7.5, that is, for an amount of Chol slightly smaller than ~7 mol%.

StnII changes the CTL microenvironment

Partitioning of a fluorescent probe between fluid and ordered membrane domains can be determined by using a phase-selective quencher (81). With the aim of studying the effect of StnII on membranes that contain SM and Chol, the fluorescent Chol analog CTL was used as a probe (56,65,82), whereas 7-SLPC was chosen as a phase-selective collisional quencher (Fig. 4). The gel-to-liquid phase transition temperature of 7-SLPC has been determined to be ~8°C (83), and thus, this lipid is in the fluid state at 23°C, the temperature at which the experiments were carried out.

POPC:7-SLPC:PSM:CTL (50:30:20:5) vesicles were employed. At this concentration, CTL is not self-quenched. The sterol content was similar to that showing the maximal enhancement in the release rate of calcein in Fig. 3. In this situation, the recorded initial F/F_0 value was 0.27, revealing that most of the CTL was accessible to the quencher (Fig. S1). The addition of StnII induced an increase in the observed F/F_0 value that revealed how StnII exerted a considerable quenching-protection effect on CTL (Fig. 4). Given that the quencher is known to partition preferentially into the fluid phase, these results can be interpreted as the protein reducing CTL contacts with fluid-phase lipids, making CTL less available for 7-SLPC quenching. If StnII binds CTL, it could also be that the bound CTL is protected by the protein and not only that StnII redistributes CTL more to the SM phase. In the absence of 7-SLPC, StnII caused an increase in the CTL quantum yield, most probably by shielding it from water. Overall, it seems that the most probable interpretation is that when 7-SLPC is present, StnII produces a change in the lipids surrounding CTL. When the vesicles employed were POPC:7-SLPC:PSM:CTL (30:20:50:5), in which the SM proportion was much higher (nearly ~50 mol%), this effect was greatly reduced (Fig. 4). Higher PSM content decreases the extent of the phase boundary as a consequence of the larger domains. This is reflected in the initial F/F_0 value (0.78), implying CTL is already shielded from the quencher. The interaction of StnII with the membrane is expected to be essentially the same, in terms of activity and affinity, to that in the previous scenario. In this new situation, CTL protection from the quencher was modest (Fig. 4). This expected result confirmed that in SM-rich bilayers, most CTL is not accessible to 7-SLPC because of the preferential partitioning of CTL into the ordered phase and its preferred interaction with PSM.

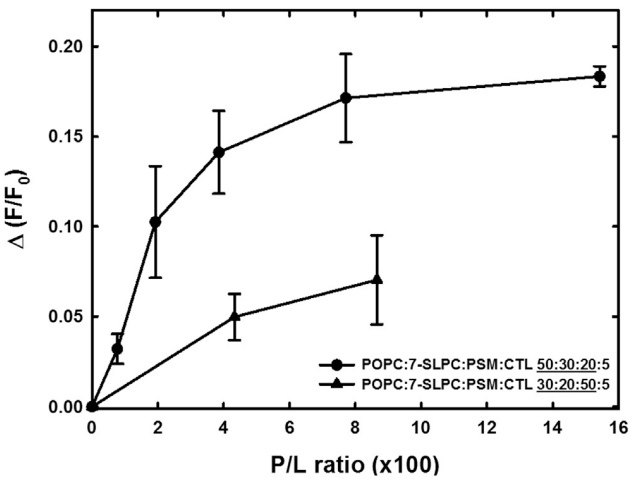

FIGURE 4 Analysis of the effect of StnII on the CTL relative quantum yield embedded in POPC:7-SLPC:PSM:CTL (50:30:20:5) (●) or (30:20:50:5) (▲) vesicles at different protein/lipid (P/L) molar ratios. This relative quantum yield change was expressed as the change in the fluorescence emission for each StnII concentration used. The excitation wavelength employed was 310 nm. CTL emission was recorded at 410 nm. All measurements were conducted at 23°C. Each value is the average mean ± SE ($n = 2$).

StnII Trp side chains move to a more hydrophobic environment in the presence of vesicles that contain SM and Chol

To study the presumed closeness between StnII and Chol in membranes that contain SM, the FRET between Trp residues in StnII and CTL was the chosen approach. Energy transfer suggests the establishment of very close StnII-Chol interactions. A collection of Trp-to-Phe mutants, which had been characterized in a previous work (58), were available. The protein variants assayed were the wild-type protein (StnII WT), a single mutant (W43F), two double mutants (W43/110F and W43/114F), one triple mutant (W43/110/114F), and one quadruple variant (W43/110/114/115F) (Fig. 1). This quadruple mutant contained only a single Trp, specifically W146.

First, titration of the different StnII variants with increasing amounts of DOPC:eSM:Chol (1:1:1) LUVs was performed (Fig. 5). DOPC was used instead of POPC because the Trp mutants employed had already been characterized in this system, in which we already knew that they displayed a considerable membrane binding (53). This vesicle composition, containing a large proportion of Chol, was indeed needed because of the low affinity of some of the Trp mutants employed for the membranes that contained low amounts of this sterol (58). In all experiments, the fluorescence emission spectra of the proteins displayed a considerable increase in the quantum yield (Fig. 5, *right column*), a blue shift in the emission maximum, and a reduction in the spectral width (Fig. S2). The first two are expected features of Trp side chains

Please cite this article in press as: Palacios-Ortega et al., Sticholysin, Sphingomyelin, and Cholesterol: A Closer Look at a Tripartite Interaction, Biophysical Journal (2019), https://doi.org/10.1016/j.bpj.2019.05.010

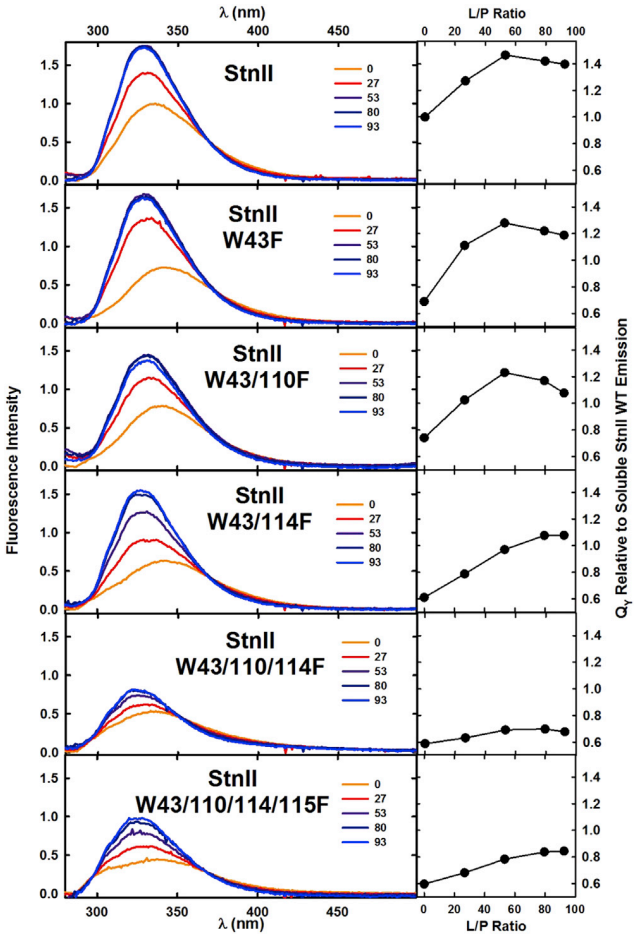

FIGURE 5 Fluorescence spectra of StnII WT and its different mutants used titrated with DOPC:eSM:Chol (1:1:1) LUVs. The panels at the right represent the relative quantum yield change as a function of the L/P ratio, using the quantum yield of StnII WT free in solution as reference. The excitation wavelength employed was 260 nm. The spectra were recorded at 25°C. The protein concentration was 200 nM in all experiments shown. Fluorescence intensities were normalized to 1.0 for the maximal emission of StnII WT in buffer, in the absence of vesicles. To see this figure in color, go online.

entering a more hydrophobic microenvironment. The third one can be also explained as Trp residues changing from varied environments to a relatively equal, nonpolar environment. The observed increases in the quantum yield suggest that W110 and W114 were responsible for most of the effects observed. Representation of the relative change in the quantum yield as a function of the lipid/protein molar ratio (L/P ratio) showed how saturation was reached at similar L/P ratios (Fig. 5, *right column*) for StnII WT, W43F, and W43/110F mutants. W43/114F reaching saturation at a higher L/P ratio confirmed, as previously described using isothermal titration calorimetry, that W114 is more important for membrane affinity than W110, although W110 is more exposed to the aqueous phase than W114 when the protein is in solution (58). Accordingly, substitution of both Trp residues by Phe produced variants in which the quantum yield was barely increased (see the results for the triple and quadruple Trp mutants in Fig. 5).

CTL is located near StnII Trp residues 110 and 114

The same StnII variants were titrated with other vesicles at the DOPC:eSM:sterol ratio of 1:1:1 but contained 5 mol% CTL. Nonradiative energy transfer from the Trp side chains to this fluorescent version of Chol was clearly observed (Fig. 6). This result suggested that the indole moiety of these amino acids was in close proximity to CTL molecules to be able to produce the observed effect. Again, the FRET was especially relevant for proteins containing Trp residues 110 and 114 (Fig. 6). Representation of the CTL emission originating from the FRET as a function of the L/P ratio led to the same conclusion and further confirmed the previous observation that saturation was reached at very similar lipid concentrations in all experiments (Fig. S3). Again, substitution of Trp110 and Trp114 for Phe rendered proteins that were capable of less energy transfer to CTL (W43/110/114F and W43/110/114/115F in Figs. 6 and 7).

There is preferential distribution of Chol near StnII

Among all 20 canonic protein amino acids, Trp stands out because of the properties of its side chain. The indole ring is not only the bulkiest side-chain group but also provides the potential to interact with various molecules. It is a rigid planar ring that can establish a wide variety of very different interactions with other groups, including hydrogen bonding, dipolar or cation-π interactions, and hydrophobic effects (64,84–87). Given that Chol also has a complex and hydrophobic rigid ring structure, it could interact with the indole ring of Trp.

To resolve whether Chol is preferentially distributed near StnII, an approach previously described by Holt et al. (67) was used. A mutant containing only one Trp, the StnII-W43/110/114/115F mutant, was used to avoid complications with the application of the model employed. This single Trp variant appeared to be one of the few soluble StnII mutants containing only one Trp residue. Furthermore, this remaining Trp did not seem to be directly involved in protein-lipid interactions, as shown in Fig. 5 and by García-Linares et al. (58). Instead, Trp146 appears to be needed for protein-protein interactions that lead to oligomerization and pore formation (Fig. 1) (19,58). The increase in the quantum yield observed for this quadruple Trp-to-Phe mutant is interpreted as the side chain of Trp146 entering a hydrophobic cavity in the neighboring actinoporin monomer in the final pore structure (19).

According to the model used (67), if the acceptor (CTL) is randomly distributed around the donor, the experimental FRET efficiencies are located on the theoretical FRET efficiency curve. If the acceptor is preferentially distributed

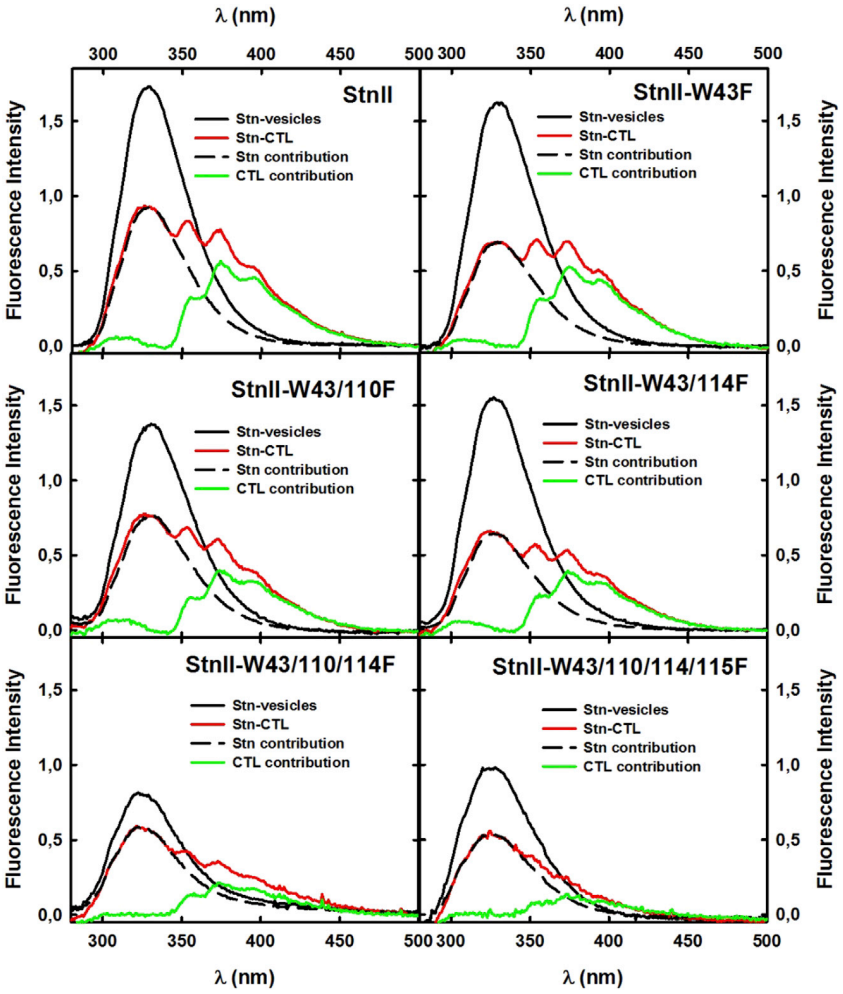

FIGURE 6 Fluorescence emission spectra of StnII WT and the Trp mutants studied in the absence or presence of DOPC:eSM:Chol:CTL (33:33:28:5) at a saturating L/P ratio of 93 (see Fig. 5). The excitation wavelength employed was 260 nm, and the spectra were recorded at 25°C. The protein concentration was 200 nM in all experiments shown. Fluorescence intensities were normalized to 1.0 for the maximal emission of StnII WT in buffer in the absence of vesicles. To see this figure in color, go online.

near the donor, the experimental values are located above it because of the reduced average distance (which still must be larger than the exclusion distance). The plot representing the empirically determined energy transfer efficiencies at several different surface densities of CTL (*dots* in Fig. 7) versus the theoretical curves for the expected energy transfer (*lines* in Fig. 7) shows that the experimental data were higher than the calculated efficiencies. This conclusion is supported even considering that CTL can be located right below the donor ($R_e = 0$ Å) while also at the shortest estimated possible distance from Trp146.

This result indicates that CTL is preferentially distributed near StnII. Given that the sterol effect on this protein's activity has been shown to be largely independent of the sterol structure (24), this result can also be extrapolated to Chol.

DISCUSSION

The presence of Chol in bilayer membranes affects several membrane properties that can influence the function and distribution of membrane proteins. Chol has an ordering effect on acyl chains of surrounding phospho- and sphingolipids, which results in more condensed bilayers. It is also well known that Chol displays high affinity for SM when embedded in a biological membrane (54,88). This observation explains the existence of SM- and Chol-rich L_o domains. Accordingly, it has been proposed that the presence of lipid domains in the membrane could explain the observed effects of Chol on actinoporin activity. The results presented here show that StnII-induced activation of the calcein release phenomenon starts to be observable at a mol% of Chol below the minimal amount needed for SM and Chol to arrange into distinct lipid domains (80) (Fig. 3). Furthermore, qualitatively speaking, OCer, another good SM intercalator (Fig. 2), does not show such behavior (Fig. 3).

SMs form extensive intramolecular hydrogen bonds (from the 3OH of the long-chain base to phosphate oxygens of the headgroup), but also intermolecular hydrogen bonding involving the NH of the long-chain base is important for SM (and sphingolipid) properties in membrane environments (89). Similar hydrogen bonds cannot be established among glycerophospholipids. Hydrogen bonding

Please cite this article in press as: Palacios-Ortega et al., Sticholysin, Sphingomyelin, and Cholesterol: A Closer Look at a Tripartite Interaction, Biophysical Journal (2019), https://doi.org/10.1016/j.bpj.2019.05.010

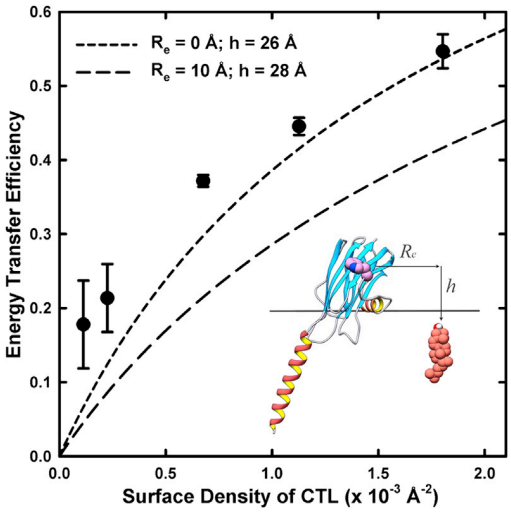

FIGURE 7 Theoretically calculated FRET efficiency curves for StnII Trp146 side chains to CTL. The R_0 of the FRET pair is 22.9 Å. The experimental values (*dots*) were calculated from fluorescence spectra of StnII W43/110/114/115F in vesicles composed of DOPC:eSM:sterol 1:1:1, with increasing amounts of CTL: 0.5, 1, 3, 5, and 8 mol%. FRET efficiencies were calculated for an L/P ratio of 93. Theoretical FRET values were calculated assuming a model based on the random distribution of the donor (StnII W43/110/114/115F) and the acceptor (CTL) and taking into account only the transfer to the *cis* leaflet (67). The distance between diffusion planes was considered to be 26–28 Å, based on the location of the equivalent Trp residue in the crystalline structure of the FraC pore (PDB: 4TSY) (19). Extreme conditions for interplanar and exclusion distances were simulated ($R_e = 0$, $h = 26$ Å; *short dashed line*), showing that even then, the experimental values (given as mean + standard error of $n = 3$) were above the predictions for random distribution. As an example, other conditions were also simulated ($R_e = 10$, $h = 28$ Å; *long dashed line*). To see this figure in color, go online.

involving SM has been also shown to markedly stabilize interactions with both Chol and ceramide in fully hydrated bilayers (90). We have demonstrated before (24,45) that the existence of a fluid phase is important for the formation of pores by actinoporins. These results, combined with the use of benzyl alcohol and several different sterols, suggested that these compounds enhance StnII action by modifying the SM interfacial hydrogen bonding network (24,34). This effect was interpreted as leading to a more favorable distribution of SM molecules in the membrane and to easier availability to StnII molecules.

Chol and OCer share an interfacial hydroxyl group as a common feature. Its location enables hydrogen bonding with other lipid headgroups, especially with SM. Thus, both OCer and Chol could potentially interfere with the hydrogen bonding networks formed by SMs, although they are likely to disturb the network differently because OCer has more possibilities to form hydrogen bonds compared to Chol. Another consequence of the arrangement of Chol in the membrane is that membrane domains with increased Chol content (i.e., lipid rafts), can have an increased bilayer thickness. This agrees with the observation that Chol is not only required for complete membrane penetration by actinoporins (46) but also for optimizing membrane thickness for StnII action (25). Our results here show, however, that the presence of an interfacial (C1)OH group is not enough to explain the observed effect of Chol-enhancing StnII activity because OCer, with a similar (C1)OH group does not induce a comparable effect. Because OCer has an unsaturated acyl chain, its molecular volume requirement in bilayers is larger than that of Chol. This implies that lateral packing is denser in Chol/SM domains or small clusters (condensing effect) than it is in OCer/SM domains or clusters. Such differences in lateral packing in the SM-rich domains could affect SM headgroup orientation differently and explain why Chol does and OCer does not activate StnII-induced bilayer permeabilization.

It has been shown that mixtures in which 1,2-dimyristoyl-*sn*-glycero-3-phosphocholine is in molar excess over PSM hinder SM to participate efficiently in the StnII-induced pore formation process (24). Considering that dimyristoyl phosphatidylcholine displays near-ideal miscibility with PSM, this observation was interpreted as StnII needing small clusters of SM to oligomerize and form pores. Building on previous work in which we used Pyr-SM to show that StnII causes SM declustering (24), in this work, we used Pyr-SM to test the effect of the presence of Chol or OCer on SM distribution. The results showed that both Chol and OCer could decluster Pyr-SM similarly, although Chol was slightly more efficient. However, based on the Pyr-SM results, it is difficult to argue whether or not SM headgroup orientation or presentation to the StnII was markedly different during Chol-induced SM declustering compared to OCer-induced SM declustering.

A question can be raised whether Chol-induced lipid rearrangement is sensed by the toxin or induced by it. According to the results shown in Fig. 4, the answer to this question seems to be, at least partially, the latter. StnII binding to the membrane resulted in a reduction in the contact of CTL with fluid-phase lipids, which could be caused by the effective removal of CTL molecules from the fluid phase. Presumably, lipids from the more ordered domain, essentially SM (Fig. 4), would then surround CTL. However, in the presence of a large amount of SM, the preferential partitioning of Chol (in this instance, CTL) into the ordered phase was more noticeable, as seen in the high initial F/F_0 values. Therefore, the observable effect in the CTL distribution after the addition of the toxin was small, indicating that the SM-CTL arrangement was better for StnII action in this case. These results suggest that StnII induced a rearrangement of CTL distribution in the membrane, probably by recruiting CTL to the pore structure or to the close vicinity of membrane-bound StnII.

Most actinoporins contain five conserved Trp residues (Fig. 1). At least two of them (W110 and W114 in StnII) have been shown to be part of an exposed and conserved cluster of aromatic residues that are implied in the interaction with membranes (8,19,37,58,91,92). Our results

showed that these two amino acids not only contribute to membrane binding but also insert into the hydrophobic region of the bilayer (Fig. 5). This result is also in strong agreement with the previous hypothesis that the key role of membrane recognition assigned to the actinoporin's tryptophan represented by W110 and W114 of StnII is based more on its participation in maintaining a hydrophobic effect than on the onset of interactions with specific SM chemical groups (58). The observed FRET indicates that CTL is located near W110 and W114. It could be argued, however, that the FRET with CTL does not originate from a specific interaction but only from the abundance of CTL available at a short distance from the Trp indole side chains. It has been shown how Chol remains homogeneously distributed in the membrane in the presence of some Trp-flanked transmembrane peptides and how the dynamics and orientation of neither Chol nor Trp located at the bilayer interface were influenced by the presence of the other molecule (67). However, when we used a very similar approach, we observed the opposite effect (Fig. 7). The FRET efficiency from W146 of StnII appeared above the theoretical curves, indicating that the acceptor (CTL) was preferentially distributed close to the donor (StnII). Because the distance measurements were based on a model obtained with detergents (19), we considered the interplanar distance to range from 26 to 28 Å. CTL preferential distribution near StnII held true even for the simulation of the limiting conditions, at which we assume that CTL can diffuse freely below W146 ($R_e = 0$ Å) and the interplanar distance, h, is 26 Å. If the StnII pores contain lipids, then an exclusion distance should be considered because lipids forming part of the pore would have a much lower diffusion rate and hinder diffusion of the remaining lipids near the complex. In that case, the theoretical FRET efficiency would be lower (Fig. 7, *long dashed lines*). The comparatively large FRET efficiencies would then support CTL being part of such a lipid-protein complex. The model, regardless of the distance constraints that are used, overestimates the expected FRET efficiencies. It considers the FRET from the donor to anywhere around it, which, in the particular case of StnII pores, is not correct because the pores themselves create a volume that cannot be transited by lipids.

CONCLUSIONS

Taken together, our results have shown that Chol and OCer behaved differently with regard to StnII-induced bilayer permeabilization. We speculate that headgroup orientation in SM clusters was different in the presence of Chol and OCer, and that the Chol-induced orientation was preferred by StnII. Because StnII activation in bilayers is markedly affected by hydrogen bonding (90), it is also possible that Chol and OCer rearranged SM hydrogen bonding differently, which in turn affected StnII-induced bilayer permeabilization. Such rearrangements of SM hydrogen bonding may also have affected SM headgroup orientation. Using FRET between Trp in StnII and the fluorescent Chol analog CTL in the bilayer, we were able to show that CTL displayed the closest proximity to Trp in positions 100 and 114 of StnII. These two Trp positions are in the membrane-binding region of StnII (Fig. 1), which makes perfect sense and further supports how StnIIs are oriented with regard to the bilayer.

SUPPORTING MATERIAL

Supporting Material can be found online at https://doi.org/10.1016/j.bpj.2019.05.010.

AUTHOR CONTRIBUTIONS

J.P.-O., S.G.-L., and E.R.-d.-T. conducted the experiments. All authors contributed to conceiving and designing the experiments, analyzing the results, and writing the manuscript.

ACKNOWLEDGMENTS

This research was supported by the Sigrid Juselius Foundation, the Jane and Aatos Erkko Foundation, and the Magnus Ehrnrooth Foundation (to J.P.S.), and by grants from UCM-Banco Santander grants PR41/17-21012 and PR75/18-21561 (to A.M.-d.-P.). J.P.-O. has a funded doctoral student position from ISB/ÅA. FPU and UCM-Banco Santander fellowships were granted to S.G.-L. and E.R.-d.-T., respectively.

REFERENCES

1. Parker, M. W., and S. C. Feil. 2005. Pore-forming protein toxins: from structure to function. *Prog. Biophys. Mol. Biol.* 88:91–142.
2. Gilbert, R. J., M. Dalla Serra, …, G. Anderluh. 2014. Membrane pore formation at protein-lipid interfaces. *Trends Biochem. Sci.* 39:510–516.
3. Burn, P. 1988. Amphitropic proteins: a new class of membrane proteins. *Trends Biochem. Sci.* 13:79–83.
4. Tanaka, K., J. M. Caaveiro, and K. Tsumoto. 2015. Bidirectional transformation of a metamorphic protein between the water-soluble and transmembrane native states. *Biochemistry.* 54:6863–6866.
5. Lella, M., and R. Mahalakshmi. 2017. Metamorphic proteins: emergence of dual protein folds from one primary sequence. *Biochemistry.* 56:2971–2984.
6. García-Linares, S., E. Rivera-de-Torre, …, A. Martínez-del-Pozo. 2017. The metamorphic transformation of a water-soluble monomeric protein into an oligomeric transmembrane pore. *In* Advances in Biomembranes and Lipid Self-Assembly. A. Iglic, A. García-Sáez, and M. Rappolt, eds. Elsevier, pp. 51–97.
7. Alegre-Cebollada, J., M. Oñaderra, …, A. M. del Pozo. 2007. Sea anemone actinoporins: the transition from a folded soluble state to a functionally active membrane-bound oligomeric pore. *Curr. Protein Pept. Sci.* 8:558–572.
8. García-Ortega, L., J. Alegre-Cebollada, …, J. G. Gavilanes. 2011. The behavior of sea anemone actinoporins at the water-membrane interface. *Biochim. Biophys. Acta.* 1808:2275–2288.
9. Rivera-de-Torre, E., Á. Martínez-Del-Pozo, and J. E. Garb. 2018. Stichodactyla helianthus' de novo transcriptome assembly: discovery of a new actinoporin isoform. *Toxicon.* 150:105–114.

Please cite this article in press as: Palacios-Ortega et al., Sticholysin, Sphingomyelin, and Cholesterol: A Closer Look at a Tripartite Interaction, Biophysical Journal (2019), https://doi.org/10.1016/j.bpj.2019.05.010

10. Leychenko, E., M. Isaeva, …, E. Kozlovskaya. 2018. Multigene family of pore-forming toxins from sea anemone Heteractis crispa. *Mar. Drugs.* 16:E183.
11. Anderluh, G., I. Krizaj, …, J. Pungercar. 1999. Equinatoxins, pore-forming proteins from the sea anemone Actinia equina, belong to a multigene family. *Toxicon.* 37:1391–1401.
12. Rojko, N., M. Dalla Serra, …, G. Anderluh. 2016. Pore formation by actinoporins, cytolysins from sea anemones. *Biochim. Biophys. Acta.* 1858:446–456.
13. Bellomio, A., K. Morante, …, J. M. González-Mañas. 2009. Purification, cloning and characterization of fragaceatoxin C, a novel actinoporin from the sea anemone Actinia fragacea. *Toxicon.* 54:869–880.
14. Athanasiadis, A., G. Anderluh, …, D. Turk. 2001. Crystal structure of the soluble form of equinatoxin II, a pore-forming toxin from the sea anemone Actinia equina. *Structure.* 9:341–346.
15. Hinds, M. G., W. Zhang, …, R. S. Norton. 2002. Solution structure of the eukaryotic pore-forming cytolysin equinatoxin II: implications for pore formation. *J. Mol. Biol.* 315:1219–1229.
16. Mancheño, J. M., J. Martín-Benito, …, J. A. Hermoso. 2003. Crystal and electron microscopy structures of sticholysin II actinoporin reveal insights into the mechanism of membrane pore formation. *Structure.* 11:1319–1328.
17. Mechaly, A. E., A. Bellomio, …, D. M. Guérin. 2011. Structural insights into the oligomerization and architecture of eukaryotic membrane pore-forming toxins. *Structure.* 19:181–191.
18. García-Linares, S., I. Castrillo, …, J. G. Gavilanes. 2013. Three-dimensional structure of the actinoporin sticholysin I. Influence of long-distance effects on protein function. *Arch. Biochem. Biophys.* 532:39–45.
19. Tanaka, K., J. M. Caaveiro, …, K. Tsumoto. 2015. Structural basis for self-assembly of a cytolytic pore lined by protein and lipid. *Nat. Commun.* 6:6337.
20. Malovrh, P., G. Viero, …, G. Anderluh. 2003. A novel mechanism of pore formation: membrane penetration by the N-terminal amphipathic region of equinatoxin. *J. Biol. Chem.* 278:22678–22685.
21. Gutiérrez-Aguirre, I., A. Barlič, …, J. M. González-Mañas. 2004. Membrane insertion of the N-terminal α-helix of equinatoxin II, a sea anemone cytolytic toxin. *Biochem. J.* 384:421–428.
22. Rojko, N., K. C. Kristan, …, G. Anderluh. 2013. Membrane damage by an α-helical pore-forming protein, equinatoxin II, proceeds through a succession of ordered steps. *J. Biol. Chem.* 288:23704–23715.
23. Antonini, V., V. Pérez-Barzaga, …, M. Tejuca. 2014. Functional characterization of sticholysin I and W111C mutant reveals the sequence of the actinoporin's pore assembly. *PLoS One.* 9:e110824.
24. Palacios-Ortega, J., S. García-Linares, …, J. P. Slotte. 2016. Regulation of sticholysin II-induced pore formation by lipid bilayer composition, phase state, and interfacial properties. *Langmuir.* 32:3476–3484.
25. Palacios-Ortega, J., S. García-Linares, …, J. P. Slotte. 2017. Differential effect of bilayer thickness on sticholysin activity. *Langmuir.* 33:11018–11027.
26. Rivera-de-Torre, E., J. Palacios-Ortega, …, Á. Martínez-Del-Pozo. 2017. One single salt bridge explains the different cytolytic activities shown by actinoporins sticholysin I and II from the venom of Stichodactyla helianthus. *Arch. Biochem. Biophys.* 636:79–89.
27. Shin, M. L., D. W. Michaels, and M. M. Mayer. 1979. Membrane damage by a toxin from the sea anemone Stoichactis helianthus. II. Effect of membrane lipid composition in a liposome system. *Biochim. Biophys. Acta.* 555:79–88.
28. Belmonte, G., C. Pederzolli, …, G. Menestrina. 1993. Pore formation by the sea anemone cytolysin equinatoxin II in red blood cells and model lipid membranes. *J. Membr. Biol.* 131:11–22.
29. Tejuca, M., M. D. Serra, …, G. Menestrina. 1996. Mechanism of membrane permeabilization by sticholysin I, a cytolysin isolated from the venom of the sea anemone Stichodactyla helianthus. *Biochemistry.* 35:14947–14957.
30. de los Ríos, V., J. M. Mancheño, …, J. G. Gavilanes. 1998. Mechanism of the leakage induced on lipid model membranes by the hemolytic protein sticholysin II from the sea anemone Stichodactyla helianthus. *Eur. J. Biochem.* 252:284–289.
31. Valcarcel, C. A., M. Dalla Serra, …, G. Menestrina. 2001. Effects of lipid composition on membrane permeabilization by sticholysin I and II, two cytolysins of the sea anemone Stichodactyla helianthus. *Biophys. J.* 80:2761–2774.
32. Martínez, D., A. Otero, …, E. Lissi. 2007. Effect of sphingomyelin and cholesterol on the interaction of St II with lipidic interfaces. *Toxicon.* 49:68–81.
33. Bakrač, B., and G. Anderluh. 2010. Molecular mechanism of sphingomyelin-specific membrane binding and pore formation by actinoporins. *Adv. Exp. Med. Biol.* 677:106–115.
34. García-Linares, S., J. Palacios-Ortega, …, J. P. Slotte. 2016. Toxin-induced pore formation is hindered by intermolecular hydrogen bonding in sphingomyelin bilayers. *Biochim. Biophys. Acta.* 1858:1189–1195.
35. García-Linares, S., E. Rivera-de-Torre, …, Á. Martínez-Del-Pozo. 2016. Differential effect of membrane composition on the pore-forming ability of four different sea anemone actinoporins. *Biochemistry.* 55:6630–6641.
36. Bernheimer, A. W., and L. S. Avigad. 1976. Properties of a toxin from the sea anemone Stoichacis helianthus, including specific binding to sphingomyelin. *Proc. Natl. Acad. Sci. USA.* 73:467–471.
37. Bakrač, B., I. Gutiérrez-Aguirre, …, G. Anderluh. 2008. Molecular determinants of sphingomyelin specificity of a eukaryotic pore-forming toxin. *J. Biol. Chem.* 283:18665–18677.
38. Maula, T., Y. J. Isaksson, …, J. P. Slotte. 2013. 2NH and 3OH are crucial structural requirements in sphingomyelin for sticholysin II binding and pore formation in bilayer membranes. *Biochim. Biophys. Acta.* 1828:1390–1395.
39. Varanda, W., and A. Finkelstein. 1980. Ion and nonelectrolyte permeability properties of channels formed in planar lipid bilayer membranes by the cytolytic toxin from the sea anemone, Stoichactis helianthus. *J. Membr. Biol.* 55:203–211.
40. Barlič, A., I. Gutiérrez-Aguirre, …, J. M. González-Mañas. 2004. Lipid phase coexistence favors membrane insertion of equinatoxin-II, a pore-forming toxin from Actinia equina. *J. Biol. Chem.* 279:34209–34216.
41. Alegre-Cebollada, J., I. Rodríguez-Crespo, …, A. M. del Pozo. 2006. Detergent-resistant membranes are platforms for actinoporin pore-forming activity on intact cells. *FEBS J.* 273:863–871.
42. Alegre-Cebollada, J., M. Cunietti, …, A. Martínez-del-Pozo. 2008. Calorimetric scrutiny of lipid binding by sticholysin II toxin mutants. *J. Mol. Biol.* 382:920–930.
43. Pedrera, L., M. L. Fanani, …, C. Álvarez. 2014. Sticholysin I-membrane interaction: an interplay between the presence of sphingomyelin and membrane fluidity. *Biochim. Biophys. Acta.* 1838:1752–1759.
44. Pedrera, L., A. B. Gomide, …, C. Álvarez. 2015. The presence of sterols favors sticholysin I-membrane association and pore formation regardless of their ability to form laterally segregated domains. *Langmuir.* 31:9911–9923.
45. Alm, I., S. García-Linares, …, J. P. Slotte. 2015. Cholesterol stimulates and ceramide inhibits sticholysin II-induced pore formation in complex bilayer membranes. *Biochim. Biophys. Acta.* 1848:925–931.
46. Wacklin, H. P., B. B. Bremec, …, R. S. Norton. 2016. Neutron reflection study of the interaction of the eukaryotic pore-forming actinoporin equinatoxin II with lipid membranes reveals intermediate states in pore formation. *Biochim. Biophys. Acta.* 1858:640–652.
47. Marchioretto, M., M. Podobnik, …, G. Anderluh. 2013. What planar lipid membranes tell us about the pore-forming activity of cholesterol-dependent cytolysins. *Biophys. Chem.* 182:64–70.

48. García-Linares, S., I. Alm, …, Á. Martínez-Del-Pozo. 2015. The effect of cholesterol on the long-range network of interactions established among sea anemone sticholysin II residues at the water-membrane interface. *Mar. Drugs.* 13:1647–1665.

49. Schön, P., A. J. García-Sáez, …, P. Schwille. 2008. Equinatoxin II permeabilizing activity depends on the presence of sphingomyelin and lipid phase coexistence. *Biophys. J.* 95:691–698.

50. Maček, P., M. Zecchini, …, G. Menestrina. 1997. Effect of membrane partitioned n-alcohols and fatty acids on pore-forming activity of a sea anemone toxin. *Eur. Biophys. J.* 25:155–162.

51. Niemelä, P., M. T. Hyvönen, and I. Vattulainen. 2004. Structure and dynamics of sphingomyelin bilayer: insight gained through systematic comparison to phosphatidylcholine. *Biophys. J.* 87:2976–2989.

52. Róg, T., and M. Pasenkiewicz-Gierula. 2006. Cholesterol-sphingomyelin interactions: a molecular dynamics simulation study. *Biophys. J.* 91:3756–3767.

53. Björkbom, A., T. Róg, …, J. P. Slotte. 2010. Effect of sphingomyelin headgroup size on molecular properties and interactions with cholesterol. *Biophys. J.* 99:3300–3308.

54. Endapally, S., D. Frias, …, A. Radhakrishnan. 2019. Molecular discrimination between two conformations of sphingomyelin in plasma membranes. *Cell.* 176:1040–1053.e17.

55. Térová, B., J. P. Slotte, and T. K. Nyholm. 2004. Miscibility of acyl-chain defined phosphatidylcholines with N-palmitoyl sphingomyelin in bilayer membranes. *Biochim. Biophys. Acta.* 1667:182–189.

56. Fischer, R. T., F. A. Stephenson, …, F. Schroeder. 1984. delta 5,7,9(11)-Cholestatrien-3 beta-ol: a fluorescent cholesterol analogue. *Chem. Phys. Lipids.* 36:1–14.

57. Alegre-Cebollada, J., G. Clementi, …, A. M. Pozo. 2007. Silent mutations at the 5′-end of the cDNA of actinoporins from the sea anemone Stichodactyla helianthus allow their heterologous overproduction in Escherichia coli. *J. Biotechnol.* 127:211–221.

58. García-Linares, S., T. Maula, …, Á. Martínez-Del-Pozo. 2016. Role of the tryptophan residues in the specific interaction of the sea anemone Stichodactyla helianthus's actinoporin sticholysin II with biological membranes. *Biochemistry.* 55:6406–6420.

59. Rouser, G., S. Fkeischer, and A. Yamamoto. 1970. Two dimensional then layer chromatographic separation of polar lipids and determination of phospholipids by phosphorus analysis of spots. *Lipids.* 5:494–496.

60. Gasset, M., A. Martínez del Pozo, …, J. G. Gavilanes. 1989. Study of the interaction between the antitumour protein α-sarcin and phospholipid vesicles. *Biochem. J.* 258:569–575.

61. Gasset, M., M. Oñaderra, …, J. G. Gavilanes. 1991. Acid phospholipid vesicles produce conformational changes on the antitumour protein α-sarcin. *Biochim. Biophys. Acta.* 1080:51–58.

62. Gasset, M., J. M. Mancheño, …, J. G. Gavilanes. 1995. Spectroscopic characterization of the alkylated α-sarcin cytotoxin: analysis of the structural requirements for the protein-lipid bilayer hydrophobic interaction. *Biochim. Biophys. Acta.* 1252:43–52.

63. Gasset, M., J. M. Mancheño, …, J. G. Gavilanes. 1995. Thermal unfolding of the cytotoxin alpha-sarcin: phospholipid binding induces destabilization of the protein structure. *Biochim. Biophys. Acta.* 1252:126–134.

64. de Antonio, C., A. Martínez del Pozo, …, J. G. Gavilanes. 2000. Assignment of the contribution of the tryptophan residues to the spectroscopic and functional properties of the ribotoxin α-sarcin. *Proteins.* 41:350–361.

65. Schroeder, F., G. Nemecz, …, T. E. Thompson. 1988. Fluorescence properties of cholestatrienol in phosphatidylcholine bilayer vesicles. *Biophys. Chem.* 32:57–72.

66. Wolber, P. K., and B. S. Hudson. 1979. An analytic solution to the Förster energy transfer problem in two dimensions. *Biophys. J.* 28:197–210.

67. Holt, A., R. F. de Almeida, …, J. A. Killian. 2008. Is there a preferential interaction between cholesterol and tryptophan residues in membrane proteins? *Biochemistry.* 47:2638–2649.

68. Lakowicz, J. R. 2006. Principles of Fluorescence Spectroscopy. Springer, New York.

69. Loura, L. M., A. Fedorov, and M. Prieto. 1996. Resonance energy transfer in a model system of membranes: application to gel and liquid crystalline phases. *Biophys. J.* 71:1823–1836.

70. Vos, W. L., R. B. Koehorst, …, M. A. Hemminga. 2005. Membrane-bound conformation of M13 major coat protein: a structure validation through FRET-derived constraints. *J. Biol. Chem.* 280:38522–38527.

71. Chen, R. F. 1967. Fluorescence quantum yields of tryptophan and tyrosine. *Anal. Lett.* 1:35–42.

72. Davenport, L., R. E. Dale, …, R. B. Cundall. 1985. Transverse location of the fluorescent probe 1,6-diphenyl-1,3,5-hexatriene in model lipid bilayer membrane systems by resonance excitation energy transfer. *Biochemistry.* 24:4097–4108.

73. Smaby, J. M., M. M. Momsen, …, R. E. Brown. 1997. Phosphatidylcholine acyl unsaturation modulates the decrease in interfacial elasticity induced by cholesterol. *Biophys. J.* 73:1492–1505.

74. Li, X. M., J. M. Smaby, …, R. E. Brown. 2000. Sphingomyelin interfacial behavior: the impact of changing acyl chain composition. *Biophys. J.* 78:1921–1931.

75. Hresko, R. C., I. P. Sugár, …, T. E. Thompson. 1987. The lateral distribution of pyrene-labeled sphingomyelin and glucosylceramide in phosphatidylcholine bilayers. *Biophys. J.* 51:725–733.

76. Hresko, R. C., I. P. Sugár, …, T. E. Thompson. 1986. Lateral distribution of a pyrene-labeled phosphatidylcholine in phosphatidylcholine bilayers: fluorescence phase and modulation study. *Biochemistry.* 25:3813–3823.

77. Jones, M. E., and B. R. Lentz. 1986. Phospholipid lateral organization in synthetic membranes as monitored by pyrene-labeled phospholipids: effects of temperature and prothrombin fragment 1 binding. *Biochemistry.* 25:567–574.

78. Kullberg, A., O. O. Ekholm, and J. P. Slotte. 2015. Miscibility of sphingomyelins and phosphatidylcholines in unsaturated phosphatidylcholine bilayers. *Biophys. J.* 109:1907–1916.

79. Ipsen, J. H., G. Karlström, …, M. J. Zuckermann. 1987. Phase equilibria in the phosphatidylcholine-cholesterol system. *Biochim. Biophys. Acta.* 905:162–172.

80. Nyholm, T. K., D. Lindroos, …, J. P. Slotte. 2011. Construction of a DOPC/PSM/cholesterol phase diagram based on the fluorescence properties of trans-parinaric acid. *Langmuir.* 27:8339–8350.

81. Wang, T. Y., and J. R. Silvius. 2003. Sphingolipid partitioning into ordered domains in cholesterol-free and cholesterol-containing lipid bilayers. *Biophys. J.* 84:367–378.

82. Björkqvist, Y. J., T. K. Nyholm, …, B. Ramstedt. 2005. Domain formation and stability in complex lipid bilayers as reported by cholestatrienol. *Biophys. J.* 88:4054–4063.

83. Koivusalo, M., J. Alvesalo, …, P. Somerharju. 2004. Partitioning of pyrene-labeled phospho- and sphingolipids between ordered and disordered bilayer domains. *Biophys. J.* 86:923–935.

84. Gasset, M., J. A. Killian, …, B. de Kruijff. 1988. Influence of cholesterol on gramicidin-induced HII phase formation in phosphatidylcholine model membranes. *Biochim. Biophys. Acta.* 939:79–88.

85. Schiffer, M., C. H. Chang, and F. J. Stevens. 1992. The functions of tryptophan residues in membrane proteins. *Protein Eng.* 5:213–214.

86. Dougherty, D. A. 1996. Cation-π interactions in chemistry and biology: a new view of benzene, Phe, Tyr, and Trp. *Science.* 271:163–168.

87. White, S. H., and W. C. Wimley. 1998. Hydrophobic interactions of peptides with membrane interfaces. *Biochim. Biophys. Acta.* 1376:339–352.

88. Lönnfors, M., J. P. Doux, …, J. P. Slotte. 2011. Sterols have higher affinity for sphingomyelin than for phosphatidylcholine bilayers even at equal acyl-chain order. *Biophys. J.* 100:2633–2641.

89. Slotte, J. P. 2016. The importance of hydrogen bonding in sphingomyelin's membrane interactions with co-lipids. *Biochim. Biophys. Acta.* 1858:304–310.

90. Yasuda, T., M. A. Al Sazzad, …, J. P. Slotte. 2016. The influence of hydrogen bonding on sphingomyelin/colipid interactions in bilayer membranes. *Biophys. J.* 110:431–440.

91. Castrillo, I., N. A. Araujo, …, M. Bruix. 2010. Specific interactions of sticholysin I with model membranes: an NMR study. *Proteins.* 78:1959–1970.

92. López-Castilla, A., F. Pazos, …, J. R. Pires. 2014. Solution NMR analysis of the interaction between the actinoporin sticholysin I and DHPC micelles–correlation with backbone dynamics. *Proteins.* 82:1022–1034.

93. Pettersen, E. F., T. D. Goddard, …, T. E. Ferrin. 2004. UCSF Chimera–a visualization system for exploratory research and analysis. *J. Comput. Chem.* 25:1605–1612.

Biophysical Journal, Volume *116*

Supplemental Information

Sticholysin, Sphingomyelin, and Cholesterol: A Closer Look at a Tripartite Interaction

Juan Palacios-Ortega, Sara García-Linares, Esperanza Rivera-de-Torre, José G. Gavilanes, Álvaro Martínez-del-Pozo, and J. Peter Slotte

Supplemental information

Sticholysin, Sphingomyelin, and Cholesterol: A Closer Look at a Tripartite Interaction.

Juan Palacios-Ortega[1,2], Sara García-Linares[1,3], Esperanza Rivera-de-Torre[1], José G. Gavilanes[1], Álvaro Martínez-del-Pozo[1]* and J. Peter Slotte[2]*

[1] Departamento de Bioquímica y Biología Molecular, Universidad Complutense, Madrid 28040, Spain

[2] Biochemistry, Faculty of Science and Engineering, Åbo Akademi University, 20500 Turku, Finland

[3] Present address: Cell Biology Department, Harvard Medical School, Boston, MA 02115, USA

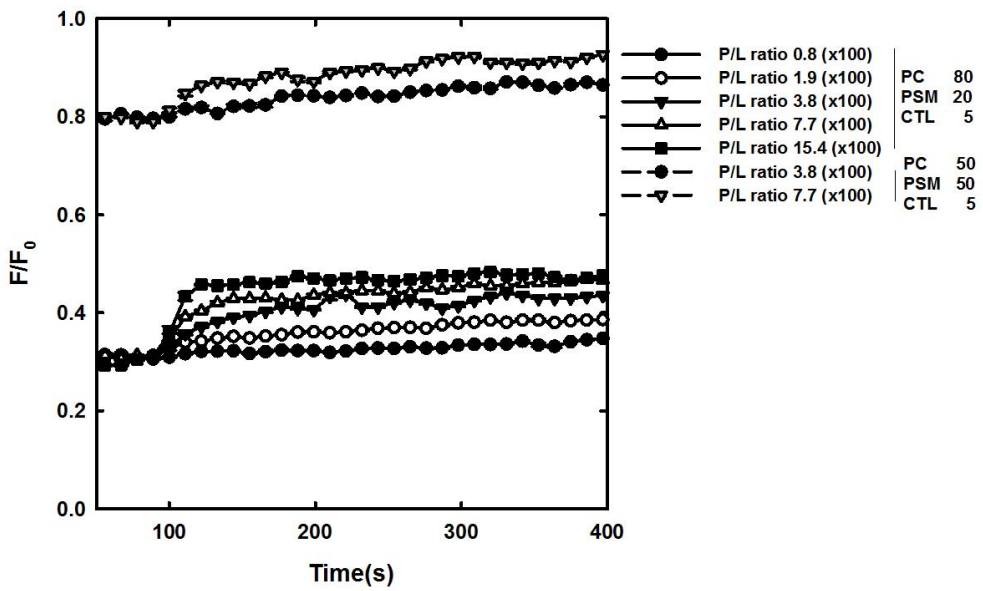

Figure S1. Representative F/F_0 traces of CTL emission as a function of time for different P/L ratios and membrane compositions. StnII was added at 100 s.

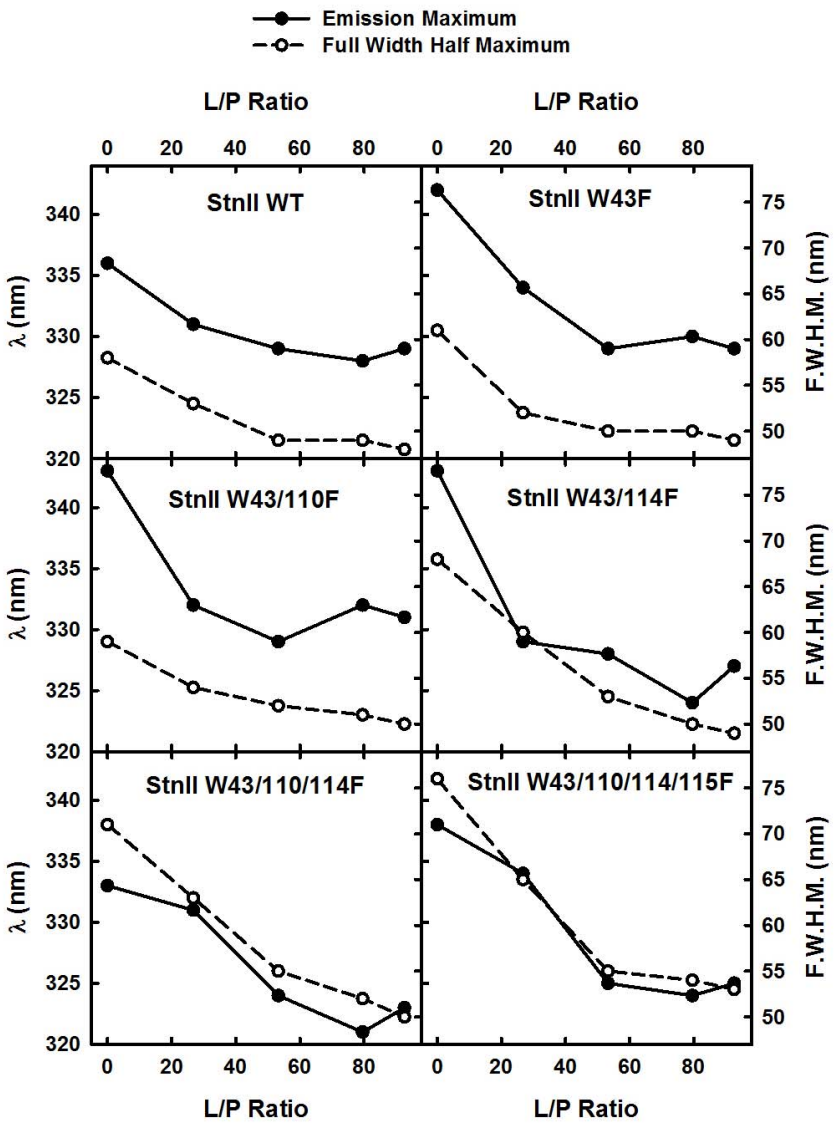

Figure S2. Graphs showing the change in the emission maximum (the right axis) and spectral width, measured as the full width at half of the maximum (FWHM, the left axis), for the emission spectra of StnII WT and the W mutants when titrated with vesicles composed of DOPC:eSM:Chol 1:1:1. The scales are the same for all panels.

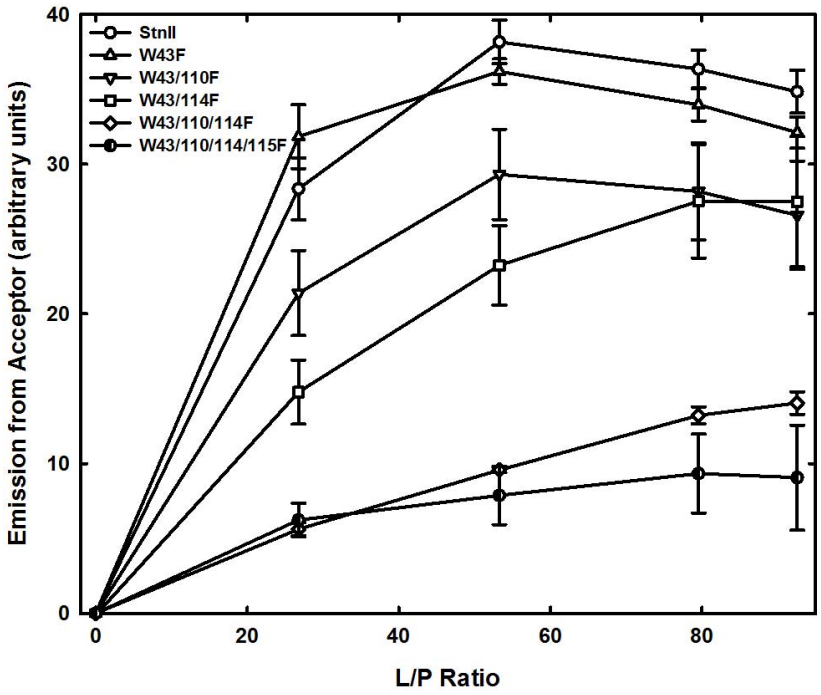

Figure S3. Representation of the energy transfer efficiency from StnII WT, or its Trp mutants studied, to CTL when titrated with DOPC:eSM:Chol:CTL (33:33:28:5) vesicles. The excitation wavelength employed was 260 nm. The spectra were recorded at 25 ºC. The protein concentration was 200 nM in all experiments shown. Fluorescence intensities were normalized to 1.0 for the maximum emission of StnII WT in buffer, in the absence of vesicles. Each value is the mean $\pm$ standard error on n=3.

BBA - Biomembranes 1862 (2020) 183311

Contents lists available at ScienceDirect

BBA - Biomembranes

journal homepage: www.elsevier.com/locate/bbamem

Evaluation of different approaches used to study membrane permeabilization by actinoporins on model lipid vesicles

Juan Palacios-Ortega[a,b], Esperanza Rivera-de-Torre[a,b], José G. Gavilanes[a], J. Peter Slotte[b,*], Álvaro Martínez-del-Pozo[a,**]

[a] Departamento de Bioquímica y Biología Molecular, Universidad Complutense, Madrid, Spain
[b] Biochemistry, Faculty of Science and Engineering, Åbo Akademi University, Turku, Finland

ARTICLE INFO

Keywords:
Pore-forming-proteins
Leakage
Calcein
Rhodamine
Terbium
NBD-dithionite

ABSTRACT

Release of aqueous contents from model lipid vesicles has been a standard procedure to evaluate pore formation efficiency by actinoporins, such as sticholysin II (StnII), for the last few decades. However, regardless of the probe of choice, the results reported that StnII action was never able to empty the vesicles completely. This was hard to explain if StnII pores were to be stable and always leaky for the probes used. To address this question, we have used a variety of probes, including rhodamine 6G or Tb^{3+}, to test the permeability of StnII's pores. Our results indicate that calcein was in fact too large to fit through StnII's pores, and that the standard method in the field is actually reporting StnII-induced transient permeation of the membrane rather than the passage of solutes through the stable assembled pores. In order to evaluate the permeability of these structures, we used a dithionite-based assay, which showed that the final pores were in fact open. Thus, our results indicate that the stable actinoporins' pores are open in spite of plateaued classic release curves. Besides the proper pore, the first stages of pore formation would inflict serious damage to living cells as well.

1. Introduction

Sea anemone actinoporins represent an optimal system to study the transition from a water-soluble monomeric protein conformation to an oligomeric transmembrane pore [1–3]. These pore-forming toxins constitute multigenic families that have been detected in many sea anemone species [3–7]. However, only four of them have been characterized in detail: Sticholysins I and II (StnI and StnII, respectively) from *Stichodactyla helianthus* [1–3], equinatoxin II from *Actinia equina* [4,8], and fragaceatoxin C from *Actinia fragacea* [9]. All show almost identical monomeric water-soluble three-dimensional structure composed of a β-sandwich motif flanked by two α-helices [10–15]. One of these helices, located at the N-terminal end, is responsible for the actual formation of the pore penetrating the membrane [16–22]. The incorporation of these proteins to the bilayer depends largely on the lipid composition and the physicochemical properties of the membrane [8,20,23–31]. Sphingomyelin (SM) is required [26,32–34], but other factors, such as the presence of sterols, the coexistence of various phases or domains, lateral packing, fluidity, membrane thickness, and the strength of the SM interfacial hydrogen bonding network, have a strong influence on the pore-forming ability of these proteins [20,26,28–31,34–47].

Almost forty years have passed since it was demonstrated, using different K^+ or Ca^{2+} containing solutions, that these proteins form cation-selective pores at neutral pH [23,35,48–52]. Altogether, those studies evidenced that actinoporins increase cell membrane permeability for monovalent and divalent cations. Only a few years later, these pores were also characterized using different electrophysiological approaches, including the use of lipid planar membranes. These studies confirmed their specificity for cations and revealed a pore size in the order of 1–2 nm of radius [16,49–52]. In fact, the only two available crystalline structures of actinoporin pores fit rather well within this size range (Fig. 1) [13,15]. Interestingly, despite the specificity of the pore for cations, most researchers in the field, including us, have been using negatively charged fluorophores, such as calcein or carboxyfluorescein, as the main probes to explore the molecular features of these pores. In this work, we challenge this approach and suggest a more sensitive procedure to study the pore-forming mechanism of these intriguing metamorphic proteins.

Abbreviations: $C_{12}E_8$, octaethylene glycol monododecyl ether; Chol, cholesterol; DOPC, 1,2-dioleoyl-sn-glycero-3-phosphocholine; eSM, egg sphingomyelin; LUV, large unilamelar vesicle; POPE-NBD, 1,2-dioleoyl-sn-glycero-3-phosphoethanolamine-N-(7-nitro-2-1,3-benzoxadiazol-4-yl); SM, sphingomyelin; Stn, sticholysin

* Correspondence to: J.P. Slotte, Biochemistry, Faculty of Science and Engineering, Åbo Akademi University, 20520 Turku, Finland.
** Correspondence to: Á. Martínez-del-Pozo, Departamento de Bioquímica y Biología Molecular, Universidad Complutense, 28040 Madrid, Spain.
E-mail addresses: jpslotte@abo.fi (J.P. Slotte), alvaromp@quim.ucm.es (Á. Martínez-del-Pozo).

https://doi.org/10.1016/j.bbamem.2020.183311
Received 26 December 2019; Received in revised form 12 March 2020; Accepted 13 April 2020
Available online 27 April 2020
0005-2736/

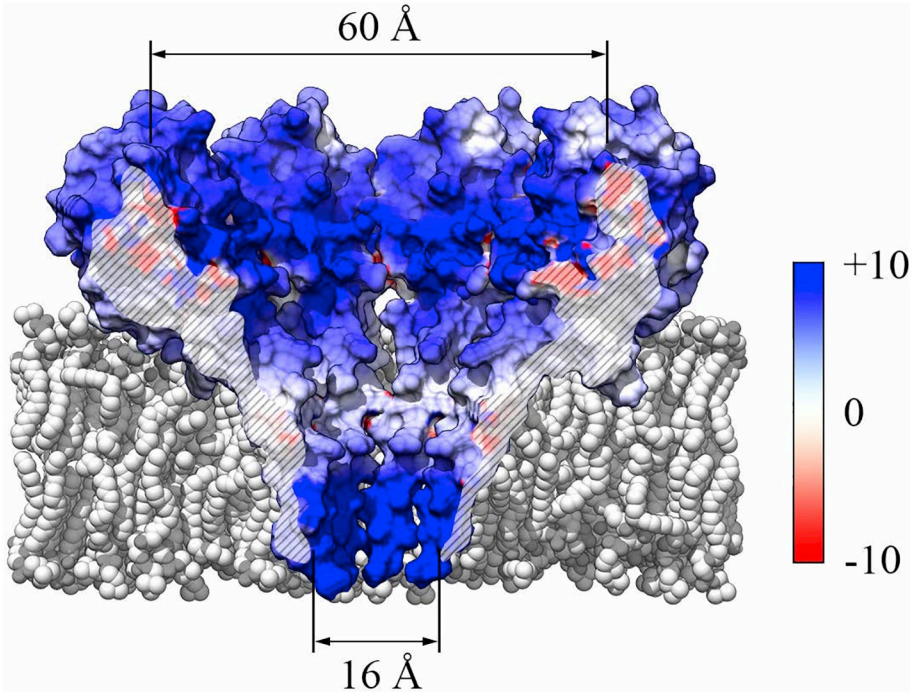

Fig. 1. Three-dimensional structure of the octameric pore of the actinoporin sticholysin II, obtained by matching StnII monomeric structure (PDB ID: 1GWY) to the octameric pore structure of fragaceatoxin C obtained in presence of detergents (PDB ID: 4TSY) [15]. The helix was constructed based on the known sequence of StnII and fitting it to the same structure. The pore has a narrowest constriction of ~16 Å in its cytoplasmic side, opening to ~60 Å in its upper vestibule. Surface was coloured according to the electrostatic potential in the protein, as calculated using APBS *via* the UCSF Chimera software [82]. The protein was prepared for APBS using the PDB2PQR tool *via* UCSF Chimera as well. Units are k_BT/e_c. Striped areas on the sides of the pore are used to outline the lumen of the pore, and enclose, approximately, the surfaces of monomer-monomer contacts as well as voids that seem to be occupied by lipids [15].

2. Materials and methods

2.1. Materials

Calcein, Rhodamine 6G, terbium chloride, dextran-labeled fluorescein, Triton X-100 and octaethylene glycol monododecyl ether (C12E8) were obtained from Sigma-Aldrich (St. Louis, MO). Cholesterol (Chol), egg sphingomyelin (eSM), 1,2-dioleoyl-sn-glycero-3-phosphocholine (DOPC), and 1,2-dioleoyl-sn-glycero-3-phosphoethanolamine-N-(7-nitro-2-1,3-benzoxadiazol-4-yl) (POPE-NBD) were from Avanti Polar Lipids (Alabaster, AL). StnII was produced in *Escherichia coli* RB791 and purified to homogeneity as described in [53].

2.2. Preparation of vesicles

Briefly, large unilamelar vesicles (LUVs) were made by extruding resuspended DOPC:eSM:Chol (1:1:1) dried lipid films as previously described [20–22,30]. This composition is the standard used in the actinoporin field, providing both recognition targets (SM) as well as the most appropriate physicochemical properties [20,22,30,31,37,38,42,43,45,47,54]. Lipid films were made from a methanol mixture of the desired lipids dried under nitrogen flow. This film was later kept under vacuum for at least 2 h to ensure complete elimination of the organic solvent. Specific details for each set of pore-forming experiments are provided in the following sections. In all cases, when measuring the release of encapsulated solutes (see below) and in order to ensure that no spontaneous leakage occurred, fluorescence emission was recorded for 5 min before toxin addition. A steady signal level, indicating intact vesicles, was observed for all samples and experiments described below.

2.3. Calcein release

Calcein-entrapped LUVs were prepared by extrusion through 200 nm filters at 60 °C [20–22,30,34,47]. Tris buffer (10 mM Tris, 140 mM NaCl, pH 7.4) containing calcein at 100 mM was employed. LUVs were separated from non-entrapped calcein by gel filtration on Sephacryl S200HR [20–22,30,34] and then used for permeabilization studies within 8 h of preparation. LUVs lipid concentration was 0.25–0.5 mM before extrusion. Lipid concentration during the calcein leakage experiments was 2.5 μM. The volume of the samples was 2.0 mL. Emission at 550 nm (emission at the 505 nm maximum was high enough as to damage the spectrofluorimeter's photomultipliers) was followed at 23 °C as a function of time (λ_{ex} = 480 nm). Fluorescence emission was measured in a PTI Quanta-Master spectrofluorimeter (Photon Technology International, Inc., Birmingham, NJ, USA). Fraction of calcein released was determined based on maximum calcein release induced by LUV disintegration using 10 μL of 10% v/v Triton X-100.

2.4. Rhodamine 6G release

Rhodamine 6G (R6G) was first diluted in distilled water to saturation. A 5× aliquot of the Tris buffer, detailed in the previous paragraph, was added to the R6G solution. R6G precipitate was removed by centrifugation. R6G concentration in encapsulation buffer was then approximately 5 mM. LUVs were again used for permeabilization studies within 8 h. Lipid concentration was the same as for calcein assays. Emission was followed at 555 nm at 23 °C as a function of time, using 525 nm excitation. Maximum release was obtained by LUVs disintegration using 10 μL of 20 mM $C_{12}E_8$. Triton X-100 was not used because it quenched R6G emission.

2.5. Terbium release

Terbium release experiments were performed using a standard protocol [55,56], with minor adaptations regarding lipid concentrations. HEPES buffer was used instead of TES. Vesicles were extruded through 400 nm filters to increase the amount of cation encapsulation and therefore increasing the sensitivity of the subsequent measurements. Fluorescence emission was recorded at 545 nm, using 270 nm excitation. Terbium must be chelated in order to remain soluble [57]. Thus, it was encapsulated chelated with citrate, with which it forms a very weakly fluorescent complex. Upon membrane permeabilization, and subsequent release, citrate is easily displaced from the complex by the impermeant aromatic chelator dipicolinic acid (DPA), located outside of the vesicles (Fig. 4). The assay is based on recording the fluorescence increase by the interaction established between the Tb^{3+} released from the interior of the vesicles and DPA. The enhancement of

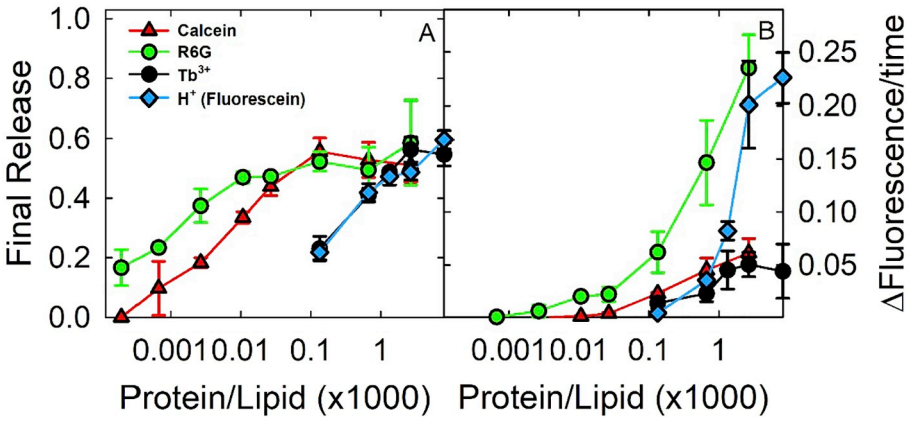

Fig. 2. Leakage experiments. (A) Percentages of final release after 5 min and (B) maximal rates of leakage of different molecules or ions entrapped in DOPC/SM/Chol (1:1:1) vesicles by StnII at different protein/lipid molar ratios. The ions used were calcein (red), rhodamine 6G (green), Tb^{3+}:citrate (black), and H^+ (fluorescein) (blue). Release was measured at 23 °C. All intensities were normalized. At the end of the measurement, a suitable detergent was added to dissolve the LUVs and obtain 100% of release. The results shown are representative of two or three different independent experiments. Each value is the average ± SEM. (For interpretation of the references to colour in this figure legend, the reader is referred to the web version of this article.)

terbium fluorescence by DPA is due to energy transfer from its aromatic ring. Due to inner filter effects, the use of Triton X-100 had to be avoided. Instead, reduced Triton X-100, which lacks the absorption band at 270 nm, was employed. Protein absorption at 270 nm was negligible at the protein concentrations assayed.

2.6. Proton release

Proton release from LUVs was measured monitoring the change in fluorescence emission of fluorescein. Fluorescein absorption spectra undergoes a significant change upon pH increase, with a new absorption maximum appearing at 488 nm, thus increasing absorption and, consequently, emission if excited at that wavelength. StnII activity should allow for proton efflux and consequent pH increase inside the vesicle. Fluorescein coupled to 3000 Da dextran was used to avoid fluorescein release from LUVs. The fluorescein-dextran complex was encapsulated at a concentration of 5 μM. The buffer was 10 mM sodium phosphate. pH was set to 4.2 inside of the LUVs, while the pH outside was kept at 7.2. Emission was recorded at 520 nm. Maximum emission was again obtained using Triton X-100 as in the calcein assays.

2.7. Peptide-induced membrane perturbation models

Experimental data from the leakage experiments were fitted by the following model:

$$\frac{F_{obs}(t)}{F_{\max}} = 1 - \exp(J_2(e^{-\nu_{relax}t} - 1)) \quad (1)$$

as defined by Andersson et al. [58]. Briefly, the model describes release curves produced by the release of aqueous contents induced by transient perturbations affecting the membrane. Once the system reached equilibrium, the perturbations cease and leakage is no more, regardless of the probe concentration in the inside and outside compartments. Here on, this model will be referred to as the perturbation model.

The model has two parameters. J_2 is proportional to the magnitude of the perturbations and, if the model fits nicely the experimental data, it can be obtained straight from $J_2 = 1 - \ln|1 - L_{\max}|$, where $L_{\max}$ is the value of the final, maximum release. ν_{relax} is related to the lifetime of the perturbations. It can be shown that the product $J_2.\nu_{relax}$ is equal to the slope of the release curves at $t = 0$.

2.8. Equilibrium pore assay

In order to evaluate transient non-equilibrium leakage phenomena, a modification of a previously described method was employed [56]. DOPC:eSM:Chol (1:1:1) LUVs containing 1 mol% of POPE-NBD were prepared. A freshly prepared solution of 0.6 M sodium dithionite in 1.0 M sodium phosphate buffer, pH 10, was employed to quench the emission of NBD in the outer leaflet. The experiments were performed by recording the fluorescence emission at 520 nm, using an excitation wavelength of 470 nm. Two different types of experiments were performed. In the first set of measurements, the vesicles were first incubated with different StnII concentrations for 90 s and then dithionite was added to final concentration of 55 mM. When a steady fluorescence emission signal was obtained, Triton X-100 was used as describe above to disintegrate the vesicles. The total drop in fluorescence was considered as the maximum effect exerted by dithionite, corresponding to reduction of all NBD molecules present in the sample. In the second set of experiments, dithionite was added first. This produced a fluorescence drop of about 50%, corresponding to reduction of POPE-NBD molecules on the outer layer of the membrane. Then, StnII was added and fluorescence was further recorded. As in the first set of experiments, vesicles were also disintegrated with Triton X-100 once reached a steady signal was reached.

3. Results

3.1. Calcein leakage

The initial aim of this study was to assess the suitability of the calcein-release approach, a well-established assay for evaluating the pore forming ability of actinoporins [20–22,24,25,27,30,31,47,51,52,59–61]. We used StnII, which has been thoroughly characterized previously, to compare the efficacy of the different approaches to the calcein release assay [20–22,30,31,43,45,47]. Calcein release experiments yielded the results shown in Fig. 2. Thus, incubation of calcein-entrapped vesicles with StnII at different protein/lipid ratios reached a plateau representing the release of only about 60% of the total fluorophore contained into the vesicles (Fig. 2A). The LC_{50} value, defined as the concentration of protein needed to obtain a final release of 50% of the maximum protein-induced release, was 52 pM (Table 1).

Most standard methods used to analyze actinoporin-induced calcein release usually rely on recording the percentage of fluorophore leaked, as calculated based on total fluorescence intensities, after a fixed amount of time. This methodological approach can artificially reduce the observed differences when using high actinoporin concentrations [31]. Thus, the maximum rate values of fluorophore release were also quantitated for the different protein/lipid ratios employed. These

Table 1
Parameters obtained from each leakage assay.

Assay	LC_{50} (nM)	Release rate at 20 nM (ΔF/s)	Saturation (% of release)
Calcein	0.052	0.061	53.2
R6G	0.009	0.235	53.5
Tb^{3+}	1.990	0.051	55.1
H^+ (fluorescein)	2.880	0.201	62.5

second set of results, shown in Fig. 2B, can be considered to represent a much more valuable parameter, containing information about both kinetic and dye-release proficiency. Considering the calcein-leakage experiments, the maximum release rate obtained at saturating concentrations of StnII (20 nM protein concentration, corresponding to a protein/lipid molar ratio of 8×10^{-3}) was 0.061 ΔF units/s (Table 1).

3.2. Rhodamine 6G leakage

Rhodamine 6G release rate (Fig. 2) was almost four-fold faster than the value obtained for calcein leakage (Table 1) at the mentioned saturating protein/lipid ratio of 8×10^{-3}. Accordingly, the LC_{50} value was also in the order of six-fold lower (Table 1). Quite unexpectedly, however, the final plateau of maximum fluorophore release did correspond again to only about 60% of the originally encapsulated probe (Fig. 2A). R6G was released much faster but the final percentage of probe release was essentially identical to the value found for calcein.

3.3. Cation (Tb^{3+} or H^+) leakage

In order to assess the ability of small cations to go through the actinoporins pore, two different assays were performed. First, the permeability of StnII pores to the lanthanide Tb^{3+} was tested. Second, we assessed the possibility of protons crossing the pore by recording the pH-sensitive emission of an encapsulated dextran-fluorescein derivative.

In both cases, very poor release values were observed, not only in kinetic terms but also considering the final release of the contents, measured at saturating concentrations (Fig. 2 and Table 1). Final release never exceeded 60%, as for the previous assays (Fig. 2A). In this case, the LC_{50} values were 1.99 and 2.88 nM for Tb^{3+} and H^+, respectively. These values were larger than those obtained for calcein or R6G release experiments. The maximum rate value of Tb^{3+} release for saturating StnII protein/lipid ratio was even lower than the value obtained for calcein (Table 1). Proton leakage was much faster (Table 1) but only at very high protein concentration (Fig. 3B). In fact, the corresponding curve was highly cooperative (Fig. 3B) probably reflecting the protonation of some key residues located at the lumen of the pore (see Discussion).

3.4. Kinetic and protein concentration-dependence modeling

The perturbation model [58] was used to evaluate the experimental leakage data. For all four types of reporters employed (calcein, R6G, Tb^{3+}:citrate, and H^+-fluorescein) the model provided very good fits (Fig. S1), indicating the consistency of the data with the theoretical basis of the model.

3.5. Equilibrium pore assays

Transient permeabilization refers to the disruption of bilayer integrity while subjected to the action of a pore forming polypeptide. In all previous assays, protein-membrane interaction took place when the tracing molecules *had already* been encapsulated. Thus, those assays cannot differentiate transient permeabilization from actual flux through the pore. With the aim of discerning the influence of this potential transient permeabilization on the rate and efficiency of actinoporins pore-formation, different experiments were performed using DOPC:eSM:Chol (1:1:1) LUVs containing 1 mol% of POPE-NBD (Fig. 3). NBD was quenched using sodium dithionite, which can be added to the sample both *before* or *after* protein-membrane interaction takes place. This way, actual flux through the pore, ruling out influence of transient permeabilization, can be measured.

As shown in Fig. 4A, incubation of NBD-labeled vesicles with sodium dithionite produced around a 40% decrease of the NBD fluorescence emission at 520 nm. This result not only confirmed the

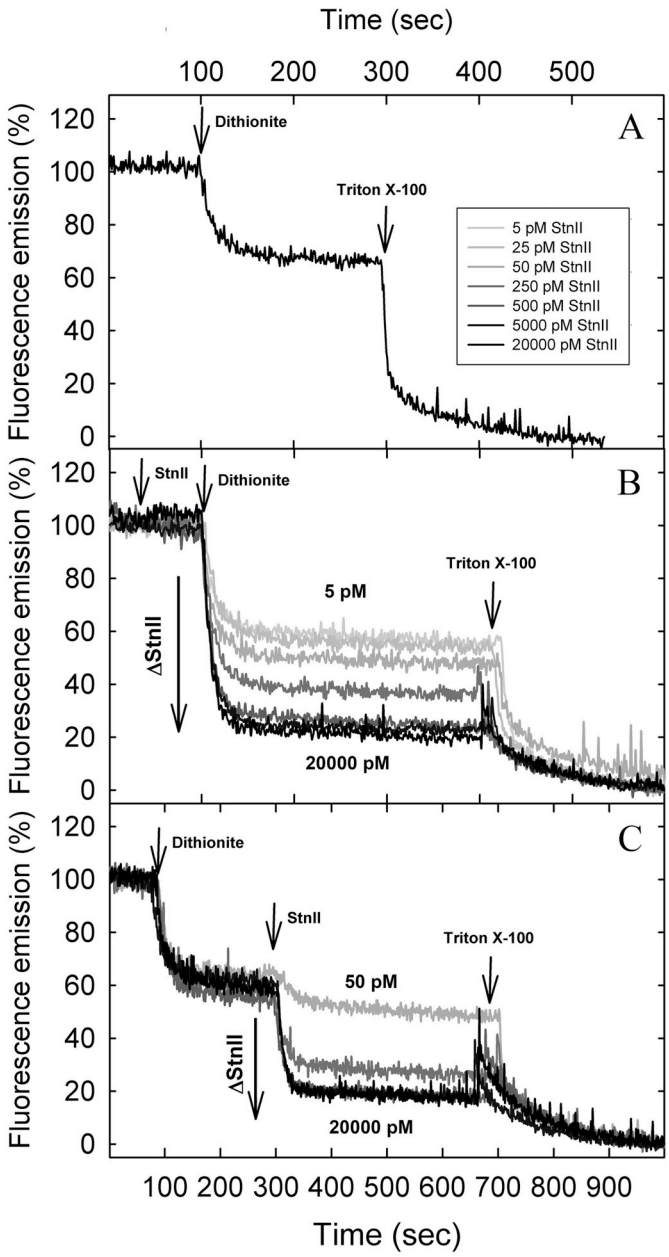

Fig. 3. Equilibrium pore assays. Sodium dithionite was added (final concentration 55 mM) to DOPC:eSM:Chol (1:1:1) LUVs containing 1 mol% of POPE-NBD. (A) The vesicles were first incubated with dithionite, and then were completely disintegrated by the addition of Triton X-100 to a final concentration of 0.045% v/v. (B) Same as in (A) but the vesicles were previously incubated with increasing concentrations of StnII. (C) Dithionite was added first, then the actinoporin StnII and, finally, the remaining vesicles were also disintegrated with Triton X-100. The protein concentrations employed were 5 pM, 25 pM, 50 pM, 250 pM, 0.5 nM, 5 nM and 20 nM.

availability to the reducing agent of most of the NBD located at the outer leaflet but also the impermeability of the intact membrane to the reducing agent (at these short time frames). In good agreement with this hypothesis, lysis of the membranes with Triton X-100 was enough to quench the remaining 60% NBD-emission. Theoretically, the fluorescence drop should be more similar and quite close to 50% in both cases. However, Triton X-100 produces a distortion in NBD fluorescence, which has not been discounted in the raw experiments shown in Fig. 3.

In a second set of experiments, these vesicles were incubated with increasing concentrations of StnII for long enough to assume the

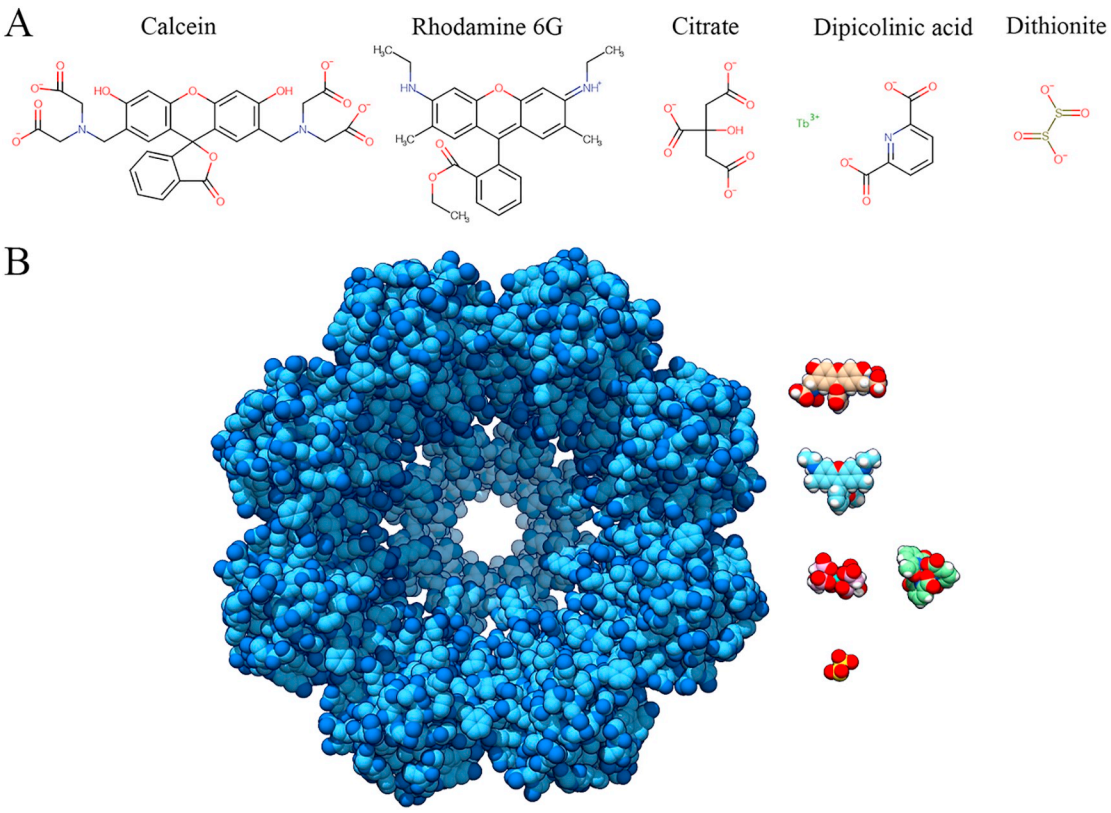

Fig. 4. (A) Chemical structures of the molecules used in this work to estimate release rates and extent through actinoporins' pores. Formula weights of the molecules and the complexes they form are: Calcein (FW 623), Rhodamine 6G (FW 479), Tb^{3+} (FW 160) in complex with two molecules of citrate (FW 189; FW of the complex 543, in practice, size is that of a ~400 Da complex), Tb^{3+} in complex with three molecules of DPA (FW 165; FW of the complex 654, in practice, size is that of a ~510 Da complex), and dithionite (FW 174). Proton is omitted in the figure. (B) Cartoon illustrating the relative size of the complexes shown above, as compared to the StnII pore from Fig. 1, using CPK representation. Tb^{3+} is shown in a 1:2 complex with citrate (pink) and a 1:3 complex with DPA (light green). Formulas were made using the Marvin 19.22 (2019) software from ChemAxon. Three-dimensional representations are rendered using UCSF Chimera [82]. (For interpretation of the references to colour in this figure legend, the reader is referred to the web version of this article.)

formation of stable protein pores. Interestingly, the subsequent addition of dithionite resulted in an almost complete quenching of all fluorescence emission, of very similar magnitude as the Triton X-100 addition in the first experiment described. Consequently, further addition of this detergent to the samples only produced a small effect on the intensity of the emission (Fig. 3B).

The third series of experiments was carried out reversing the order of the reagents involved. The vesicles were first incubated with dithionite, which yielded the already observed fluorescence decrease of ~40% (Fig. 3A and C). Once a stable signal was reached, the protein was then added, again in increasing concentrations. When the amount of protein was large enough to exert a saturating effect, the fluorescence was extinguished for a further 40%. The subsequent addition of Triton X-100 produced quenching of the remaining 20% fluorescence emission. This final effect is most likely a consequence of to the aforementioned effect of Triton X-100 on NBD emission.

Considering these sets of experiments, it could be concluded that, independently of the presumable transient permeability of some pore intermediates, an equilibrium was finally reached and the final stable StnII pores were permeable to the dithionite anion ($S_2O_4^{2-}$).

4. Discussion

The very first articles in which the cation-specificity and dimensions of actinoporin pores were established were mainly based on electrophysiological measurements [23,26,35,49,50]. However, many of the later reports were obtained using bulkier experiments based on the employment of artificial lipid vesicles. These studies focused on deciphering the actinoporins' pore formation mechanism by means of measuring the release of encapsulated fluorophores, such as calcein [14,20–22,24,25,30,31,34,42–45,47,54] or carboxyfluorescein [62–66]. This is however a striking remark, considering that not only calcein and carboxyfluorescein are negatively charged at the pH values employed in all those experiments, but that they also have hydrodynamic radii of about 0.74 [67] and 0.50 nm [68], respectively (Fig. 4 and Table 2). Those are smaller values than actinoporins' pore radius but quite close to the 1–2 nm values reported in the literature (Fig. 1) [12,13,15,16,26,49–52,69]. In fact, it was using liposomes encapsulating NADH (net charge of −2) and dextran FD-4 (0.6 nm and 1.2 nm Stokes radius, respectively) (Table 2) [70] that it was confirmed that StnII pores on SM-containing liposomes show a hydrodynamic pore

Table 2
Estimated ionic radius for the different ions or fluorescence probes used in this and other studies.

Ion	Calcein	Rhodamine 6G	Carboxyfluorescein	Terbium	H^+	Dithionite	Potassium	Calcium	NADH	Dextran FD-4
Estimated radius (nm)	0.74	0.59	0.50	0.12	0.10[a]	0.20[b]	0.14	0.10	0.60	1.40

[a] [81].
[b] Estimated approximate value for dithionite ($S_2O_4^{2-}$). For comparison, SO_4^{2-} ionic radius is 0.26 nm.

size within the mentioned range. NADH leaked out of the vesicles, while FD-4 remained encapsulated under identical assay conditions [26], a result in good agreement with the dimensions later found in the most accepted actinoporin pore crystalline structure [15]. In this example, the actinoporin fragaceatoxin C, isolated using detergents, assembles into an octameric pore with an inner radius ranging between 3.0 nm at the upper vestibule side, and 0.8 nm at is narrowest constriction connected to the vesicle's lumen (Fig. 1). Therefore, though the actinoporins' pore seems to be selective for atomic cations, the calcein-release assay would rather measure the actinoporin-induced membrane permeability to negatively charged solutes of ~700 Da. These measurements would account mostly for StnII molecules destabilizing the membrane while assembling into the final oligomeric pore structures (see below).

R6G is a cationic water-soluble highly fluorescent probe (Fig. 2). Thus, it was initially considered as a better molecule to evaluate the actinoporins' pore forming ability. In good agreement with this working hypothesis, the R6G release rate was much faster. Its maximum value was about 3.7-fold higher at the saturating protein/lipid molar ratio of 8×10^{-3}, in comparison with the values obtained for calcein release experiments (Fig. 2 and Table 1). Therefore, as expected, the net charge of the fluorophore probe employed would be a key factor for membrane pore-mediated permeation by actinoporins. However, and quite intriguingly, in both types of assays final leakage at saturating protein concentrations was plateaued at only 60% of the fluorescence intensity, referred to the intensity obtained in the presence of a detergent concentration (Triton X-100 or $C_{12}E_8$) producing 100% of vesicle lysis. Taking into account the very similar size of R6G (hydrodynamic radius of about 0.59 nm [71]; Table 2) and the negatively charged NADH, calcein, and carboxyfluorescein molecules (Fig. 4), these results suggest a pore-forming mechanism where membrane impermeability, regarding these molecules, would be initially compromised, but later restored, after reaching the final equilibrium of protein integration into the membrane. A mechanism suggesting that the initial leakage observed was not due to stable pore-formation but rather to the transient appearance of intermediates that compromise membrane integrity. This interpretation would also agree with several articles that have convincingly suggested the existence of different actinoporin protomer arrangements capable of transiently altering membrane permeability [18,19,69,72–78]. According to this interpretation, once the final and thermodynamically stable pores are formed [15], neither calcein nor R6G would have the right size to keep on crossing the membrane through the pore lumen and, consequently, would remain within the vesicles. After all, the hydrodynamic ionic radii of Ca^{2+} and K^+, which are supposed to be the natural cations flowing through the actinoporins pore lumen [23,35,48–52], are only about 0.10 and 0.14 nm, respectively, much smaller than the radius estimated for calcein, carboxyfluorescein, or R6G (Table 2).

Smaller cations were also considered as potential probes for the study of actinoporins' pores. At first glance, the most obvious candidate was Tb^{3+}, which ionic radius is only ~0.12 nm, and emits light when chelated by DPA. Unfortunately, these experiments yielded very poor results in both kinetic and total final leakage terms (Fig. 2; Table 2). The easiest explanation resides in the fact that Tb^{3+} solubility in water is low and the assay is not feasible if Tb^{3+} is not chelated and solubilized by citrate. Tb^{3+} is chelated with two citrate ions, which each displays three negative charges, yielding Tb^{3+}:citrate complexes, which would have net charge of −3, and size much larger than expected (Fig. 4). The real situation would then be very similar to the one found with calcein or R6G: size would impede permeation thorough the pore lumen once the final thermodynamically stable structures are assembled. An alternative explanation would be that the assays cannot just be made with any atomic cation. At neutral pH, the channel seems to be quite specific. It has been described how Ni^{2+} can inhibit hemolysis exerted by equinatoxin II [50,51], another well-known actinoporin. From this point of view, and regardless of the chelation with citrate, Tb^{3+} might have not been a good option either.

Leakage of protons can be monitored using a pH sensitive fluorescent probe bound to dextran of enough size as to be impermeable to the membrane permeabilization by actinoporins. This approach was also considered worth trying since protons are the smallest possible cations. LUVs containing fluorescein coupled to 3000 Da dextran were used to perform a fourth set of leakage experiments. The pH value was set to 4.2 inside of the LUVs, while the pH outside was kept at 7.2. Unfortunately, leakage was very slow and only noticeable at the highest StnII concentrations assayed (Fig. 2). This could be explained taking into account that it has been described how above pH 7.0 the membranes containing actinoporins pores are highly specific for K^+, whereas below pH 4.0 they are poorly selective [35], being its maximum at pH values of 8.0–9.0 [51]. The pK_a value for the mentioned titratable groups was found to be 5.0 [35]. Therefore, the assay herein described would not be measuring directly the proton permeability of the pores but rather the pH influence on their ion selectivity.

Another consideration to be discussed would be how this cation selectivity and the observed rectification of the actinoporins' pore channel have been already interpreted as being a reflection of charges asymmetrically distributed along the pore [50]. Electrophysiological experiments performed by other authors with Ca^{2+} solutions yielded results that were interpreted as the Ca^{2+} cations screening negatively charged groups along the channel, most probably carboxylate groups [35]. These groups would be also asymmetrically distributed, closer to the “entrance” of the channel, the wider opening in Fig. 1. Accordingly, these groups were not titratable from the other side, the narrower one. In summary, cation passage through the channel is not symmetrical and the experiments employing model lipid vesicles would measure the less favorable flow of cations exiting the vesicles interior from the narrow to the wider opening, when the pores seem to be designed to perform the opposite function: allowing cations in.

Transient permeation refers to the interruption of bilayer integrity while subjected to a pore-forming polypeptide. In fact, many peptide-induced membrane permeation events occur through unbalanced transient processes [56,79,80]. In these examples, leakage occurs only in the minutes immediately after peptide addition. The system then relaxes to a state where leaking slows down, or stops completely, despite the presence of the polypeptides in the bilayer. This concept has been coined for small membrane-disturbing peptides, such as melittin [80], for example, but in the view of the results shown here, it could be also applicable to actinoporins mechanism of action. In fact, the data was consistent with a previously published model that describes transient leakage through membrane perturbations [58], supporting our hypothesis.

This is a rather interesting conclusion, since the formation of transient pore conformations has been already described for actinoporins [8,19]. Therefore, the question that remained was whether Stn-induced leakage was solely due to transient permeation, as appears to be when calcein or R6G are the probes employed, or if pores remained open to other substances with suitable features. These aspects were then studied through the equilibrium pore experiments described in Fig. 3.

In a first set of experiments, the vesicles were incubated with increasing concentrations of StnII for long enough as to assume the formation of stable protein pores. Then, the subsequent addition of dithionite resulted in almost complete quenching of all fluorescence emission, suggesting that NBD would be available to dithionite at both sides of the bilayer. The reverse set of experiments was also performed as control. Dithionite was added first and, once it had reacted with all the NBD available at the outer lipid layer, increasing concentrations of StnII were added. Again, fluorescence quenching was complete, showing that the remaining reagent was also able to enter the vesicles. Altogether, all these experiments in Fig. 3 rather suggest that dithionite, a negatively charged but very small molecule, would be able to cross the channel of the actinoporins' pore. Even considering that the pores are cation-specific, size appears to be the key factor for allowing

passage, at least when using assays based on the measurement of molecule release from model lipid vesicles.

5. Conclusion

In the light of the experiments reported so far in the literature, and our own results shown here, we conclude that size, rather than charge, would be the key factor for discriminating passage through actinoporins pore. This assertion does not contradict the well-established fact that it is a cation specific channel, especially in kinetic terms, considering the asymmetry of the cations flow through the channel. Leakage observed using model lipid vesicles and the archetypical fluorescent probes generally employed in the field would most likely only reflect transient instability of membrane impermeability, probably mediated by dynamic, not completely assembled, pore intermediates, and initiated by helix insertion in the membrane. These intermediates, however, are of great significance for the molecular mechanism conducing to the final and more thermodynamically stable assemblies of the still controversial structure of actinoporins' pore. In our opinion, calcein can still be used with this purpose, but results should be interpreted with caution in the light of the new evidences shown here. R6G can be a better probe in terms of sensitivity but, as calcein, is too big for actinoporin's pores. Formation of competent pores should be checked using the NBD-dithionite assay.

Supplementary data to this article can be found online at https://doi.org/10.1016/j.bbamem.2020.183311.

Author contributions

JPO and ERT performed the experiments. All authors contributed to conceiving the project, designing the experiments, discussing and interpreting the results, and writing the manuscript.

Declaration of competing interest

The authors declare that they have no known competing financial interests or personal relationships that could have appeared to influence the work reported in this paper.

Acknowledgements

This research was supported by the Sigrid Jusélius Foundation, the Jane and Aatos Erkko Foundation, and the Magnus Ehrnrooth Foundation (to J.P.S.), and by UCM-Banco Santander grant PR75/18-21561 (to A.M.-d.-P.). J.P.-O. has a funded doctoral student position from ISB/ÅA. UCM-Banco Santander fellowship was granted to E.R.-d.-T.

References

[1] J. Alegre-Cebollada, M. Oñaderra, J.G. Gavilanes, A. Martínez-del-Pozo, Sea anemone actinoporins: the transition from a folded soluble state to a functionally active membrane-bound oligomeric pore, Curr. Protein Pept. Sci. 8 (2007) 558–572.

[2] L. García-Ortega, J. Alegre-Cebollada, S. García-Linares, M. Bruix, A. Martínez-del-Pozo, J.G. Gavilanes, The behavior of sea anemone actinoporins at the water-membrane interface, Biochim. Biophys. Acta 1808 (2011) 2275–2288.

[3] S. García-Linares, E. Rivera-de-Torre, J. Palacios-Ortega, J.G. Gavilanes, A. Martínez-del-Pozo, The metamorphic transformation of a water-soluble monomeric protein into an oligomeric transmembrane pore, in: A. Iglič, M. Rappolt, A.J. García-Sáez (Eds.), Advances in Biomembranes and Lipid Self-assembly, vol. 26, 2017, pp. 51–97.

[4] G. Anderluh, I. Krizaj, B. Strukelj, F. Gubensek, P. Maček, J. Pungercar, Equinatoxins, pore-forming proteins from the sea anemone *Actinia equina*, belong to a multigene family, Toxicon 37 (1999) 1391–1401.

[5] E.V. Leychenko, M. Isaeva, E. Tkacheva, E. Zelepuga, A. Kvetkina, K. Guzev, M. Monastyrnaya, E. Kozlovskaya, Multigene family of pore-forming toxins from sea anemone *Heteractis crispa*, Mar. Drugs 16 (2018) 183.

[6] E. Rivera-de-Torre, A. Martínez-del-Pozo, J.E. Garb, *Stichodactyla helianthus*' de novo transcriptome assembly: discovery of a new actinoporin isoform, Toxicon 150 (2018) 105–114.

[7] E. Rivera-de-Torre, J. Palacios-Ortega, J.G. Gavilanes, A. Martínez-del-Pozo, S. García-Linares, Pore-forming proteins from cnidarians and arachnids as potential biotechnological tools, Toxins (Basel) 11 (2019).

[8] N. Rojko, M. Dalla Serra, P. Maček, G. Anderluh, Pore formation by actinoporins, cytolysins from sea anemones, Biochim. Biophys. Acta 1858 (2016) 446–456.

[9] A. Bellomio, K. Morante, A. Barlič, I. Gutiérrez-Aguirre, A.R. Viguera, J.M. González-Mañas, Purification, cloning and characterization of fragaceatoxin C, a novel actinoporin from the sea anemone *Actinia fragacea*, Toxicon 54 (2009) 869–880.

[10] A. Athanasiadis, G. Anderluh, P. Maček, D. Turk, Crystal structure of the soluble form of equinatoxin II, a pore-forming toxin from the sea anemone *Actinia equina*, Structure 9 (2001) 341–346.

[11] M.G. Hinds, W. Zhang, G. Anderluh, P.E. Hansen, R.S. Norton, Solution structure of the eukaryotic pore-forming cytolysin equinatoxin II: implications for pore formation, J. Mol. Biol. 315 (2002) 1219–1229.

[12] J.M. Mancheño, J. Martín-Benito, M. Martínez-Ripoll, J.G. Gavilanes, J.A. Hermoso, Crystal and electron microscopy structures of sticholysin II actinoporin reveal insights into the mechanism of membrane pore formation, Structure 11 (2003) 1319–1328.

[13] A.E. Mechaly, A. Bellomio, D. Gil-Carton, K. Morante, M. Valle, J.M. González-Mañas, D.M. Guerin, Structural insights into the oligomerization and architecture of eukaryotic membrane pore-forming toxins, Structure 19 (2011) 181–191.

[14] S. García-Linares, I. Castrillo, M. Bruix, M. Menéndez, J. Alegre-Cebollada, A. Martínez-del-Pozo, J.G. Gavilanes, Three-dimensional structure of the actinoporin sticholysin I. Influence of long-distance effects on protein function, Arch. Biochem. Biophys. 532 (2013) 39–45.

[15] K. Tanaka, J.M. Caaveiro, K. Morante, J.M. González-Mañas, K. Tsumoto, Structural basis for self-assembly of a cytolytic pore lined by protein and lipid, Nat. Commun. 6 (2015) 6337.

[16] P. Malovrh, G. Viero, M.D. Serra, Z. Podlesek, J.H. Lakey, P. Maček, G. Menestrina, G. Anderluh, A novel mechanism of pore formation: membrane penetration by the N-terminal amphipathic region of equinatoxin, J. Biol. Chem. 278 (2003) 22678–22685.

[17] I. Gutiérrez-Aguirre, A. Barlič, Z. Podlesek, P. Maček, G. Anderluh, J.M. González-Mañas, Membrane insertion of the N-terminal α-helix of equinatoxin II, a sea anemone cytolytic toxin, Biochem. J. 384 (2004) 421–428.

[18] N. Rojko, K.C. Kristan, G. Viero, E. Zerovnik, P. Maček, M. Dalla Serra, G. Anderluh, Membrane damage by an α-helical pore-forming protein, Equinatoxin II, proceeds through a succession of ordered steps, J. Biol. Chem. 288 (2013) 23704–23715.

[19] V. Antonini, V. Perez-Barzaga, S. Bampi, D. Penton, D. Martinez, M. Dalla Serra, M. Tejuca, Functional characterization of sticholysin I and W111C mutant reveals the sequence of the actinoporin's pore assembly, PLoS One 9 (2014) e110824.

[20] J. Palacios-Ortega, S. García-Linares, M. Astrand, M.A. Al Sazzad, J.G. Gavilanes, A. Martínez-del-Pozo, J.P. Slotte, Regulation of sticholysin II-induced pore formation by lipid bilayer composition, phase state, and interfacial properties, Langmuir 32 (2016) 3476–3484.

[21] J. Palacios-Ortega, S. García-Linares, E. Rivera-de-Torre, J.G. Gavilanes, A. Martínez-del-Pozo, J.P. Slotte, Differential effect of bilayer thickness on sticholysin activity, Langmuir 33 (2017) 11018–11027.

[22] E. Rivera-de-Torre, J. Palacios-Ortega, S. García-Linares, J.G. Gavilanes, A. Martínez-del-Pozo, One single salt bridge explains the different cytolytic activities shown by actinoporins sticholysin I and II from the venom of *Stichodactyla helianthus*, Arch. Biochem. Biophys. 636 (2017) 79–89.

[23] M.L. Shin, D.W. Michaels, M.M. Mayer, Membrane damage by a toxin from the sea anemone *Stoichactis helianthus*. II. Effect of membrane lipid composition in a liposome system, Biochim. Biophys. Acta 555 (1979) 79–88.

[24] G. Belmonte, C. Pederzolli, P. Maček, G. Menestrina, Pore formation by the sea anemone cytolysin equinatoxin-II in red blood cells and model lipid membranes, J. Membr. Biol. 131 (1993) 11–22.

[25] M. Tejuca, M.D. Serra, M. Ferreras, M.E. Lanio, G. Menestrina, Mechanism of membrane permeabilization by sticholysin I, a cytolysin isolated from the venom of the sea anemone *Stichodactyla helianthus*, Biochemistry 35 (1996) 14947–14957.

[26] V. De los Ríos, J.M. Mancheño, M.E. Lanio, M. Oñaderra, J.G. Gavilanes, Mechanism of the leakage induced on lipid model membranes by the hemolytic protein sticholysin II from the sea anemone *Stichodactyla helianthus*, Eur. J. Biochem. 252 (1998) 284–289.

[27] C.A. Valcarcel, M. Dalla Serra, C. Potrich, I. Bernhart, M. Tejuca, D. Martínez, F. Pazos, M.E. Lanio, G. Menestrina, Effects of lipid composition on membrane permeabilization by sticholysin I and II, two cytolysins of the sea anemone *Stichodactyla helianthus*, Biophys. J. 80 (2001) 2761–2774.

[28] D. Martínez, A. Otero, C. Álvarez, F. Pazos, M. Tejuca, M.E. Lanio, I. Gutiérrez-Aguirre, A. Barlič, I. Iloro, J.L. Arrondo, J.M. González-Mañas, E. Lissi, Effect of sphingomyelin and cholesterol on the interaction of St II with lipidic interfaces, Toxicon 49 (2007) 68–81.

[29] B. Bakrač, G. Anderluh, Molecular mechanism of sphingomyelin-specific membrane binding and pore formation by actinoporins, Adv. Exp. Med. Biol. 677 (2009) 106–115.

[30] S. García-Linares, J. Palacios-Ortega, T. Yasuda, M. Astrand, J.G. Gavilanes, A. Martínez-del-Pozo, J.P. Slotte, Toxin-induced pore formation is hindered by intermolecular hydrogen bonding in sphingomyelin bilayers, Biochim. Biophys. Acta 1858 (2016) 1189–1195.

[31] S. García-Linares, E. Rivera-de-Torre, K. Morante, K. Tsumoto, J.M. Caaveiro, J.G. Gavilanes, J.P. Slotte, Á. Martínez-del-Pozo, Differential effect of membrane composition on the pore-forming ability of four different sea anemone actinoporins, Biochemistry 55 (2016) 6630–6641.

[32] A.W. Bernheimer, L.S. Avigad, Properties of a toxin from the sea anemone

Stoichactis helianthus, including specific binding to sphingomyelin, Proc. Natl. Acad. Sci. U. S. A. 73 (1976) 467–471.
[33] B. Bakrač, I. Gutierrez-Aguirre, Z. Podlesek, A.F. Sonnen, R.J. Gilbert, P. Maček, J.H. Lakey, G. Anderluh, Molecular determinants of sphingomyelin specificity of a eukaryotic pore-forming toxin, J. Biol. Chem. 283 (2008) 18665–18677.
[34] T. Maula, Y.J. Isaksson, S. García-Linares, S. Niinivehmas, O.T. Pentikainen, M. Kurita, S. Yamaguchi, T. Yamamoto, S. Katsumura, J.G. Gavilanes, A. Martínez-del-Pozo, J.P. Slotte, 2NH and 3OH are crucial structural requirements in sphingomyelin for sticholysin II binding and pore formation in bilayer membranes, Biochim. Biophys. Acta 1828 (2013) 1390–1395.
[35] W. Varanda, A. Finkelstein, Ion and nonelectrolyte permeability properties of channels formed in planar lipid bilayer membranes by the cytolytic toxin from the sea anemone, *Stoichactis helianthus*, J. Membr. Biol. 55 (1980) 203–211.
[36] A. Barlič, I. Gutiérrez-Aguirre, J.M. Caaveiro, A. Cruz, M.B. Ruiz-Argüello, J. Pérez-Gil, J.M. González-Mañas, Lipid phase coexistence favors membrane insertion of equinatoxin-II, a pore-forming toxin from *Actinia equina*, J. Biol. Chem. 279 (2004) 34209–34216.
[37] J. Alegre-Cebollada, I. Rodríguez-Crespo, J.G. Gavilanes, A. Martínez-del-Pozo, Detergent-resistant membranes are platforms for actinoporin pore-forming activity on intact cells, FEBS J. 273 (2006) 863–871.
[38] J. Alegre-Cebollada, M. Cunietti, E. Herrero-Galán, J.G. Gavilanes, A. Martínez-del-Pozo, Calorimetric scrutiny of lipid binding by sticholysin II toxin mutants, J. Mol. Biol. 382 (2008) 920–930.
[39] M. Marchioretto, M. Podobnik, M. Dalla Serra, G. Anderluh, What planar lipid membranes tell us about the pore-forming activity of cholesterol-dependent cytolysins, Biophys. Chem. 182 (2013) 64–70.
[40] L. Pedrera, M.L. Fanani, U. Ros, M.E. Lanio, B. Maggio, C. Álvarez, Sticholysin I-membrane interaction: an interplay between the presence of sphingomyelin and membrane fluidity, Biochim. Biophys. Acta 1838 (2014) 1752–1759.
[41] L. Pedrera, A.B. Gomide, R.E. Sánchez, U. Ros, N. Wilke, F. Pazos, M.E. Lanio, R. Itri, M.L. Fanani, C. Álvarez, The presence of sterols favors sticholysin I-membrane association and pore formation regardless of their ability to form laterally segregated domains, Langmuir 31 (2015) 9911–9923.
[42] I. Alm, S. García-Linares, J.G. Gavilanes, A. Martínez-del-Pozo, J.P. Slotte, Cholesterol stimulates and ceramide inhibits sticholysin II-induced pore formation in complex bilayer membranes, Biochim. Biophys. Acta Biomembr. 1848 (2015) 925–931.
[43] S. García-Linares, I. Alm, T. Maula, J.G. Gavilanes, J.P. Slotte, A. Martínez-del-Pozo, The effect of cholesterol on the long-range network of interactions established among sea anemone Sticholysin II residues at the water-membrane interface, Mar. Drugs 13 (2015) 1647–1665.
[44] S. García-Linares, T. Maula, E. Rivera-de-Torre, J.G. Gavilanes, J.P. Slotte, A. Martínez-del-Pozo, Role of the tryptophan residues in the specific interaction of the sea anemone *Stichodactyla helianthus*'s actinoporin Sticholysin II with biological membranes, Biochemistry 55 (2016) 6406–6420.
[45] E. Rivera-de-Torre, S. García-Linares, J. Alegre-Cebollada, J. Lacadena, J.G. Gavilanes, A. Martínez-del-Pozo, Synergistic action of actinoporin isoforms from the same sea anemone species assembled into functionally active heteropores, J. Biol. Chem. 291 (2016) 14109–14119.
[46] H.P. Wacklin, B.B. Bremec, M. Moulin, N. Rojko, M. Haertlein, T. Forsyth, G. Anderluh, R.S. Norton, Neutron reflection study of the interaction of the eukaryotic pore-forming actinoporin equinatoxin II with lipid membranes reveals intermediate states in pore formation, Biochim. Biophys. Acta 1858 (2016) 640–652.
[47] J. Palacios-Ortega, S. García-Linares, E. Rivera-de-Torre, J.G. Gavilanes, A. Martínez-del-Pozo, J.P. Slotte, Sticholysin, sphingomyelin, and cholesterol: a closer look at a tripartite interaction, Biophys. J. 116 (2019) 2253–2265.
[48] D. Suput, Effects of equinatoxin on the membrane of skeletal-muscle fiber, Period. Biol. 88 (1986) 210–211.
[49] R. Zorec, M. Tester, P. Maček, W.T. Mason, Cytotoxicity of equinatoxin II from the sea anemone *Actinia equina* involves ion channel formation and an increase in intracellular calcium activity, J. Membr. Biol. 118 (1990) 243–249.
[50] P. Maček, Polypeptide cytolytic toxins from sea anemones (Actiniaria), FEMS Microbiol. Immunol. 5 (1992) 121–129.
[51] P. Maček, G. Belmonte, C. Pederzolli, G. Menestrina, Mechanism of action of equinatoxin II, a cytolysin from the sea anemone *Actinia equina* L. belonging to the family of actinoporins, Toxicology 87 (1994) 205–227.
[52] C. Alvarez, F. Casallanovo, C.S. Shida, L.V. Nogueira, D. Martínez, M. Tejuca, I.F. Pazos, M.E. Lanio, G. Menestrina, E. Lissi, S. Schreier, Binding of sea anemone pore-forming toxins sticholysins I and II to interfaces-modulation of conformation and activity, and lipid-protein interaction, Chem. Phys. Lipids 122 (2003) 97–105.
[53] J. Alegre-Cebollada, G. Clementi, M. Cunietti, C. Porres, M. Oñaderra, J.G. Gavilanes, A. Martínez-del-Pozo, Silent mutations at the 5′-end of the cDNA of actinoporins from the sea anemone *Stichodactyla helianthus* allow their heterologous overproduction in *Escherichia coli*, J. Biotechnol. 127 (2007) 211–221.
[54] S. García-Linares, R. Richmond, M.F. García-Mayoral, N. Bustamante, M. Bruix, J.G. Gavilanes, A. Martínez-del-Pozo, The sea anemone actinoporin (Arg-Gly-Asp) conserved motif is involved in maintaining the competent oligomerization state of these pore-forming toxins, FEBS J. 281 (2014) 1465–1478.
[55] J.M. Rausch, W.C. Wimley, A high-throughput screen for identifying transmembrane pore-forming peptides, Anal. Biochem. 293 (2001) 258–263.
[56] W.C. Wimley, Determining the effects of membrane-interacting peptides on membrane integrity, Methods Mol. Biol. 1324 (2015) 89–106.
[57] J. Wilschut, D. Papahadjopoulos, Ca^{2+}-induced fusion of phospholipid vesicles monitored by mixing of aqueous contents, Nature 281 (1979) 690–692.
[58] A. Andersson, J. Danielsson, A. Graslund, L. Maler, Kinetic models for peptide-induced leakage from vesicles and cells, Eur. Biophys. J. 36 (2007) 621–635.
[59] P. Maček, M. Zecchini, C. Pederzolli, M. Dalla Serra, G. Menestrina, Intrinsic tryptophan fluorescence of equinatoxin II, a pore-forming polypeptide from the sea anemone *Actinia equina* L, monitors its interaction with lipid membranes, Eur. J. Biochem. 234 (1995) 329–335.
[60] X. Jiang, H. Chen, W. Yang, Y. Liu, W. Liu, J. Wei, H. Tu, X. Xie, L. Wang, A. Xu, Functional expression and characterization of an acidic actinoporin from sea anemone *Sagartia rosea*, Biochem. Biophys. Res. Commun. 312 (2003) 562–570.
[61] M. Ahumada, C. Calderon, E. Lissi, C. Alvarez, M.E. Lanio, F. Pazos, The pore forming capacity of Sticholysin I in dipalmitoyl phosphatidyl vesicles is tuned by osmotic stress, Chem. Phys. Lipids 203 (2017) 87–93.
[62] G.P.B. Carretero, E.F. Vicente, E.M. Cilli, C.M. Alvarez, H. Jenssen, S. Schreier, Dissecting the mechanism of action of actinoporins. Role of the N-terminal amphipathic alpha-helix in membrane binding and pore activity of sticholysins I and II, PLoS One 13 (2018) e0202981.
[63] C. Soto, A. Del Valle, P.A. Valiente, U. Ros, M.E. Lanio, A.M. Hernandez, C. Alvarez, Differential binding and activity of the pore-forming toxin sticholysin II in model membranes containing diverse ceramide-derived lipids, Biochimie 138 (2017) 20–31.
[64] U. Ros, G.P.B. Carretero, J. Paulino, E. Crusca Jr., F. Pazos, E.M. Cilli, M.E. Lanio, S. Schreier, C. Alvarez, Self-association and folding in membrane determine the mode of action of peptides from the lytic segment of sticholysins, Biochimie 156 (2019) 109–117.
[65] H. Mesa-Galloso, K.H. Delgado-Magnero, S. Cabezas, A. Lopez-Castilla, J.E. Hernandez-Gonzalez, L. Pedrera, C. Alvarez, D. Peter Tieleman, A.J. Garcia-Saez, M.E. Lanio, U. Ros, P.A. Valiente, Disrupting a key hydrophobic pair in the oligomerization interface of the actinoporins impairs their pore-forming activity, Protein Sci. 26 (2017) 550–565.
[66] R.J. Laborde, O. Sanchez-Ferras, M.C. Luzardo, Y. Cruz-Leal, A. Fernandez, C. Mesa, L. Oliver, L. Canet, L. Abreu-Butin, C.V. Nogueira, M. Tejuca, F. Pazos, C. Alvarez, M.E. Alonso, I.M. Longo-Maugeri, M.N. Starnbach, D.E. Higgins, L.E. Fernandez, M.E. Lanio, Novel adjuvant based on the pore-forming protein sticholysin II encapsulated into liposomes effectively enhances the antigen-specific CTL-mediated immune response, J. Immunol. 198 (2017) 2772–2784.
[67] Y. Tamba, H. Ariyama, V. Levadny, M. Yamazaki, Kinetic pathway of antimicrobial peptide magainin 2-induced pore formation in lipid membranes, J. Phys. Chem. B 114 (2010) 12018–12026.
[68] M.B. Mustafa, D.L. Tipton, M.D. Barkley, P.S. Russo, F.D. Blum, Dye diffusion in isotropic and liquid-crystalline aqueous (hydroxypropyl)cellulose, Macromolecules 26 (1993) 370–378.
[69] J. Martín-Benito, F. Gavilanes, V. de Los Ríos, J.M. Mancheño, J.J. Fernández, J.G. Gavilanes, Two-dimensional crystallization on lipid monolayers and three-dimensional structure of sticholysin II, a cytolysin from the sea anemone *Stichodactyla helianthus*, Biophys. J. 78 (2000) 3186–3194.
[70] R. Peters, Fluorescence microphotolysis to measure nucleocytoplasmic transport and intracellular mobility, Biochim. Biophys. Acta 864 (1986) 305–359.
[71] C.B. Muller, A. Loman, V. Pacheco, F. Koberling, D. Willbold, W. Richtering, J. Enderlein, Precise measurement of diffusion by multi-color dual-focus fluorescence correlation spectroscopy, Epl Europhys. Lett. 83 (2008) 46001.
[72] M.A. Baker, N. Rojko, B. Cronin, G. Anderluh, M.I. Wallace, Photobleaching reveals heterogeneous stoichiometry for equinatoxin II oligomers, Chembiochem 15 (2014) 2139–2145.
[73] K. Tanaka, J.M. Caaveiro, K. Tsumoto, Bidirectional transformation of a metamorphic protein between the water-soluble and transmembrane native states, Biochemistry 54 (2015) 6863–6866.
[74] J. Alegre-Cebollada, A. Martínez-del-Pozo, J.G. Gavilanes, E. Goormaghtigh, Infrared spectroscopy study on the conformational changes leading to pore formation of the toxin sticholysin II, Biophys. J. 93 (2007) 3191–3201.
[75] K.C. Kristan, G. Viero, M. Dalla Serra, P. Maček, G. Anderluh, Molecular mechanism of pore formation by actinoporins, Toxicon 54 (2009) 1125–1134.
[76] Y. Subburaj, U. Ros, E. Hermann, R. Tong, A.J. García-Sáez, Toxicity of an α-pore-forming toxin depends on the assembly mechanism on the target membrane as revealed by single-molecule imaging, J. Biol. Chem. 290 (2015) 4856–4865.
[77] K. Cosentino, U. Ros, A.J. García-Sáez, Assembling the puzzle: oligomerization of α-pore forming proteins in membranes, Biochim. Biophys. Acta 1858 (2016) 457–466.
[78] K. Morante, A. Bellomio, D. Gil-Carton, L. Redondo-Morata, J. Sot, S. Scheuring, M. Valle, J.M. Gonzalez-Manas, K. Tsumoto, J.M.M. Caaveiro, Identification of a membrane-bound prepore species clarifies the lytic mechanism of actinoporins, J. Biol. Chem. 291 (2016) 19210–19219.
[79] A.J. Krauson, J. He, W.C. Wimley, Determining the mechanism of membrane permeabilizing peptides: identification of potent, equilibrium pore-formers, Biochim. Biophys. Acta 1818 (2012) 1625–1632.
[80] A.J. Krauson, J. He, W.C. Wimley, Gain-of-function analogues of the pore-forming peptide melittin selected by orthogonal high-throughput screening, J. Am. Chem. Soc. 134 (2012) 12732–12741.
[81] Y. Marcus, Volumes of aqueous hydrogen and hydroxide ions at 0 to 200°C, J. Chem. Phys. 137 (2012) 154501.
[82] E.F. Pettersen, T.D. Goddard, C.C. Huang, G.S. Couch, D.M. Greenblatt, E.C. Meng, T.E. Ferrin, UCSF Chimera—a visualization system for exploratory research and analysis, J. Comput. Chem. 25 (2004) 1605–1612.

Figure S1

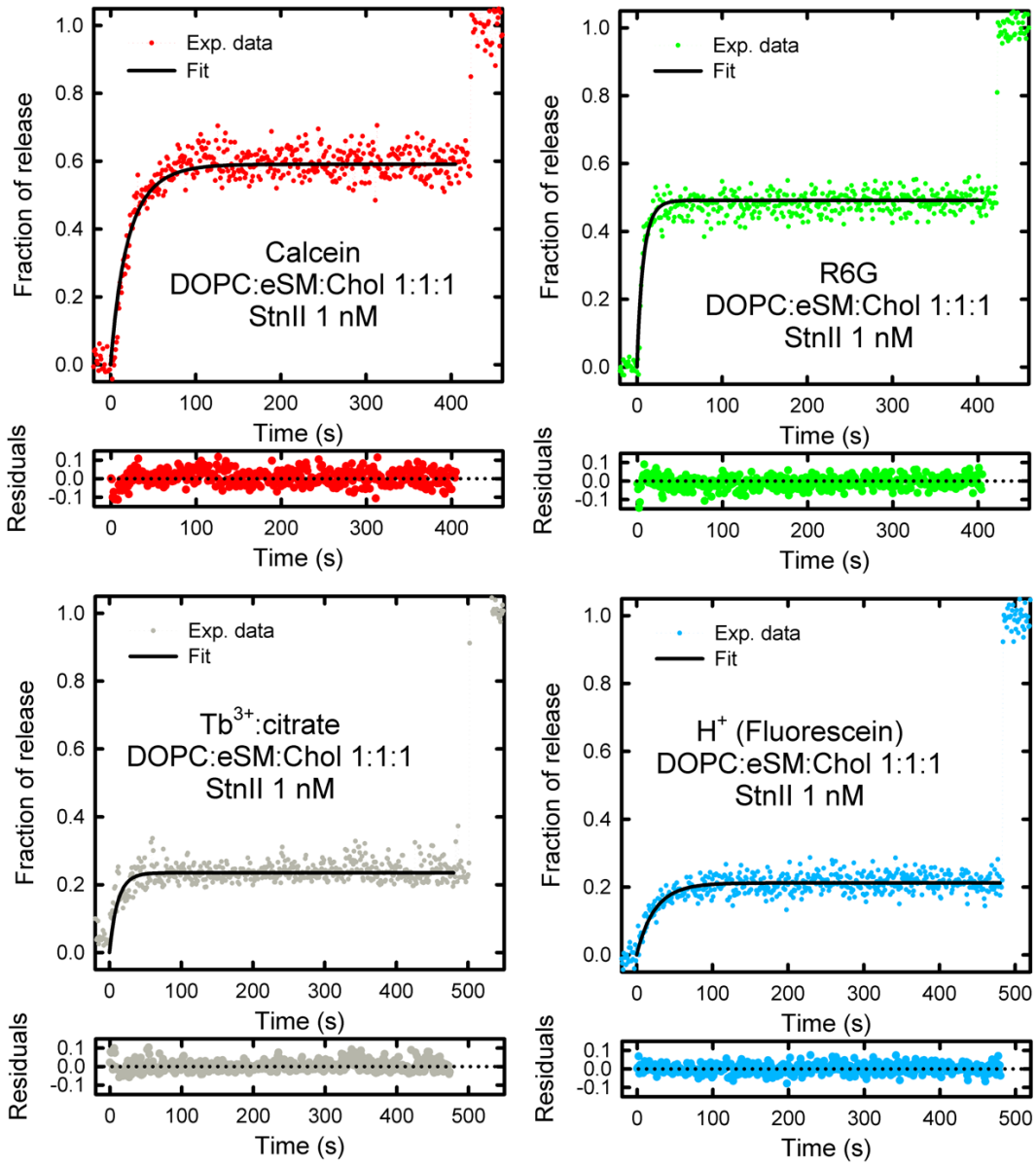

Fig. S1. Representative experimental data from calcein (red), R6G (green), Tb^{3+}:citrate (grey), and H^+ (fluorescein) (blue) release from LUVs. In black solid lines the fits to each trace of the perturbation model are shown. Small panels show the residuals of each fit.

Biochemistry

pubs.acs.org/biochemistry Article

Oligomerization of Sticholysins from Förster Resonance Energy Transfer

Juan Palacios-Ortega,* Esperanza Rivera-de-Torre, Sara García-Linares, José G. Gavilanes, Álvaro Martínez-del-Pozo, and J. Peter Slotte

Cite This: *Biochemistry* 2021, 60, 314−323 Read Online

ACCESS | Metrics & More | Article Recommendations | Supporting Information

ABSTRACT: Sticholysins are pore-forming toxins produced by sea anemones that are members of the actinoporin family. They exert their activity by forming pores on membranes, provided they have sphingomyelin. To assemble into pores, specific recognition, binding, and oligomerization are required. While recognition and binding have been extensively studied, delving into the oligomerization process and the stoichiometry of the pores has been more difficult. Here, we present evidence that these toxins are capable of oligomerizing in solution and suggesting that the interaction of sticholysin II (StnII) with its isoform sticholysin I (StnI) is stronger than that of StnI with itself. We also show that the stoichiometry of the final, thermodynamically stable StnI pores is, at least, heptameric. Furthermore, our results indicate that this association maintains its oligomerization number when StnII is included, indicating that the stoichiometry of StnII is also of that order, and not tetrameric, as previously thought. These results are compatible with the stoichiometry observed for the crystallized pore of FraC, another very similar actinoporin produced by a different sea anemone species. Our results also indicate that the stoichiometry of actinoporin pores in equilibrium is conserved regardless of the particular composition of a given pore ensemble, which we have shown for mixed sticholysin pores.

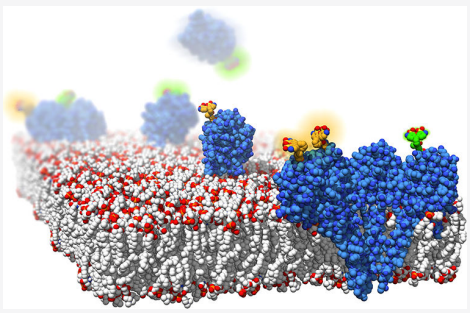

The production of venom containing very similar toxins is a common feature of sea anemones around the globe.[1−8] Sticholysins are similar toxic proteins produced by the Caribbean Sea anemone *Stichodactyla helianthus*.[9,10] They belong to a family of cytolytic proteins known as actinoporins. They are pore-forming toxins and, as such, exert their activity by creating pores in selected target membranes.[11−13] These membranes feature sphingomyelin (SM), a lipid that is specifically recognized by these proteins and whose absence in the membranes of sea anemones provides the basis for avoiding self-toxicity.[9,10,14−19]

Thanks to years of research, many details of the functionality of these proteins have been elucidated. The knowledge acquired includes the role of specific residues and the influence of the lipid composition of the membrane. SM selectivity, the role of tryptophan residues, the enhancing effect of cholesterol (Chol) on activity, and the crucial intervention of the N-terminal α-helix in the process of pore formation are some of the aspects that have been elucidated.[9,10,14−16,20−26] Studies have traditionally been performed using one (or several) of the following proteins: sticholysins I and II (StnI, UniProtKB P81662; and StnII, UniProtKB P07845), equinatoxin II (EqtII), and/or fragaceatoxin C (FraC). The soluble, monomeric structures of these four proteins have been revealed in atomic detail.[7,27−30] All of them display a common fold, which consists of a β-sandwich flanked by two α-helices (Figure 1). The α-helix located at the N-terminus is responsible for membrane penetration.[22−26]

The aforementioned soluble structures were obtained using X-ray crystallography and/or nuclear magnetic resonance. However, the structure of the pore complex into which these toxins assemble in SM-containing membranes, revealing all of the structural changes and the stoichiometry of these complexes, has not been easy to resolve. To penetrate the membrane and form a pore, the structure of an actinoporin has to undergo conformational changes. These changes include oligomerization, the concomitant monomer−monomer contacts, and the deployment and extension of the N-terminal α-helix, the most significant one at the monomer level. All of these are structural modifications that take place exclusively in the presence of suitable membranes.

Therefore, the presence of lipids appears to be necessary if the complexes formed by actinoporins are to be understood. Accordingly, early attempts to understand these complexes used StnII crystallized on egg phosphatidylcholine (egg-PC)

Received: October 15, 2020
Revised: January 11, 2021
Published: January 14, 2021

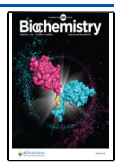

https://dx.doi.org/10.1021/acs.biochem.0c00840
Biochemistry 2021, 60, 314−323

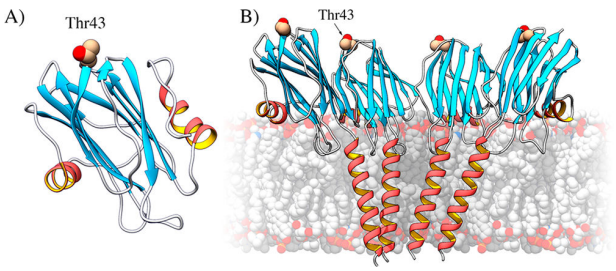

Figure 1. (A) Position of the mutated residue, Thr43, in the structure of StnI (Protein Data Bank entry 2KS4). Its replacement by a Cys residue would not affect the membrane-binding region (α-helix below) or the protein−protein interface (side of the protein in the front). (B) Mutated residue in the context of an oligomer, showing that it is unlikely to interfere with oligomerization (see Figure S2 for further details). The figure was made by fitting the structure of StnI to that of the octameric pore of FraC (Protein Data Bank entry 4TSY). Made with UCSF Chimera.[31]

and dioleoylphosphatidylcholine (DOPC) monolayers, with the crystallization process appearing to force membrane binding despite the absence of SM.[28] These experiments yielded three-dimensional maps at 18 Å resolution that were used to fit the previously available structure of the soluble monomers. In this case, it appeared that the stoichiometry of StnII pores was tetrameric. Years later, a new approach was devised. It overcame the limitation imposed by lipids for X-ray crystallography by removing or replacing them with detergents in a way that, in principle, conserved the lipid−protein and protein−protein interactions that stabilize the membrane-bound conformation of actinoporins.[32,33] These experiments were performed using FraC. Several structures were obtained, including that of a nonameric prepore ensemble and, most importantly, an octameric pore, at a resolution of 3.2 Å.[33]

Tetrameric, heptameric, and octameric ensembles, represented by the toroidal pore, the conical pore, and the hybrid pore models, are currently the most accepted candidates for the pore structures in the field of actinoporins. There are, however, many clear indications about the simultaneity of several other stoichiometries during the process leading to the formation of the final pore structures in equilibrium. Nevertheless, some questions remain unanswered or, at least, poorly understood. For example, is the stoichiometry of the pores of all actinoporins the same? Are multiple stoichiometries possible under the same conditions? Could it be that detergent treatments favor the formation of specific complexes? Do the final pore structures constitute a thermodynamically stable assembly? Do different toxin isoforms produced by the same sea anemone species assemble into the same structure and yield heteropores?

To answer these questions, we conceived a new approach, taking advantage of the fact that the wild-type (WT) variants of most actinoporins lack cysteine (Cys) residues in their sequences. Building on the accumulated functional and structural knowledge on actinoporins, and particularly sticholysins, we created a single-cysteine mutant, StnI-T43C, that enabled specific labeling with a high-quantum yield fluorescent probe while keeping functional disturbance to a minimum. Using this mutant, we have been able to study the behavior of these proteins in solution and on membranes and, using a FRET (Förster resonance energy transfer) approach, to elucidate the stoichiometry of StnI and StnI−StnII pores.

MATERIALS AND METHODS

Materials. 1,2-Dioleoyl-*sn*-glycero-3-phosphocholine (DOPC), 1-palmitoyl-2-oleoyl-*sn*-glycero-3-phosphocholine (POPC), *N*-palmitoyl-D-*erythro*-sphingosylphosphorylcholine (PSM), and egg sphingomyelin (eSM) were obtained from Avanti Polar Lipids (Alabaster, AL). Maleimide-modified ATTO-488 and ATTO-542 were obtained from Atto-Tec GmbH (Siegen, Germany). All sticholysin variants were produced in *Escherichia coli*, strain RB791, and purified to homogeneity as described in refs 21 and 34. Briefly, purification was performed using ion-exchange chromatography (carboxymethyl-cellulose, CM-52) eluted using a linear gradient of NaCl (0 to 0.3 M) followed by size-exclusion chromatography (Biogel P2). Homogeneity of the preparation was evaluated by means of sodium dodecyl sulfate−polyacrylamide gel electrophoresis and amino acid analysis.

Methods. *Protein Preparation.* The mutant StnI-T43C was produced using site-directed mutagenesis. Its design takes advantage of the lack of Cys residues in sticholysins, enabling them to be specifically labeled at a convenient position, safe from the perspective of functionality, where the label is not expected to interfere with either protein−protein interactions or membrane recognition and binding (Figure 1).

The new mutant was characterized structurally and functionally using circular dichroism, and hemolytic assays as previously described.[35] Its hemolytic activity was essentially the same as that of the WT StnI variant, indicating that the mutation did not affect any functionally important region of the protein (Figure S1), as expected from the design (Figure 1 and Figure S2). For these assays, the mutant was previously incubated with 0.5 mM TCEP to ensure that all potential disulfide bonds were reduced.

StnI-T43C was specifically labeled at the introduced -SH group using maleimide-modified ATTO probes (5−8-fold molar excess) overnight after a previous 2 day incubation with TCEP [tris(2-carboxyethyl)phosphine; 50:1 molar excess] in phosphate buffer (140 mM NaCl and 10 mM phosphate) at pH 7.4. The excess of free label was effectively removed using Pierce Dye Removal Columns (Thermo Fisher Scientific) following the manufacturer's specifications. The yield of the labeling procedures ranged between 17% and 25%, depending on the batch. The efficiency of labeling was evaluated by means of the absorption spectra of the sample, using the following extinction coefficients: ε = 49450 M^{-1} cm^{-1} for StnI-T43C at 280 nm, $\varepsilon = 9.0 \times 10^4$ M^{-1} cm^{-1} at 500 nm for ATTO-488, and $\varepsilon = 1.2 \times 10^5$ M^{-1} cm^{-1} at 542 nm for ATTO-542. Corrections for label contributions at 280 nm were made using the corresponding correction factors provided by the manufacturer, which are 0.09 and 0.08 for ATTO-488 and ATTO-542, respectively (see Figure S3 for the complete absorption spectra). These correction factors represent the absorbance of the label at 280 nm relative to their respective maximum absorbances.

Vesicle Preparation. Lipid vesicles were prepared by mixing selected methanol (hexane for Chol) solutions of lipids in the desired lipid molar proportion. The organic solvent was evaporated under a nitrogen flow at 40 °C. Dried lipid films were then hydrated at 65 °C in a water bath for at least 30 min. Suspended lipid vesicles were then extruded at hydration temperature through 200 nm diameter polycarbonate filters.

Time-Resolved Fluorescence Anisotropy. Time-resolved fluorescence measurements were performed using a Fluo-

https://dx.doi.org/10.1021/acs.biochem.0c00840
Biochemistry 2021, 60, 314−323

Time100 spectrofluorimeter equipped with a PicoHarp300E time-correlated single photon-counting module (PicoQuant GmbH, Berlin, Germany) and polarizers. A 457 ± 15 nm pulsed diode laser was used for excitation. Emission was collected through a long-pass filter (>480 nm). When required, neutral density filters were used to attenuate the excitation intensity. The instrument response function (IRF) was acquired using light scattered by buffer in the absence of colored filters up to 10000 counts in the peak channel. Each sample decay was recorded up to ∼20000 counts in the peak channel. To avoid inner filter effects, the concentration of the fluorophores was such that the optical density at the excitation wavelength was $OD_{l/2} < 0.05$. Experiments were performed under constant stirring. The temperature was controlled by a Peltier element.

Anisotropy decays were analyzed using FluoFit Pro software from PicoQuant. The G factor was recorded for each sample and was always between 0.98 and 1.02. The fluorescence anisotropy decay curves $[r(t)]$ were fit using a model consisting of the sum of discrete exponential terms:[36]

$$r(t) = \sum_{i=1}^{n} \alpha_i \exp\left(-\frac{t}{\theta_i}\right) + r_\infty \tag{1}$$

where α_i and θ_i are the normalized amplitude and the rotational correlation time of the ith component of the anisotropy decay, respectively. The symbol r_∞ is the limiting anisotropy, which is related to the restrictions in the process of depolarization. The number of exponential terms was always the smallest required to obtain a satisfactory fit, as judged from the value of the reduced χ^2, the distribution of the residuals, and the trace of the autocorrelation plot.

Rotational correlation times were used to estimate molecular diameters, according to

$$Ø\ (Å) = 20\sqrt[3]{\frac{\theta RT}{\eta N_A} \times 10^{27}\frac{3}{4\pi}} \tag{2}$$

which is derived from the Perrin equation,[36] modified to yield the molecular diameter directly in angstroms, where θ is the correlation time of the rotating unit in seconds, R is the ideal gas constant (8.314 m^3 Pa mol^{-1} K^{-1}), T is the temperature in kelvin, η is the viscosity of the solvent (0.94×10^{-3} Pa s), and N_A is Avogadro's number. The numerical constants appearing in the equation transform the radius into the diameter while also transforming the output units. When using this equation, an assumption is made that the overall shape of the rotating unit is that of a sphere. This can be expected for molecules that display a single correlation time.[36]

Calculation of the Förster Distance. The Förster distance (R_0) of the donor−acceptor pair used was calculated as

$$R_0 = 0.2108\sqrt[6]{\kappa^2 n^{-4} Q_D J(\lambda)} \tag{3}$$

which yields R_0 directly in angstroms. In the expression, κ^2 is the orientation factor, set to $^2/_3$, which represents the dynamic isotropic limit (see Figure S4), n is the refractive index of the medium, set to 1.33 (water), Q_D is the quantum yield of the donor (0.8, according to the supplier), and $J(\lambda)$ is the overlap integral between the emission spectra of the donor and the absorption spectra of the acceptor. The overlap integral is calculated as

$$J(\lambda) = \int_0^\infty F_D(\lambda)\varepsilon_A(\lambda)\lambda^4\, d\lambda \tag{4}$$

where $F_D(\lambda)$ is the emission spectra of the donor with its area normalized to 1 and $\varepsilon_A(\lambda)$ is the acceptor spectra in M^{-1} cm^{-1}. The calculated R_0 for the ATTO-488/ATTO-542 FRET pair was 63.8 Å. The R_0 for the ATTO-488 self-transfer was 49.3 Å.

Steady-State Fluorescence Spectroscopy. Steady-state fluorescence measurements were performed on a PTI QuantaMaster spectrofluorimeter (Photon Technology International, Lawrenceville, NJ). Sample excitation was set at 500 nm. Emission was recorded between 507 and 675 nm to encompass the spectra of both fluorophores. To avoid inner filter effects, the concentration of the fluorophores was such that the optical density at the excitation wavelength was $OD_{l/2} < 0.05$. Experiments were performed under constant stirring. The temperature was controlled by a Peltier element.

Stoichiometry of Oligomers from FRET. A model was constructed to calculate the expected FRET efficiencies for each possible stoichiometry in a way that was dependent on the fraction of acceptor-labeled toxin in the sample, while the fraction of donor was kept constant. Single-point mutants allowed the assumption that the fluorophores were distributed as the vertices of regular polygons (see Figure S5 for further details about this and the method). The distance from the fluorophores to the center of the polygon is expressed as

$$r_c = \frac{r_{mm}}{2\sin\frac{\pi}{N}} \tag{5}$$

where r_c is the radius of the polygon, r_{mm} is the distance between fluorophores on adjacent subunits, and N is the number of subunits per pore.

The value for r_{mm} was 29.0 Å, as measured for a sticholysin subunit (calculated from the correlation times). However, r_c cannot be used directly. Instead, the offset of the fluorophore relative to the center of the protein has to be taken into account. The distance to the center of the polygon to the fluorophore is then

$$r_{cf} = \sqrt{[r_c + r_f\cos(\omega)]^2 + [r_f\sin(\omega)]^2} \tag{6}$$

where r_f is the distance from the mass center of the protein to the labeled position as observed from above (distance on the z-axis is not required) and ω is the angle between the line that joins them and the prolongation of the line that unites the center of the monomer and the center of the oligomer. The values of r_f and ω were measured as 10 Å and 66°, respectively, based on the position of residue T43 on the three-dimensional structure of StnI [Protein Data Bank (PDB) entry 2KS4].

Once r_{cf} is known, the distance between any two subunits can be calculated as

$$r_{ij} = 2r_{cf}\sin\frac{\pi(i-j)}{N} \tag{7}$$

where i and j are the indices of the subunits of interest. Usually, assuming $j = 1$, as will be done from here onward (omitting subscript j), eq 7 yields the distance between the selected subunit (number 1) and the ith subunit. Distance values were then used to calculate the corresponding rates of energy transfer, according to

$$k_T(r_i) = \frac{1}{\tau_D}\left(\frac{R_0}{r_i}\right)^6 \tag{8}$$

https://dx.doi.org/10.1021/acs.biochem.0c00840
Biochemistry 2021, 60, 314−323

where τ_D is the lifetime of the donor, which in our case is 4.1 ns.

To ensure the greatest precision, all possible arrangements of all possible combinations of unlabeled and donor- and acceptor-labeled subunits were calculated for each of the stoichiometries considered, assuming that monomer associations were random and unbiased by the labeling. This was achieved with a homemade Python program. The arrangements of subunits were calculated taking into account possible redundancies due to rotational symmetry. In all cases, it must be maintained that $N_D + N_A + N_U = N$ [i.e., the sum of unlabeled (N_U), donor-labeled (N_D), and acceptor-labeled (N_A) subunits must equal the total number of subunits].

For each of the possible arrangements, the expected FRET efficiency was calculated using the additive property of rates,[36] as

$$E_{Nq\nu} = \frac{\sum_{i=2}^{N} k_T(r_i)}{\frac{1}{\tau_D} + \sum_{i=2}^{N} k_T(r_i)} \quad (9)$$

where $E_{Nq\nu}$ indicates that it is the FRET efficiency for a stoichiometry of N subunits (for example, $N = 8$), a combination q of unlabeled and donor- and acceptor-labeled subunits (for example, $N_D = 1$, $N_A = 3$, and $N_U = 4$), ordered in a particular arrangement ν. For each arrangement, the observed FRET efficiency will depend on how the subunits are ordered within the oligomer. We assumed that monomer associations were random and unaffected by the labeling; hence, the observed FRET efficiency for each combination q will be the average of the E values for all of the possible arrangements, because we are assuming that all arrangements are equally possible within each combination.

The observed FRET efficiency would then depend on the fraction of donor- and acceptor-labeled toxins in the sample (f_A and f_D, respectively). These fractions control which combinations are more likely to occur. The respective fractions of labeled and unlabeled subunits must equal one (i.e., $f_A + f_D + f_U = 1$). The probability of each combination, including all of its possible arrangements, is calculated as

$$P(N_D, N_A, N_U, f_D, f_A, f_U) = \frac{(N-1)!}{(N_D-1)!N_A!N_U!} f_D^{N_D-1} f_A^{N_A} f_U^{N_U} \quad (10)$$

which is a version of the trinomial distribution adapted to rule out redundancies due to rotational symmetries. The sum of all probabilities calculated in this manner must equal 1. This probability is the weighting factor for the energy transfer efficiencies of each combination. The final result yields the expected FRET efficiency for a given stoichiometry and fraction of labeling.

FRET efficiencies were measured in a large lipid:protein (L:P) molar ratio to avoid energy transfer between different pore complexes. The estimation of the right L:P ratio was made as $r_{av} = \frac{\sqrt{\sigma}}{2}$, where r_{av} is the average distance between oligomers and σ is the surface density of the complexes.[37] Thus, if the stoichiometry was 8, the average separation between complexes would be $\sim 3R_0$. Under these conditions, if the stoichiometry was equal to 4, the average separation would still be $\sim 2R_0$, at which the energy transfer efficiency is <2%. Larger L:P ratios could not be used due to experimental limitations, namely, light scattering by large unilamellar vesicles (LUVs), the availability of materials, and instrument sensitivity. Comparison of the experimental data with the model using root-mean-square deviations (RMSDs) allowed us to estimate the stoichiometry of the pores of sticholysins. For the calculation of the RMSDs, the error in each value was used to calculate weighting factors, so that the most accurate values contributed to the final RMSD.

Final protein mixtures were made by combination of aliquots from WT (StnI and StnII, as indicated) and labeled StnI (with donor or acceptor) stocks. The amounts of donor- and acceptor-labeled mutants were calculated according to the corresponding stock concentration and degree of labeling. The same procedure was used when StnII was included. WT StnI was added last, if needed, to adjust the final overall fraction of labeling and total protein concentration to the desired values. Throughout the study, StnI has been considered to be equal, structurally and in terms of activity, to the unlabeled StnI-T43C mutant, as evidenced by their practically indistinguishable CD spectra (both near and far UV) and hemolytic activity (Figure S1).

All fluorescence experiments were performed in PBS (10 mM phosphate and 140 mM NaCl) at pH 7.4.

RESULTS

Motions of Sticholysins in Solution and on Membranes. StnI-T43C was labeled with ATTO-488. The time-resolved anisotropy decays of the toxin and the free label were recorded for the following reasons: (1) as a way to further ascertain that the labeling process had succeeded, (2) to observe if the label was able to interact with the LUVs by itself, and (3) with the intention of measuring the average hydrodynamic size of the StnI monomers. For these measurements, solutions in which only 2% of the total sticholysin was labeled were used (i.e., WT StnI was added to the 17−25% labeled mutant preparation to decrease the final overall degree of labeling to 2%) (Figure 2). Under these conditions, only a single, very short correlation time (0.2 ns) could be resolved for the free label. StnI displayed two correlation times. The faster one was ∼0.3 ns, very close to that of the free label, accounting for segmental motions of the fluorophore. The slower one was ∼2.95 ns and corresponded to the rotational motions of the proteins within the solvent (Table 1). This last correlation time could be used to estimate the molecular diameters of the different sticholysin species presumably present in the solution studied. The value obtained, 29.0 ± 1.3 Å, agrees with the molecular structures available, as demonstrated when placing a sphere at the mass centers of those structures. The time-dependent anisotropy did not decay to zero, displaying a limiting anisotropy of ∼0.014.

These same anisotropy decays were then recorded in the presence of DOPC/eSM/Chol LUVs (1:1:1 molar ratio) or POPC/PSM LUVs (4:1 molar ratio). The anisotropy decay of the free label in the presence of lipids was essentially identical (Table 1) to that observed in their absence, indicating that no direct interaction was established between the fluorophore and the vesicles. Energy transfer is a phenomenon that is known to reduce anisotropy.[36−38] Hence, the fractional labeling of sticholysins was kept low, at 2%, to minimize potential energy transfer between neighboring subunits in the pores. The L:P molar ratio was also high, beyond saturation, so that energy transfer between subunits of different pores was unlikely. At the same time, maximum possible binding of the available toxin was achieved. The observed rapid correlation time did not substantially vary from the previously measured time in

https://dx.doi.org/10.1021/acs.biochem.0c00840
Biochemistry 2021, 60, 314−323

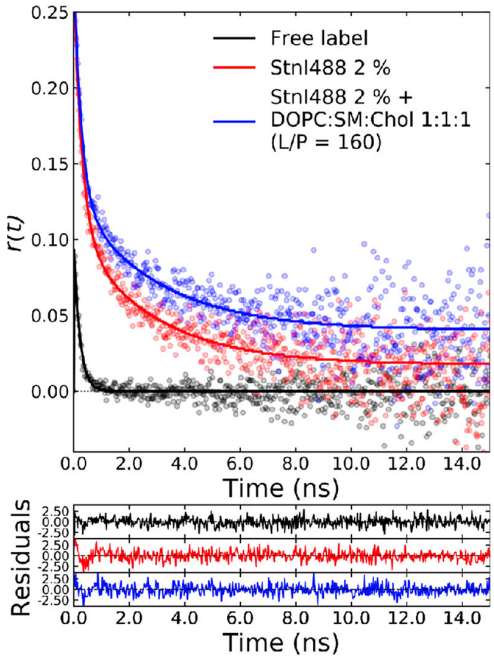

Figure 2. Time-dependent anisotropy decays of StnI labeled with ATTO-488 free in solution (degree of labeling of 2%, red) or in the presence of DOPC/eSM/Chol (1:1:1) membranes (L:P molar ratio of 160, blue). The decay of the free ATTO-488 label was also recorded (black). Traces of residuals for each of the fits are shown below. The order of the graphs is the same as that of the legend. The decay recorded using a 4:1 POPC:PSM ratio has been omitted for the sake of clarity.

any of the subsequent measurements. The slow correlation time was slightly increased when Chol-containing LUVs were used but decreased when LUVs lacking Chol were employed. The limiting anisotropy was larger in both cases, in the range of 0.03−0.04, indicating the restricted mobility of the membrane-bound proteins (Table 1). Correlation times could not be used to calculate molecular sizes this time due to the restrictions imposed by the membrane on the mobility of the proteins.

Oligomerization in Solution. Previous reports have shown that StnII can oligomerize in solution.[39] Hence, energy transfer in solution, prior to pore formation on membranes, could be expected to occur, at least to some extent. With this background, and as a first approach, steady-state anisotropy of StnI-ATTO-488 was also measured. Anisotropy is expected to decrease as a consequence of energy transfer.[36−38] This is consequence of an effective larger displacement of the emission dipole (that of the acceptor molecule) relative to the original absorption dipole (of the molecule acting as a donor), larger than what could be achieved solely by molecular motions. Hence, the steady-state anisotropy of ATTO-488-labeled StnI in solution was measured at increasing degrees of labeling (DoL) (Figure S6). Only at high DoL values did the anisotropy appear to decrease slightly, though not significantly. This effect was more noticeable for membrane-bound toxins (Figure S6).

Therefore, to improve the resolution of the experiment, a sample of ATTO-488-labeled StnI-T43C (hereafter StnI-488 or donor) was titrated with ATTO-542-labeled StnI-T43C (hereafter StnI-542 or acceptor). The R_0 of this FRET pair was significantly larger than the distance over which the previous approach was effective (only at $r < 0.8R_0$[38]). WT StnI was included to control the exact fractions of donor- and acceptor-labeled populations. The relative fractions of both the donor and the acceptor in the sample varied as a consequence of the titration process, while the total amount of donor (which is responsible for the measured signal) was constant. The measured FRET efficiencies were plotted as a function of the fraction of the acceptor, which was deemed more representative than the fraction of the donor or unlabeled toxin (Figure 3). A small increase in the level of energy transfer was observed as a function of the level of the acceptor in the sample, indicative of the presence of oligomers.

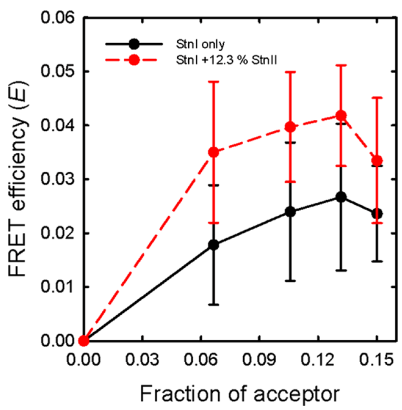

Figure 3. FRET efficiency observed for donor-labeled StnI with WT StnI (solid black trace) or WT StnII (dashed red trace). Initially, both samples contained 11.9% of donor-labeled StnI and 29.1% of the indicated WT variant, with the remainder being unlabeled StnI-T43C. The samples were then titrated with acceptor-labeled StnI (labeled 25.9%) to a final composition of 5% donor, 15% acceptor, and 12.3% WT variant, the remainder being unlabeled StnI-T43C. Values are averages of three replicates ± the standard error of the mean. A version of this figure showing the standard deviation is provided as Figure S7.

Table 1. Parameters of the Anisotropy Decays of ATTO-488, StnI (degree of labeling of 2%), in the Absence and Presence of Lipids (1:1:1 DOPC:eSM:Chol with an L:P molar ratio of 160; 4:1 POPC:PSM with an L:P molar ratio of 160)[a]

	r_1	θ_1 (ns)	r_2	θ_2 (ns)	r_∞
ATTO-488	0.125 ± 0.005	0.228 ± 0.012	–	–	0.000 ± 0.0004
ATTO-488 with DOPC/eSM/Chol	0.135 ± 0.006	0.232 ± 0.012	–	–	0.001 ± 0.0004
StnI	0.200 ± 0.008	0.299 ± 0.030	0.089 ± 0.006	2.851 ± 0.530	0.014 ± 0.002
StnI with DOPC/eSM/Chol	0.195 ± 0.009	0.267 ± 0.034	0.088 ± 0.004	2.979 ± 0.587	0.040 ± 0.003
StnI with POPC/PSM	0.157 ± 0.007	0.224 ± 0.020	0.103 ± 0.005	2.273 ± 0.170	0.031 ± 0.002

[a]The initial anisotropies (r_i) and correlation times (θ_i) of each component together with the limiting anisotropy (r_∞) are indicated. Values were obtained from fitting, and errors from bootstrap analysis.

https://dx.doi.org/10.1021/acs.biochem.0c00840
Biochemistry 2021, 60, 314−323

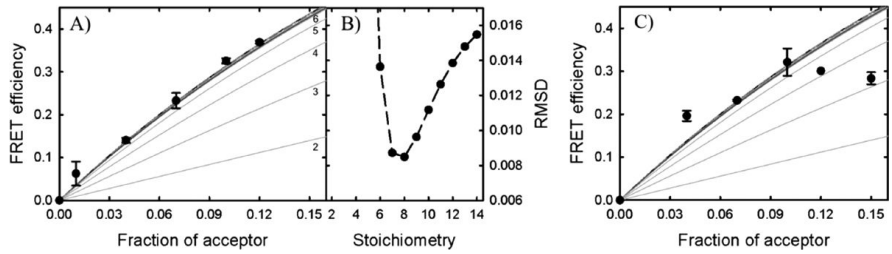

Figure 4. (A) Experimental energy transfer efficiency values (●) obtained using labeled StnI in a combination of 1:1:1 DOPC/eSM/Chol membranes plotted with the theoretical predictions made for stoichiometries from 2 to 10 (11 to 14 removed for the sake of clarity). From bottom to top, predictions for 2, 3, 4, 5, etc., respectively (as indicated in the figure). Predictions from 6 on can barely be distinguished at this scale. With the conditions considered, the maximum FRET efficiency is reached for heptamers, being slowly reduced for higher values (see Figure S9). (B) Root-mean-square deviations (RMSDs) obtained for the experimental values on the left compared to each of the predictions. (C) FRET efficiency values observed for labeled StnI in combination with 4:1 POPC:PSM LUVs. Experimental values do not follow the expected trends.

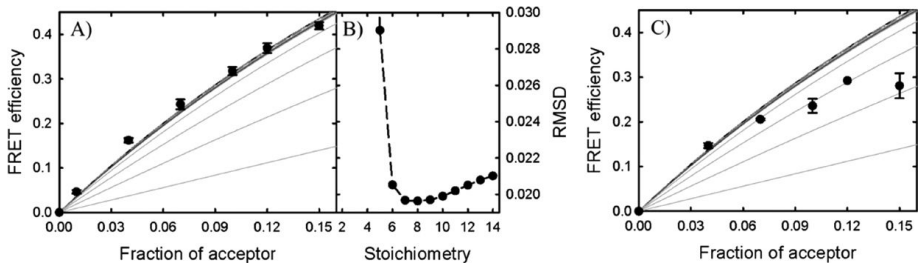

Figure 5. (A) Experimental energy transfer efficiency values (●) obtained using labeled StnI with 12.3% StnII in a combination of 1:1:1 DOPC/eSM/Chol membranes plotted with the theoretical predictions as in Figure 4. (B) RMSDs for each of the predictions. In this case, the difference observed between the stoichiometries is reduced compared with the previous result in the absence of StnII. (C) FRET efficiency values observed for labeled StnI in the presence of 12.3% StnII in combination with 4:1 POPC/PSM LUVs. Again, the experimental values do not follow the expected trends.

Incidentally, it has been shown that a minimal amount of StnII, just 1%, is capable of greatly enhancing the hemolytic activity of StnI, presumably by facilitating the binding step of the pore formation process.[40] If that is so, then StnII could also be expected to oligomerize with StnI while in solution. The results of titrating StnI-488 with StnI-542, albeit replacing WT StnI with StnII, showed that the efficiency of energy transfer was more pronouncedly increased than that observed using WT StnI (Figure 3).

Stoichiometry of StnI Pores from FRET in 1:1:1 DOPC/eSM/Chol LUVs. Energy transfer was also measured directly in sticholysin oligomers assembled on membranes. For that reason, lipid vesicles were added to a 100 nM mixture of StnI to achieve a final L:P molar ratio of 160. The fraction of donor-labeled proteins in the sample was kept constant at 0.05, whereas the fraction of acceptor-labeled monomers was varied between experiments and increased to ≤0.15. FRET efficiency values were obtained from steady-state data using quenched donor emission as measured from the deconvoluted total sample emission (Figure S8). These values were plotted as a function of the acceptor content in the sample and compared with the theoretical predictions (Figure 4a). To properly evaluate which of the theoretical traces better described the experimental data, the RMSD was calculated for the experimental values relative to each of the theoretical traces, using the error of each experimental value for weighting the calculation (Figure 4b). The signal of StnI pores on 1:1:1 DOPC/eSM/Chol membranes best agreed with that of octameric ensembles. However, experimental resolution and model limitations did not permit us to rule out the formation of oligomers equal to or larger than heptamers, based solely on this result.

Is the Stoichiometry of StnI Pores from FRET in 4:1 POPC/PSM Membranes Different? The experiment and subsequent analysis were repeated with vesicles without Chol, to determine if the presence of Chol had a substantial effect on oligomerization. This time, the L:P molar ratio was increased to 320, in spite of increased lipid-induced light scattering, to ensure complete binding due to the comparatively lower affinity of StnI for membranes lacking Chol.[41] Surprisingly, the results showed that the signal from StnI did not follow the trend expected from any of the theoretical predictions (Figure 4c), indicating that the assumptions of the model are not valid for this situation.

A 12% StnII in the StnI Sample Does Not Affect the Stoichiometry. The experiment was performed again for each lipid composition. This time, however, the sample included 12.3% StnII, to ascertain the stoichiometry of the pores formed when using a mixture of both proteins. The results showed that the presence of StnII did not change the trends observed in its absence (Figure 5a,c). The distribution of RMSD values of the experiment performed in the presence of Chol (Figure 5b) closely resembled that observed in the absence of StnII, indicating that the stoichiometry is conserved in Chol-containing membranes. The unexpected experimental trend that we had observed for membranes without Chol was also maintained, again showing that the theoretical assumptions regarding the process of pore formation do not adequately describe the process that takes place in the absence of Chol (Figure 5c).

https://dx.doi.org/10.1021/acs.biochem.0c00840
Biochemistry 2021, 60, 314−323

Sticholysin Pores Are Not Remodeled Once Formed. The results from studies using electrophysiological measurements suggested that sticholysin pores might be unstable, based on the noise level of the conductance measured compared with those observed for β-pore-forming toxins.[42] One possibility is that this noisiness was simply caused by thermal oscillations of the system, because the lumen of the pore would be lined by the N-terminal α-helices of sticholysins and lipids, with few direct interactions between the components other than van der Waals forces. However, the possibility that, once formed, pores would be under continuous remodeling, with monomers moving from one complex to another, has also been proposed.

To test this idea, StnI or StnII, to a final increment of 57 nM, was added to 100 nM StnI preincubated with lipids, already including 5% donor and 15% acceptor proteins. The L:P molar ratio was initially set to 240. That way, the final L:P molar ratio after the addition of the extra protein was 160, comparable to the results of the assays described above. In neither case did the observed FRET efficiency vary after the addition of extra unlabeled protein, regardless of whether it was StnI or StnII (Figure 6 and 7, respectively). This suggested

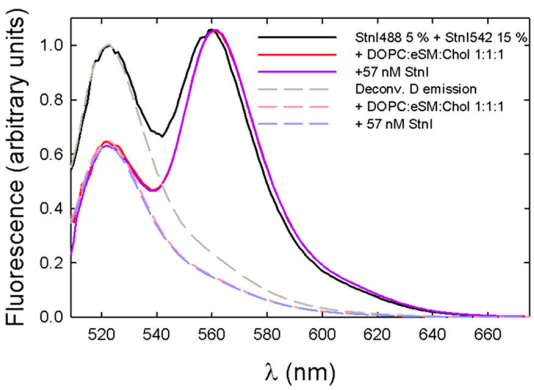

Figure 6. Emission spectra of StnI with 5% donor labeling and 15% acceptor labeling in solution (solid black line), with 1:1:1 DOPC/eSM/Chol membranes (solid red line), and after addition of extra 57 nM unlabeled StnI (solid purple line). Deconvoluted donor emission is also shown as the corresponding dashed line. The later addition of StnI did not affect the FRET efficiency, indicating that pores are not remodeled.

that once equilibrium was reached, previously formed pores were not disturbed by newly added toxin molecules and maintained the same monomers that oligomerized in the first place, resulting in a constant FRET signal.

DISCUSSION

In this study, several aspects of the process of pore formation by sticholysins were investigated using the single-cysteine StnI mutant T43C, labeled with ATTO-488 and ATTO-542. Using time-resolved measurements, the hydrodynamic size of StnI was measured as 29.0 ± 1.3 Å, which is in good agreement with the dimensions of a sticholysin monomer according to structural determination techniques.[27,28] The anisotropy decay of the soluble protein reveals a correlation time that agrees with the molecular size of the protein but also shows that some oligomers are present, as indicated by the fact that the limiting anisotropy was slightly larger than 0 (Figure 2 and Table 1). These results agree with the previous observations on StnII,

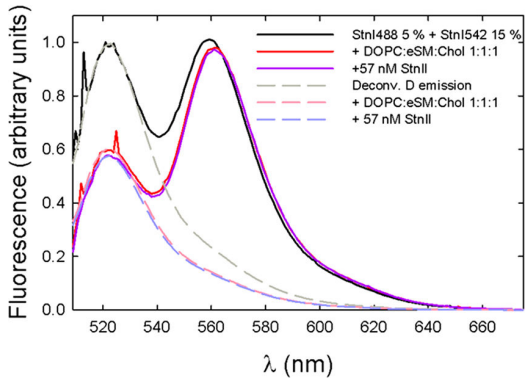

Figure 7. Emission spectra of StnI with 5% donor labeling and 15% acceptor labeling in solution (solid black line), with 1:1:1 DOPC/eSM/Chol membranes (solid red line), and after addition of extra 57 nM unlabeled StnII (solid purple line). Deconvoluted donor emission is shown as the corresponding dashed line. As for StnI, the addition of StnII did not affect FRET efficiency, indicating stable pores.

showing that it can oligomerize up to tetrameric ensembles in solution while mainly maintaining a monomeric nature.[39]

Delving further into that line of research, titration experiments were used to corroborate the presence of oligomers in solution. Using solely StnI, the presence of oligomers was detected as a slight increase in FRET efficiency. When StnII was included, a further increase in the efficiency of energy transfer was observed (Figure 3). This result supports the previously observed behavior indicating that StnII promotes the binding of StnI to the membrane, presumably by binding to it while still in solution.[40] This result suggests not only that the number of oligomers in solution is larger but also that there are higher-order oligomers, such as trimers and tetramers (given that StnII was not labeled, it could increase FRET efficiency only if trimers and/or tetramers occur).

The FRET approach was then taken one step further to calculate the stoichiometry of sticholysin pores in lipid model vesicles. The signal from labeled-StnI in 1:1:1 DOPC/eSM/Chol membranes was best described by the theoretical prediction that assumed an octameric complex. However, due to physical constraints, namely, the R_0 of the FRET pair and the distance between labels on neighboring subunits, the prediction of the model became increasingly similar as the oligomerization number was increased (Figure S9). These experimental results rule out the existence of a detectable number of oligomers of five or fewer subunits, but simultaneously, any larger stoichiometry should not be entirely discarded, even if the prediction obtained under the assumptions of octamers is the one that best agrees with the experiment (Figure 4a). Using a strategy similar to ours but based on spin labeling and electron paramagnetic resonance spectroscopy, it has been recently concluded that StnI in a membrane would exhibit an oligomeric architecture with heterogeneous stoichiometry of predominantly eight or nine protomers, which agrees with the available structural models.[33,43] In fact, the results presented here are compatible with the possibility that several other stoichiometries occurred at once, yielding the same signal as if all were octamers. It is also important to remark that our approach observes oligomeric structures in equilibrium, without contemplating the trajectory on the membrane followed by the different

https://dx.doi.org/10.1021/acs.biochem.0c00840
Biochemistry 2021, 60, 314−323

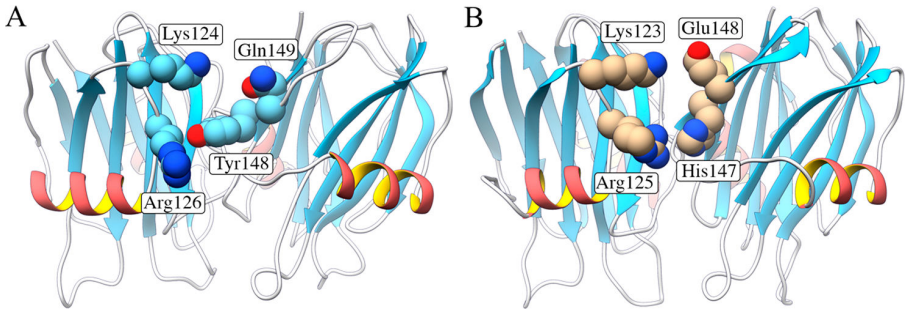

Figure 8. Model homodimers of (A) StnI and (B) StnII. The residues shown are the same in both cases for the monomer on the left, Lys124 and Arg126 of StnI (Lys123 and Arg125 of StnII). For the monomer on the right, the amino acids differ. For StnI, they are Tyr148 and Gln149, whereas for StnII, they are His147 and Glu148. The orientation of the residues is not necessarily that found upon oligomerization, because the structures were obtained in solution (A) and by crystallization (B). The Arg residue could interact with either of the aromatic residues, by hydrogen bonding or by a cation−π interaction. The latter can, in fact, be observed in the dimer structure published for FraC (PDB entry 4TSL[32]) between its equivalent amino acids. The Lys residue probably forms a hydrogen bond with Gln149 and a salt bridge with Glu148. This figure was made using the three-dimensional structures of StnI (PDB entry 2KS4) and StnII (PDB entry 1GWY), superimposing them with the octameric pore of FraC (PDB entry 4TSY), which has been shown to be compatible with the stoichiometry of sticholysins.

oligomeric structures during pore formation and/or remodeling before reaching their stable final assembly.

Interestingly, the inclusion of 12.3% StnII did not affect the distribution of the RMSD values observed for StnI alone, indicating that StnII did not affect the overall stoichiometry of the pores at equilibrium. It could be argued that StnII did not oligomerize with StnI. However, this would contradict the observed ability of StnII to enhance StnI binding[40] and imply that the observed signal should shift upward because the partial fraction of labeling would be larger in the StnI-only complexes than accounted for in the calculations, which assume that StnII is part of the total toxin population. This effect was not observed. In fact, the presence of oligomeric structures containing both StnI and StnII has been detected before, in the presence of vesicles with a composition identical to the ones used now, employing cross-linking experiments.[40] This is the first time, however, that it has been shown that the stoichiometry is conserved when both proteins are mixed. This fact also suggests that the essential residues responsible for protein−protein interactions should be conserved between both sticholysin isoforms. At this point, it is interesting to remember that oligomerization is promoted by the presence of StnII and that two of the only 12 residues that differ between StnI and StnII are located very close to or at the protein−protein interfaces. These two residues are Tyr148 and Gln149 in StnI and His147 and Glu148 in StnII. Overall, the properties of these amino acids are conserved in both residue pairs. On this basis, we can predict the nature of the complementary residues located on the other side of the protein. Those should be capable of both hydrogen bonding and perhaps also establishing salt bridges, and one of them would have to be cationic so that it could establish a cation−π interaction with the aromatic rings observed. Inspection of the three-dimensional structures reveals that there is, in fact, such a pair of residues, appropriately standing out from the protein. These are Arg126 and Lys124 in StnI and Arg125 and Lys123 in StnII. So far, the difference in activity between StnI and StnII has been attributed, to a very large degree, to the different strength of attachment of the N-terminal α-helix to the β-sandwich, as well as to its different hydropathy profile.[35] However, it is also possible that a stronger monomer−monomer interaction, which is feasible only with the residues of StnII (a possible salt bridge between Glu148 and Lys123/Lys124), could intervene, shifting the equilibrium in solution to the multimeric forms, which could in turn favor membrane binding and, certainly, oligomerization (Figure 8).

The results obtained when using membranes that lack Chol are, at first glance, surprising. In all cases, the experimental values do not follow the predictions. In addition, their trend does not agree with what would be expected if the pores clustered, which would be higher than expected E values, which would be the consequence of an increased probability of energy transfer between different oligomers due to their higher-than-expected proximity. The fact that the first points, corresponding to the lower acceptor fractions, are closer to the estimations and then cease to rise accordingly, at larger fraction values, could indicate that the binding unit for membranes without Chol would be sticholysin dimers/oligomers. At low acceptor levels in the sample, the expected E is less dependent on the presence of acceptors at subunit $i + 1$ (from a donor placed at i). However, the more the acceptor fraction increases, the greater the relevance is of the probability of finding acceptors, simultaneously, at positions $i + 1$ and $i - 1$. Because donor- and acceptor-labeled proteins are mixed right before the measurements are performed, and in the total final volume, complete shuffling of the variants in the oligomers might not occur quickly enough. Consequently, oligomers in the sample would rarely have donor−acceptor pairs, yielding the observed effect. This is compatible with previous results indicating that, in fact, dimers are required for membrane binding in the absence of Chol.[33,44] It is, therefore, possible that Chol's effect on SM's headgroup orientation[45] aids in SM recognition, permitting the dominant form in solution, monomers, to directly bind those membranes. We confirmed that, in all cases, FRET was a consequence of specific membrane binding and SM recognition by incubation of a labeled sample with POPC vesicles, which did not affect the emission of the sample (Figure S10).

Finally, we have shown that sticholysin pores are stable once in equilibrium and do not undergo any kind of subunit exchange when new monomers are added to the sample. This certainly does not happen on the time scale used (2−5 min), which is much greater (seconds) than that used in the electrophysiology experiments that prompted the question.

https://dx.doi.org/10.1021/acs.biochem.0c00840
Biochemistry 2021, 60, 314−323

CONCLUSIONS

In this work, we have presented evidence disproving that tetramers are the oligomerization assembly of StnI at equilibrium. The inclusion of 12.3% StnII showed no significant effect on the stoichiometry-dependent energy transfer efficiency, indicating that the stoichiometry is conserved regardless of the composition of the pores. Both of these results would support the X-ray structure obtained for FraC, suggesting that the assembly is probably the same for all known actinoporins.

ASSOCIATED CONTENT

Supporting Information

The Supporting Information is available free of charge at https://pubs.acs.org/doi/10.1021/acs.biochem.0c00840.

Structural and functional characterization of the StnI-T43C mutant, selection of the mutated residue and reach of the label, absorption spectra of the mutant StnI-T43C before and after labeling, overlap of the anisotropy and intensity decays of the labeled toxin in solution and on membranes, schematic representation of the model used to calculate FRET efficiencies on membranes, and dependence of the steady-state anisotropy on the degree of labeling (in solution and on membranes, example of fluorescence signal deconvolution, dependence of predicted FRET on the stoichiometry for 15% acceptor in the sample, and negative control for the activity of the labeled mutants) (PDF)

Accession Codes

StnI, UniProtKB P81662; StnII, UniProtKB P07845.

AUTHOR INFORMATION

Corresponding Author

Juan Palacios-Ortega − *Departamento de Bioquímica y Biología Molecular, Universidad Complutense, 28040 Madrid, Spain; Biochemistry, Faculty of Science and Engineering, Åbo Akademi University, 20520 Turku, Finland;* orcid.org/0000-0002-4629-0221; Email: juan.palaciosb1a@gmail.com

Authors

Esperanza Rivera-de-Torre − *Departamento de Bioquímica y Biología Molecular, Universidad Complutense, 28040 Madrid, Spain*

Sara García-Linares − *Departamento de Bioquímica y Biología Molecular, Universidad Complutense, 28040 Madrid, Spain*

José G. Gavilanes − *Departamento de Bioquímica y Biología Molecular, Universidad Complutense, 28040 Madrid, Spain*

Álvaro Martínez-del-Pozo − *Departamento de Bioquímica y Biología Molecular, Universidad Complutense, 28040 Madrid, Spain;* orcid.org/0000-0003-0043-5939

J. Peter Slotte − *Biochemistry, Faculty of Science and Engineering, Åbo Akademi University, 20520 Turku, Finland;* orcid.org/0000-0002-4850-5759

Complete contact information is available at: https://pubs.acs.org/10.1021/acs.biochem.0c00840

Author Contributions

J.P.-O., E.R.-d.-T., and S.G.-L. participated in the design of the mutant and in the production of all proteins used. J.P.-O. and E.R.-d.-T. conducted the experiments. All authors discussed the results, wrote and corrected the manuscript, and suggested modifications.

Funding

This research was supported by the Sigrid Jusélius Foundation, the Jane and Aatos Erkko Foundation, and the Magnus Ehrnrooth Foundation (to J.P.S.) and by UCM-Banco Santander Grants PR75/18-21561 and PR87/19-22556 (to A.M.-d.-P.). J.P.-O. has a funded doctoral student position from ISB/ÅA. A UCM-Banco Santander fellowship was granted to E.R.-d.-T.

Notes

The authors declare no competing financial interest.

REFERENCES

(1) Ferlan, I., and Lebez, D. (1974) Equinatoxin, a lethal protein from Actinia equina—I Purification and characterization. *Toxicon 12*, 57−58.

(2) Maček, P. (1992) Polypeptide cytolytic toxins from sea anemones (Actiniaria). *FEMS Microbiol. Lett. 105*, 121−129.

(3) Bernheimer, A. W., and Avigad, L. S. (1982) Toxins of the sea anemone Epiactis prolifera. *Arch. Biochem. Biophys. 217*, 174−180.

(4) Bernheimer, A. W., Avigad, L. S., and Lai, C. (1982) Purification and properties of a toxin from the sea anemone Condylactis gigantea. *Arch. Biochem. Biophys. 214*, 840−845.

(5) Bernheimer, A. W., Avigad, L. S., Branch, G., Dowdle, E., and Lai, C. Y. (1984) Purification and properties of a toxin from the South African sea anemone, Pseudactinia varia. *Toxicon 22*, 183−191.

(6) Bernheimer, A. W., and Lai, C. Y. (1985) Properties of a cytolytic toxin from the sea anemone, Stoichactis kenti. *Toxicon 23*, 791−799.

(7) Mechaly, A. E., Bellomio, A., Morante, K., González-Mañas, J. M., and Guerin, D. M. (2009) Crystallization and preliminary crystallographic analysis of fragaceatoxin C, a pore-forming toxin from the sea anemone Actinia fragacea. *Acta Crystallogr., Sect. F: Struct. Biol. Cryst. Commun. 65*, 357−360.

(8) Rivera-de-Torre, E., Martínez-del-Pozo, A., and Garb, J. E. (2018) Stichodactyla helianthus' de novo transcriptome assembly: Discovery of a new actinoporin isoform. *Toxicon 150*, 105−114.

(9) Tejuca, M., Dalla Serra, M., Ferreras, M., Lanio, M. E., and Menestrina, G. (1996) Mechanism of membrane permeabilization by sticholysin I, a cytolysin isolated from the venom of the sea anemone Stichodactyla helianthus. *Biochemistry 35*, 14947−14957.

(10) De los Ríos, V., Mancheño, J. M., Lanio, M. E., Oñaderra, M., and Gavilanes, J. G. (1998) Mechanism of the leakage induced on lipid model membranes by the hemolytic protein sticholysin II from the sea anemone Stichodactyla helianthus. *Eur. J. Biochem. 252*, 284−289.

(11) Alegre-Cebollada, J., Oñaderra, M., Gavilanes, J. G., and Martínez-del-Pozo, A. (2007) Sea anemone actinoporins: The transition from a folded soluble state to a functionally active membrane-bound oligomeric pore. *Curr. Protein Pept. Sci. 8*, 558−572.

(12) García-Ortega, L., Alegre-Cebollada, J., García-Linares, S., Bruix, M., Martínez-del-Pozo, A., and Gavilanes, J. G. (2011) The behavior of sea anemone actinoporins at the water-membrane interface. *Biochim. Biophys. Acta, Biomembr. 1808*, 2275−2288.

(13) García-Linares, S., Rivera-de-Torre, E., Palacios-Ortega, J., Gavilanes, J. G., and Martínez-del-Pozo, A. (2017) The metamorphic transformation of a water-soluble monomeric protein into an oligomeric transmembrane pore. In *Advances in Biomembranes and Lipid Self-Assembly* (Iglič, A., Rappolt, M., and García-Sáez, A. J., Eds.) pp 51−97, Elsevier.

(14) Shin, M. L., Michaels, D. W., and Mayer, M. M. (1979) Membrane damage by a toxin from the sea anemone Stoichactis helianthus. II. Effect of membrane lipid composition in a liposome system. *Biochim. Biophys. Acta, Biomembr. 555*, 79−88.

(15) Belmonte, G., Pederzolli, C., Maček, P., and Menestrina, G. (1993) Pore formation by the sea anemone cytolysin equinatoxin-II in

red blood cells and model lipid membranes. *J. Membr. Biol. 131*, 11−22.
(16) Valcarcel, C. A., Dalla Serra, M., Potrich, C., Bernhart, I., Tejuca, M., Martínez, D., Pazos, F., Lanio, M. E., and Menestrina, G. (2001) Effects of lipid composition on membrane permeabilization by sticholysin I and II, two cytolysins of the sea anemone Stichodactyla helianthus. *Biophys. J. 80*, 2761−2774.
(17) Meinardi, E., Florin-Christensen, M., Paratcha, G., Azcurra, J. M., and Florin-Christensen, J. (1995) The molecular basis of the self/nonself selectivity of a coelenterate toxin. *Biochem. Biophys. Res. Commun. 216*, 348−354.
(18) Simon, G., and Rouser, G. (1967) Phospholipids of the sea anemone: Quantitative distribution; absence of carbon-phosphorus linkages in glycerol phospholipids; structural elucidation of ceramide aminoethylphosphonate. *Lipids 2*, 55−59.
(19) Meneses, P., and Navarro, N. (1992) 31P NMR phospholipid profile study of seven sea anemone species. *Comparative Biochemistry Physiology Part B: Comparative Biochemistry 102*, 403−407.
(20) Alm, I., García-Linares, S., Gavilanes, J. G., Martínez-del-Pozo, A., and Slotte, J. P. (2015) Cholesterol stimulates and ceramide inhibits sticholysin II-induced pore formation in complex bilayer membranes. *Biochim. Biophys. Acta, Biomembr. 1848*, 925−931.
(21) García-Linares, S., Maula, T., Rivera-de-Torre, E., Gavilanes, J. G., Slotte, J. P., and Martínez-del-Pozo, A. (2016) Role of the tryptophan residues in the specific interaction of the sea anemone Stichodactyla helianthus's actinoporin Sticholysin II with biological membranes. *Biochemistry 55*, 6406−6420.
(22) Malovrh, P., Viero, G., Serra, M. D., Podlesek, Z., Lakey, J. H., Maček, P., Menestrina, G., and Anderluh, G. (2003) A novel mechanism of pore formation: membrane penetration by the N-terminal amphipathic region of equinatoxin. *J. Biol. Chem. 278*, 22678−22685.
(23) Hong, Q., Gutiérrez-Aguirre, I., Barlič, A., Malovrh, P., Kristan, K., Podlesek, Z., Maček, P., Turk, D., González-Mañas, J. M., Lakey, J. H., and Anderluh, G. (2002) Two-step Membrane Binding by Equinatoxin II, a Pore-forming Toxin from the Sea Anemone, Involves an Exposed Aromatic Cluster and a Flexible Helix. *J. Biol. Chem. 277*, 41916−41924.
(24) Kristan, K., Podlesek, Z., Hojnik, V., Gutiérrez-Aguirre, I., Guncar, G., Turk, D., González-Mañas, J. M., Lakey, J. H., Maček, P., and Anderluh, G. (2004) Pore Formation by Equinatoxin, a Eukaryotic Pore-forming Toxin, Requires a Flexible N-terminal Region and a Stable b-Sandwich. *J. Biol. Chem. 279*, 46509−46517.
(25) Alegre-Cebollada, J., Martínez-del-Pozo, A., Gavilanes, J. G., and Goormaghtigh, E. (2007) Infrared spectroscopy study on the conformational changes leading to pore formation of the toxin sticholysin II. *Biophys. J. 93*, 3191−3201.
(26) Alegre-Cebollada, J., Cunietti, M., Herrero-Galán, E., Gavilanes, J. G., and Martínez-del-Pozo, A. (2008) Calorimetric scrutiny of lipid binding by sticholysin II toxin mutants. *J. Mol. Biol. 382*, 920−930.
(27) García-Linares, S., Castrillo, I., Bruix, M., Menéndez, M., Alegre-Cebollada, J., Martínez-del-Pozo, A., and Gavilanes, J. G. (2013) Three-dimensional structure of the actinoporin sticholysin I. Influence of long-distance effects on protein function. *Arch. Biochem. Biophys. 532*, 39−45.
(28) Mancheño, J. M., Martín-Benito, J., Martínez-Ripoll, M., Gavilanes, J. G., and Hermoso, J. A. (2003) Crystal and electron microscopy structures of sticholysin II actinoporin reveal insights into the mechanism of membrane pore formation. *Structure 11*, 1319−1328.
(29) Athanasiadis, A., Anderluh, G., Maček, P., and Turk, D. (2001) Crystal structure of the soluble form of equinatoxin II, a pore-forming toxin from the sea anemone Actinia equina. *Structure 9*, 341−346.
(30) Hinds, M. G., Zhang, W., Anderluh, G., Hansen, P. E., and Norton, R. S. (2002) Solution structure of the eukaryotic pore-forming cytolysin equinatoxin II: Implications for pore formation. *J. Mol. Biol. 315*, 1219−1229.
(31) Pettersen, E. F., Goddard, T. D., Huang, C. C., Couch, G. S., Greenblatt, D. M., Meng, E. C., and Ferrin, T. E. (2004) UCSF Chimera–a visualization system for exploratory research and analysis. *J. Comput. Chem. 25*, 1605−1612.
(32) Mechaly, A. E., Bellomio, A., Gil-Carton, D., Morante, K., Valle, M., González-Mañas, J. M., and Guerin, D. M. (2011) Structural insights into the oligomerization and architecture of eukaryotic membrane pore-forming toxins. *Structure 19*, 181−191.
(33) Tanaka, K., Caaveiro, J. M., Morante, K., González-Mañas, J. M., and Tsumoto, K. (2015) Structural basis for self-assembly of a cytolytic pore lined by protein and lipid. *Nat. Commun. 6*, 6337.
(34) Alegre-Cebollada, J., Clementi, G., Cunietti, M., Porres, C., Oñaderra, M., Gavilanes, J. G., and Martínez-del-Pozo, A. (2007) Silent mutations at the 5′-end of the cDNA of actinoporins from the sea anemone Stichodactyla helianthus allow their heterologous overproduction in Escherichia coli. *J. Biotechnol. 127*, 211−221.
(35) Rivera-de-Torre, E., Palacios-Ortega, J., García-Linares, S., Gavilanes, J. G., and Martínez-del-Pozo, A. (2017) One single salt bridge explains the different cytolytic activities shown by actinoporins sticholysin I and II from the venom of Stichodactyla helianthus. *Arch. Biochem. Biophys. 636*, 79−89.
(36) Lakowicz, J. R. (2006) *Principles of fluorescence spectroscopy*, Springer Science & Business Media.
(37) Valeur, B., and Berberan-Santos, M. N. (2012) *Molecular Fluorescence, Principles and Applications*, Wiley-VCH Verlag GmbH & Co. KGaA.
(38) Runnels, L. W., and Scarlata, S. F. (1995) Theory and application of fluorescence homotransfer to melittin oligomerization. *Biophys. J. 69*, 1569−1583.
(39) De los Ríos, V., Mancheño, J. M., Martínez-del-Pozo, A., Alfonso, C., Rivas, G., Oñaderra, M., and Gavilanes, J. G. (1999) Sticholysin II, a cytolysin from the sea anemone Stichodactyla helianthus, is a monomer-tetramer associating protein. *FEBS Lett. 455*, 27−30.
(40) Rivera-de-Torre, E., García-Linares, S., Alegre-Cebollada, J., Lacadena, J., Gavilanes, J. G., and Martínez-del-Pozo, A. (2016) Synergistic action of actinoporin isoforms from the same sea anemone species assembled into functionally active heteropores. *J. Biol. Chem. 291*, 14109−14119.
(41) García-Linares, S., Rivera-de-Torre, E., Morante, K., Tsumoto, K., Caaveiro, J. M., Gavilanes, J. G., Slotte, J. P., and Martínez-del-Pozo, Á. (2016) Differential effect of membrane composition on the pore-forming ability of four different sea anemone actinoporins. *Biochemistry 55*, 6630−6641.
(42) Kristan, K. C., Viero, G., Dalla Serra, M., Maček, P., and Anderluh, G. (2009) Molecular mechanism of pore formation by actinoporins. *Toxicon 54*, 1125−1134.
(43) Hervis, Y. P., Valle, A., Dunkel, S., Klare, J. P., Canet, L., Lanio, M. E., Alvarez, C., Pazos, I. F., and Steinhoff, H.-J. (2019) Architecture of the pore forming toxin sticholysin I in membranes. *J. Struct. Biol. 208*, 30−42.
(44) Subburaj, Y., Ros, U., Hermann, E., Tong, R., and García-Sáez, A. J. (2015) Toxicity of an a-pore-forming toxin depends on the assembly mechanism on the target membrane as revealed by single-molecule imaging. *J. Biol. Chem. 290*, 4856−4865.
(45) Björkbom, A., Róg, T., Kaszuba, K., Kurita, M., Yamaguchi, S., Lönnfors, M., Nyholm, T. K., Vattulainen, I., Katsumura, S., and Slotte, J. P. (2010) Effect of Sphingomyelin Headgroup Size on Molecular Properties and Interactions with Cholesterol. *Biophys. J. 99*, 3300−3308.

https://dx.doi.org/10.1021/acs.biochem.0c00840
Biochemistry 2021, 60, 314−323

Supplementary Information File for

Oligomerization of sticholysins from Förster resonance energy transfer

Juan Palacios-Ortega,*[1,2] Esperanza Rivera-de-Torre,[1] Sara García-Linares,[1] José G. Gavilanes,[1] Álvaro Martínez-del-Pozo,[1] J. Peter Slotte[2]

[1] Depto. de Bioquímica y Biología Molecular, Universidad Complutense, Madrid, Spain
[2] Biochemistry, Faculty of Science and Engineering, Åbo Akademi University, Turku, Finland

Corresponding author: Juan Palacios-Ortega
Email: juan.palaciosb1a@gmail.com (ORCID 0000-0002-4629-0221)

This file includes:

Figures S1 to S10

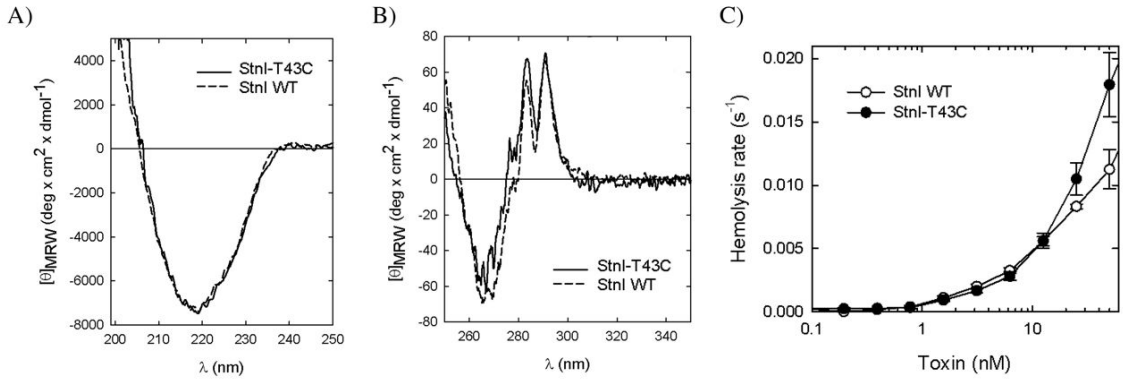

Figure S1. Structural and functional characterization of the StnI-T43C mutant. A) Far-UV circular dichroism of the mutant StnI-T43C (solid line), compared with that of the WT variant of StnI (dashed line). B) Near-UV circular dichroism of StnI-T43C. compared to that of StnI-WT (lines as in A). C) Hemolysis rates displayed by preparations of erythrocytes when exposed to different concentrations of StnI WT (open circles) or StnI-T43C (solid circles).

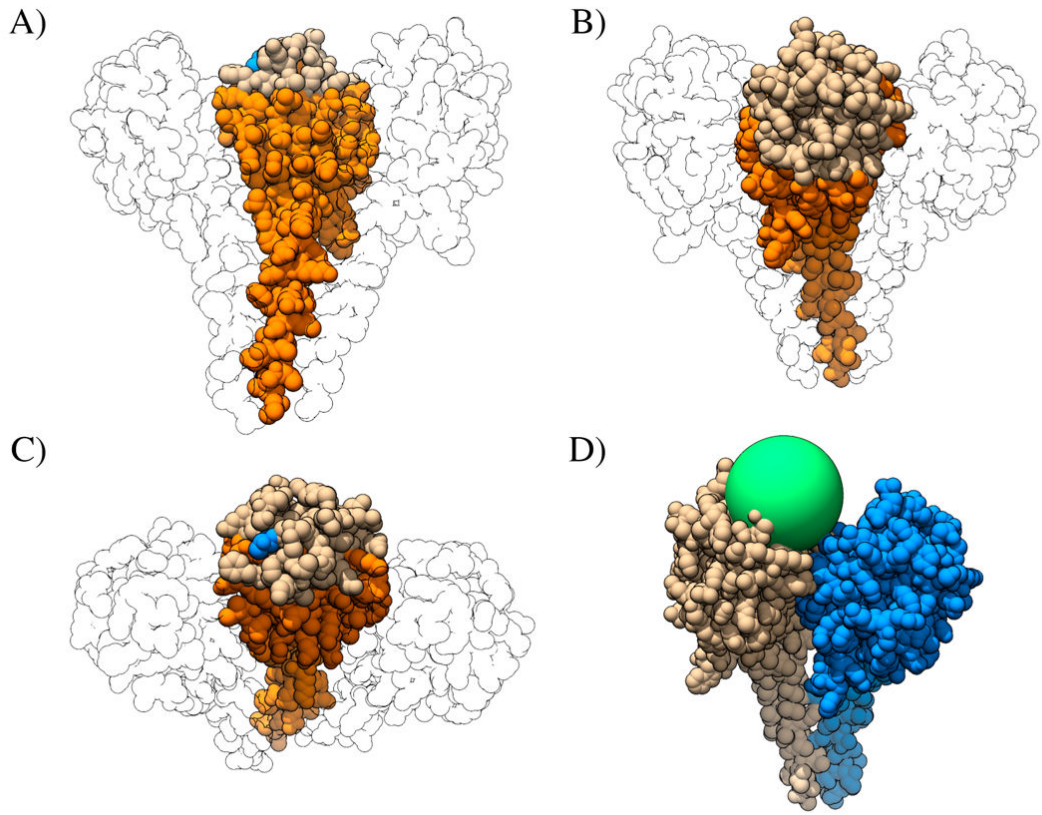

Figure S2. A) Space-filling representation of three StnI monomers (PDB ID: 2KS4) fitted to the structure of the octameric pore of FraC (PDB ID: 4TSY), as viewed from the lumen of the pore. The residues that were discarded due to their potential implication in the functionality of StnI, i.e. membrane binding, structural transition of the N-terminal α-helix, and monomer-monomer interactions, are shown in orange. Those that were supposedly not involved in the aforementioned functions are shown in tan. Residue T43 is highlighted in blue. B) Back view of the same structure depicted in A). C) Top view of the structure depicted in A). D) Two monomers of the structure in A) have been isolated and, in one of them, a sphere of 12 Å radius, corresponding to the approximate maximum length of the probes used, has been centered at the oxygen atom of T43. It can be seen that the probe would not interfere in the interaction with the neighboring monomer.

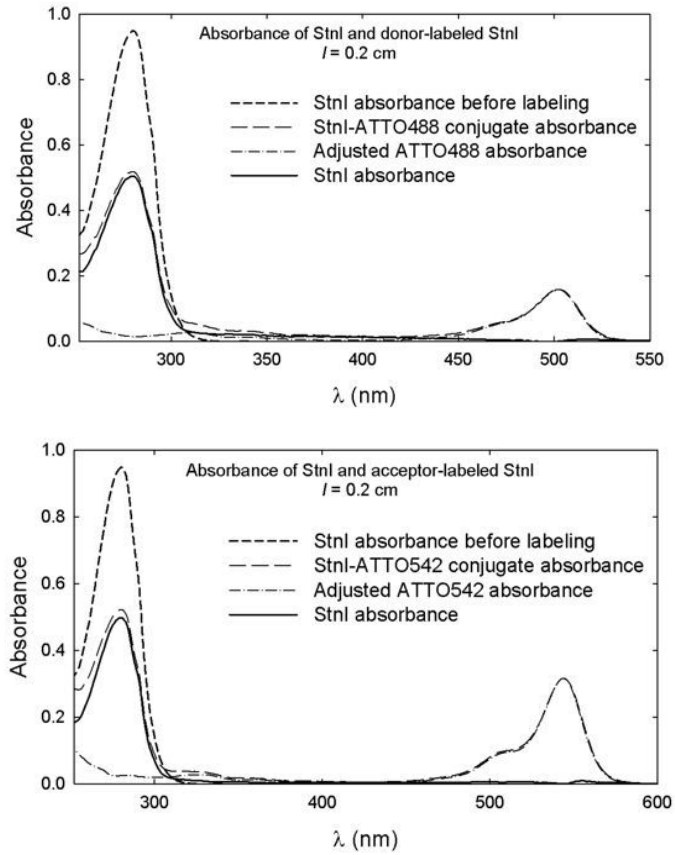

Figure S3. Absorption spectra of StnI-T43C before and after labeling with ATTO probes. Top: absorbance of StnI-T43C before and after labeling with ATTO-488. The absorption of the protein corrected for probe contributions is also shown. Bottom: absorbance of StnI-T43C before and after labeling with ATTO-542. The absorption of the protein corrected for probe contributions is also shown. Notice the different scale on the *x*-axis between both graphs.

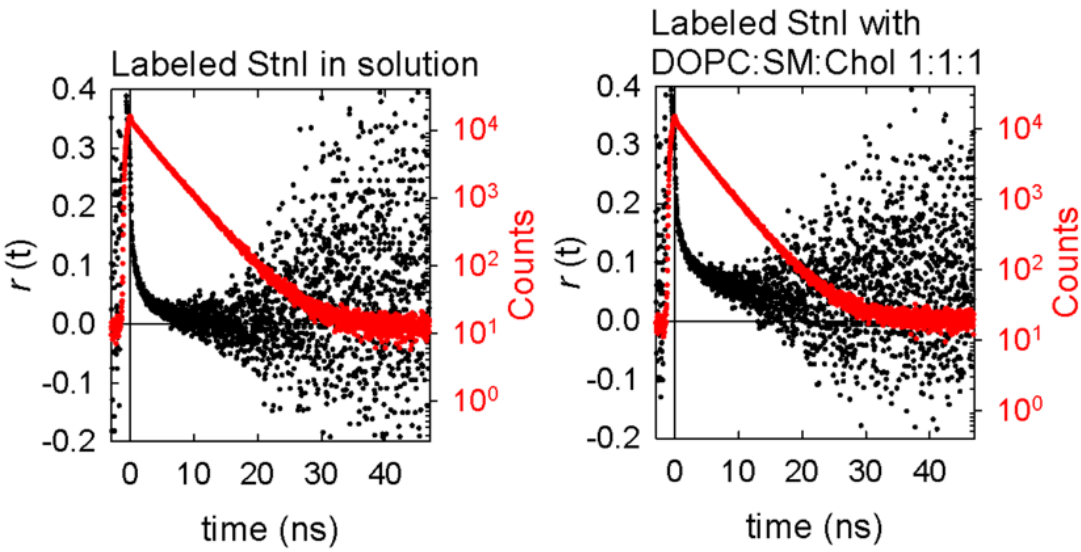

Figure S4. Anisotropy (black) and intensity (red) decays of ATTO-488 labeled StnI-T43C in solution (left) and bound to DOPC:SM:Chol (1:1:1 molar ratio) LUVs (right). In both cases, the anisotropy decay is over before the intensity decay, indicating that the order parameter κ^2, required to calculate the Förster distance (R_0) can be set to 2/3, according to the dynamic isotropic limit. Notice the logarithmic scale for the intensity decay.

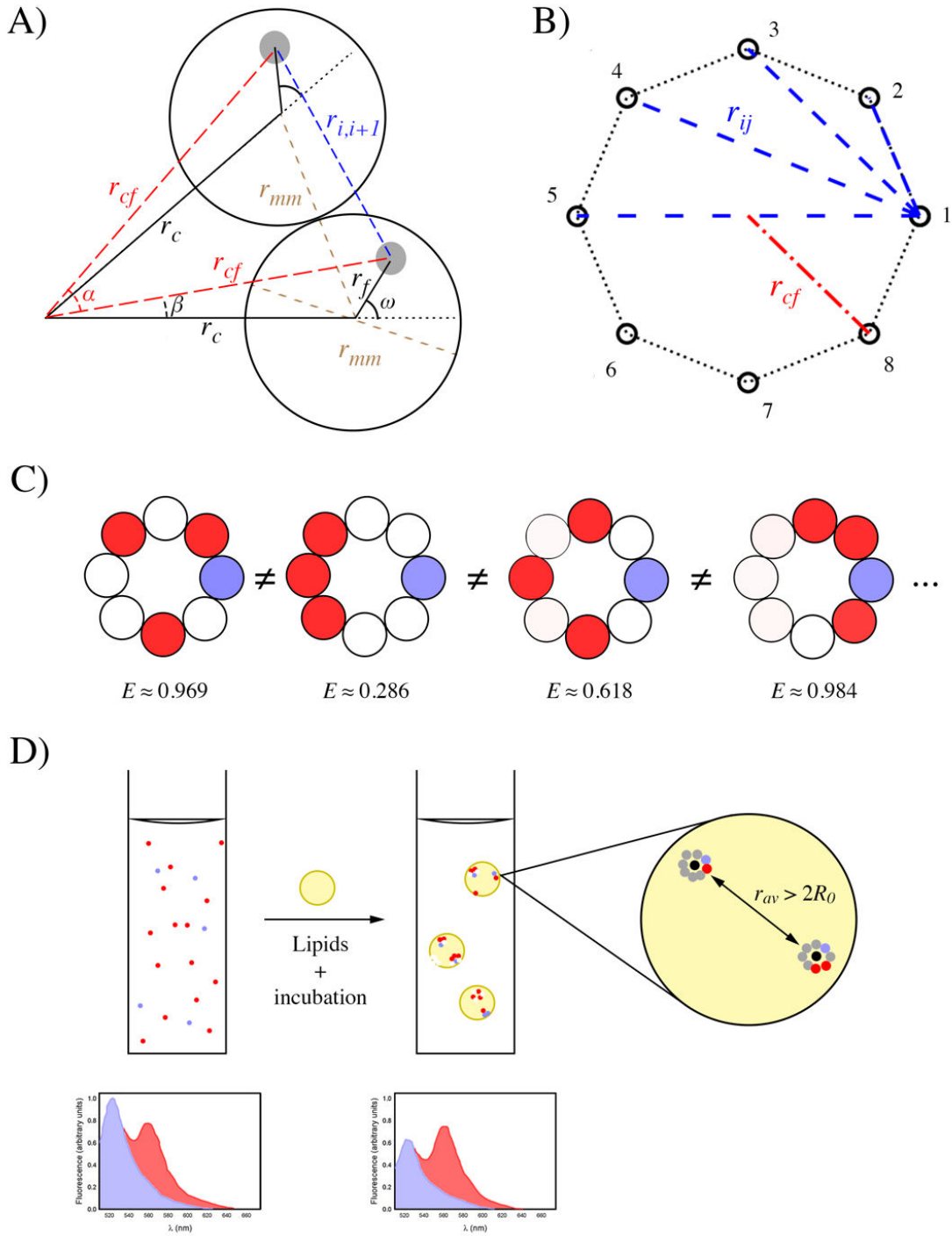

Figure S5. A) Representation of the geometrical arrangement of the two labeled proteins in a given n-mer. Only two subunits are shown. Fluorophores are depicted in grey. Parameters shown are those in eqs. 5 to 7. The value of r_{mm}, the distance between the centers of two adjacent subunits, is equal to the diameter of one subunit. This cannot be applied to the position of the fluorophores, since they are not placed at the center of the protein. Instead, they have an offset of r_f, at an angle ω, For that reason, $r_{mm} \neq r_{i,i+1}$. This is solved by using eq. 6., which enables to calculate r_{cf}, enabling to calculate the correct values for $r_{i,j}$. The angle α has a value of $2\pi/N$ radians, where N is the number of subunits of the oligomer. The angle β represents the offset of r_{cf} relative to r_c, and is a function of r_c, r_f, and ω. It is because of this offset that r_{mm} and $r_{i,i+1}$ are not parallel. This scheme is valid for any n-mer. B) Representation of an exemplary oligomer, an octamer. Circles represent fluorophores in oligomerizing proteins (omitted). The

parameter $r_{i,j}$ is represented by blue dashed lines. Some are omitted for clarity. C) Following the example given in the main text of eight subunits, with the N_D = 1 (in purple), N_A = 3 (in red), and N_U = 4 (in white), we have that those can assemble into 35 possible arrangements (discarding those that only differ by circular symmetries). Four of those arrangements are depicted in the figure. In our model, we assume that the probability of those subunits (N_D = 1, N_A = 3, and N_U = 4) assembling into any of the 35 possible arrangements is the same. However, the FRET that a donor experiences from each arrangement is different (see figure), hence the need to average them. Then, that average need to be weighted, since the probability of an assembly as those considered (regardless of the arrangement) is different to that of those with a composition, say, N_D = 1, N_A = 1, and N_U = 6. Those probabilities depend on the fractional population of donor- and acceptor-labeled proteins in the sample. D) Scheme of the experimental design. Non-labeled toxins, together with donor- and acceptor-labeled toxins are placed in a cuvette, and the emission is registered (colors as in C). After that, lipids are added. The sample is left for a few minutes to ensure that binding is complete. After that, emission is registered again, revealing FRET from a diminished donor emission. The L/P ratio is such that the average distance, r_{av}, between oligomers is, at least, larger than $2R_0$.

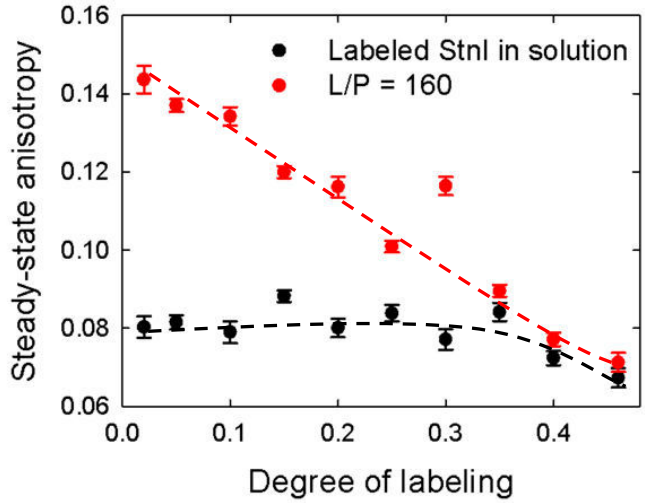

Figure S6. Steady-state anisotropy was dependent on the degree of labeling of StnI with ATTO-488, in solution (solid black dots, the dashed line is a guide to the eye) and, especially, when bound to membranes (solid red dots, the dashed line is a guide to the eye).

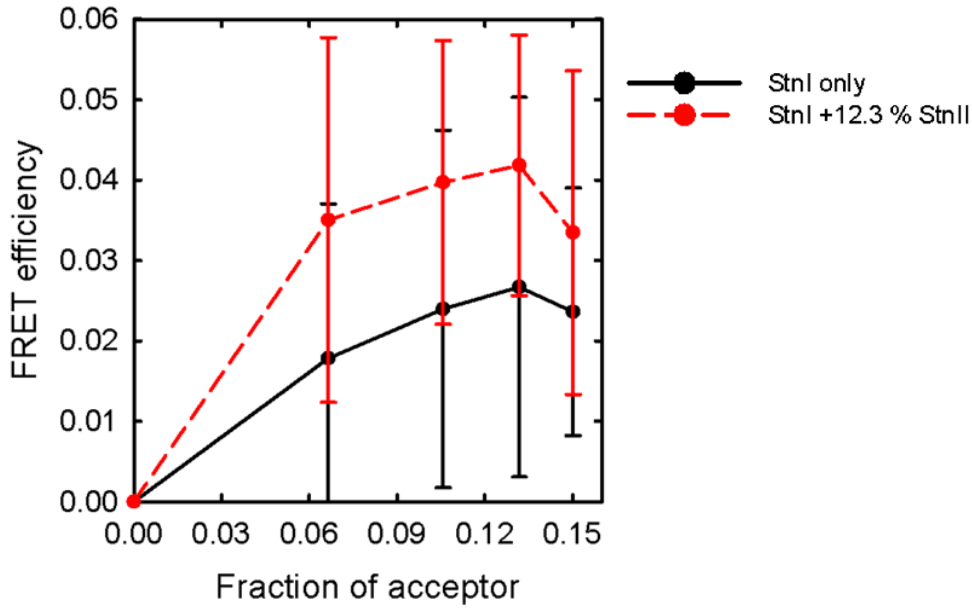

Figure S7. FRET efficiency observed for donor-labeled StnI with WT StnI (solid black trace) or with WT StnII (dashed red trace). Initially, both samples contained 11.9% of donor-labeled StnI, and 29.1% of the indicated WT variant, with the remainder being unlabeled StnI-T43C. The samples were then titrated with acceptor-labeled StnI (labeled 25.9%) to a final composition of 5% donor, 15% acceptor, and 12.3% of the WT variant used, the remainder being unlabeled StnI-T43C. Values are average of n = 3 (SD).

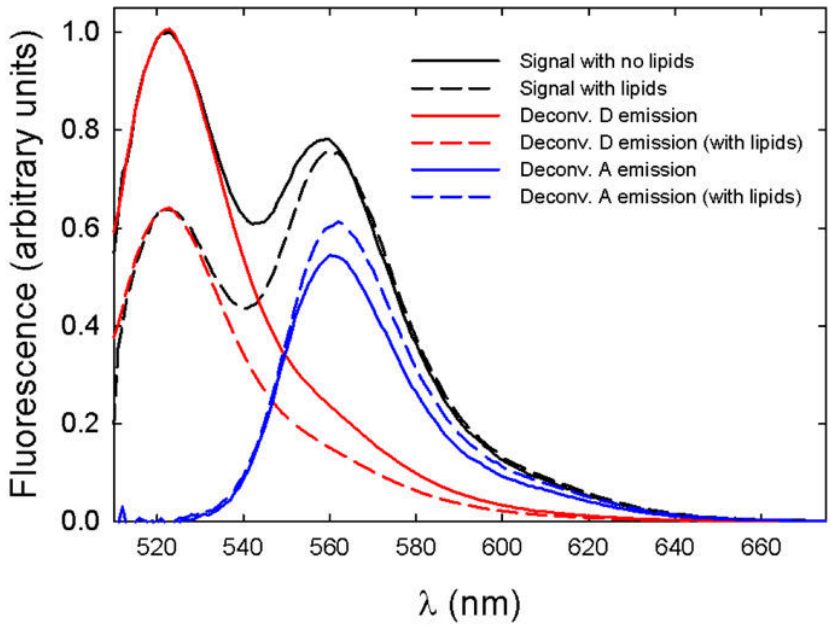

Figure S8. Example of signal deconvolution. The represented spectra have all already been corrected for arbitrary signal contributions, such as Raman peak and scattering from lipids. The deconvoluted emissions of the donor (red) were used to calculate the FRET efficiency for each sample.

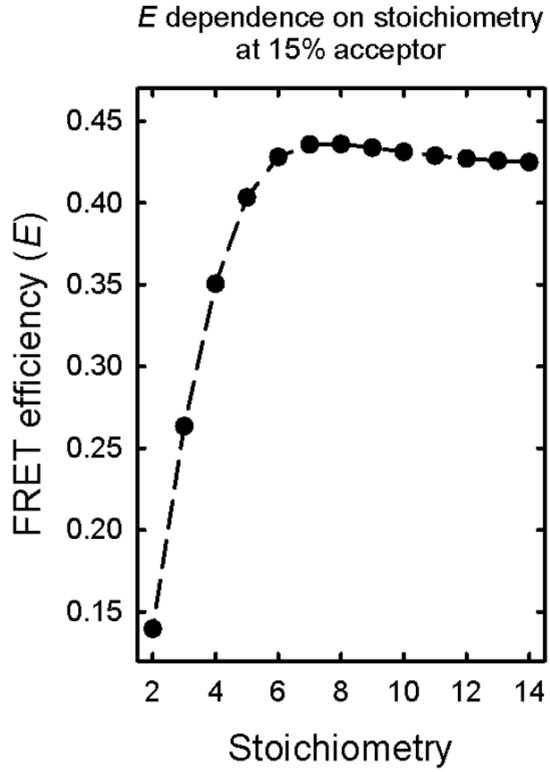

Figure S9. Predicted change of the FRET efficiency at 15% acceptor content in the sample as a function of complex stoichiometry, given the physical restrictions imposed by the size of sticholysins, the labeling position, and the photophysical characteristics of the labels used. The differences in the predictions were also reduced as the acceptor content was increased.

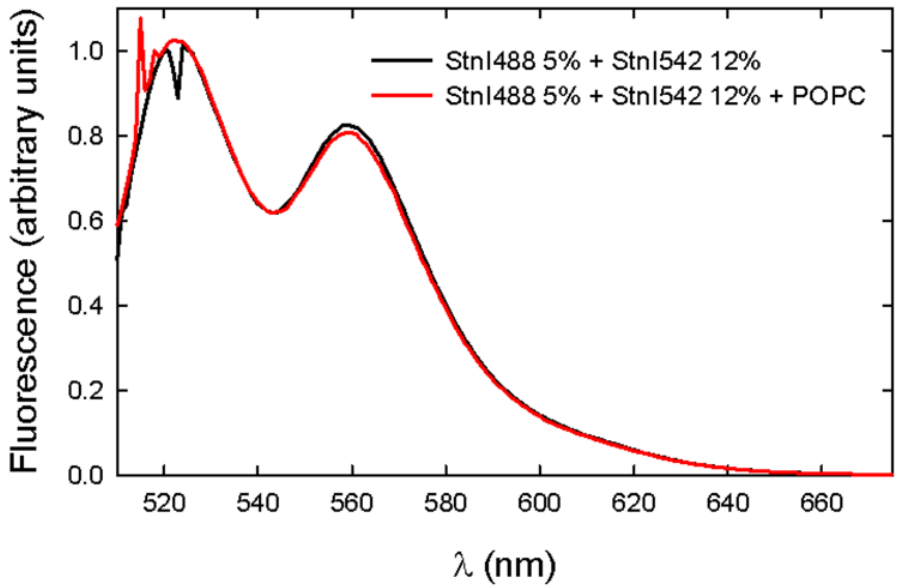

Figure S10. Fluorescence emission of a sample containing 5% of StnI488 and 12% of StnI542 before (black line) and after (red line) incubation with POPC vesicles to a final L/P molar ratio of 320. Emission did not change after the inclusion of lipids, revealing absence of membrane-binding and associated FRET.